Basic Principles of Wave Propagation

Gerard T. Schuster

September 5, 2016

Contents

Preface

This book describes basic seismology in the context of earthquakes and exploration seismology. The first part of the book describes the basic physics of acoustic wave propagation, which includes Fermat, principle Huygens principle, Green's theorem, Snell's law, reflection and transmission coefficients for a layered medium, Rayleigh resolution, diffraction, specular rays, eikonal equation, ray tracing, the acoustic wave equation in space-time and the Helmholtz equation in space-frequency. A general solution of the wave equation can be obtained by using the acoustic reciprocity equation of convolution type, otherwise known as Green's theorem.

The second part of the book describes the numerical modeling of the eikonal and acoustic wave equations using the finite difference method. The eikonal equation is used to describe rays and compute traveltimes of arrivals, while the wave equation solutions by finite differences provide the full seismograms. These methods are then used to image the earth's parameter distributions using traveltime tomography and migration, as described in the third part of the book.

The last part of the book describes the physics of elastic wave propagation. The reciprocity equation of convolution and correlation types are derived, and their use in the context of interferometry is described.

This book is written at the level where it can be understood by physical scientists who have some familiarity with the principles of wave propagation, Fourier transforms, and numerical analysis. The book can be taught as a one-semester course for advanced seniors and graduate students in the physical sciences and engineering. Exercises are given at the end of each chapter, and many chapters come with MATLAB codes that illustrate important ideas.

Part I

Physics of Acoustic Wave Propagation

Chapter 1

Physics of Acoustic Wave Propagation

The theory of acoustic wave propagation is now described. This is an important theory in its own right because explorationists often assume that wave propagation in rocks can be approximated by acoustic theory so that they can simplify their data processing algorithms. The acoustic approximation says that shear effects in the data are negligible and the dominant wave type is a *compressional* wave, a wave where the particle motion is parallel to the propagation direction. This is an acceptable approximation for somewhat layered media, near-offset traces recorded by vertical component phones, and surface-wave filtered data. To deepen our understanding of this acoustic approximation we now present an overview of the physics of the acoustic wave equation. A good background reference book is Aki and Richards (1980) and Kinlser and Frey (1961).

1.1 Acoustic Media and Acoustic Waves

Assume a compressible, non-viscous (i.e., no attenuation) fluid with no shear strength and in equilibrium (i.e., no inertial forces); this will be denoted as an **acoustic medium**. Small localized displacements of the fluid will propagate as an acoustic wave, also known as a compressional wave. Due to the lack of shear strength, localized deformations of the medium do not result in shear deformations but instead cause changes in the fluid element's volume, as shown in Figure 1.1.

The equilibrium force/unit area on the faces of a volume element will be called the time-independent equilibrium pressure $P_{eq}(\mathbf{r})$, while the *change* in pressure due to a localized compressional wave will be denoted as $P(\mathbf{r}, t)$. For example, the atmospheric pressure decreases with increases in elevation and can be considered to be independent of time. If I begin talking, however, I excite transient acoustic waves $P(\mathbf{r}, t)$ that locally disturb the equilibrium pressure outside my lips by fresh injections or extractions of air from my lungs. To restore the system's equilibrium this local disturbance propagates outward from the source and is known as a **pressure wave**.

Snapshots of the particle distribution for the condensation and rarefaction portions of wave propagation are shown in Figure 1.1. In the compressional case the element volume is

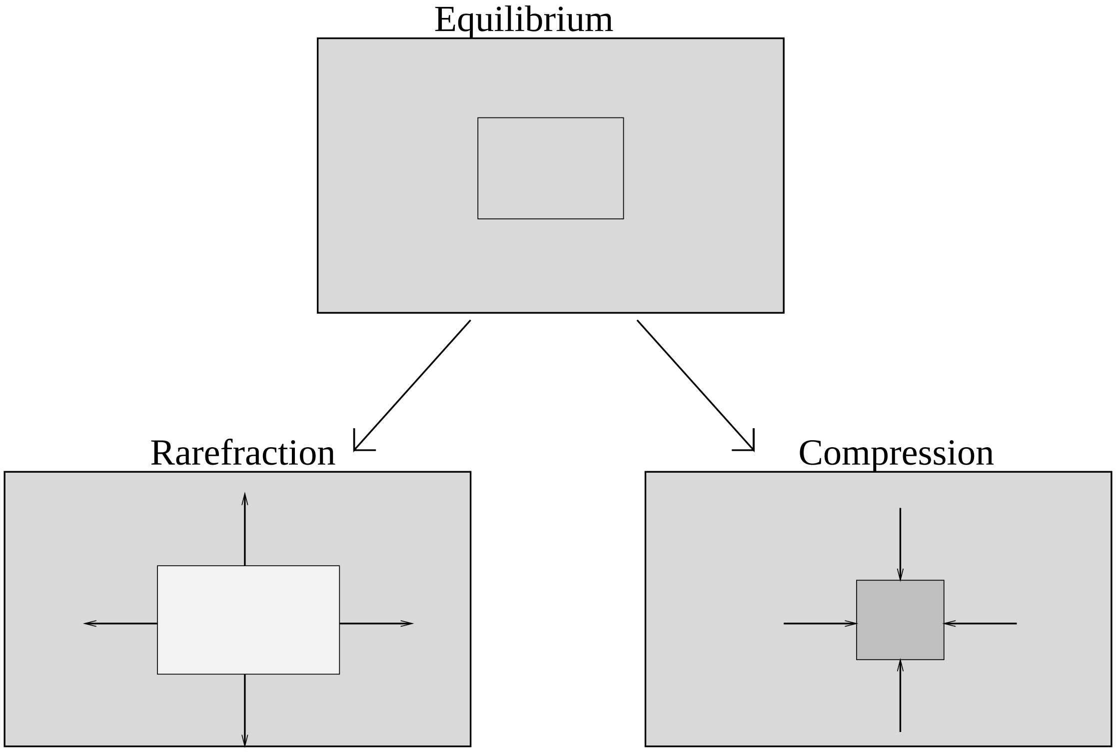

Figure 1.1: Cube of air in (top) equilibrium and (bottom) disturbed from equilibrium. The lower left diagram depicts a rarefaction where the surrounding medium pulls the cube (i.e., smaller cube outlined by dark lines) into a larger volume so that the air density in the white cube is less than that in the surrounding medium. The cause of his "pull" is that the pressure in the ambient medium is less than that of the air inside the cube. The lower right diagram is similar, except the surrounding medium compresses the cube into a smaller volume resulting in denser air. In this case the pressure in the ambient medium is greater than that inside the small cube.

filled with denser (shaded) air while in the rarefaction case the element volume has lighter (unshaded) air than the surrounding medium. We can physically create the condensation wave just outside our lips by injecting air from our lungs into the medium (HELLLL!), and the rarefaction wave by sucking air into our lungs (UHHHHH!). Using a spring-mass model, rarefactions are modeled by pulling a spring (i.e., tension) and condensations by compressing a spring (compressions).

1.2 Acoustic Hooke's Law: $P = -\kappa\nabla \cdot \mathbf{u}$

Hooke's law for an acoustic medium says that stress is linearly proportional to strain for small "enough" strains. A simple 1-D example will first be given to demonstrate Hooke's law, and then we will apply it to the case of an acoustic medium.

1. **1-D Spring:** The force on a mass connected to a spring disturbed from equilibrium (see Figure 1.2) is given by

$$\mathbf{F} \;=\; -k(du/l)\hat{k}, \tag{1.1}$$

where du is the displacement from equilibrium[1], k is the spring constant, l is the length of the spring in equilibrium, and $\hat{k}$ is the downward point unit vector in Figure 1.2. The ratio du/l is normalized by the length of the spring l and is known as the compressional strain of the spring model[2]. Note that in the equilibrium position there is no motion because the gravitational force balances the spring (i.e., elastic) force. When disturbed, the equation of equilibrium is given by the above equation where **F** is the sum of all the other forces acting on the weight. If the elastic force is non-zero (e.g., pull the mass downward and let go!) then this unbalanced force will be equilibrated by the inertial force $m\partial^2 u/\partial t^2$, which will pull the mass back towards its equilibrium position.

2. **3-D Acoustic Springy Cube:** A solid cube of acoustic material can be deformed by external forces acting on its faces. If the deformation is "small" enough then Hooke's law says that the measure of deformation can be linearly related to the force/area on each face. In the 3D case, the measure of deformation is the normalized volume change of the cube dV/V where V is the original volume and dV is the volume change after the disturbance. Therefore Hooke's law becomes,

$$P \;=\; -\kappa dV/V, \tag{1.2}$$

where κ is the bulk modulus. Note that a volume change is the 3-D equivalent of a 1-D displacement change.

Figure 1.2 shows that the relative volume change dV/V is given by:

$$\begin{aligned} \frac{dV}{V} &= \frac{-\overbrace{dxdydz}^{original} + \overbrace{(dx+\delta u)(dy+\delta v)(dz+\delta w)}^{deformed}}{dxdydz}, \\ &= \frac{\delta udydz + \delta vdxdz + \delta wdxdy}{dxdydz} + O(2nd - order\ terms) \\ &\approx \frac{\partial u}{\partial x} + \frac{\partial v}{\partial y} + \frac{\partial w}{\partial z} = \nabla \mathbf{u}. \end{aligned} \tag{1.3}$$

Substituting equation 1.3 into equation 1.2 yields:

$$P \;=\; -\kappa(x,y,z)\nabla \cdot \mathbf{u} + S(x,y,z,t), \tag{1.4}$$

where $\mathbf{u} = (u, v, w)$ are the cartesian components of displacement along the x, y, and z axes and $S(x,y,z,t)$ is a time-dependent **body source** term that is independent of

---

[1] The convention we will adopt here is that positive values of dl indicate downward displacements, and negative values indicate upward displacements in a right-handed coordinate system.

[2] Normalization is necessary because the strain value should be the same no matter how long the spring. For example, a spring twice as long as the original will deform by $2du$ to give the same strain value as the original spring.

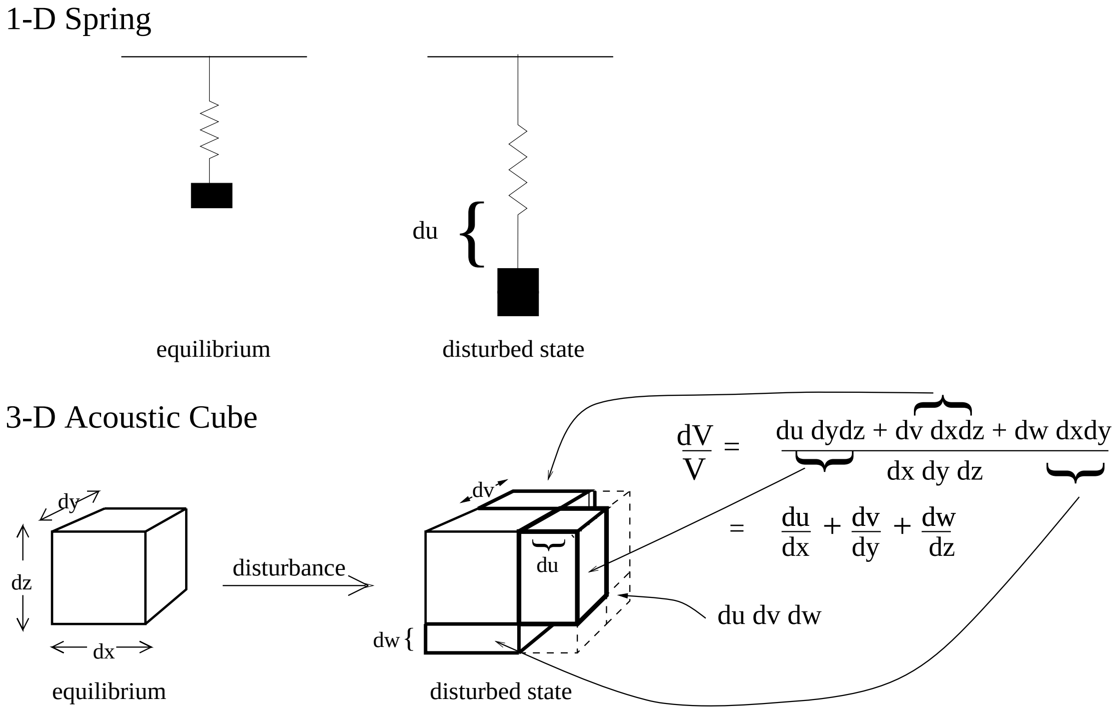

Figure 1.2: (Top) Spring in (left) equilibrium and (right) disturbed from equilibrium. (Bottom) Elemental cube of air in (left) equilibrium and (right) disturbed from equilibrium. In this case the cube has expanded so net tensional forces of surrounding medium must be expanding cube. Note that the 1st-order volume change is outlined by the solid heavy lines, where the higher-order terms are associated with the corner parts.

the displacement field[3]. Often the spatial and temporal variables are suppressed for the P and $\mathbf{u}$ field variables, but the spatial coordinates are explicitly expressed for the bulk modulus to remind the reader that the physical properties of the medium can vary with location[4].

Note:

- Neglecting second-order terms is the small displacement approximation, valid for $\delta V/V < 10^{-4}$ or sound quieter than a jet engine (Kinsler and Frey, 1961).

- Sign convention: P is the force/area that the surrounding medium exerts on the face of the elemental cube, where tensions (force pointing away from cube into external medium) are negative and compressions (force pointing into cube) are positive. For example, the divergence of $\mathbf{u}$ is positive if the volume expands by tensional forces, which is consistent with the sign in equation 1.4.

Geological Strain Exercises

1. Utah and California are moving apart at a rate of roughly 1 cm/year in an E-W direction due to tensional stresses in the Intermountain Basin region. If the distance between San Francisco, California and Salt Lake City, Utah is approximately 1600 km what is the tensional strain rate (i.e., strain per unit time) in Salt Lake City for this movement? Show work. Reno is about midway between San Francisco and Salt Lake City; what is the strain rate measured in Reno compared to that in Salt Lake City.

2. As you will soon find out, a plane P-wave solution to the acoustic wave equation is $\mathbf{u}(x, y, z, t) = \cos(kx - \omega t)\hat{\mathbf{i}}$, where ω is angular frequency and k is the wavenumber; here $\mathbf{u}$ is the displacement deformation of the medium in the x-direction, and $v = w = 0$ for all time and space. Does the volume of a small acoustic cube (with deformations governed by $\mathbf{u}(x, y, z, t) = \cos(kx - \omega t)\hat{\mathbf{i}}$) change with time as a plane wave passes through the medium? For $k = 2\pi$ and $\omega = 2\pi$ plot $\mathbf{u}(x, y, z, t)$ in the x-coordinate for $-6 < x < 6$ for t=0. Also, plot out $\nabla \cdot \mathbf{u}$, which indicates the relative volume change of a small cube (recall negative values of dV/V indicate compressions and positive values indicate expansions).

3. From your previous plots, roughly draw the deformed shape of the small acoustic cube for different values of $u(x, y, z, t)$ in your plot. At what spatial increments do the cube volumes get smaller and which spatial increments do they expand from the equilibrium position.

4. Repeat above exercise except use t=.5 for the plots.

---

[3] For example, heating up the cube will cause it to expand and this body force is independent of the acoustic deformation force. Another example, $S(x, y, z, t)$ can be a source that injects material into the medium such as an air gun used for marine seismic surveys.

[4] The bulk modulus κ is assumed to be time independent for acoustic wave propagation in rocks.

1.3 Newton's Law: $\partial P/\partial x = -\rho(x,y,z)\partial^2\mathbf{u}/\partial t^2$

The external force on an acoustic cube is illustrated in Figure 1.3. These forces have a non-zero gradient along the x-axis, and so there is a net elastic force imposed upon the cube by the external medium[5]. This net force must be balanced by an inertial force (i.e., force associated with acceleration) so that Newton's law says that the x-component of acoustic force is given by:

$$\overbrace{[P(x+dx,y,z,t) - P(x,y,z,t)]dydz}^{}\, Net\ F_x\ on\ Cube\ Faces \quad \approx \quad -\overbrace{[\rho(x,y,z)dxdydz]}^{mass\ of\ cube}\, \ddot{u}(x,y,z,t), \tag{1.5}$$

where the double dot corresponds to two time derivatives. Expanding the LHS in a Taylor series about the point (x,y,z) we get

$$\begin{aligned}[P(x,y,z,t) - P(x,y,z,t) + \frac{\partial P}{\partial x}dx + high - order\ terms]dydz \quad &\approx \\ -[\rho dxdydz]\ddot{u}(x,y,z,t); \quad & \end{aligned} \tag{1.6}$$

dividing by $dxdydz$ and neglecting higher-order terms we get the x-component part of the acoustic wave equation:

$$\frac{\partial P(x,y,z,t)}{\partial x} \quad = \quad -\rho(x,y,z)\ddot{u}(x,y,z,t). \tag{1.7}$$

For an arbitrary force distribution the vector form of Newton's law in a linear acoustic medium is:

$$\nabla P \quad = \quad -\rho(x,y,z)\ddot{\mathbf{u}}(x,y,z,t), \tag{1.8}$$

where $\ddot{\mathbf{u}}(x,y,z,t) = (\ddot{u},\ddot{v},\ddot{w})$ is the particle acceleration vector and $\nabla P = (\partial P/\partial x, \partial P/\partial y, \partial P/\partial z)$.

Note:

- The minus sign is used so that we are consistent with the notation for pressure. If the external presume $P(x+dx,y,z,t)$ is positive and less than $P(x,y,z,t)$ in Figure 1.3 then the cube should accelerate to the left, which it will according to the above form of Newton's Law.

1.4 Acoustic Wave Equation

Notice that the vectorial equation 1.8 consists of 3 component equations, yet there are 4 unknown field values: (u,v,w) and P. At the least, we need one more equation of constraint in order to identify a unique solution. This extra equation comes from the scalar Hooke's

---

[5] Recall, the net component of force on the cube is determined by adding together the vectorial components of force acting in one direction along each face of the cube.

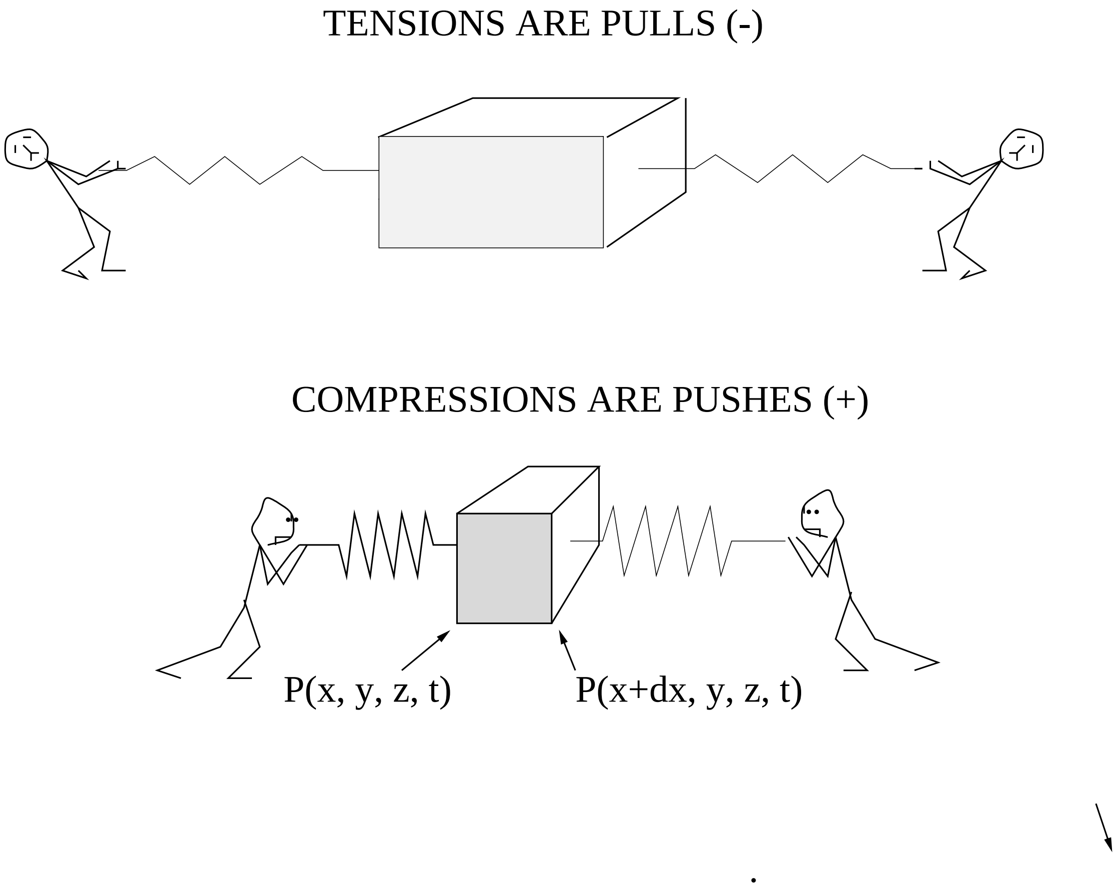

Figure 1.3: External (top) tension and (bottom) compressional forces on an elemental cube. In the lower case there exists a spatial gradient of the disturbed pressure field along the x-axis so that the cube accelerates to the right.

law in equation 1.4. We can combine Hooke's law and the three component equations of Newton's law to get the 1st-order equations of motion; and, as seen below, manipulate them to get a single scalar equation with just one unknown field variable P. Let us now derive the scalar wave equation.

Applying $\partial^2/\partial t^2$ to equation 1.4 and applying $\nabla\cdot$ to equation 1.8 after dividing by $\rho(x,y,z)$ gives the 1st-order acoustic equations of motion:

$$\ddot{P} \;=\; -\kappa(x,y,z)\nabla\cdot\ddot{\mathbf{u}} + \ddot{S}(x,y,z,t), \tag{1.9}$$

$$\nabla\cdot[1/\rho(x,y,z)\nabla P] \;=\; -\nabla\cdot\ddot{\mathbf{u}}, \tag{1.10}$$

where $\ddot{\mathbf{u}}= \partial^2\mathbf{u}/\partial t^2$. Substituting $\nabla\cdot\ddot{\mathbf{u}}$ from equation 1.9 into equation 1.10 yields the 2nd-order acoustic wave equation:

$$\nabla\cdot(1/\rho(x,y,z)\nabla P) - 1/\kappa(x,y,z)\ddot{P} = -\ddot{S}(x,y,z,t)/\kappa(x,y,z), \tag{1.11}$$

which is valid for acoustic wave propagation in arbitrary velocity and density distributions.

Assuming negligible density gradients the above equation reduces to the constant-density scalar wave equation:

$$\nabla^2 P - \tfrac{1}{c^2}\tfrac{\partial^2 P}{\partial t^2} = -\rho(x,y,z)\ddot{S}(x,y,z,t)/\kappa(x,y,z), \tag{1.12}$$

where

$$c = \sqrt{\kappa(x,y,z)/\rho(x,y,z)} \quad , \tag{1.13}$$

and, as we will see in the next section, $c = c(x,y,z)$ describes the compressional wave propagation velocity.

The above equation is known as the inhomogeneous acoustic wave equation for negligible density variations, expressed as

$$\nabla^2 P - c^{-2}\partial^2 P/\partial t^2 = F \quad , \tag{1.14}$$

where $F = -\ddot{S}(x,y,z,t)/c(x,y,z)^2$ is the inhomogeneous source term that specifies the location and time history of the source. For example, F specifies the strength of the hammer blow and its location in an experiment. It is this last equation that is most often used in imaging (i.e., migration) of exploration seismic data.

1.5 Solutions of the Wave Equation

The physics of wave propagation will now be examined using some special solutions to the wave equation 1.14. A harmonic plane wave propagating in a homogeneous medium will be first examined, and then the case of a 2-layered medium will be studied. Figure 1.4 depicts the oscillations of a harmonic wave as recorded by a geophone.

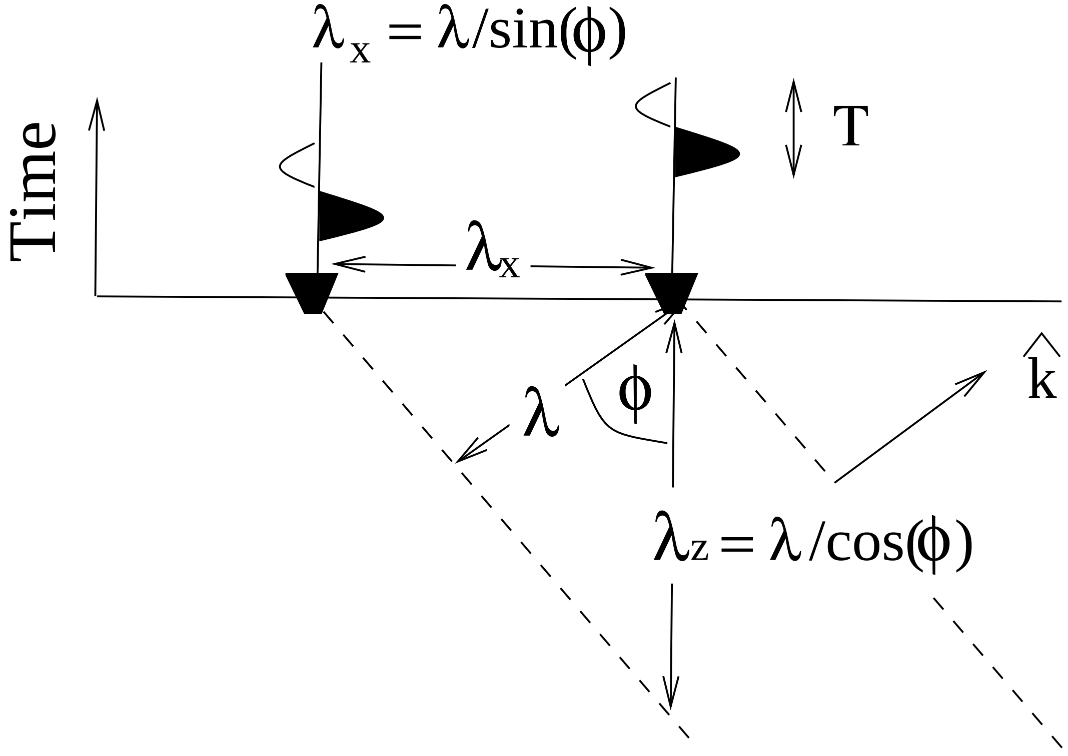

Figure 1.4: Snapshot of a 2-D wave propagating in $x - z$ space along the direction parallel to the wavenumber **k** vector; the upper plot shows the corresponding seismograms in $x - t$ space. The actual propagation velocity is $c = \lambda/T$ and the shortest distance between adjacent dashed lines (i.e., peaks of the wavefront) is defined to be the wavelength λ. The darkened (undarkened) portions of the seismograms correspond to downward (upward) particle displacements of the ground from its equilibrium position. Large amplitude values in a seismogram corresponds to large ground displacements.

1.5.1 1-D Wave Propagation in an Homogeneous Medium

A harmonic wave oscillates with period T and has a temporal dependence usually given by $e^{i\omega t}$, where $\omega = 2\pi/T$ is the **angular frequency** inversely proportional to the **period** T; the units of frequency $f = 1/T$ are cycles/sec while T has units of sec/cycle. The **period** is the shortest time in which the wave repeats one cycle of motion.

A plane propagating wave is one in which the wavefronts (**wavefronts** are defined as the locus of points in (x, y, z) space with constant phase at a fixed time) line up along straight lines, and a **harmonic plane wave** can be described by the following function:

$$P(x,t) \quad = \quad A_0 e^{i(kx-\omega t)}, \tag{1.15}$$

where the constant A_0 is the **amplitude** and the real part $kx - \omega t$ of the exponential argument is defined as the **phase**. Equation 1.15 also solves the homogeneous wave equation 1.12 for the constant amplitude term A_0[6]. A plane wave propagating in the x-direction appears as a rippling rug, where the shortest distance between adjacent crests is defined as the **wavelength** λ. The **wavenumber** $k = 2\pi/\lambda$ is inversely proportional to the wavelength and the units of wavelength are distance per cycle.

The function $e^{i(kx-\omega t)}$ describes a right-going plane wave and $e^{i(kx+\omega t)}$ describes a left-going wave. To see this for the rightgoing wave, note that we follow a wavefront (using $x(t)$ as a marker) by keeping the phase $\phi = (kx - \omega t)$ constant. Because x must increase to keep the phase constant with increasing time (such that $x/t = \omega/k$) this means that the wave is moving to right with the compressional velocity given by ω/k. Conversely, $\phi = (kx + \omega t)$ is a constant if t increases and x decreases; thus, the wave is moving to the left.

An equivalent way of keeping track of the wavefront is to recognize that the phase $\phi = kx - \omega t$ of the wavefront does not change with time if we (that is $x(t)$) are riding on its peak, implying that $d\phi/dt = kdx/dt - \omega = 0$, or

$$dx/dt \quad = \quad \omega/k = \lambda/T. \tag{1.16}$$

This implies that the peak of the wavefront propagates with **phase velocity** of

$$v_{phase} \quad = \quad \omega/k = \lambda/T. \tag{1.17}$$

We can show that a propagating plane wave solves the wave equation in a homogeneous medium by plugging equation 1.15 into equation 1.12 to get

$$(k^2 - (\omega/c)^2)P(x,y,z,t) = 0, \tag{1.18}$$

which admits non-trivial solutions if

$$k^2 = (\omega/c)^2. \tag{1.19}$$

This equation is known as the **dispersion equation** and imposes a constraint on wavenumber and frequency variables in the Fourier domain. Since $c = \sqrt{\kappa/\rho}$ is constant in a homogeneous medium, it says that the frequency-to-wavenumber ratio $c = \omega/k$ must be fixed no

---

[6] This plane wave propagates strictly along the x direction and so does not vary in either the y or z coordinates; we also assume a sourceless medium so $F = 0$ everywhere.

matter what the value of frequency; thus, higher frequencies of a propagating plane wave imply shorter wavelengths. It also says, according to equation 1.17, that the wavefront will move a distance of one wavelength λ during one period T of elapsed time, and according to the dispersion equation the **propagation velocity** of this movement is equal to $c = \sqrt{\kappa/\rho}$. That is, we have connected the static rock parameters of κ and ρ to the velocity c that characterizes the dynamics of wave propagation.

1.5.2 2-D Wave Propagation in an Homogeneous Medium

The following function

$$P(x, z, t) \quad = \quad A_0 e^{i(\mathbf{k}\cdot\mathbf{r} - \omega t)}, \tag{1.20}$$

solves the wave equation 1.12, where the **wavenumber vector** is given by $\mathbf{k} = (k_x, k_z)$ and the observation vector is given by $\mathbf{r} = (x, z)$. This describes a plane traveling obliquely to the x-axis but its propagation vector is strictly in the $x - z$ plane as shown in Figure 1.4. The wavenumber vector $\mathbf{k}$ is parallel to the propagation direction.

Similar to the 1-D dispersion equation, the **2-D dispersion equation** can be derived by plugging 1.20 into equation 1.12 to get

$$k_x^2 + k_z^2 - (\omega/c)^2 \quad = \quad 0. \tag{1.21}$$

The real part of equation 1.20, i.e., $\cos(k_x x + k_z z - \omega t)$, plots out as straight lines perpendicular to the wavenumber vector $\mathbf{k}$, and these lines propagate in a direction parallel to $\mathbf{k}$ as t increases. This is easy to prove because the general equation for a straight line is given by $\mathbf{k} \cdot \mathbf{r} = cnst$, where $\mathbf{k}$ is a fixed vector perpendicular to the straight line. The locus of points $\mathbf{r}$ that satisfy this equation of constant phase defines the wavefront where the phase (i.e., $\phi = k_x x + k_z z - \omega t$) is a constant. Thus as the time increases, i.e. as $cnst$ increases, the straight line also moves such that the direction of movement is parallel to the fixed $\mathbf{k}$ vector, as shown in Figure 1.4.

Therefore equation 1.20 represents a harmonic plane wave propagating along the direction parallel to $\mathbf{k}$. Similar to the discussion for a 1-D plane wave, the shortest distance between two adjacent peaks of the wavefront is defined to be the wavelength λ and is given by $\lambda = 2\pi/k$, where $k = \sqrt{k_x^2 + k_z^2}$ is known as the wavenumber. Using this definition of k and that for ω the 2-D dispersion relation takes the same form as equation 1.19.

An illustration of the relationship between the wavenumber vector and the direction of wave propagation is given in Figure 1.4 snapshot. Note, that as the length of the wavenumber vector increases the wavelength decreases, and as the wavenumber direction changes so does the direction of the propagating wave.

Note:

- As illustrated in Figure 1.4, the **apparent wavelength** $\lambda_x = \lambda/\sin\phi$ in the x-direction is the shortest distance between adjacent peaks measured along the x-axis in x-z space for a single snapshot.
- Identifying the crest of a single event in the seismograms (in x-t space) allows us to compute the speed at which this event races from one geophone to the next. This

apparent speed of propagation in the x-direction is known as the apparent velocity $v_x = \lambda_x/T$; it can be measured by drawing a straight line that connects the crests from one seismogram to the next and calculating it's slope as dt/dx. This slope dt/dx is defined as the apparent slowness in the x-direction, and the reciprocal slope $v_x = dx/dt$ is the **apparent velocity** in the x-direction. As illustrated in Figure 1.4, the apparent velocity v_x is given by $v_x = v/sin\phi$ and says that the apparent velocity is infinite for vertically propagating waves. Conversely, the apparent velocity is equal to the actual propagation velocity for horizontally traveling waves.

- The apparent velocity in the vertical direction v_z is given by $v_z = v/\cos\phi$. In this case, vertically traveling waves travel with $v_z = c$, while horizontally traveling waves travel with $v_z = \infty$.
- The apparent wavelength in the horizontal direction is given by $\lambda_x = v_x/f = c/\sin\phi$ and the apparent wavelength in the z-direction is $\lambda_z = v_z/f = c/\cos\phi$.
- A simple way to measure the apparent velocity of events in seismograms is to freeze time at some t_0, and draw a horizontal line at t_0 across the shot gather so that it intersects a peak at some seismogram. Find the distance between this seismogram and the nearest neighboring seismogram where the line intersects a peak again. See Figure 1.5 for the apparent wavelengths measured for three different events.
- The particle motion vector is given by **u**$= (u, v, w)$ and is perpendicular to the wavefront in an isotropic medium. This can be shown for an harmonic plane wave by noting that the gradient of a plane pressure wave is $\nabla P = iP\mathbf{k}$, which according to Newton's law is proportional to the particle displacement vector **u**. Since **k** is perpendicular to the wavefront then so is the particle displacement vector.

Plane Wave Exercises

1. Assume a plane wave with the same wavelength as that in Figure 1.4, except the wave is propagating vertically to the surface (i.e., $\phi = 0$). Draw the associated seismograms and visually estimate the apparent wavelength along the horizontal axis. Does this estimated apparent wavelength agree with value calculated from the formula $\lambda/\sin\phi$?
2. Same question as previous one except assume a horizontally propagating plane wave.
3. Recall $\partial\cos kx/\partial x = -k\sin kx$ and that $\partial\sin kx/\partial x = k\cos kx$. Show that $\partial e^{ikx}/\partial x = ike^{ikx}$, where $e^{ikx} = \cos kx + i\sin kx$.
4. Show that $P(x, y, z, t) = e^{i(kx-\omega t)}$ solves the 3D wave equation

$$\frac{\partial^2 P}{\partial x^2} + \frac{\partial^2 P}{\partial y^2} + \frac{\partial^2 P}{\partial z^2} - \frac{\partial^2 P}{c^2 \partial t^2} = 0. \tag{1.22}$$

where ω is angular frequency.

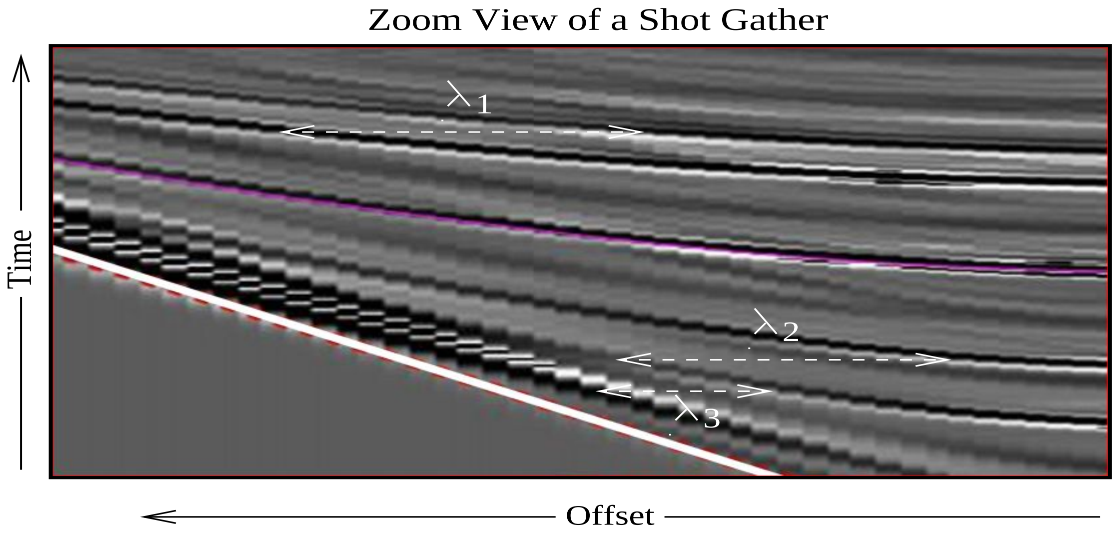

Figure 1.5: Zoom view of a shot gather and estimate of apparent wavelengths λ_i for $i = 1, 2, 3$. The distance between adjacent troughs (i.e., dark portions of an event) along a horizontal dashed line represents the apparent wavelength; different types of events have different wavelengths here.

5. Show that $P = e^{ikx}$ solves the Helmholtz equation

$$\frac{\partial^2 P}{\partial x^2} + \frac{\partial^2 P}{\partial y^2} + \frac{\partial^2 P}{\partial z^2} + k^2 P = 0, \tag{1.23}$$

   where $k^2 = \omega^2/c^2$.

6. Which way does the plane wave $e^{ik_z z + i\omega t}$ propagate, up or down? Plot two snapshots of this plane wave, one for $t = 0$ and the other for $t = T/4$ where $\omega = 2\pi/T$. Assume wavelengths and periods as shown in Figure 1.4.

1.5.3 Plane Wave Propagation in a Layered Medium

Figure 1.6 depicts a plane harmonic wave normally incident on an interface separating two half-spaces of unequal stiffness. The functions are those for the up and downgoing solutions of the wave equation, but it is understood that the geophones record the sum of the **up- and down-going wavefields**, the **total wavefield**. That is, the total pressure fields in the upper (+) and lower (-) media are expressed as

$$P^+(z) \quad = \quad e^{ikz} + R_p e^{-ikz}, \tag{1.24}$$

$$P^-(z) \quad = \quad T_p e^{ik'z}, \tag{1.25}$$

where R_p and T_p denote the pressure reflection and transmission coefficients, respectively; here $k' = \omega/c'$ in the lower medium and $k = \omega/c$ in the upper medium. The harmonic

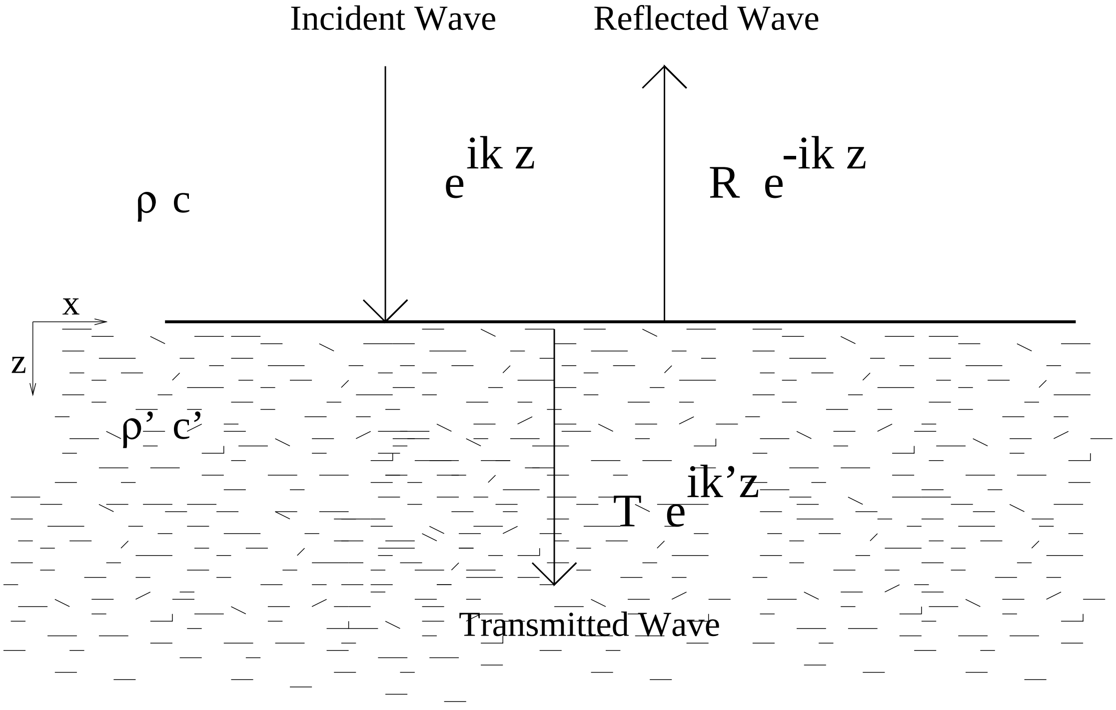

Figure 1.6: Plane wavefront normally incident on a flat interface that separates two homogeneous media. The unprimed medium indicates that of the incident wave.

function $e^{i\omega t}$ has been harmlessly dropped because it cancels out in the final expressions for P_p and T_p.

The two unknowns in these linear equations, R_p and T_p, can be determined by imposing two equations of constraints at the interface at $z = 0$: continuity of pressure across the interface

$$P^+(z=0) = P^-(z=0) \quad \rightarrow \quad [e^{ikz} + R_p e^{-ikz}]|_{z=0} = T_p e^{ik'z}|_{z=0}, \tag{1.26}$$

or evaluating e^{ikz} and $e^{ik'z}$ at $z = 0$ we get

$$1 + R_p \;=\; T_p; \tag{1.27}$$

and imposing continuity of particle velocity (recall Newton's Law in equation 1.8) across the interface gives

$$1/\rho \partial P^+/\partial z|_{z=0} = 1/\rho' \partial P^-/\partial z|_{z=0} \quad \rightarrow \quad 1/\rho \partial/\partial z(e^{ikz} + R_p e^{-ikz})|_{z=0} = 1/\rho' \partial/\partial z(T_p e^{ik'z})|_{z=0},$$

$$\textit{or}$$

$$(k/\rho)(1 - R_p) \;=\; (k'/\rho')T_p, \tag{1.28}$$

Setting $k = \omega/c$ and $k' = \omega/c'$, and solving for R_p in equations 1.27 and 1.28 yields the pressure reflection and transmission coefficients for a normally incident plane wave on a flat interface:

$$R_p \;=\; (\rho' c' - \rho c)/(\rho' c' + \rho c), \tag{1.29}$$

$$T_p \;=\; 2\rho' c'/(\rho' c' + \rho c). \tag{1.30}$$

Here ρc is known as the **impedance** of the medium, and roughly indicates the stiffness of a medium. For example, a plane harmonic plane wave in a homogeneous medium exerts a pressure denoted by $P = e^{ikx-i\omega t}$ and has a particle velocity denoted by $\dot{u} = k/(\rho\omega)P = 1/(\rho c)P$. Therefore, the ratio $P/\dot{u}$ becomes

$$P/\dot{u} \;=\; \rho c. \tag{1.31}$$

This says that decreasing impedances imply larger particle velocities for a fixed elastic pressure on a cube's face. This is exactly what one would expect in a really soft medium: larger displacements for springier-softer rocks, which is one of the reasons that earthquakes shake sediment-filled valleys more than the surrounding bedrock. Conversely, stiffer media lead to smaller displacements for a given elastic pressure.

Note:

- The pressure reflection coefficient is negative if the impedance of the incident layer is greater than that of the refracting layer, i.e., $\rho c > \rho' c'$. Thus gas sands (which typically have lower velocity than the overlying brine sand) have negative polarity reflections.

- For all practical purposes we can consider air density as nearly zero so its impedance is nearly zero as well. Therefore, the free-surface reflection coefficient associated with an upcoming wave is $R_p = -1$ because the rock impedance of the incident layer is greater than that of air. Equation 1.24 says that the total pressure field value on the free surface is $P = 1 + R = 1 - 1 = 0$! See Figure 1.7.

- In a land experiment geophones record particle velocity of the ground while a marine experiment records pressure with hydrophones; see Figure 1.8 for pictures of such recording cables. If $P = 0$ on the free surface then we must lower the hydrophones several feet beneath the water surface, otherwise we record nothing.

- The pressure transmission coefficient T_p is larger than 1 if the incident medium has a lower impedance than the refracting medium, i.e. $\rho c < \rho' c'$. For example, waves entering a really soft medium will yield larger amplitudes of pressure variations compared to waves entering a stiffer medium.

1.5.4 Reflection and Transmission Coefficients for Particle Velocity

Marine experiments measure the pressure field, so this is why the hydrophones must be sufficiently below the sea surface in order to measure a non-zero pressure. On the other hand, land experiments use geophones that measure the particle velocity. Typically, only the vertical component of particle velocity is measured. The reflection coefficient for particle

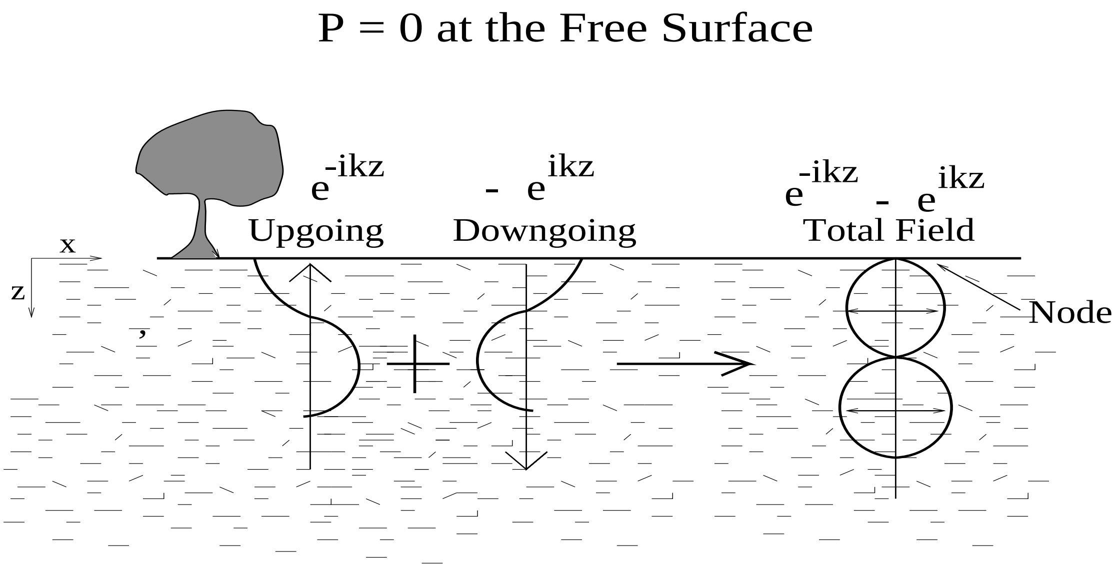

Figure 1.7: Snapshots of the upgoing, downgoing, and total pressure fields. The total pressure at the free surface is always zero because the air has no stiffness to resist motion. Mathematically, the downgoing wave has equal and opposite amplitude to the upgoing wave *at* the free surface. The hydrophone measures the total pressure field, not just the up or downgoing pressure fields.

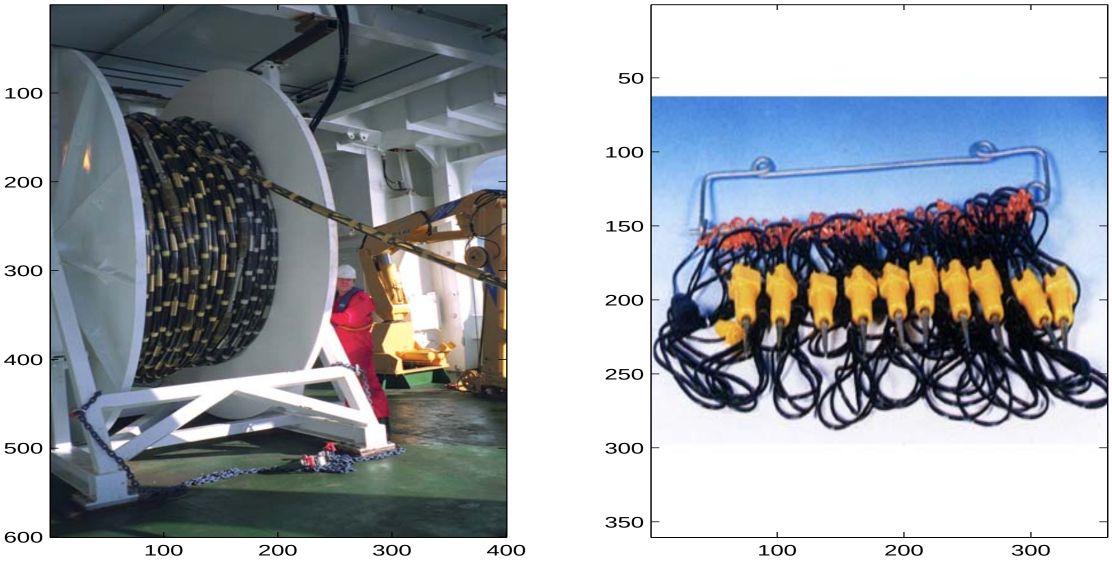

Figure 1.8: Marine hydrophone and land geophone cables.

velocity has a different form than that for pressure. To see this, assume that the total vertical particle-velocity fields in the top and bottom layers are given by

$$\begin{aligned} \dot{w}^+(z) &= e^{ikz} + R_w e^{-ikz}, \\ \dot{w}^-(z) &= T_w e^{ik'z}. \end{aligned} \qquad (1.32)$$

The boundary conditions at the interface are continuity of vertical-particle velocity $\dot{w}^+|_{z=0} = \dot{w}^-|_{z=0}$ and pressure $\kappa\partial\dot{w}^+/\partial z|_{z=0} = \kappa'\dot{\partial} w^-/\partial z|_{z=0}$, where Hooke's law is used $w = -\kappa\partial P/\partial z = -\rho c^2 \partial P/\partial z$.

These two continuity conditions yield the following boundary conditions:

$$\begin{aligned} 1 + R_w &= T_w, \\ \rho c(1 - R_w) &= (1 + R_w)\rho' c', \end{aligned} \qquad (1.33)$$

which can be solved for the particle velocity reflection and transmission coefficients:

$$R_w = (\rho c - \rho' c')/(\rho' c' + \rho c), \qquad (1.34)$$

$$T_w = 2\rho c/(\rho' c' + \rho c), \qquad (1.35)$$

where the unprimed variables again refer to the medium of the incident wave, and the subscript $\dot{w}$ denotes vertical-particle velocity. Note that the reflection coefficient above will have opposite polarity compared to the pressure reflection coefficients. Also, note that in some cases the transmitted amplitude can be greater than the amplitude of the incident wave! Does this violate conservation of energy? No, energy is the squared modulus of amplitude scaled by the impedance (see later section). Thus, a weaker medium with weak rocks (small impedance) can transmit larger amplitude waves than the incident waves in a much stronger (larger impedance) medium. It takes much more energy to rapidly displace strong rock 1 mm than it does in a weak rock.

Free-Surface Reflection Coefficient. The particle velocity reflection coefficient is equal to +1 at the free surface, so the total particle velocity field at the free surface is $1 + R_w = 2$. Thus the free surface, because it straddles a zero stiffness medium, can oscillate with great vigor and has the largest amplitude compared to the underlying rock motion in a half-space. When an earthquake hits, dig a hole, jump in, and cover yourself with dirt! See Figure 1.9.

Reflection Coefficients and Bright Spots. In the 1970s oil and gas companies discovered a new tool, known as ”Bright Spot” technology, for finding hydrocarbons in young sedimentary basins in the Gulf of Mexico. Structural oil deposits in young sedimentary sands typically were characterized by a gas cap at the top of the structure, where the cap consisted of some gas and brine that filled the pore spaces in the sand matrix. The gassy brine in the sandstone matrix caused the cap to be less rigid than the oil-sand below it and the trap rock just above it. Thus, the velocity of the gas sand was typically less than 5 or 10% lower than that of the surrounding strata. This meant that the pressure reflection coefficient was negative and relatively large in magnitude and could easily be identified in

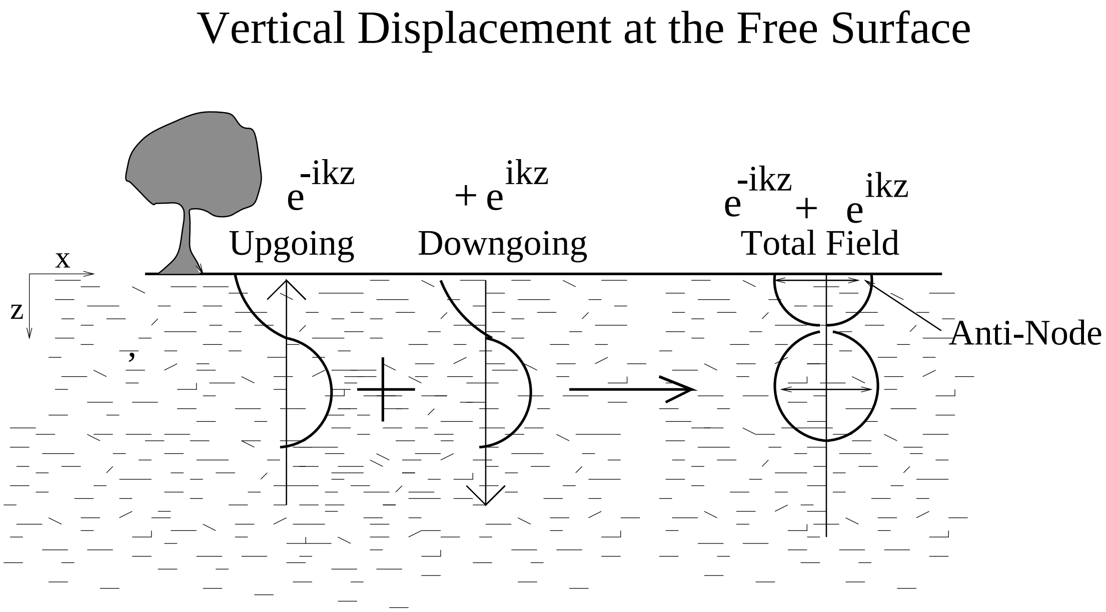

Figure 1.9: The vertical displacement at the free surface is maximum because no elastic resistance at $z = 0$ means vigorous ground shaking. Mathematically, the downgoing wave has equal amplitude to the upgoing wave *at* the free surface.

seismic sections. In particular, a stacked "relative amplitude" section (i.e., RAP section) would show a "bright" negative response along the structural high if this high was a gas deposit above the oil reservoir. Figure 1.10 shows a RAP section from a Gulf of Mexico survey.

1.5.5 Oblique Incidence Angles, Reflection Coefficients and Snell's Law

Figure 1.11 depicts the rays associated with an harmonic plane wave obliquely incident on an interface in a two-layer medium; the amplitude of the incident plane wave is 1 and propagates in the upper layer with velocity v_1 and in the bottom layer with velocity v_2. Equating the sum of the pressure fields in the top medium to that in the lower medium is given by

$$e^{i(k_x x + k_z z - \omega t)} + R_p e^{i(k_x x - k_z z - \omega t)} \quad = \quad T_p e^{i(k'_x x + k'_z z - \omega t)}, \tag{1.36}$$

where the primed and unprimed wavenumbers refer to the lower and upper mediums, respectively. Similarly the total vertical particle velocity field in the upper medium can be equated to that in the lower medium:

$$k_z[e^{i(k_x x + k_z z - \omega t)} - R_p e^{i(k_x x - k_z z - \omega t)}]/\rho \quad = \quad k'_z T_p e^{i(k'_x x + k'_z z - \omega t)}/\rho', \tag{1.37}$$

Evaluating the above two equations at $z = 0$ gives

$$[1 + R_p]e^{ik_x x} = T_p e^{ik'_x x}; \qquad k_z[1 - R_p]e^{ik_x x}/\rho = k'_z T_p e^{ik'_x x}/\rho', \tag{1.38}$$

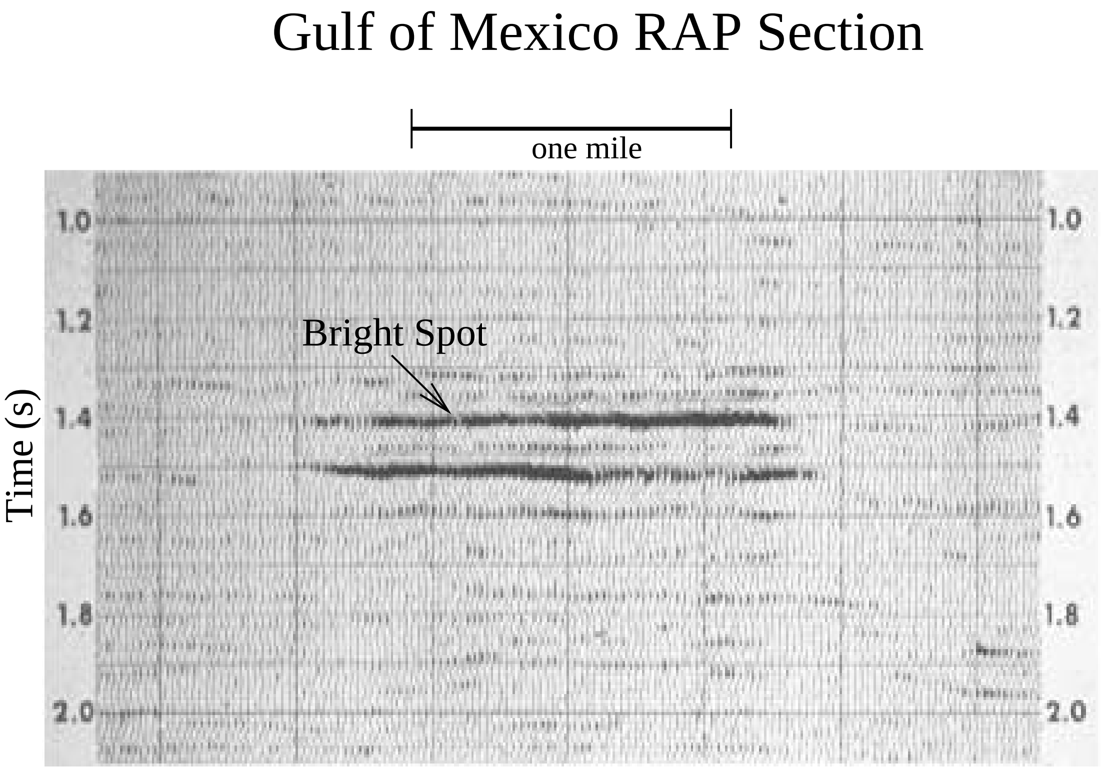

Figure 1.10: RAP (relative amplitude) stacked section from a Gulf of Mexico survey showing a bright spot.

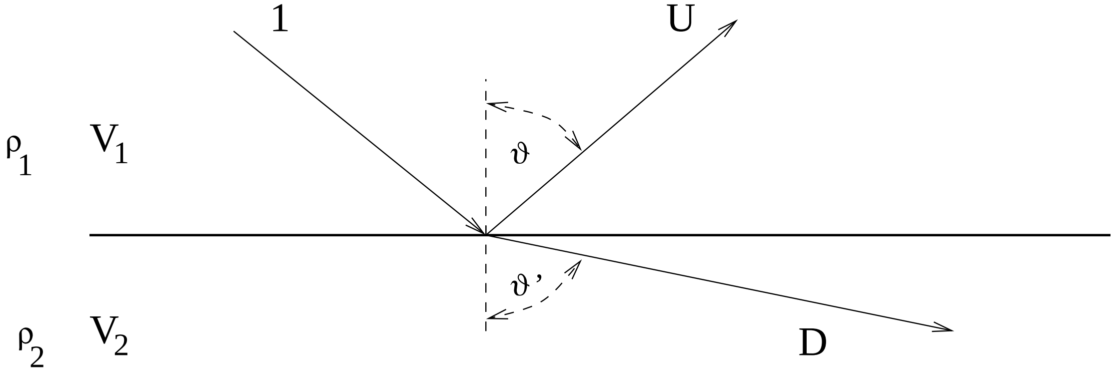

Figure 1.11: Harmonic plane wave incident on an horizontal interface separating two layers, where the downgoing and upgoing waves are denoted by D and U, respectively.

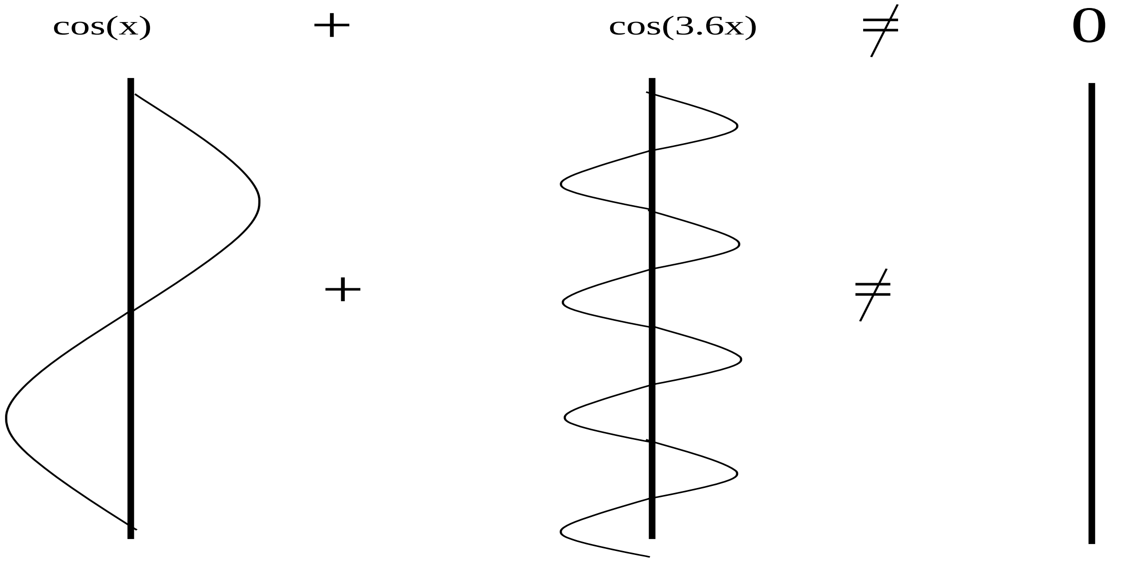

Figure 1.12: It is impossible to sum two weighted cosines with different wavenumbers to get zero everywhere; thus the cosines are linearly independent functions for different wavenumber values.

where the exponential function in time has been divided out. The above equations say that the weighted exponential with wavenumber k_x must be equal to the one with wavenumber k_x' for all values of x. This is impossible because $e^{ik_x x}$ is a linearly independent function in x as illustrated in Figure 1.12.

Therefore, the horizontal wavenumber in the upper ($k_x = \omega \sin\theta/c$) must be equated to that in the lower medium ($k_x' = \omega \sin\theta/c'$) to give **Snell's law**:

$$k_x = k_x' \quad \rightarrow \quad \sin\theta/c = \sin\theta'/c'. \tag{1.39}$$

This equation says that transmission rays bend across an interface, bending towards the vertical when entering a slower velocity medium and bending towards the horizontal when entering a faster medium (see Figure 1.13). At the **critical incidence angle** θ_{crit} the refraction angle of the transmitted ray θ' is 90 degrees so that Snell's law says $\theta_{crit} = arcsin(c/c')$ if $c' > c$. This gives rise to refraction head waves that propagate parallel to the interface at the velocity c' of the underlying medium (see the horizontal dashed ray in middle diagram of Figure 1.14).

A consequence of Snell's law is that a medium with a velocity that increases linearly with depth always turns a downgoing ray back towards the surface, as shown in Figure 1.13. This can easily be shown by approximating the linear velocity gradient medium with a stack of thinly-spaced layers, each with a homogeneous velocity that slightly increases with depth. The velocity increase is the same across each layer. Applying Snell's law to a downgoing ray shows that each ray transmitted across an interface bends a little bit more towards the horizontal until it goes back up. As the thickness of each layer decreases, the ray trajectory will be the arc of a circle if the velocity linearly increases with depth.

The reflection and transmission coefficients can be derived by dividing out the exponen-

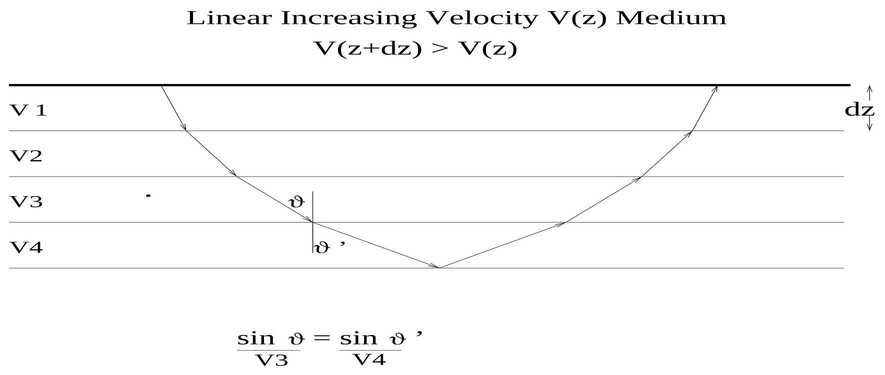

Figure 1.13: Downgoing rays bend across an interface towards the horizontal if the velocity increases with depth. For a medium where $c(z) = a + bz$, all downgoing rays eventually bend back towards the surface.

tials in equation 1.38 to give

$$1 + R_p = T_p; \qquad (k_z/\rho)(1 - R_p) = (k_z'/\rho')T_p, \tag{1.40}$$

where R_p and T_p represent the reflection and transmission coefficients that are a function of incidence angle. Defining $k_z = 2\pi \cos\theta/\lambda$ and $k_z' = 2\pi \cos\theta'/\lambda'$ changes the equation of particle velocity continuity to

$$(\cos\theta/(\lambda\rho))(1 - R_p) \quad = \quad (\cos\theta'/(\lambda'\rho'))T_p; \tag{1.41}$$

and because $\lambda = c/f$ we have

$$(\cos\theta/(c\rho))(1 - R_p) \quad = \quad (\cos\theta'/(c'\rho'))T_p. \tag{1.42}$$

Solving for the pressure reflection coefficient in equations 1.42 and 1.40 yields the plane-wave reflection coefficient for pressure waves with oblique angles of incidence:

$$R_p \quad = \quad (-\cos\theta'\rho c + \cos\theta\rho'c')/(\cos\theta\rho'c' + \cos\theta'\rho c). \tag{1.43}$$

An illustration of a reflection ray and associated seismograms is shown in Figure 1.14. If the source is a point source and the receivers are offset from the source the collection of seismograms is denoted as a shot gather. The associated reflection traveltime curves (see lower diagram in Figure 1.14) plot out as hyperbolas. In a 2-layer medium with a homogeneous upper-layer velocity of v, the reflection traveltime curve is described by the hyperbolic equation $t(x) = \sqrt{(x/v)^2 + (2d/v)^2}$ where d is the thickness of the first layer and x is the horizontal offset between the source and receiver.

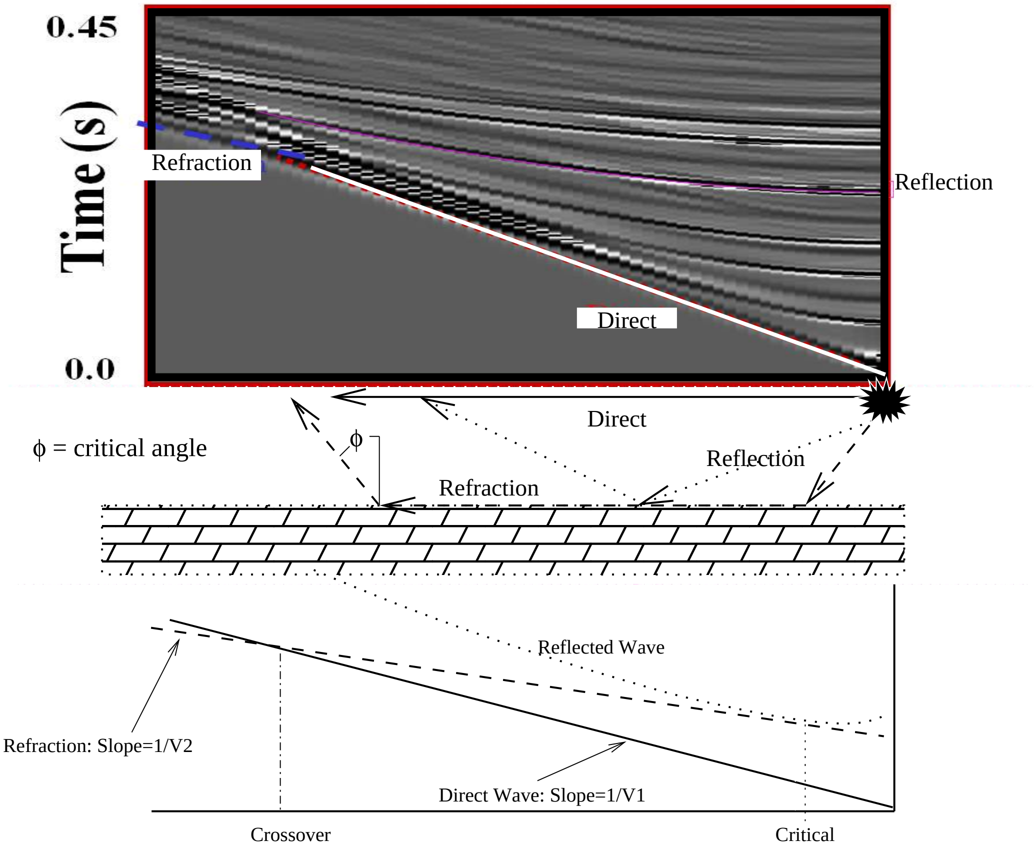

Figure 1.14: (Top) Shot gather, (middle) ray diagrams for direct, reflection, and refraction arrivals, and (bottom) associated traveltime curves. The refraction event (also called a head wave) can only be excited in this two-layer model if the underlying layer has a faster velocity V_2 than the overlying layer with velocity V_1.

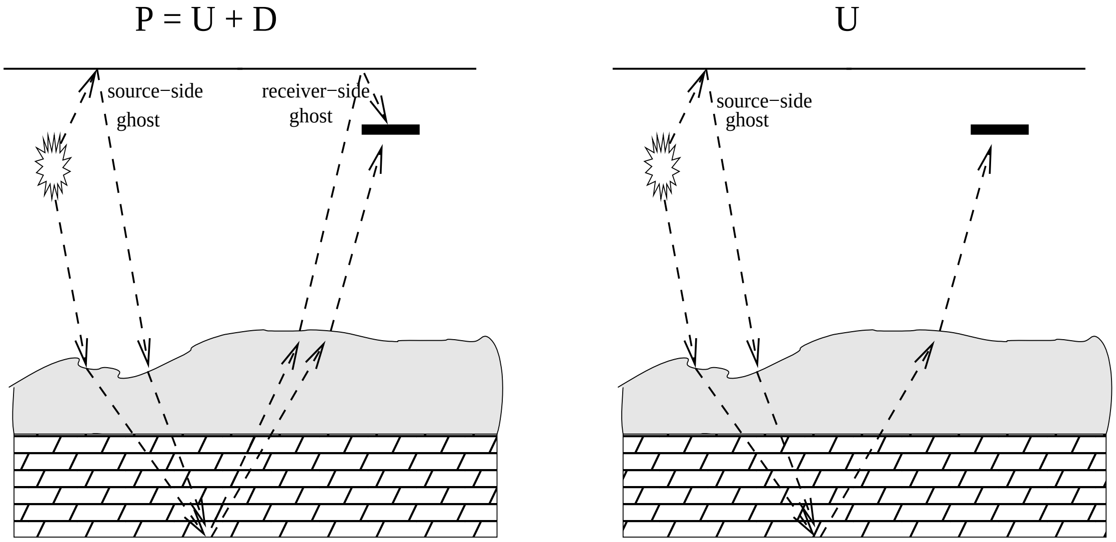

Figure 1.15: Reflection rays related to (left) the total pressure field P and (right) upgoing field U. The "deghosted" U field does not contain the distorting effects from the receiver-side ghost and is, therefore, more desirable than the P field; however, it still contains the distorting effects from the source-side ghost.

1.5.6 Upgoing and Dowgoing Waves

Hydrophones only record the total pressure field $P = U + D$, not the desired U field. This upgoing pressure field is more useful than the total pressure because it is not polluted by the distorting downgoing "receiver-side ghost" reflection from the free surface, as shown in Figure 1.15. Thus it is desirable to extract just the U field from the recorded data P.

To derive the U and D fields from the pressure and particle velocity fields, recall that if $P = U + D$ then Newton's law says that the vertical particle $W = \dot{w}$ in a homogeneous medium is given by

$$\begin{aligned} P &= U + D, \\ W &= k_z(-D + U)/(\omega\rho). \end{aligned} \tag{1.44}$$

Solving for D and U gives

$$\begin{aligned} U &= 1/2(P + \rho\omega/k_z W), \\ D &= 1/2(P - \rho\omega/k_z W). \end{aligned} \tag{1.45}$$

Recent advances in recording now provide the capability of recording both pressure and vertical particle velocity fields in the same streamer cable. In this case the above equation can be used to estimate both U and D from the data[7].

---

[7] An alternative deghosting technology is the over-under acquisition cable, where two cables vertically separated by small distance are used to record the pressure fields at depths z and $z + \Delta z$. In this case the vertical derivative of P can be estimated by $dP/dz \approx [P(x, z + \Delta z) - P(x, z)]/\Delta z$; and from this gradient the vertical particle velocity W can be estimated from Newton's law. Plugging these field values P and W in the above equations is an alternative way to estimate U and D.

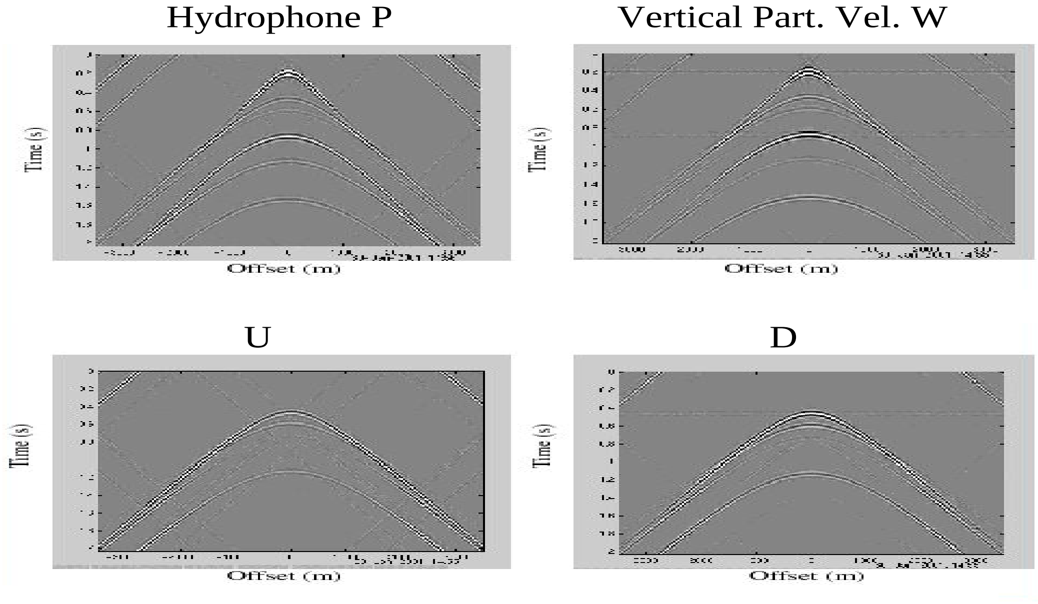

Figure 1.16: Bottom row displays U and D shot gathers obtained from the P and W images along the top row (from Yan and Brown, 2001). Note, the P and W fields contain the confusing downgoing receiver-side ghosts D from the free surface, while the desirable U field is free of the receiver-side ghosts.

An example of separating upgoing and downgoing arrivals in synthetic data is shown in Figure 1.16 (Yan and Brown, 2001). Here, synthetic data were generated for a 2D marine model where receivers on the sea floor record the wavefields generated by sources near the ocean surface. In this case both pressure and particle velocity are recorded by OBS receivers on the ocean floor. Receiver-side free-surface multiples are suppressed in the U field image, but they still contain source-side multiples.

If the velocity records are not available then there is a theoretical (but not always practical) method for estimating the velocity records from the pressure field data. Assuming zero-incidence angle and a flat sea floor then the pressure field can be obtained from the upgoing field U by

$$P = U + D, \tag{1.46}$$

but the D field is a time delayed polarity reversed version of the U field due to the reflection from the free surface:

$$D = -Ue^{ikz_0}, \tag{1.47}$$

where $k = \omega/c_{water}$ and z_0 is the 2-way distance between the hydrophone string and free surface. Substituting the above equation into equation 1.46 yields

$$P = [1 - e^{ikz_0}]U, \tag{1.48}$$

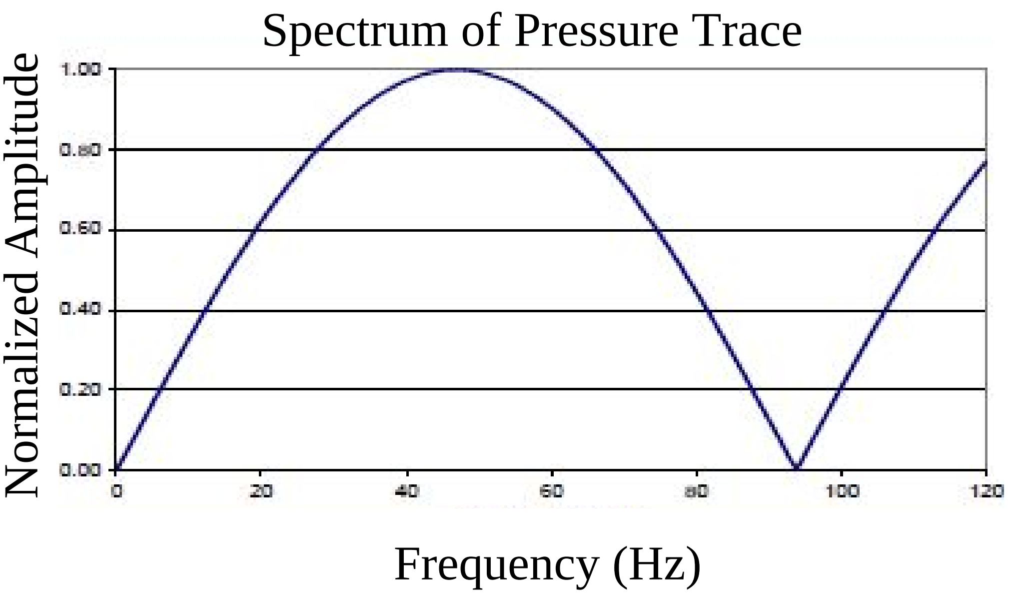

Figure 1.17: Spectrum of a pressure trace for a 8-meter tow depth (Tenghamn et al., 2007). A deeper towing depth is desirable because it would reduce the weather-related noise from the sea surface, but it would introduce more notches into the spectrum.

Similar considerations show that the vertical particle velocity W is

$$Wc_{water}\rho \;=\; [1+e^{ikz_0}]U. \tag{1.49}$$

Setting $\tilde{W} = Wc_{water}\rho$ and solving for U in the above equation gives

$$U \;=\; [1+e^{ikz_0}]^{-1}\tilde{W}. \tag{1.50}$$

Substituting equation 1.50 into equation 1.48 yields the relationship between particle velocity and pressure for vertically incident waves recorded just below the free surface:

$$\tilde{W} \;=\; P[1+e^{ikz_0}]/[1-e^{ikz_0}]. \tag{1.51}$$

According to Tenghamn et al. (2007), the pressure data are Fourier transformed into ω and k_x space, and corrected for oblique angle effects in order for the above equation to be used. However, this equation cannot easily be used due to notches in the pressure field spectrum, as explained below.

Practical Decomposition of U from P and W Streamer Records. Reconstructing $\tilde{W}$ from pressure data recorded by a streamer cannot be performed accurately with equation 1.51 because of notches in the P records. Notches in the P spectrum are associated with placing the hydrophone cable at the depth of a node shown in Figure 1.7. The frequencies at which the notch occurs are at f_0, $2f_0$, $3f_0, ...$, where $f_0 = c_{water}/z_0$ and $z_0/2$ is the depth of the streamer below the free surface.

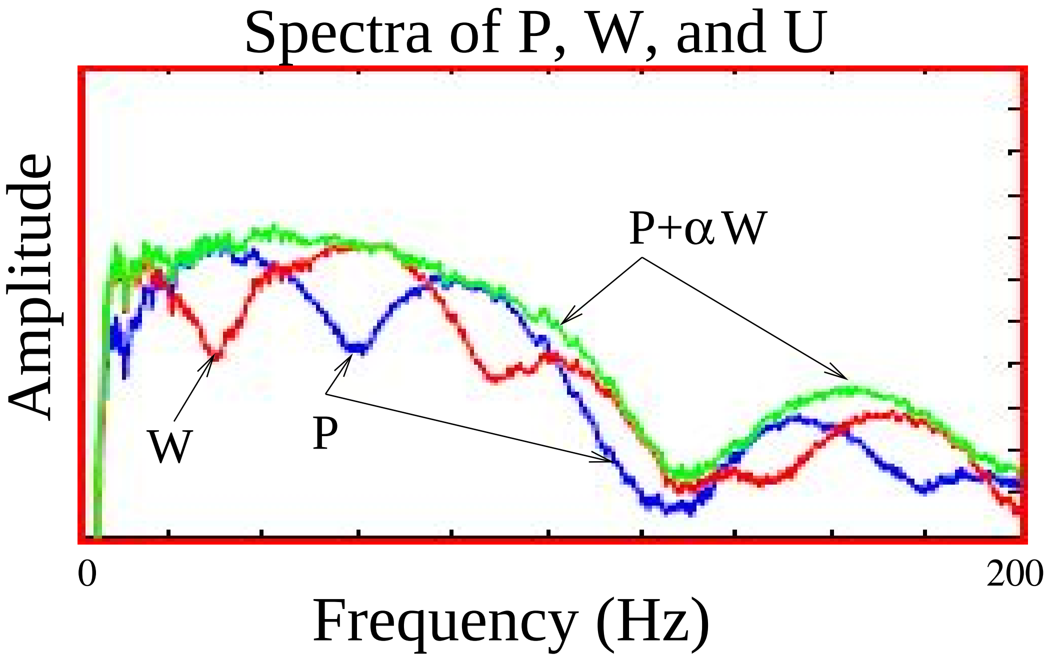

Figure 1.18: Spectrums of pressure and particle velocity traces (Tenghamn et al., 2007) and the spectrum of the combined data to get the green $U = P + \alpha W$ field. Notice how the notches are filled with the combined data. Low frequency noise below 20 Hz has been eliminated by a low-cut filter in the particle velocity data and the resulting gap is filled in with the pressure data and equation 1.51. The α is the constant in equation 1.45.

As shown in Figures 1.7 and 1.9, notches in the pressure spectrum occur at the antinodes of the particle velocity spectrum. This means that both pressure and particle velocity records can be combined with equation 1.45 to completely fill the spectrum over a wide range of frequencies and eliminate the ghosts. Hence, this motivates the simultaneous streamer recording of both pressure and particle velocity records and the use of equation 1.45 to get the U field.

However, one of the problems in the particle velocity record is strum noise below 20 Hz. Strum noise is canceled by pressure hydrophones but is quite noticeable on particle velocity recordings.[8]. Therefore, a low-cut filter (0-20 Hz) is used to eliminate the noise in the particle velocity records and this portion of the spectrum is filled in using the pressure data and equation 1.51.

As an example, a streamer is used to record both P and W and the resulting spectra are illustrated in Figure 1.18 (Tenghamn et al., 2007). Notice that the notches for the P records are at different frequencies compared to those of the W spectrum. Combining these two records gives the upgoing record U, whose spectrum is denoted by the green line. This combination of W and P to get U will be denoted as deghosting.

---

[8] A problem in directly measuring particle velocity with geophones in a streamer is strum noise. Strum noise is the low-frequency noise generated by transverse mechanical vibrations that propagate along the streamer's stress members (Tenghamn et al., 2007).

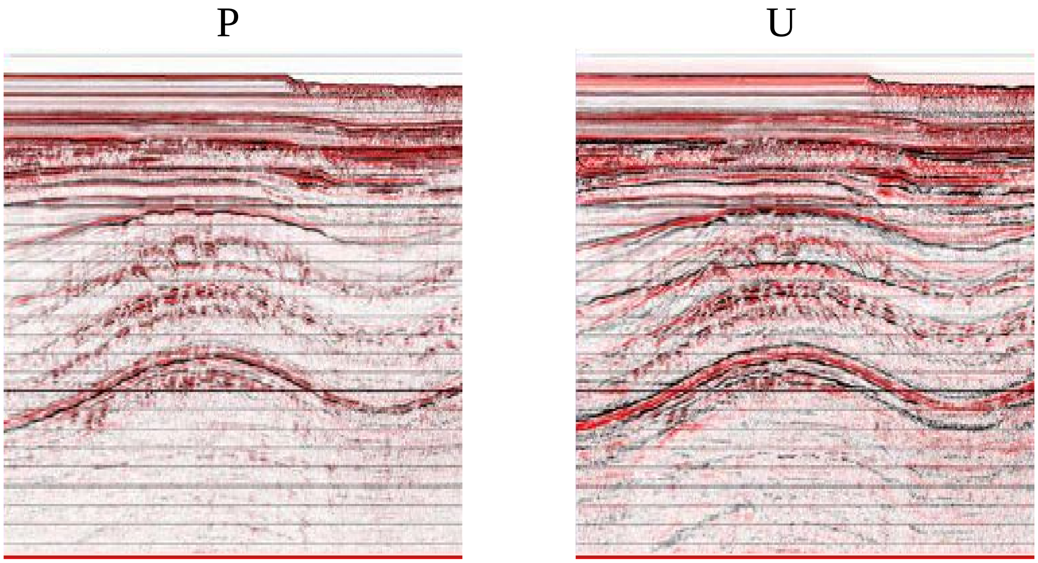

Figure 1.19: (Left) Conventional stacked section from P records and (right) stacked section obtained by combining P and W records (Tenghamn et al., 2007).

This procedure for deghosting the data is applied to stacked marine records, and the comparison of conventional and deghosted stacked sections is shown in Figure 1.19. Here, the deghosted section shows higher signal because the ghosts are largely eliminated.

1.6 Energy of Propagating Acoustic Waves

Elastic energy is stored in a cube of acoustic material as it is deformed from equilibrium. That is, squeeze a cube of acoustic material, release it, and then the cube undeforms to perform work on the medium. In the deformed state at any instant of time of a propagating wave the potential energy of a small cube of deformed material, according to Figure 1.20, shows that the instantaneous work (i.e., area · force/area · distance cube deformed) performed by the surrounding medium on a cube along the $z-axis$ is given by $-\int(Pdxdy)dz$, where the limits of integration are from the undeformed volume to the deformed volume at some given time. This figure shows that, using equation 1.3 and 1.2 and $\kappa = c^2\rho$, the expression for **instantaneous potential energy density** is given by

$$PE \quad = \quad P^2/(2\rho c^2), \tag{1.52}$$

which is also called the strain energy. However, the **total instantaneous energy density** of an acoustic plane wave propagating along the x-axis in a homogeneous medium is given by a sum of the instantaneous kinetic energy and potential energy densities:

$$\epsilon = KE + PE \quad = \quad 1/2\rho[\quad \overbrace{\|\dot{u}\|^2}^{kinetic\ energy} \quad + \quad \overbrace{P^2/(\rho c)^2}^{potential\ energy} \quad], \tag{1.53}$$

where u is the particle displacement along the x coordinate. For a harmonic plane wave $\rho c = P/\dot{u}$, so this equation becomes:

$$\epsilon \;=\; \rho\|\dot{u}\|^2. \tag{1.54}$$

Substituting the plane wave expression $u = e^{i(kx-\omega t)}$ into the above equation yields

$$\epsilon \;=\; \rho\omega^2\|u\|^2, \tag{1.55}$$

which says that energy density increases with increasing frequency. This makes sense because, over the same distance, the snapshot of a harmonic wave passing through a rock shows more "strained" distortions at higher frequencies. As one might expect, it takes more energy to deform denser rock with the same particle velocity compared to distorting lighter rock.

Finally, the energy flux is a measure of energy passing through a fixed area per unit time. The energy density is in units of energy per volume, so multiplying the energy density by propagation velocity c gives the **energy flux** of a plane wave in a homogeneous medium, i.e.,

$$c\epsilon \;=\; c\rho\omega^2\|u\|^2. \tag{1.56}$$

We conclude that energy flux is greater for faster waves propagating at higher frequencies through denser rock. Equivalently, for a fixed energy flux higher frequencies are associated with smaller amplitudes of particle displacement. This suggests that with broadband earthquakes the lower frequencies should tend to shake a house with greater displacement than at higher frequencies.

R, T, U, and D Exercises

1. Derive the plane-wave reflection coefficient and transmission formulas for particle displacement at an oblique angle. Compare these formulas to those for a pressure wave, and explain their differences in polarity for the reflection coefficients.

2. Can a refraction arrival propagate along the free surface for an upcoming plane wave? Explain your reasoning.

3. Using the appropriate reflection and transmission coefficient formulas for a pressure field, show that energy flux is conserved for a plane wave normally incident on a horizontal interface that gives rise to a reflected wave with amplitude R_p and transmitted arrival with amplitude T_p. That is, energy flux from equation 1.52 is $|P|^2/(\rho c)$ for an incident wave so prove that $1^2/(\rho c) = R_p^2/(\rho c) + T_p^2/(\rho' c')$ is correct.

4. Same as previous problem except assume an oblique angle of incidence.

5. How does the formula for transmission coefficient in equation 1.35 change for an oblique incidence angle?

6. If a streamer is at a 16 m depth, what frequencies contain notches over the bandwidth of 0-200 Hz? Where do the notches occur if the streamer is at a depth of 1 m? Velocity of water is roughly 1.5 km/s. Which of the above streamer depths is more conducive to wave noise?

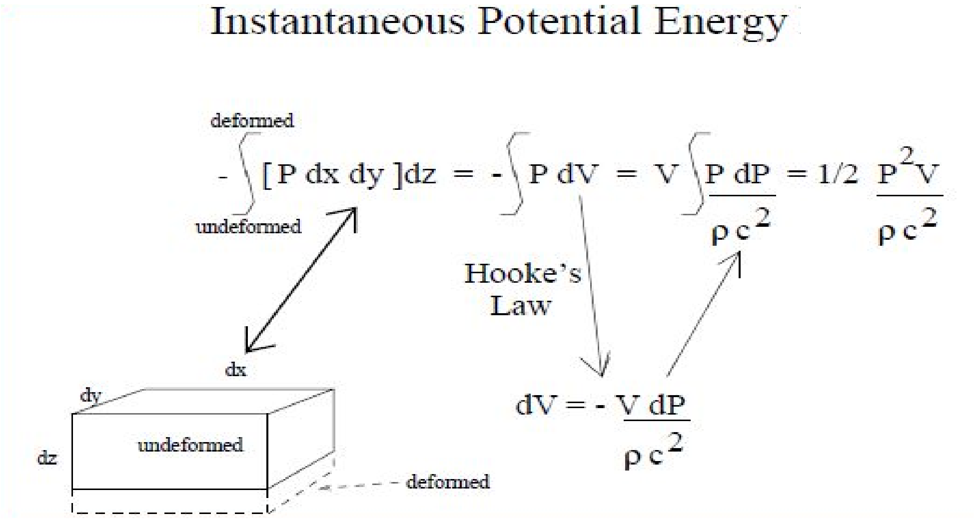

Figure 1.20: The potential strain energy of a cube of material with volume V deformed along the z-axis is $P^2V/(2\rho c^2)$. Therefore the potential strain energy density is $P^2/(2\rho c^2)$.

7. A valley is filled with soft soil with velocity of 2 km/s and density of 1 g/m^3, while the surrounding bedrock is filled with hard rock of velocity 5 km/s and density of 3 g/m^3. How many more times stronger should the particle displacement be in the valley compared to the bedrock for an incident wave with the same energy? Which is the best place to build your house, bedrock or valley?

1.7 Geometrical Spreading and Attenuation of Propagating Acoustic Waves

It is of interest to examine the solution to the wave equation when the source term on the right hand side of equation 1.14 is a point source:

$$\nabla^2 G(\mathbf{x}, t|\mathbf{x}', t') - \frac{1}{c^2}\frac{\partial^2 G(\mathbf{x}, t|\mathbf{x}', t')}{\partial t^2} = -\delta(\mathbf{x}-\mathbf{x}')\delta(t-t'), \tag{1.57}$$

where $\delta(\mathbf{x}-\mathbf{x}')$ is a Dirac delta function that is infinite when the argument is zero (i.e., $\mathbf{x} = \mathbf{x}'$) and zero otherwise. This says that the source is localized to the point $\mathbf{x}'$ and only is excited when the source initiation time t' is equal to the observation time t. The $G(\mathbf{x}, t|\mathbf{x}', t')$ is known as the impulsive point source response of the medium, also known as the Green's function. The spatial and temporal variables to the right of the vertical bar denote the spatial location and temporal excitation time of the point source and the variables to the left of the vertical bar denote the receiver variables.

The property of the delta function is that it picks out the value of a function at the time t and location $\mathbf{x}$. For example, let $f(x, t)$ be a smooth finite-valued function, so that if we

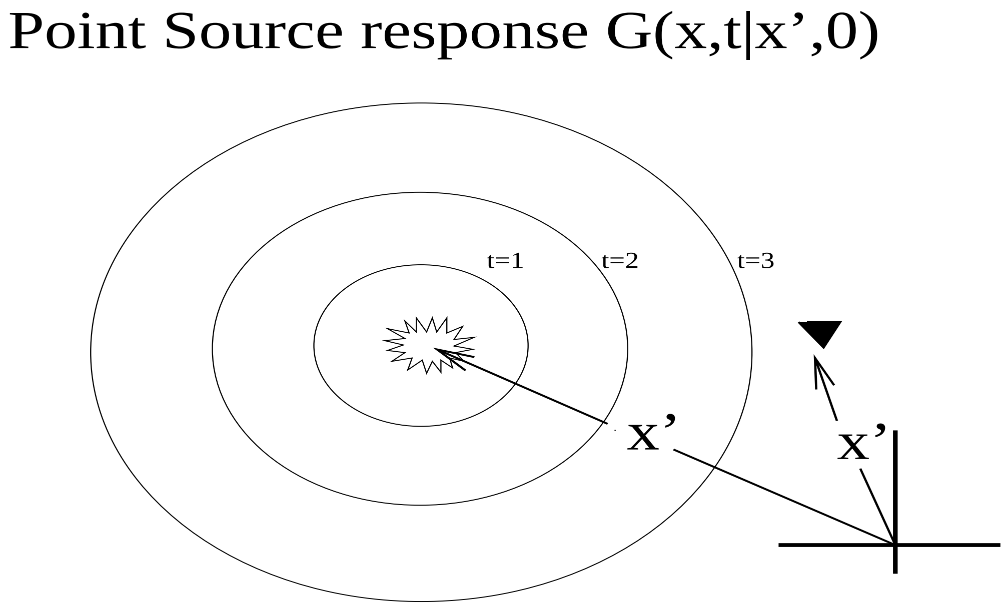

Figure 1.21: Expanding spherical wave fronts for a point source in a homogeneous medium.

integrate the product $f(x,t)\delta(x-x')\delta(t-t')$ then

$$f(x',t') = \int_{-\infty}^{\infty}\int_{-\infty}^{\infty} f(x,t)\delta(x,t)dxdt. \tag{1.58}$$

This ability to evaluate $f(x,t)$ at the variables x' and t' is known as the sifting property.

Often we will assume an initiation time of $t'=0$, so that a solution to the above equation for a homogeneous medium with velocity c is given as (Aki and Richards, 1980)

$$G(\mathbf{x},t|\mathbf{x}',0) = -\frac{e^{i(k|\mathbf{x}-\mathbf{x}'|-\omega t)}}{4\pi|\mathbf{x}-\mathbf{x}'|} \tag{1.59}$$

where $1/|\mathbf{x}-\mathbf{x}'| = 1/r$ is the geometrical spreading factor. Note, the numerator is just like our plane wave solution, except the wavefronts of constant value form concentric spheres centered about the source point at $\mathbf{x}'$ as shown in Figure 1.21. As time increases the spheres increase in radius at the propagation speed c, where $k=\omega/c$. The amount of energy E on this sphere remains constant but the energy density is $E/A = E/r^2$. From the previous section, the amplitude of the wave is proportional to the square root of the energy density so the amplitude should fall off as $1/r$ from the source point. This is exactly the behavior described by equation 1.59. The $1/r$ is known as the geometrical spreading factor and is a characteristic of body waves propagating in three dimensions. As time increases, the radius of the outwardly propagating sphere increases so that the area of the sphere increases as Note the weakening of amplitudes in the the shot gather of Figure 1.22.

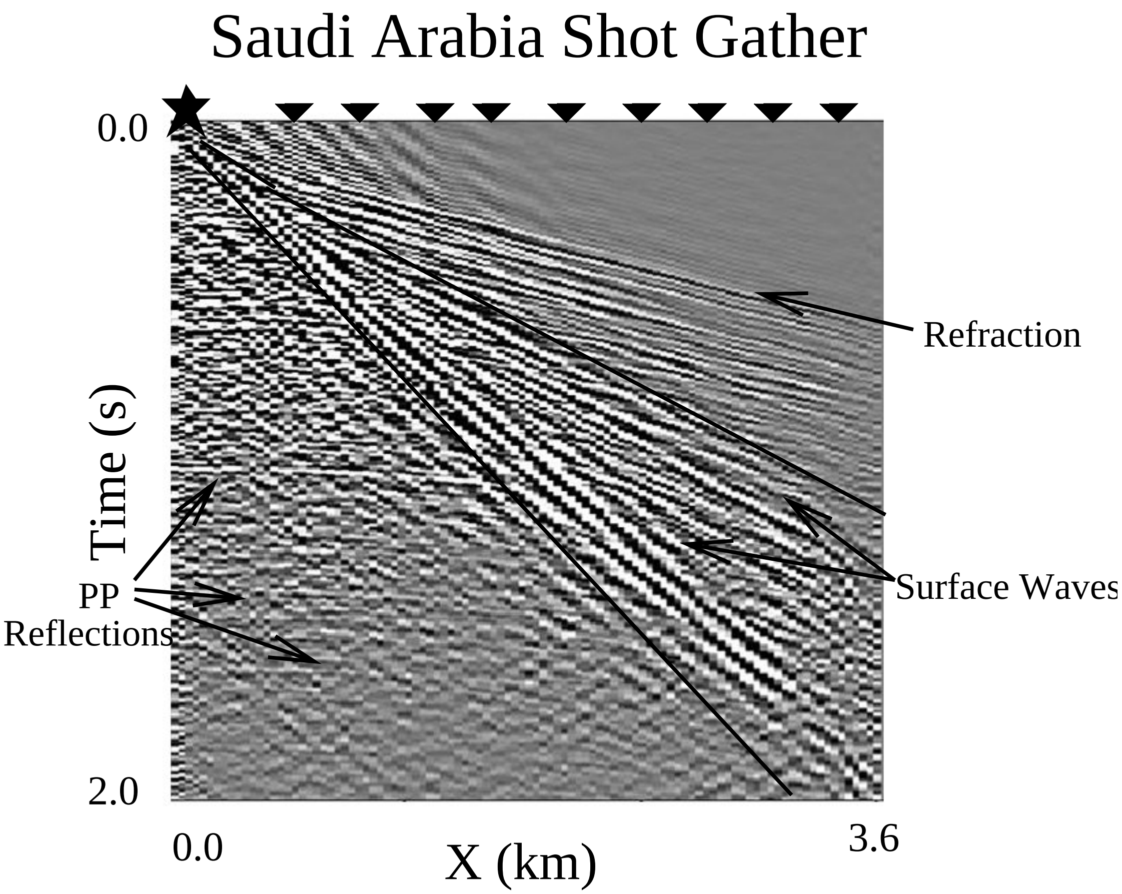

Figure 1.22: Shot gather from Saudi Arabia. Note the weakening of amplitudes with increasing time.

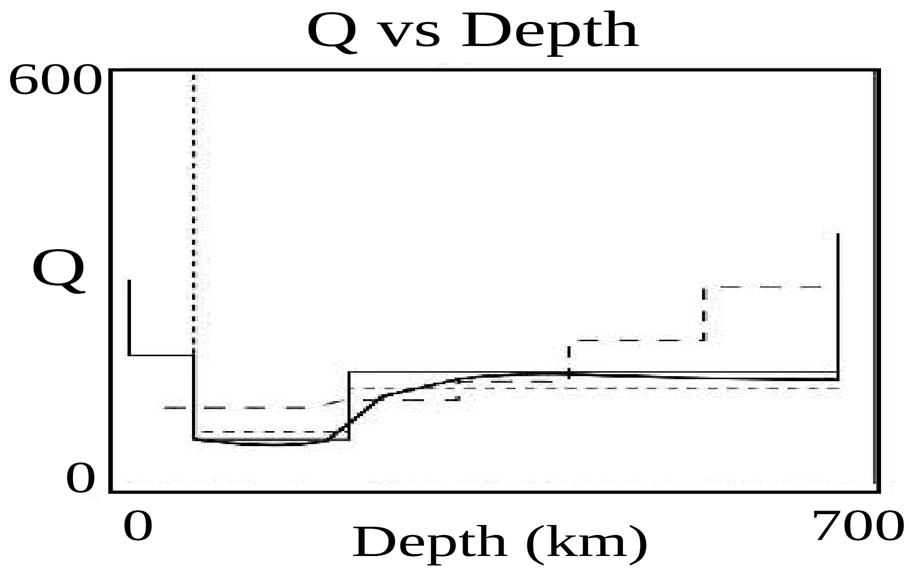

Figure 1.23: Different Q vs depth curves obtained from earthquakes.

Attenuation

As a seismic wave deforms the rock, elastic energy is lost to frictional forces within the rock as the rock is squeezed many times per second. The result is that the seismic amplitude diminishes with distance from the source as energy is lost to the earth by "frictional forces"; i.e., higher frequencies attenuate more quickly than lower frequencies in dissipating the energy of the seismic wave. An extra term can be incorporated into the Green's function in equation 1.59 to account for attenuation:

$$G(\mathbf{x}, t|\mathbf{x}', 0) = -\frac{e^{(ikr-i\omega t)}e^{-\omega r/(2cQ)}}{4\pi r}, \tag{1.60}$$

where Q is the positive attenuation factor that accounts for frictional losses in the rock and c is the local velocity. Note, the amplitudes will more rapidly attenuate with smaller values of Q and increasing distances from the source. Typical Q values for tight granites are greater than 200 while for young Miocene sedimentary rock in the Gulf of Mexico the Q values range from 5 to 100 or so. Sometimes Q is absorbed into the wavenumber k to make it a complex valued function (Aki and Richards, 1980), i.e., $k \rightarrow k + i|k|/Q$. A plot of the Q vs depth from the earth's surface is given in Figure 1.23.

1.8 Wavefronts and Rays

A **wavefront** is defined as the contiguous points in model space that have the same phase for a fixed time. In the case of a propagating plane wave these points fall along a plane with a normal perpendicular to the direction of propagation. The **ray** is defined to be the line that is perpendicular to the wavefront that starts at the source and ends at a specified point in the medium. For example, the ray associated with the plane wave is a straight

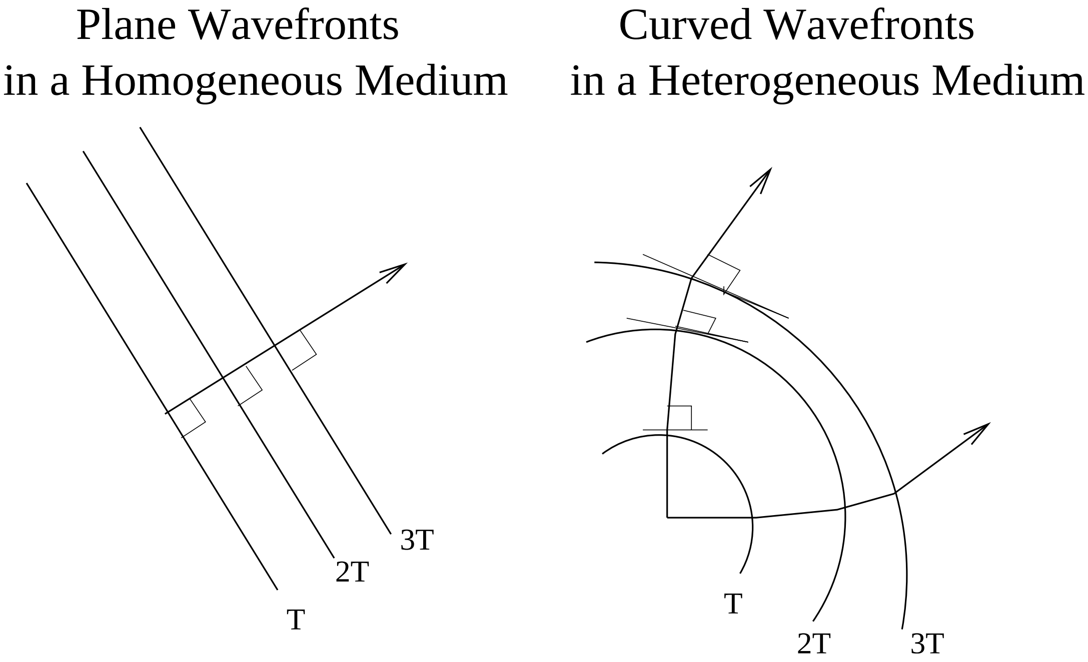

Figure 1.24: Wavefronts and rays (arrows) for a planar wavefront and a non-planar wavefront at times T, $2T$ and $3T$.

line as shown in Figure 1.24. For a heterogeneous medium the rays that start out from the source point and follow a curved trajectory that honors Snell's law everywhere along the ray.

In general, the Green's function in a heterogeneous medium asymptotically can be represented by the harmonic formula

$$G(\mathbf{x},t|\mathbf{x}',0) = -A(\mathbf{x}|\mathbf{x}')e^{i\omega\tau_{xx'}}, \tag{1.61}$$

where $\tau_{xx'}$ represents the time[9] to go from $\mathbf{x}'$ to $\mathbf{x}$ along the curved ray trajectory, and $A(\mathbf{x}|\mathbf{x}')$ is the generalized geometrical spreading term. This Green's function is valid when the wavelength $\lambda = \omega/c$ of the local wavefront is at least 3 times shorter than the variation wavelength of the velocity fluctuation. Here, c is the local velocity of the medium and this assumption is also called a high-frequency approximation valid for sufficiently smooth medium. In this case the orientation of the ray must be perpendicular to the constant traveltime wavefront, i.e., it is parallel to the gradient of the traveltime function $\tau_{xx'}$:

$$\nabla\tau_{xx'} \; || \; \textit{ray direction}, \tag{1.62}$$

In fact the direction cosines of the ray are given by

$$\hat{n}_i \;\; = \;\; \frac{1}{|\partial\tau_{xx'}/\partial x_i|}\frac{\partial\tau_{xx'}}{\partial x_i}. \tag{1.63}$$

---

[9] This is not the symbol for the stress tensor.

and the equations for the ray are given by

$$\frac{dx_1}{\partial\tau_{xx'}/\partial x_1} = \frac{dx_2}{\partial\tau_{xx'}/\partial x_2} = \frac{dx_3}{\partial\tau_{xx'}/\partial x_3}. \tag{1.64}$$

These equations can be used to trace rays in a heterogeneous medium, and details for estimating the rays and traveltimes will be discussed in the chapter on the eikonal equation.

1.9 Summary

The basic physics of acoustic wave propagation are described. Plane wave solutions to the wave equation are derived for a homogeneous medium, and the concepts of frequency and wavelength were discussed for both 1D and 2D. Snell's law resulted from imposing boundary conditions across an acoustic interface. For a two-layered medium, the reflection and transmission coefficients are derived and showed that a low to high impedance contrast lead to positive reflection coefficients for the incident pressure field. It is noted that the reflection coefficient varies as a function of incidence angles, which leads to the concept of AVO (amplitude vs offset) characterization of lithology. Impedance is defined as ρc for normal incidence plane waves and is equal to the ratio of the pressure to particle velocity. It is a measure of rock stiffness, with large impedances corresponding to small particle velocities that generate large pressures.

The energy of a propagating wave is the sum of the kinetic and potential energies. For a plane wave in a homogeneous medium propagating in the x direction, this energy is given as $\rho\dot{u}^2$. There are two reasons for amplitude decay in a propagating spherical wave: geometrical spreading and intrinsic rock attenuation. The latter is also seen in plane waves but there is no geometrical spreading in plane waves. However, plane waves without geometrical spreading is a mathematical idealization and not physically possible in practice.

Exercises

1. Identify the direct arrival, air wave, surface waves, refraction arrivals, and reflection arrivals in the CSG shown in Figure 1.25. Computing the slopes dx/dt of these events, estimate the apparent velocity in the x-direction V_x and the associated period for each event. From these calculations determine the wavelengths. Show work.

2. Compute the apparent wavelengths λ_x of the events in the previous problem by using the method shown in Figure 1.5. Do these new estimates roughly agree with the apparent wavelengths computed from slope measurements?

3. Which arrivals have the same apparent velocity as the actual propagation velocity of that event? Why?

4. The 1-D SH wave equation is the same form as the 1-D acoustic wave equation, except c becomes the shear wave velocity, P becomes the y-component of displacement v, and $c = \sqrt{(}\mu/\rho)$ where μ is the shear modulus. The SH wave equation is

$$1/c^2\partial^2 v/\partial t^2 - \partial^2 v/\partial z^2 = 0 \quad , \tag{1.65}$$

where SH (or shear horizontal) refers to the fact that the shear wave particle motion is perpendicular to the direction of particle motion, and is along the horizontal direction (in and out of plane of paper). The SH continuity conditions at the interface at z=0 are a). Continuity of y-displacement $v^+ = v^-$., b). Continuity of shear traction: $\mu \partial v/\partial z^+ = \mu \partial v/\partial z^-$, where μ is the shear modulus.

Derive the y-displacement reflection and transmission coefficients for a plane SH wave normally incident on a planar interface in an elastic medium.

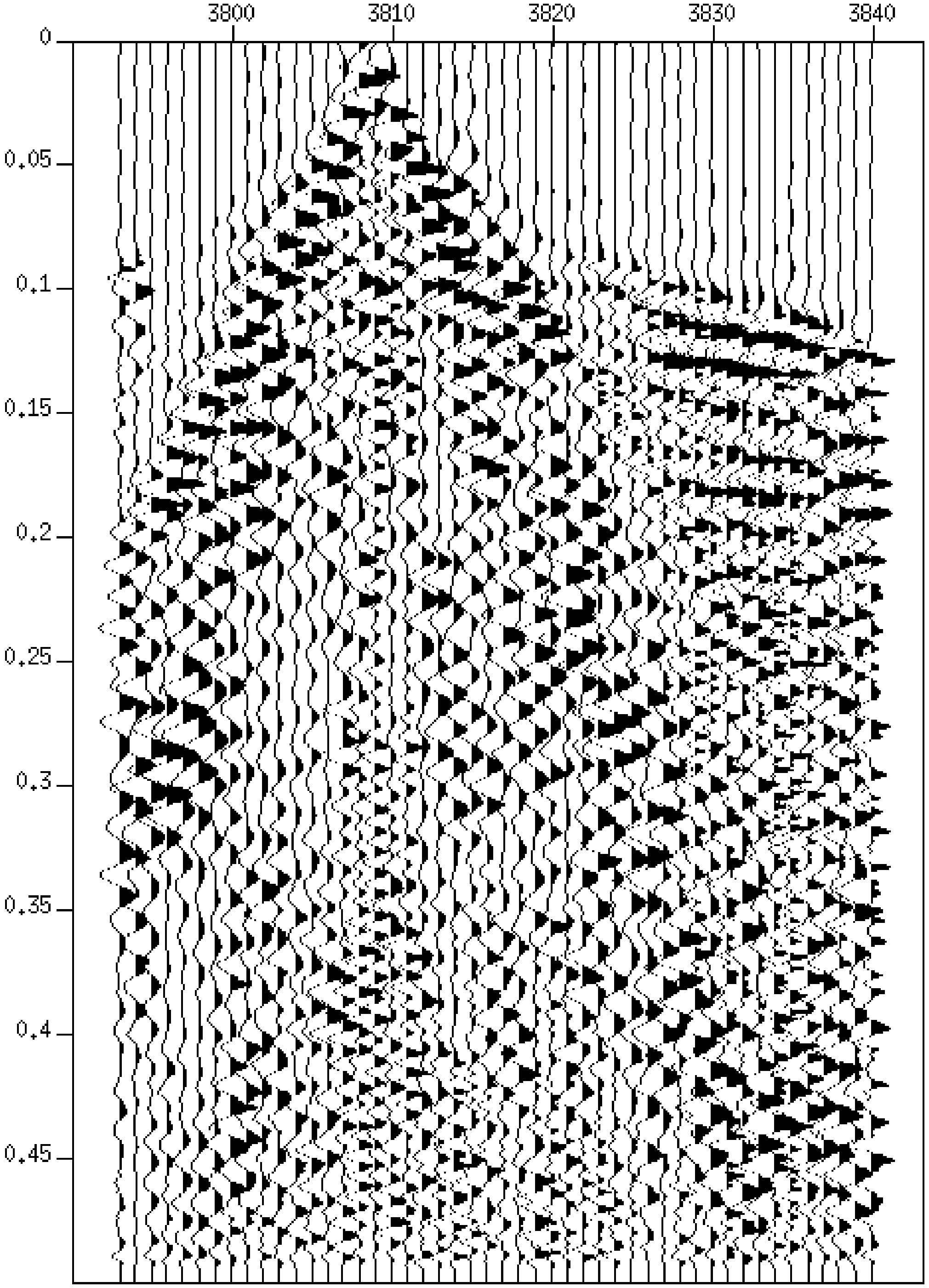

Figure 1.25: Shot gather from Salt Lake valley. The trace interval is 5 feet along the horizontal axis and the time units along the vertical axis are seconds.

Chapter 2

Signals, Systems, and 1D Convolutional Modeling

This chapter will present the definitions of signals and linear systems. In general, a linear discrete system can be represented by a matrix-vector operation; and a special case of a linear system is that of the operation known as convolution, or linear time-invariant systems (LTI). The convolution operation is used to generate synthetic seismograms for a layered earth model, which are then used to understand the actual seismograms recorded in a seismic experiment.

2.1 Signals

A general continuous signal can be represented by the multi-variate function $x(a, b, c, d, ...)$, where $a,\ b,\ c,\ d, ...$ are continuous variables. We will now be chiefly concerned with 1-D time signals represented by $x(t)$, although the time dimension can be replaced by another type of dimension such as space, frequency, temperature, etc.. Some examples of 1-D time signals include seismogram recordings from an earthquake, magnetotelluric (MT) recordings, or ground penetrating radar (GPR) data. If the time variable is a continuous variable then $x(t)$ is a continuous signal. If the time variable is a discrete variable then $x(t)$ is a discrete signal. Practically most signals are sampled uniformly in time with a sampling interval of dt , and the square bracket notation $x[n] = x(ndt)$ is used to represent a uniform sampling of the continuous signal $x(t)$. Here n belongs to the set of integers.

A discrete signal can be mathematically represented with the aid of the Kronecker delta function $\delta[i - j]$ defined as

$$\delta[i-j] \;=\; \left\{ \begin{array}{c} 1\ if\ \ i=j \\ \\ 0 \quad otherwise \end{array} \right\}, \tag{2.1}$$

Therefore the discrete signal $x[n]$ is given by

$$x[n] \;=\; \sum_{i=-\infty}^{\infty} x[i]\delta[i-n], \tag{2.2}$$

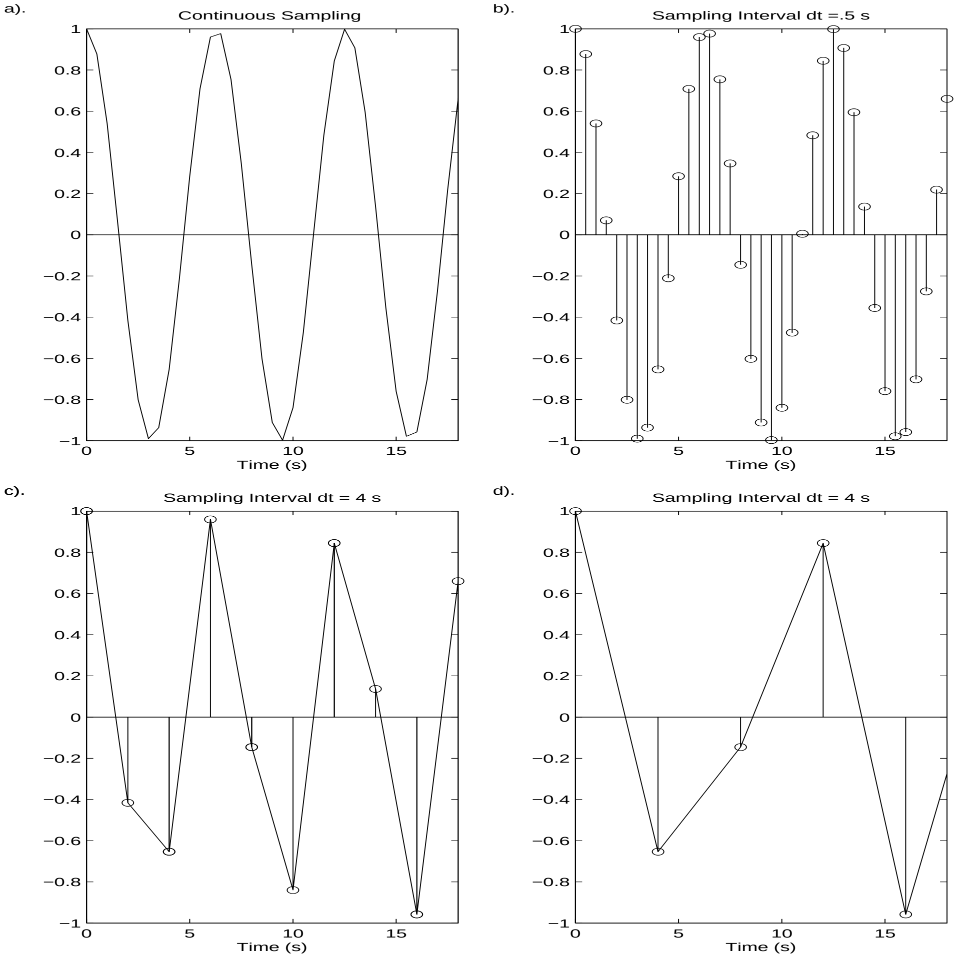

Figure 2.1: a). Cosine signal with a period of 6 s and its discrete representations at sampling intervals of b). .5 s, c). 2 s and d). 4. s. If the sampling interval is too coarse ($dt \geq 3s$), the discrete signal is *aliased* so that a high frequency signal masquerades as a low frequency signal.

or in vector notation

$$\mathbf{x} \;=\; [x[1]\; x[2] ...\; x[N]]^T, \tag{2.3}$$

where N is the number of data points in the signal and the superscript T represents transpose. Sometime we represent a sample with the subscript notation $x_j = x[j]$.

Note that the process of sampling a continuous signal can distort the character of the signal as shown in Figure 2.1.

The period of the continuously sampled signal is 6 s, and this period is roughly preserved with sampling intervals of $dt = .5\ s$ and $dt = 2.0\ s$. However, the discrete signal with $dt = 4\ s$ in Figure 2.1d has lost the original character of the cosine signal; in particular it appears as a lower frequency signal with a period of about 12, rather than 6 s. In other words the sampling rate of 1 sample/4 time units was too slow to capture the rapidly varying parts of the cosine. The discrete signal masqueraded as a lower frequency signal, that is the discrete signal appeared to be of lower frequency than the actual signal.

The exponential $x[n] = |A|e^{in2pi/12}$ can be plotted as a sequence of vectors on a circle in the complex plane for $n = 0, 1, 2, 3, ..12$; the circle has radius A. In the complex plane each time sample is complex and can be given as the vector components $x[n] = |A|(real(x[n]), imag(x[n])) = (cos(\omega n), sin(\omega n))$ where the first and second components are plotted along the real and imaginary axes, respectively. Note that if we were to play a movie of the vector $x[n]$ then we would see a spinning arrow rotating about the origin with constant angular speed and length. In fact the angular speed can be determined by taking the magnitude of the derivative of vector $x(t)$ with respect to t to get "$A\omega$". Dividing through by A gives the angular rate of spinning as ω, or the angular frequency in units of radians/sec. Larger values of ω correspond to faster spinning arrows.

2.2 Sampling Theorem

At what sampling frequency does the signal become aliased? The following theorem answers this question.

Sampling Theorem: Let $x(t)$ be a bandlimited signal such that f_{max} is the maximum frequency found in the data. We say that $x(t)$ is properly sampled (at the sampling interval dt) if there are more than two samples per minimum period: $2dt < T_{min}$, or $f_{max} = 2/T_{min} < 1/dt = f_{sampling}$. Note that the reciprocal of the minimum period is the maximum frequency $1/T_{min} = f_{max}$. Given these samples $x[n]$ we can perfectly reconstruct the original continuous signal. In other words the sampling theorem is telling us that the sampling rate $1/dt$ (i.e., the sampling frequency) should be greater than 1/2 the maximum frequency of the signal. We define $f_{Nyquist} = 1/(2dt)$ as the Nyquist frequency ; in units of radians we have $\omega_{Nyquist} = \pi/dt$. Another way of stating the Sampling theorem is that the highest frequency in the data should be less than the Nyquist frequency.

It is not obvious that we can perfectly reconstruct the continuous signal from its samples, but it is reasonable that for a well-sampled signal we can guess at the period of the original signal from $x[n]$. In Figure 2.1c the period is preserved because the sample rate $1/dt$ was less than 1/2 the period of the cosine. If the sample rate was exactly at 1/2 the period of the cosine (i.e., $dt = \pi$) then the sampled signal would have no variation at all. That is, it would appear to have a lower frequency than the original signal.

2.3 Systems

A system is defined to be any process that alters an input signal $x(t)$ to produce an altered output signal $y(t)$. For example, the input image of Europa on the lens of the Voyager II spacecraft gets transmitted through the ionosphere of Jupiter, which corrupts the signal $x(t)$ to yield $y(t) = x(t) + n(t)$. Therefore the ionosphere of Jupiter can be considered as a system that alters the original signal by adding static noise to the image. Another example is the input of signal as a transient EM source on the earth's surface, and the output signal is the recorded earth response $y(t)$.

Mathematically the system is represented as an operator $H[]$ that is applied to the input to yield the output, i.e., $y(t) = H[x(t)]$. Mathematically we say that the operator $H[]$ maps the space of single-variate continuous functions to the space of single-variate continuous functions. Another way of representing this system is by the input/output notation:

$$x[n] \rightarrow \left[\ H\ \right] \rightarrow y[n] \tag{2.4}$$

For a discrete signal the operator $H[\ ]$ maps an N-dimensional vector space (where the $Nx1$ vector $x[n]$ exists) to an M-dimensional vector space (where the $Mx1$ vector $y[n]$ exists).

2.4 Properties of Systems

We will be concerned with 7 properties of systems : Linearity, Time Invariance, Stability, Causality, Invariance, Stability and Invertibility.

1. Scaling: $H(\alpha x) = \alpha H(x)$, where α is an arbitrary scalar and x is an input signal. Scaling says that if you boost the input signal by the multiplicative factor α then the output signal will be α times louder. If you double your explosive charge then you will double the amplitude of the recorded seismograms. Scaling obviously does not work when non-linear effects come into play. For example, if you increase your explosive source by a factor of one million then you will not see the same increase in seismogram amplitude because such a large charge will spend much of its energy pulverizing the rock instead of just shaking the rock.

Example 1: Scaling property illustrated by explosive input and seismogram output.

```
             -------               ++++++
            |       |              +    +
  x  -----> | Earth | ------> ++++++    +  ++++++++++++
boom        |       |                   +  +    Seismic Trace
            --------                    ++++


                                   ++++++
                                   +    +
              ------               +    +
            |       |              +    +
 2x  -----> | Earth | ------> ++++++    +   ++++++++++++
BOOM        |       |                   +   +    Seismic trace
             -------                    +   +    with double amplitude
                                        +   +
                                        +++++
```

2. Additivity: $H(x_1 + x_2) = H(x_1) + H(x_2)$, where x_1 and x_2 are two input signals. If you do two separate seismic experiments, one with an input seismic signal using 1 lb of dynamite and the other with 2 lbs of dynamite, then add the two separate outputs $H(x_1) + H(x_2) = y_1 + y_2$ gives the same recording as one experiment with 3 lbs of dynamite $H(x_1 + x_2) = y_3$.

Example 2: Additivity property illustrated by explosive input and seismogram output.

```
             -------               ++++++
            |       |              +    +
  x  -----> | Earth | ------> ++++++    +  +++++++++++++
boom        |       |                   +  +    Seismic Trace
            --------                    ++++

                                     |
                                   -----
                                     |

                             ++++++
                             *    +
              ------         *    +
            |       |        *    +
 2x  -----> | Earth | --->++++*    +   +++++++++++++
BOOM        |       |             +   +  Seismic Trace with
             -------              +   +  doubled amplitude
                                  +   +
                                  +++++
```

3. Superposition: $H(\sum_i a_i x_i) = \sum_i a_i H(x_i)$, which is a consequence of the scaling and additivity properties.

The most general form of a discrete linear system is represented by a matrix-vector multiplication, i.e.,

$$y[i] = \sum_{j=1}^{N} h_{ij} x[j], \tag{2.5}$$

or in more compact notation $\mathbf{y} = \mathbf{Hx}$ or

$$\overbrace{\left|\begin{array}{c} y_1 \\ y_2 \\ . \\ . \\ y_M \end{array}\right|}^{Trace} = \overbrace{\left|\begin{array}{cccc} h_{11} & h_{12} & ... & h_{1N} \\ h_{21} & h_{22} & ... & h_{2N} \\ . & . & ... & . \\ . & . & ... & . \\ h_{M1} & h_{M2} & ... & h_{MN} \end{array}\right|}^{Earth's\ impulse\ response} \overbrace{\left|\begin{array}{c} x_1 \\ x_2 \\ . \\ . \\ x_N \end{array}\right|}^{Source}. \tag{2.6}$$

If the input signal is an impulse that turned on only at time k then $x_n = \delta[n-k]$. In explicit vector notation the impulse looks like:

$$\begin{vmatrix} x_1 \\ x_2 \\ . \\ x_k \\ . \\ x_N \end{vmatrix} = \begin{vmatrix} 0 \\ 0 \\ . \\ 1 \\ . \\ 0 \end{vmatrix} . \tag{2.7}$$

Plugging equation 2.7 into 2.6 yields:

$$\begin{vmatrix} h_{11} & h_{12} \ldots & \overbrace{h_{1k}}^{kth\ impulse\ response} & \ldots\ h_{1N} \\ h_{21} & h_{22} \ldots & h_{2k} & \ldots\ h_{2N} \\ . & . \ \ldots & h_{3k} & \ldots\ . \\ . & . \ \ldots & . & \ldots\ . \\ . & . \ \ldots & . & \ldots\ . \\ . & . \ \ldots & . & \ldots\ . \\ h_{M1} & h_{M2} \ \ldots & h_{Mk} & \ldots\ h_{MN} \end{vmatrix} \overbrace{\begin{vmatrix} 0 \\ 0 \\ . \\ 1 \\ . \\ . \\ 0 \end{vmatrix}}^{Input\ impulse\ at\ kdt} = \overbrace{\begin{vmatrix} h_{1k} \\ h_{2k} \\ . \\ . \\ . \\ . \\ h_{Mk} \end{vmatrix}}^{kth\ impulse\ respoinse} . \tag{2.8}$$

Therefore the *kth* column vector of the MxN matrix **H** is the impulse response of the system for an impulsive input $x_n = \delta[n-k]$.

4. Time or Shift Invariance. A system is time invariant if a k-shifted input leads to the original output, except shifted by k units. As an example, the time invariance property is illustrated by an explosive impulsive input and seismogram output, where the output seismogram is described by the first column of the system matrix **H** below.

$$\mathbf{H} = \begin{vmatrix} \alpha & 0 & 0 & 0 \\ \beta & \alpha & 0 & 0 \\ 0 & \beta & \alpha & 0 \\ 0 & 0 & \beta & \alpha \end{vmatrix} \tag{2.9}$$

If the input were delayed by one unit then the output would be the 2nd column of $\mathbf{H}$ above, which is a 1-sample shifted version of the first column. Note the physical interpretation of the indices in h_{ij}, it is the observed response at time i to the unit input at the start time j.

Time invariance implies that the elements along any subdiagonal are equal to one another, as illustrated in the above matrix. Therefore the element values only depend on the subdiagonal location; thus the element values h_{ij} can be denoted as h_{i-j}, i.e., the matrix elements in an LTI system can be represented as

$$h(i,j) \quad \rightarrow \quad h(i-j), \tag{2.10}$$

In terms of a seismic experiment time invariance says that the outcome seismogram of the experiment is not determined by the day or hour it started, the outcome depends on the temporal difference between the start time and observation time (i.e., the earth's impulse response is time invariant). For example, the seismogram amplitude observed 3 seconds after I hit the ground is the same whether I hit the ground on a Monday or a Tuesday or etc..

It now follows that a Linear Time Invariant (LTI) system can be mathematically described as

$$\begin{aligned} y(i) &= \sum_j h(i,j)x(j) \quad (matrix - vector\ multiply), \\ &\rightarrow \sum_j h(i-j)x(j) \quad (dot - product\ of\ reflected - shifted\ vector), \\ \mathbf{y} &= \mathbf{h} \star \mathbf{x}, \end{aligned} \tag{2.11}$$

which $\star$ denotes convolution. More generally the upper and lower limits in the equation 2.9 summation extend to plus and minus infinity.

Note that if a system is LTI then the output $\mathbf{y}$ is a convolution of $\mathbf{x} = (...x(-3)\ x(-2)\ x(-1)\ x(0)\ x(1)\ x(2)\ x(3)...)^T$ with the vector $\mathbf{h} = (...h(-3)\ h(-2)\ h(-1)\ h(0)\ h(1)\ h(2)\ h(3)...)$; this also can be described as a dot product of the shifted vector $\mathbf{h}$ with the vector $\mathbf{x}$. If the shift units are something other than time then the LTI system is usually referred to as a Linear Shift Invariant (LSI) system.

5. Convolution. The previous section tells us that any LTI system can be represented by a convolution operation. Convolution is described by equation 2.11, and can be viewed in a number of different ways:

Convolution is a running "average" of the elements in the input vector, where the weighting elements are given by $(..h(-1)h(0)h(1)...)$ and the length of the 1-D averaging mask is the same as the length of the vector $\mathbf{h}$. For two-dimensional convolution, the input is a matrix with elements given by $x(i,j)$, and the convolutional $filter$ is a 2-D mask with elements denoted by $h(i,j)$. The 2-D *running average* is given by

$$\begin{aligned} y(i,j) &= \sum_{i'}\sum_{j} h(i-i',j-j')x(i',j') \qquad (matrix - matrix\ multiply), \\ & \quad or\ symbolically \\ y &= h \star x \qquad (double\ convolution\ of\ matrices\ h\ and\ x), \end{aligned} \tag{2.12}$$

We say convolution is a shifted-reflected dot product of the vectors **h** and **x** because $h(-2)$ is a reflected version of $h(2)$ across the origin, and $h(j-2)$ is a rfelcted version of $h(2)$, except it is shifted by two time samples.

Example 1: Convolve the trace $\mathbf{x} = [1 \ \ -1 \ \ 1]$ with $\mathbf{x} = [1 \ \ -1 \ 1]^T$ and $\mathbf{h} = [2 \ 6 \ 9]^T$.

```
                                  Multiply Window

Shift=-1      h(2)  h(1)  h(0) | h(-1) h(-2) h(-3)|            |y(-1)|
Shift=0             h(2)  h(1) | h(0)  h(-1) h(-2)||x(0)|      |y(0) |
Shift=1                   h(2) | h(1)  h(0)  h(-1)||x(1)|      |y(1) |
Shift=2                        | h(2)  h(1)  h(0) ||x(2)| =    |y(2) |
Shift=3                        | h(3)  h(2)  h(1) |            |y(3) |
Shift=5                        | h(4)  h(3)  h(2) |            |y(4) |
```

```
                     Multiply Window

Shift=-1      9  6  2 | 0  0  0    |            |y(-1)|    | 0 |
Shift=0          9  6 | 2  0  0    || 1 |       |y(0) |    | 2 |
Shift=1             9 | 6  2  0    ||-1 |       |y(1) |    | 4 |
Shift=2               | 9  6  2    ||-1 |   =   |y(2) | =  | 1 |
Shift=3               | 0  9  6    |            |y(3) |    |15 |
Shift=5               | 0  0  9    |            |y(4) |    |-9 |
```

```
The top row of above matrix-vector equation is not needed
so we have a more compact form of the above:

Shift=0          9  6 | 2  0  0    || 1 |       |y(0) |    | 2 |
Shift=1             9 | 6  2  0    ||-1 |       |y(1) |    | 4 |
Shift=2               | 9  6  2    ||-1 |   =   |y(2) | =  | 1 |
Shift=3               | 0  9  6    |            |y(3) |    |15 |
Shift=5               | 0  0  9    |            |y(4) |    |-9 |
```

6. Causality. If the system output reacts prior to the input then the system is acausal. If the system only reacts during or after an input then the system is causal. Mathematically the system is causal if

$$h(n-k) = 0 \quad for\ all\ k \quad greater\ than\ n. \tag{2.13}$$

This condition makes sense because n is the observation time of the output and k is the time at which the input turns on. The output better not turn on prior to the excitation of the input. Examples of a causal system are non-real time signals that have been previously recorded, such as your smoothing filter for the Dow Jones Index $[f(-1) \ f(0) \ f(1)]$. Here the future values of the DJI are used to give a present average DJI value.

7. Stability. A system is stable if its impulse response is absolutely summable:

$$\sum_{n=-\infty}^{\infty} |h(n)| < \infty. \tag{2.14}$$

Some systems with infinitely long vectors, an IIR or *infinite Impulse Response* system, are stable and others are not. A *Finite Impulse Response* or FIR system is always stable if the amplitudes are finite.

8. Invertibility. If $y = h \star x$ then the system is invertible if $x = inv(h) \star x$. We will learn more about this property when we cover the least squares deconvolution.

2.5 Seismic Reflection Data as LTI System: $s(t) = r(t) \star w(t)$.

The velocity structure of a 1-D layered earth with constant density can be described by $v(z)$, where $v(z)$ is the propagation velocity as a function of depth. Assuming a uniform sampling in depth with a sampling interval of dz we have the vector $\mathbf{v} = [v(0)\ v(1) .... v(N)]^T$, and the associated reflection coefficient vector as function of depth $\mathbf{r} = [r(0)\ r(1) ... r(N)]^T$ where:

$$r(i) \quad = \quad \{v(i) - v(i-1)\}/\{v(i) + v(i-1)\}, \tag{2.15}$$

and the time it takes a plane wave to go from the the $i\ dz$ depth to the $(i+1)dz$ depth is $dz/v(i)$. Thus the 2-way time $t(z)$ that seismic energy takes to go from the surface to the Kth (i.e., $z = dz\ K$) depth level and back up to the surface is:

```
               K                       BOOM      Geophone
              +---         --------------------
               +                   |         ^       v(1)
t(K*dz)   =     + 2*dz/v(j)        V         |
               +            -------------------
              +---               |         ^
              j = 1              V         |         v(2)
                            --------------------
                                     .
                                     .
                                     .
                            --------------------
                                 |         ^         v(K)
                                 V         |
                            --------------------
```

Using $t(z)$ we can get $z(t)$; thus we can convert the reflection coefficent as a function of depth $r(z)$ to the reflection coefficent as a function of time $r(t) = r(z(t))$. The physical meaning of the $r(t)$ is that it is the impulse response of the 1-D layered earth for an impulsive source and a receiver at the surface. It assumes no multiples, no attenuation and no transmission losses in the earth.

For example, if the earth model is of uniform velocity v = 1 km/s except for a layer with reflectivity -.5 at $z = 1$ km then an impulsive source wavelet with amplitude A $\delta[n]$ launched from the surface will generate the following reflection response:

$$r(t) \ = \ [r(0)\ \ r(1)\ \ r(2)\ ...] \ = \ [A\ \ 0\ \ -.5 \star A\ \ 0\ \ 0\ \ 0...], \tag{2.16}$$

where dt = 1 s. The first term $r(0) = A$ is the direct wave and the $r(2) = -.5 * A$ is the primary reflection from the first layer interface.

If we consider the earth's impulse response as LTI, the time history of the seismic source wavelet as $w(t)$, and the synthetic seismogram seismogram $s(t)$ as the output, then $s(t) = r(t) \star w(t)$, where $r(t)$ is the earth's impulse response. This is known as the 1-D convolution model of a seismogram. Is the earth really an LTI system? Does the earth system really satisfy linearity and scaling properties? What experiments can you devise to test this hypothesis?

An example of computing the seismogram from a synthetic sonic velocity log is is given in Figure 2.2 and a field data example is given in Figure 2.3.

The mathematical description for describing two-way traveltime as a function of depth in continuous variables is given by

$$t(z) \quad = \quad 2\int_0^z dz'/v(z')', \tag{2.17}$$

where $t(z)$ is the 2-way propagation time for energy to go vertically downward from the surface to the horizontal reflector at depth z and back up to the surface in the 1D layered model. A MATLAB script for this mapping from depth to time is given as

```
%%%%%%%%%%%%%%%%%%%%%%%%%%%%%%
% Finds t(z) from v(z). Assumes
% v(z) starts at free surface.
% v(z)   - input- sonic log as function of z
% dz     - input- depth sampling interval of sonic log
% t(z)   - input- 2-way time as function of z
%%%%%%%%%%%%%%%%%%%%%%%%%%%%%%
function [time]=depth2time(v,dz)
nz=length(v);time=zeros(nz,1); time(1)=dz/v(1);
for i=2:nz; time(i)=time(i-1)+dz/v(i); end
time=time*2; plot(dz*[1:nz],time);
xlabel('Depth (ft)'); ylabel('Time (s)')
title('Depth vs 2-way Time');figure
plot(time,v);xlabel('Time (s)');ylabel('Velocity (ft/s)')
```

The velocity model as a function of time $v(t)$ (see Figure 2.2b) is usually unevenly sampled. To perform convolutional forward modeling, we must convert to an evenly sampled function in time $v(t) = v(t(z))'$; the MATLAB code for getting an even sampled function sampled at the sampling interval *dt* from an unevenly sampled function is given in Appendix D.

Assuming that the velocity function $v(t)$ is now an evenly sampled function, the evenly sampled zero-offset (ZO) reflection coefficients as a function of time can be estimated by $r(t) = (\rho(t)v(t) - \rho(t-dt)v(t-dt))/((\rho(t)v(t) + \rho(t-dt)v(t-dt))$, which in MATLAB script becomes for constant density:

```
y=diff(vpp);nl=length(y);dt=diff(time);add=vpp(1:nl)+vpp(2:nl+1);
rc=y(1:nl)./add(1:nl);stem(time(1:nl),rc(1:nl));
```

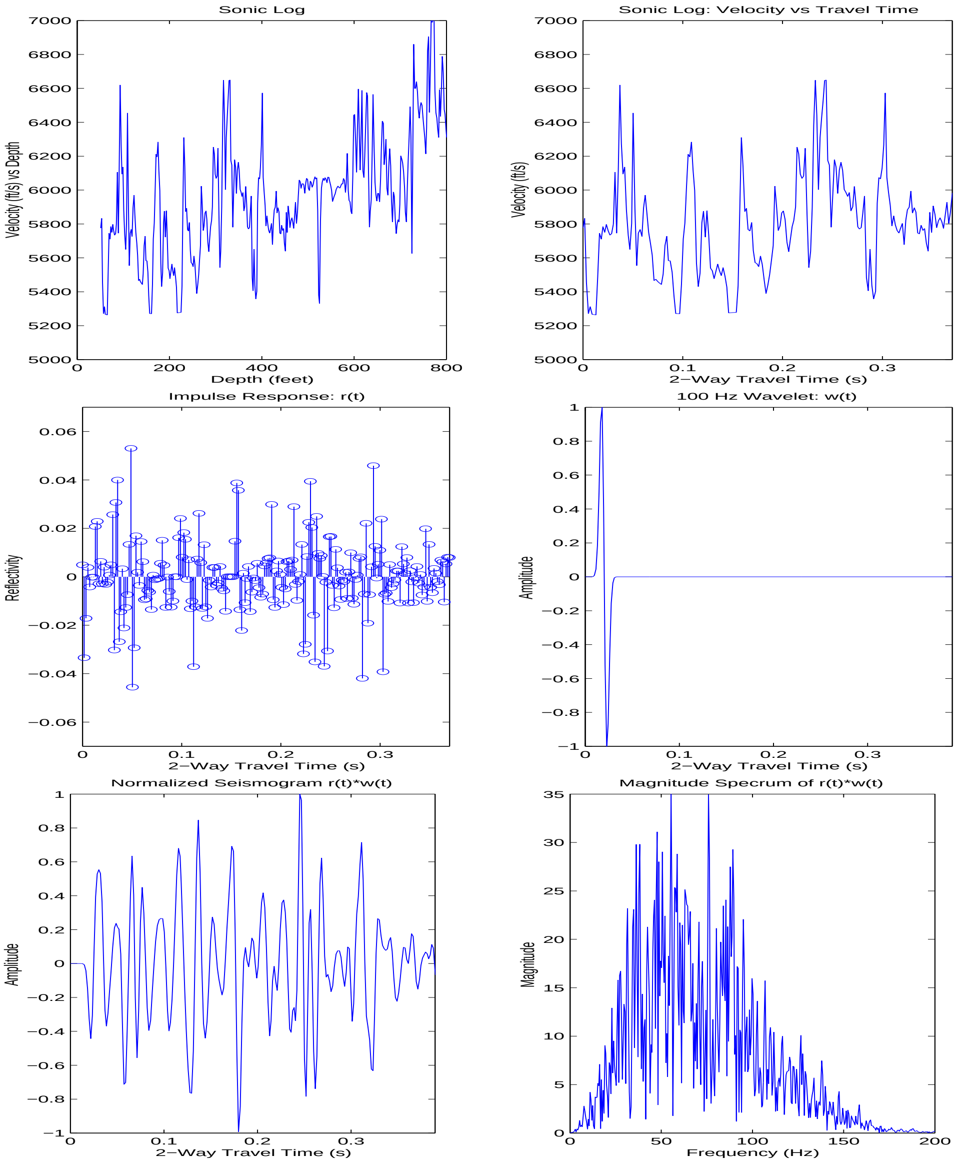

Figure 2.2: Synthetic (a). sonic log in depth, (b). sonic log in 2-way travel time , c). impulse response $r(t)$, d). 100 Hz wavelet $w(t)$, e). seismogram $s(t) = r(r) \star w(t)$ and f). associated magnitude spectrum.

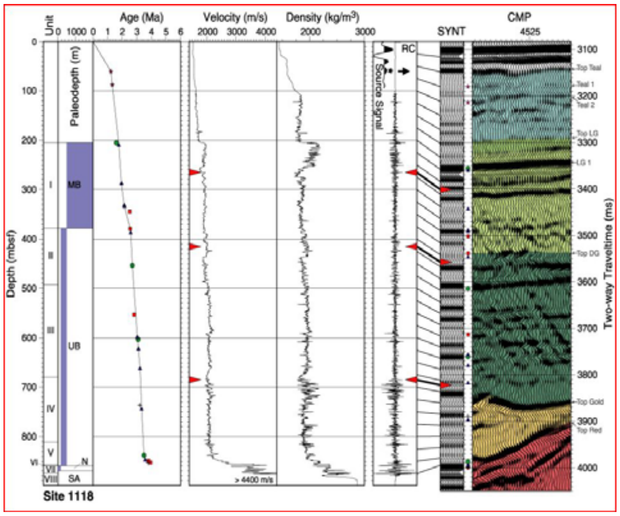

Figure 2.3: Field stacked section on far right and associated logs on left. Synthetic seismograms (derived from well logs) are shown just to the left of stacked section and correlate well with the recorded seismograms.

If the density profile is known then the density can be put into the above reflection coefficient formula.

The bandlimited response of the medium for a plane wave input (with source wavelet $w(t)$ as shown in Figure 2.2d) into the surface is a combination of arrivals, including primary and multiple reflections. If attenuation, transmission losses and multiples are excluded then the 1D convolutional model of the seismogram $s(t)$ is given by

$$s(t) = \int_{-\infty}^{\infty} r(\tau) w(t-\tau) d\tau, \tag{2.18}$$

which is the definition of convolution of $r(t)$ with $w(t)$, often abbreviated as $s(t) = r(t) \star w(t)$.

The above formula can be derived by taking the special case of the impulse response where the source wavelet is a Dirac delta function that is excited at time equal to zero: $w(t) = \delta(t)$, where the delta function is defined as $\delta(t) = 0$ if $t \neq 0$, otherwise $\delta(t) = 1$ in the sense $\int \delta(t) dt = 1$. Plugging this impulse wavelet into the above equation yields:

$$\begin{aligned} s(t) &= \int_{-\infty}^{\infty} r(\tau) \delta(t-\tau) d\tau, \\ &= r(t), \end{aligned} \tag{2.19}$$

which describes the reflection coefficient series shown in Figure 2.2c. Thus, the 1D impulse response of the earth under the above assumptions perfectly describes the reflection coefficient series as a function of 2-way traveltime. If the source wavelet were weighted by the scalar weight $w(\tau_i)$ and delayed by time τ_i then $w(t) = w(\tau_i)\delta(t - \tau_i)$ then the delayed impulse response of the earth would be

$$\begin{aligned} s(t)' &= \int_{-\infty}^{\infty} r(\tau) w(\tau_i) \delta(t - \tau_i - \tau) d\tau, \\ &= w(\tau_i) r(t - \tau_i), \end{aligned} \tag{2.20}$$

which is a weighted delayed version of the original impulse response in equation 2.18. If we were to sum these two seismograms we would get, by linearity of integration,

$$s(t)' + s(t) = w(\tau_0) r(t - \tau_0) + w(\tau_i) r(t - \tau_i), \tag{2.21}$$

where $\tau_0 = 0$ and $w(\tau_0) = 1$. By the superposition property of waves (i.e., interfering wave motions add together), we could have performed these two seismic experiments at the same time and the resulting seismograms would be identical mathematically to equation 2.21. More generally, the earth's response to an arbitrary wavelet $w(\tau)$ is given by

$$\begin{aligned} s(t) &= \sum_i w(\tau_i) r(t - \tau_i), \\ &\approx \int_{-\infty}^{\infty} w(\tau) r(t - \tau) d\tau, \end{aligned} \tag{2.22}$$

and in the limit of vanishing sampling interval $dt = \tau_{i+1} - \tau_i$ the approximation becomes an equality (see Figure 2.2e). Under the transformation of variables $\tau' = t - \tau$ equation 2.22 becomes

$$s(t) = \int_{-\infty}^{\infty} w(t - \tau') r(\tau') d\tau', \tag{2.23}$$

which is precisely the convolution equation shown in equation 2.18. The equality of equations 2.22 and 2.23 also shows that convolution commutes, i.e., $s(t) = r(t) \star w(t) = w(t) \star r(t)$. The convolutional modeling equation was practically used by many oil companies starting in the 1950's, and is still in use today for correlation of well logs to surface seismic data.

2.5.1 Multiples

Multiples associated with a strong reflector and the free surface can be accounted for in the 1D modeling equations. For a sea-bottom with depth d and two-way ZO traveltime τ_w, the sea-bed impulse response for ZO downgoing pressure waves with a source and pressure receiver just below the sea surface is given by

$$\overbrace{m(t)}^{Sea-floormultiplepointsrc.response} = w(t) + \sum_{i=1}^{\infty}(-R)^i w(t - i\tau_w) \tag{2.24}$$

where R is the ZO reflection coefficient of the sea floor; the -1 accounts for the free surface reversal of polarity and $w(t)$ is the source wavelet of the airgun modified by the interaction with the sea-surface reflectivity[1]. We assume that the propagation time between the surface and hydrophone streamer is negligible compared to the propagation time from the surface to the sea floor. See Figure **??**a for an example of the water-related multiples, and those generated by a single primary reflection with 2-way time of τ_1.

The upgoing multiples each act as a secondary source on the sea surface, so we can consider the "generalized" source wavelet to be $m(t)$. Thus the response of the medium is given by

$$s(t) = r(t) \star m(t), \tag{2.25}$$

as illustrated by the single sub-water reflector model in Figure **??**b. These multiples tend to blur the reflectivity response so we should try to deconvolve, i.e., eliminate, the multiples.

2.5.2 Multiple Prediction and Subtraction

The previous section showed how the free-surface multiples can be predicted if the water bottom topography was known. If there is non-zero offset between the source and receiver then the multiple associated with the water-bottom can be predicted by ray tracing through the water layer to generate all useful orders of the water bottom multiple.

These multiple predictions for zero-offset traces can be formed into $m(t)$, as described by equation 2.24. Therefore $m(t)$ can be used to predict the multiples and then they are subtracted from the original data to give primary reflections unpolluted by water-bottom multiples. This assumes that the direct wave $\delta m(t)$ is excluded from the multiple prediction, as illustrated in Figure 2.4.

The steps for this procedure are outlined below.

---

[1] We implicitly assume upgoing arrivals here and ignore the contributions from the source-side and receiver-side ghosts.

a). Water−bottom multiple generator m(t)

$$m(t) = \delta(t) + R\delta(t-\tau) - R^2\delta(t-2\tau) + R^3\delta(t-3\tau) - R^4\delta(t-4\tau)$$

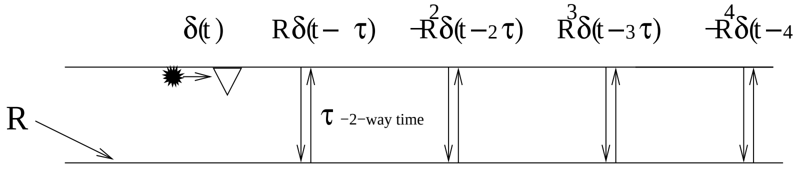

b). Primary exciting water−bottom multiples

$$r(t) = [\ \delta(t) + R\delta(t-\tau) - R^2\delta(t-2\tau) + R^3\delta(t-3\tau) - R^4\delta(t-4\tau)\ ] R_1\delta(t-\tau_1)$$

$$= [\ \delta(t-\tau_1) + R\delta(t-\tau_1-\tau) - R^2\delta(t-\tau_1-2\tau) + R^3\delta(t-\tau_1-3\tau) - R^4\delta(t-\tau_1-4\tau)\ \ R_1]$$

$$R_1\delta(t-\tau_1) \ * [\delta(t) + R\delta(t-\tau) - R^2\delta(t-2\tau) + R^3\delta(t-3\tau) - R^4\delta(t-4\tau)\ ]$$

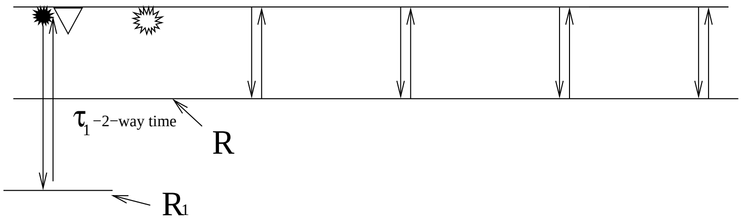

c). Prediction of multiples only; exclude direct wave $\delta(t)$ in m(t)

$$r(t) = [\ R\delta(t-\tau) - R^2\delta(t-2\tau) + R^3\delta(t-3\tau) - R^4\delta(t-4\tau)\ ] R_1\delta(t-\tau_1)$$

$$= [R\delta(t-\tau_1-\tau) - R^2\delta(t-\tau_1-2\tau) + R^3\delta(t-\tau_1-3\tau) - R^4\delta(t-\tau_1-4\tau)]\ R_1$$

$$R_1\delta(t-\tau_1) \ * [\ R\delta(t-\tau) - R^2\delta(t-2\tau) + R^3\delta(t-3\tau) - R^4\delta(t-4\tau)\ ]$$

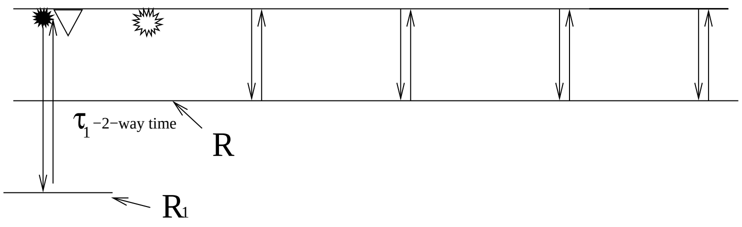

Figure 2.4: a). Upgoing multiples $m(t)$ associated with the water bottom, b). upgoing water-bottom multiples excited by an upgoing primary reflection $r(t) = R_1\delta(t-\tau_1)$ arriving at time τ_1 with strength R_1 to give the impulse response of $m(t) * r(t)$, and c). prediction of multiples only by excluding the direct arrival in $m(t)$. If the reflectivity series is given by the general time series $r(t)$, then the impulse response associated with water-bottom ringing and primary reflections is given by $r(t) \star m(t)$. All free-surface ghosts are neglected here.

1. Estimate $m(t)$ for zero-offset traces from equation 2.24. Ray tracing can be used to estimate the non-zero water-multiple generator. Mute out the direct wave in $m(t)$ and this function will still be denoted as $m(t)$.

2. For zero-offset traces, convolve $m(t)$ with the recorded data $s(t) = r(t) + m(t)$ to get $m(t) \star s(t) = r(t) \star m(t) + m(t) \star m(t)$. This is almost a good estimate of the water-bottom generated multiples $r(t) \star m(t)$, except for the errors given by $m(t) \star m(t)$.

3. We assume that $m(t) \star m(t)$ errors are small and so assume $s(t) \star m(t)$ is a good estimate of the water-bottom multiples. Therefore we use $s(t) \star m(t)$ to adaptively subtract from $s(t)$, i.e., $s(t) - s(t) \star m(t) \approx r(t)$. If this is not a good estimate of $r(t)$ we use $s(t) - s(t) \star m(t)$ as a good starting point to replace $s(t)$ in step 2. Note, in these steps we have assumed an impulsive wavelet and also that the direct wave $\delta(t)$ in $m(t)$ is muted.

4. If the wavelet is not impulsive (as it always is) then we deconvolve $w(t)$ after each step. If the traces are non-zero offset then the shot gather traces are given by $s(x,t)$ and the multiple generator is given by $m(x,t)$, where x is offset from the source. In this case the prediction strategy is $s(x,t) \star\star m(x,t)$, where $\star\star$ denotes both temporal and spatial convolution. The reason we need spatial convolution is a detail not needed at this point.

Figure 2.5 illustrate an original shot gather and it's prediction by a method that roughly resembles $m(x,t) \star s(x,t)$. Figure 2.6 depicts migration images before and after multiple prediction and subtraction.

2.6 Summary

We introduced the concept of a discrete linear time-invariant system, which is expressed mathematically as the convolution of the system's impulse response $h[t]$ with the input vector $x[t]$: $y[t] = x[t] \star h[t]$. The MA system produces an output vector that is a weighted summation of the input values: $\mathbf{y} = \mathbf{h} \star \mathbf{x}$. The AR system produces an output that is a weighted combination of input values and previous output values: $\mathbf{y} = \mathbf{f} \star \mathbf{y}$.

Seismic data $s(t)$ can be modeled by assuming the 1-D convolutional model of the earth: $s(t) = r(t) \star w(t)$, where $w(t)$ is the wavelet and $r(t)$ is the reflectivity series. This 1-D model assumes no multiples, no geometric spreading or anelastic losses. The seismic signal must be sampled according to the Nyquist sampling theorem: $dt < 2T^{minimum}$.

Multiples in seismic data blur the valuable information from the primary reflections. For water-bottom multiples, the strategy is to predict the multiples, and then adaptively subtract them form the data to get primaries only. The prediction is accomplished by generating a water-bottom multiple operator $m(t)$ and estimating the primaries by $r(t) \approx s(t) - m(t) \star s(t)$.

2.7 Exercises

1. Your first convolutions.

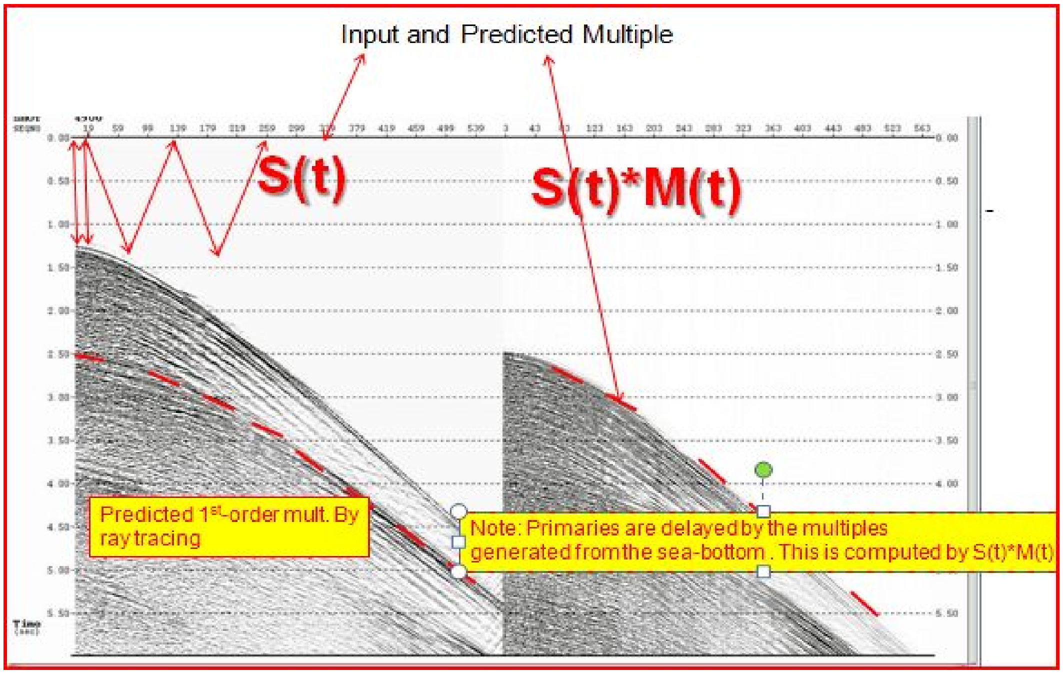

Figure 2.5: Illustration of a). a marine shot gather and b). the prediction of the multiples by a process that roughly approximates $m(x,t) \star\star s(x,t)$, where $s(x,t)$ represents the seismograms in a shot gather and x represents the source-receiver offset.

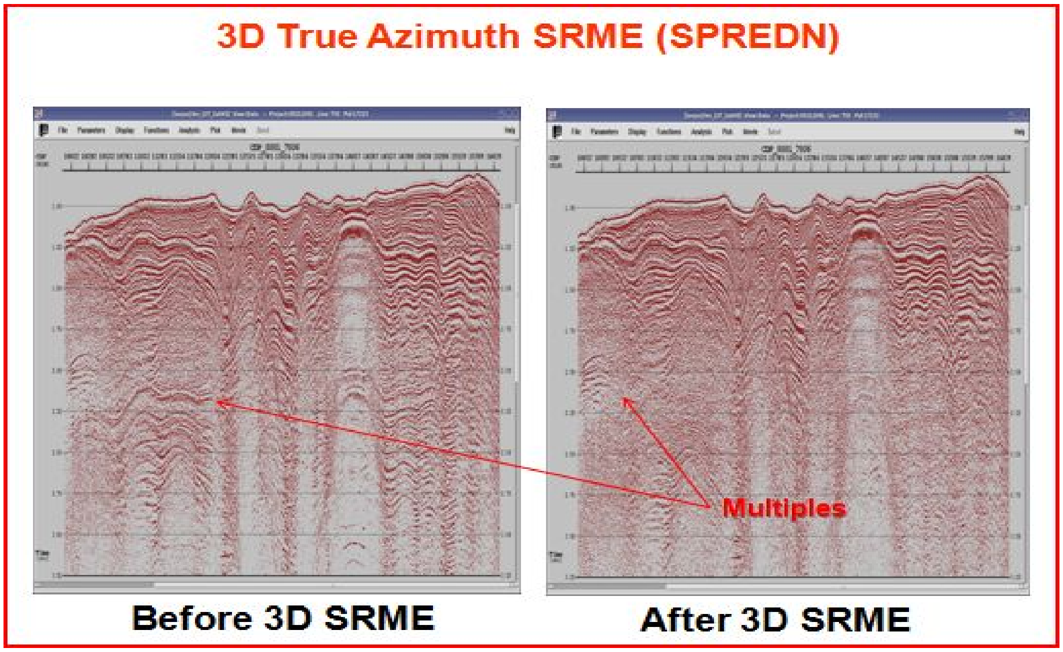

Figure 2.6: Migration images before and after multiple prediction and subtraction by the SRME method (courtesy of Aramco).

- Plot $x[n] = [x(0)\ x(1)\ x(2)] = [1\ .5\ .25]$. Now plot $x[-n+3]$, $x[n-3]$, $x[-n-3]$ and $x[n+3]$; which is the delayed and which is the advanced version of $x[n]$ (make sure you plot against the correct time values, including negative time if necessary)? Plot $x[-n]$ and explain why we say $x[-n]$ is a reflected version of $x[n]$. Explain why we say that $x[n-3]$ is a reflected-shifted version of $x[n]$.
- Convolve $[h(-1)\ h(0)] = [-1\ 1]$ with $\mathbf{x}$ (i.e., $y = h \star x$).
- Now convolve $\mathbf{x}$ with $[h(-1)\ h(0)]$ (i.e., $y' = x \star h$), where the elements of $\mathbf{x}$ comprise the matrix and $\mathbf{h}$ is the vector in the matrix-vector multiply. Note that $y^T = y$, which is true for any LTI system; the property of $\mathbf{x} \star \mathbf{h} = \mathbf{h} \star \mathbf{x}$ is the commutative property of any LTI systems. Note that, in general, matrix-matrix multiplication is not commutative.
- How long is the output vector $\mathbf{y}'$? What is the length of the output of convolving an Nx1 vector $\mathbf{x}$ with the Mx1 vector $\mathbf{h}$? Explain.

```
                    COMMUTATIVE PROPERTY OF CONVOLUTION

           ------                                ------
          I     I                               I     I
x  -----> I  H  I ------> y   or      h  -----> I  X  I ------> y
          I     I                               I     I
           ------                                 ------
```

- In general, multiplying an Nx1 vector by an MxN matrix costs $O(MN)$ algebraic operations. Explain why convolving the $Mx1$ h vector with the $Nx1$ $\mathbf{x}$ vector also costs $O(MN)$ algebraic operations.
- Convolve $[h(-10)\ h(-9)] = [-1\ 1]$ with $\mathbf{x}$ (i.e., $y = h \star x$).

3. Create an electrical or impedance layered model of the earth; make the model thick enough to be tailored to your interests (Moho?).

- Create synthetic seismograms or MT records associated with your model. Create the 5 figures associated with Figure 2.2, except use your model (see my Matlab script pltsonic.m). Adjust your source wavelet so that its dominant wavelength is about half the thickness of your thinnest layer. You might want to use a Ricker wavelet for your source function so examine my rick.m file. Actually, a better source wavelet might be the derivative of the Ricker wavelet, which can be obtained by using the Matlab command "diff(rick)", which differentiates the "rick" vector. The system model can be thought of as inputing a seismic wavelet $w(t)$ into the earth model represented by $r(t)$ to give $s(t) = r \star w$.
- The geophone has a non-impulsive response represented by $g(t)$ and perturbs the seismic response according to $s(t)' = s(t) \star g(t)$. Assume that the impulse response of the geophone is a 50 Hz Ricker wavelet and generate $s(t)'$.

- The first layer of your earth model generates multiples that generate a reverberation time signal
$$m(t) = (1\ 0\ \ -r\ 0\ r^2\ 0\ \ -r^3\ 0\ r^4....). \tag{2.26}$$
Here $m(t)$ can be considered as the downgoing impulse response of the reverberation layer. This assumes that it takes 2 time units to go from the surface to the reflecting layer and back up to the free surface, the reflection coefficient at the interface is r, and that the free-surface reflection coefficient is -1. Now generate the seismogram with multiples in it, i.e., $s' = s \star m \star w \star g$.

```
      m(0)     m(2)         m(4)    m(6)  ..........
----------------------------------------   Free-surface Refl.
      |         ^ |        ^ |     ^ |     Coefficient = -1
      |         | |        | |     | |
     1|       r | |-r  -r^2| |r^2  | |-r^3
      V         | V        | V     | V
------------------------------------   Water Table Int. Refl.
                                       Coefficient = r
```

```
np=input('type # points Ricker wavelet. output file=out ')
fr=input('type peak frequency of Ricker wavelet')
clear out
dt=.001;
npt=np*dt;
t=(-npt/2):dt:npt/2;
out=(1-t .*t * fr^2 *pi^2  ) .*exp(- t.^2 * pi^2 * fr^2 ) ;
plot(t,out);
axis([min(t) max(t) min(out) max(out)])
title([num2str(fr),' Hz Ricker Wavelet at ...
Sampling Interval = ',num2str(dt),' sec'])
xlabel('Time (s)')

load vpp.mat;load depth.mat;
subplot(321);plot(depth,vpp);xlabel('Depth (feet)');
ylabel('Velocity (ft/s)');
title('Sonic Log');axis([0 800 4000 9000]);

subplot(322);
time(1)=0;for i=2:623;time(i)=2*dz/(vpp(i)) + time(i-1);end;
plot(time(1:623),vpp(1:623)); axis([0 .39 4000 9000])
xlabel('2-Way Travel Time (s)');
ylabel('Velocity (ft/s)');title('Sonic Log: Velocity vs Travel Time')

subplot(323);y=diff(vpp);dt=diff(time);add=vpp(1:622)+vpp(2:623);
rc=y(1:622)./add(1:622);stem(time(1:622),rc(1:622));
axis([0 .39 -.3 .3])
xlabel('2-Way Travel Time (s)');
ylabel('Reflectivity ');title('Impulse Response: r(t)')

x=[0:1:622]*time(622)/622;
 subplot(324);delay=0.021101;
w=diff( exp(-62000*(delay-x).^2 )/2 );w=w/max(w);
plot(x(1:622),w(1:622));axis([0 .39 -1 1])
xlabel('2-Way Travel Time (s)');
ylabel('Amplitude ');title('100 Hz Wavelet: w(t) ')

dt=time(300)-time(299);
subplot(325);s=conv(w,rc);s=s/max(s);plot(time(1:622),s(1:622));
xlabel('2-Way Travel Time (s)');ylabel('Amplitude ');
```

```
title('Normalized Seismogram r(t)*w(t) ')
axis([0 .39 -1 1])
```

Part II

Traveltime and Acoustic Waveform Modeling Methods

Chapter 1

Finite-Difference Approximation to the Acoustic Wave Equation

1.1 Introduction

The Kirchhoff migration method relies on a high frequency approximation to estimate the Green's function $g(\mathbf{x}, t|\mathbf{x}', 0) \approx A(\mathbf{x}, \mathbf{x}')\delta(\tau_{xx'} - t)$, where the geometrical spreading term $A(\mathbf{x}, \mathbf{x}')$ and traveltimes $\tau_{xx'}$ are computed by an efficient raytracing code. This has the advantage of being computationally efficient, but it typically avoids multiples and turning waves that can be used to image subsalt. For example, Figure **??** depicts the salt flank imaged by a single-arrival Kirchhoff migration code and a 1-way wave equation migration code. Here, the flat portions of reflectors are well imaged but the salt flanks are still somewhat invisible. In comparison, the 2-way reverse time migration image clearly reveals the salt flank by migrating the primary reflections from nearly flat layers as well as the multiple reflections off the flanks (i.e., prism ray). The multiple prism wave reflections illuminate the salt flank that is mostly invisible to the primary reflections in this experiment. In this chapter we introduce the finite-difference method for approximating solutions to the acoustic wave equation. In the limit as the grid spacing becomes small the solutions should be exact and so include all primary and multiple scattering seen in the actual data. It is for this reason that the finite-difference method is used in reverse time migration codes. And the FD method is also uised to compute the band-limited Green's functions for wave equation inversion.

1.2 Finite Difference Method

This section discusses how to compute finite-difference solutions to the wave equation. These solutions provide approximations to the Greens functions for forward and backward wavefield propagation.

Table 1 contains various finite-difference approximations to 1st- and 2nd-order derivative operators. The order of accuracy can be estimated by using a Taylor series expansion. For

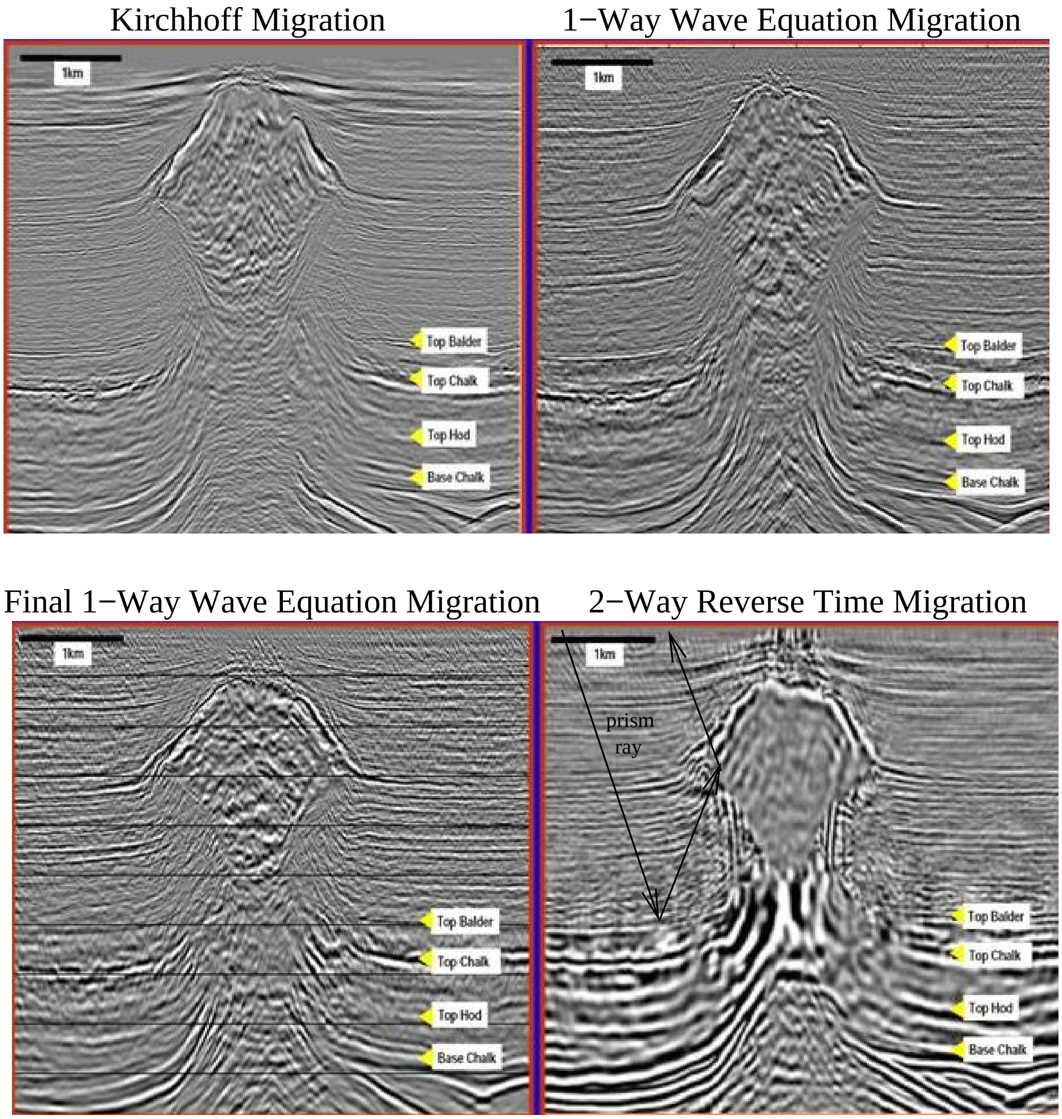

Kirchhoff Migration

1−Way Wave Equation Migration

Final 1−Way Wave Equation Migration

2−Way Reverse Time Migration

Figure 1.1: Images of salt flank formed by using single-arrival Kirchhoff migration, 1-way wave equation migration, and a 2-way reverse time migration code. Note the prism ray that illuminates the salt flank, and is only migrated by the RTM code. Taken from Farmer et al. (2007, TLE).

Table 1.1: Finite Difference (FD) formulae for 1st- and 2nd-order differential operators, where dx is the difference interval.

Differential Operator	FD Approx.	FD Name	Order of Accuracy
$df(x)/dx$	$[f(x+dx)-f(x)]/dx$	Forward FD	$O(dx)$
$df(x)/dx$	$[f(x)-f(x-dx)]/dx$	Backward FD	$O(dx)$
$df(x)/dx$	$[f(x+dx)-f(x-dx)]/2dx$	Central FD	$O(dx^2)$
$d^2f(x)/dx^2$	$[f(x+dx)-2f(x)$ $+f(x-dx)]/dx$	Central FD	$O(dx^2)$

example, in the forward FD approximation we have:

$$\begin{aligned}\frac{f(x+dx)-f(x)}{dx} &= \frac{f(x)+\partial f(x)/\partial x\cdot dx+0.5\partial^2 f(x)/\partial x^2\cdot dx^2+...-f(x)}{dx},\\ &= \frac{\partial f(x)}{\partial x}+1/2\frac{\partial^2 f(x)}{\partial x^2}\cdot dx+....,\\ &= \frac{\partial f(x)}{\partial x}+O(dx),\end{aligned} \tag{1.1}$$

which says that this FD approximation is first-order accurate in the sample interval dx. Similarly, the central FD approximation to a second derivative $\partial[\partial f(x)/\partial x]/\partial x$ can be proved by applying a forward FD approximation to the term in brackets and a backward FD approximation to the outer term.

1.2.1 Finite-Difference Approximation to the Wave Equation

The 2-D acoustic wave equation for a medium with no density variations is given by:

$$\frac{\partial^2 p(\mathbf{x},t)}{\partial x^2}+\frac{\partial^2 p(\mathbf{x},t)}{\partial z^2}-\frac{1}{c(x,z)^2}\frac{\partial^2 p(\mathbf{x},t)}{\partial^2 t} \;=\; f(\mathbf{x},t), \tag{1.2}$$

where $c(x,z)$ is the velocity field, $p(\mathbf{x},t)$ is the pressure field and $f(\mathbf{x},t)$ is the inhomogeneous source term. The continuous wave equation and its solution can be discretized onto an evenly sampled grid in the space-time domain, i.e.,

$$
\begin{aligned}
(x,z,t) \quad &------> \quad (i*dx, j*dz, t*dt),\\
&\qquad\qquad\quad \textit{where } i,j,t \textit{ are integers}\\
p(x,z,t) \quad &------> \quad p_{ij}^{t},\\
f(x,z,t) \quad &------> \quad f_{ij}^{t},\\
c(x,z) \quad &------> \quad c_{ij}. \qquad (1.3)
\end{aligned}
$$

and for convenience it will be assumed that the vertical gridpoint spacing dz is the same as the horizontal spacing dx.

It is convenient to visualize wave propagation in a data cube (see Figure 1.2), with two cartesian axis oriented along the x and z axes and the third axis is for the time variable t. The depth of the data cube is given by $Mdz = D$, the width of the cube is $Ndx = X$, and the temporal extent of the cube is $Ldt = T$, where M, N and L are integers.

Pivoting (i.e., evaluating) the pressure field at (i,j,t) and approximating the second-order derivatives in equation 1.2 by 2nd-order correct central-difference approximations yields:

$$
\begin{aligned}
p_{ij}^{t+1} \quad = \quad & a[p_{i+1j}^{t} - 2p_{ij}^{t} + p_{i-1j}^{t}] + a[p_{ij+1}^{t} - 2p_{ij}^{t}\\
& + p_{ij-1}^{t}] + 2p_{ij}^{t} - p_{ij}^{t-1} - dx^2 a f_{ij}^{t}, \qquad (1.4)
\end{aligned}
$$

where $a = (dtc_{ij}/dx)^2$. If the initial conditions are given (i.e., $p(\mathbf{x}, t=0)$ and $\partial p(\mathbf{x}, t=0)/\partial t$ are known for all (x,z)) then the present panel at $t=0$ and past panel at $t=-dt$ can be used in equation 1.4 to find the panel of pressure field values at $t=dt$ for all (x,z). These field values at $t=dt$ can then be used in conjunction with equation 1.4 to iteratively find the pressure field at panels with increasing increments of time, as illustrated in Figure 1.

A transformation of coordinates from $t=-t'$, i.e., time reversal, will leave the form of the wave equation equation 1.2 unchanged. Thus, the wave equation is invariant under a sign reversal in time. The Green's function of the time-reversed wave equation will be the same as the original Green's function, except for a change in the sign of the temporal variable. Time will flow backward in this case, where the forward light cone in Figure 1.3 will become a backward light cone. The important point is that backward light cones can be generated with the finite-difference equations by solving backward in time rather than forward in time.

1.2.2 Stability and Accuracy

The accuracy of the 2-2 (i.e., 2nd-order accurate in time and space) scheme is empirically found (Kelly et al., 1976) to be acceptable in a homogeneous medium if there are at least 10 points per minimum wavelength. However, 15-20 points per wavelength is usually used for heterogeneous media. A higher-order FD scheme such as a 2-4 scheme requires about 5 points/wavelength in a homogeneous medium (Levander, 1989), but 10-15 points per wavelength is needed in an heterogeneous medium. If the gridpoint spacing is too coarse, dipping interfaces appear as stair-steps, where the edge of each step acts as a strong diffractor.

The CFL (Courant-Friedrichs-Levy) stability condition can be determined by noting that a FD solution satisfying both the wave equation and the initial conditions at $t=0$

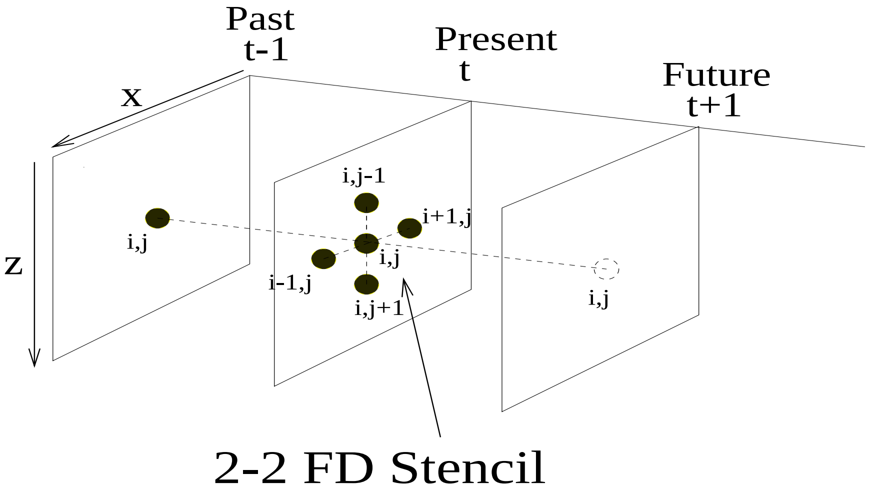

Figure 1.2: Depiction of 2-2 FD stencil for the 2-D acoustic wave equation. The future value of the pressure at the (i, j) node (open dashed circle) is computed from the present and past values of the pressure that neighbor the (i, j) node at the present time t. The stencil can shifted within the t plane to compute the pressure values within the $t+1$ plane. The pressure values at the boundaries of these planes must be specified.

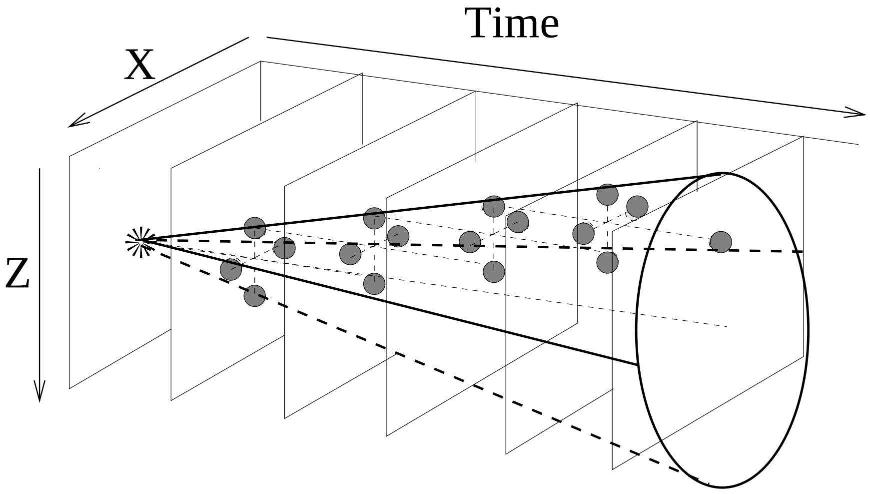

Figure 1.3: Depiction of forward light cone generated by a FD solution to the wave equation for a point source at depth. The Numerical Domain of Influence for the poitn source is alive within the conical boundaries, but is quiescent outside the cone. Note that the physical propagation velocity should be slower than the cone velocity in order for the FD solution to emulate the actual wave phenomenon.

must have a Numerical Domain of Dependence (DOD) (shown in Figure 1.4) larger than the Analytical DOD (Mitchell and Griffiths, 1980). Otherwise the FD solution will be partly ignorant of the initial conditions that influenced the solution at (x_0, t_0). This ignorance will lead to an unstable FD solution. To avoid such ignorance the numerical propagation velocity (defined by dx/dt in 1-D) must be faster than the actual propagation velocity c. This condition is equivalent to the 1-D CFL stability criterion:

$$\frac{1}{c} \quad > \quad \frac{dt}{dx}, \tag{1.5}$$

which in two dimensions takes the form: and the 2-D stability criterion:

$$\frac{1}{\sqrt{2}} \quad > \quad \frac{cdt}{dx}. \tag{1.6}$$

Therefore, dx is selected to satisfy the accuracy condition and dt is selected to satisfy the stability condition.

FD Exercises

1. Using a Taylor's series, prove that $[p(i+1) - 2p(i){+}p(i-1)]/(dx^2)$ is a 2nd-order correct approximation to the second derivative.

2. Prove that $[-p(i{+}2) + 16p(i{+}1) - 30p(i){+}16p(i-1) - p(i-2)]/(12dx^2)$ is a 4th-order correct approximation to the second derivative.

3. Prove the 2-D stability condition given by equation 1.6. This is a necessary condition for stability.

4. Prove that the stability condition for a 2-2 scheme in 3-D is the same as that for the 2-D case except the square root of 2 is replaced by the square root of 3.

1.3 Numerical Implementation of 2-2 FD Modeling

MATLAB codes will now be described which can be used for waveform inversion.

1.3.1 2-2 FD MATLAB Code

The MATLAB code for a 2-2 FD solution to the acoustic wave equation is given below.

```
%%%%%%%%%%%%%%%%%%%%%%%%%%%%%%%%%%%%%%%%%%%%%%%%%%%%%%%%%%%%%%%%%%%%%%
% (NX,NZ,NT) - input- (Horizontal,Vertical) gridpt dimens. of vel
% model & # Time Steps
% FR - input- Peak frequency of Ricker wavelet
% BVEL - input- NXxNZ matrix of background velocity model
% (dx,dt) - input- (space, time) sample intervals
% (xs,zs) - input- (x,z) coordinates of line source
% RICKER(NT) - input- NT vector of source time histories
% (p2,p1,p0) -calcul- (future,present,past) NXxNZ matrices of
```

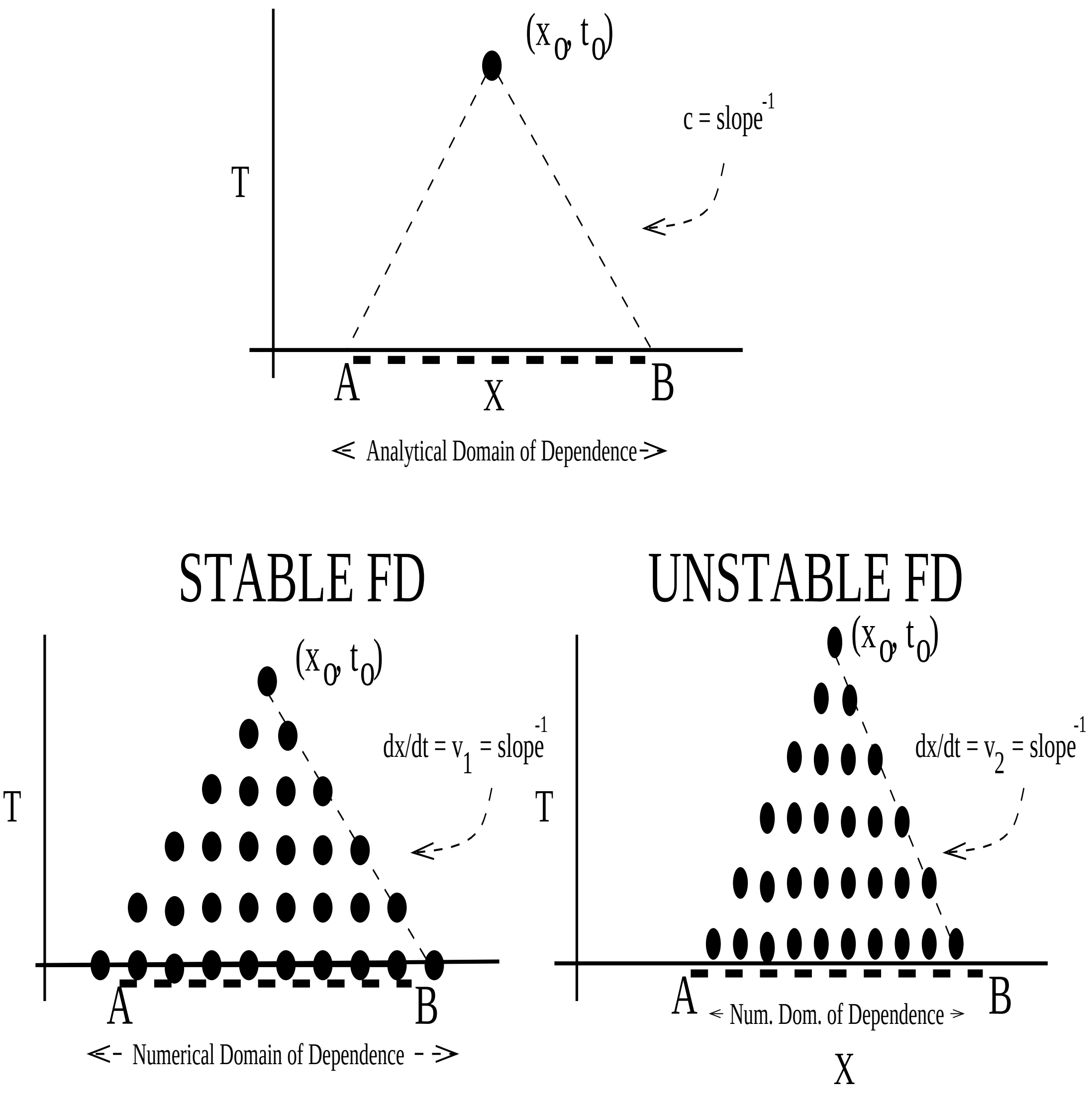

Figure 1.4: (Top) The dashed triangle outlines the region that influences the pressure value at (x_0, t_0), and the heavy dashed horizontal line $\vec{AB}$ at at $t = 0$ defines the analytical domain of dependence (DOD). Here the physical propagation velocity is defined as c. The dotted triangular region in the bottom left figure defines the region that influences the pressure field at (x_0, t_0) computed by a FD scheme. This FD scheme is stable because the numerical propagation velocity dx/dt is faster than the actual velocity c, or equivalently the Numerical DOD is wider than the analytical DOD $\vec{AB}$. This is not true for the figure at the bottom right.

```
% modeled pressure field
% (p0,p1) -output- Old and present pressure panels at time NT.
% REALDATA(NX,NT) -output- CSG seismograms at z=2
%%%%%%%%%%%%%%%%%%%%%%%%%%%%%%%%%%%%%%%%%%%%%%%%%%%%%%%%%%%%%%%%
c=4.0;FRE=20;
NX=300;NZ=NX; dx=c/FRE/20;dt=.5*dx/c;
xs=round(NX/2.3); zs=round(NX/2);NT=600;
t=[0:1:NT-1]*dt-0.95/FRE;RICKER=zeros(length(t));
RICKER= (1-t .*t * FRE^2 *pi^2 ) .*exp(- t.^2 * pi^2 * FRE^2 ) ;
plot([0:NT-1]*dt,RICKER);
title('Ricker Wavelet');xlabel('Time (s)')
BVEL=ones(NX,NZ)*c;
BVEL(NX-round(NX/2):NX,:)= BVEL(NX-round(NX/2):NX,:)*1.2;
REALDATA=zeros(NX,NT);
p0=zeros(NX,NZ);p1=p0;p2=p0;
cns=(dt/dx*BVEL).^2;
NX=200;NZ=NX;
for it=1:1:NT
p2 = 2*p1 - p0 + cns.*del2(p1);
p2(xs,zs) = p2(xs,zs) + RICKER(it);
REALDATA(:,it) = p2(xs,:)';
p0=p1;p1=p2;
if round(it/20)*20==it;p00=p0/max(abs(p0(:))+.001);
imagesc([1:NX]*dx,[1:NX]*dx,(p00+BVEL)); colorbar;
pause(.1);end
end;
p1=p0;p0=p2;
title('Snapshot of Acoustic Waves')
xlabel('X (km)')
ylabel('Z (km)')
```

No absorbing boundary conditions have been included in the above code, but this problem can be rectified by absorbing boundary conditions (Kelly et al., 1976; Keys, 1985).

1.4 Sponge Absorbing Boundary Conditions

The boundaries along the side of the model reflect incident waves back into the model, and therefore interfere with the desired waves. To minimize these spurious reflections from the sides of the model absorbing boundary conditions are applied to the sides of the model. The simplest absorbing boundary condition is that of a damping zone with thickness of about 50 grid points that are next to the sides of the model. Inside this region an exponential damping function $f(x,y)$ is applied to the waves at each time step: $f(x,y) = e^{-\alpha r}$ where $f(x,y) = 1$ if (x,y) are further than 50 grid points from the sides, and r is the distance between the grid point at (x,y) and the nearest side boundary. The damping parameter α is selected to minimize boundary reflections; usually a good value is such that the exponential

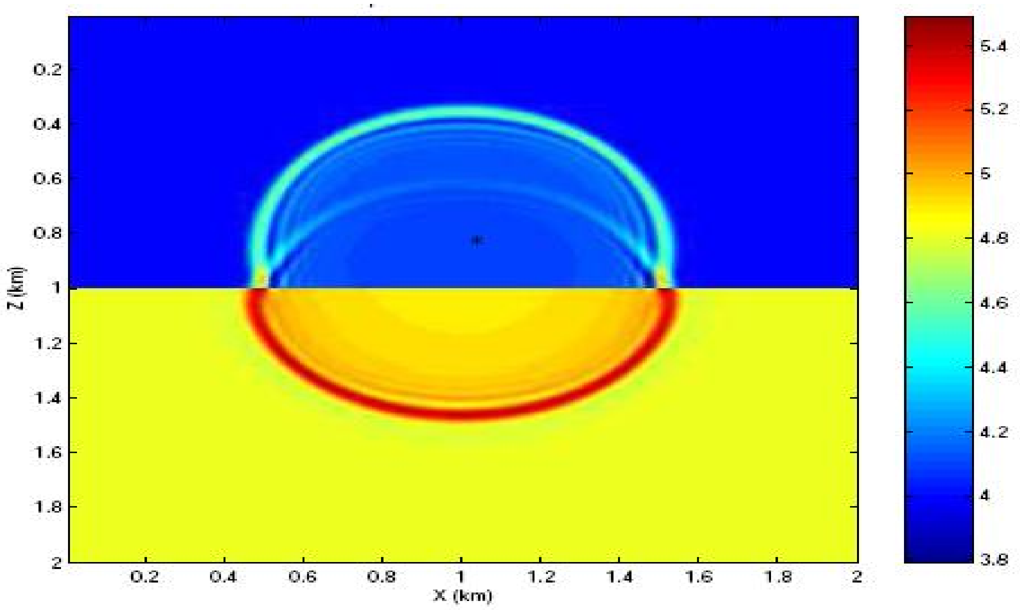

Figure 1.5: Snapshot of an acoustic simulation in a 2-layer medium. The star denotes the location of the point source.

damping is about .96 at the outer boundary of the model. An example of snapshot of a propagating wave in a 2-layer medium is shown in Figure 1.5.

ABC Exercises

1. Prove that the stability condition for a 2-2 scheme in 3-D is the same as that for the 2-D case except the square root of 2 is replaced by the square root of 3.

2. Write a MATLAB code that computes a 4th-order finite difference solution to the acoustic wave equation.

3. Show that the rightgoing propagating plane wave $p = e^{i\omega x/c - i\omega t}$ exactly satisfies the absorbing boundary condition $\partial p/\partial t + c^{-1}\partial p/\partial x = 0$. Show how a 1-1 FD approximation to this equation can be used to update the right-hand-side boundary values of the $t+1$ panel in Figure 1.2. Describe the absorbing boundary conditions that absorb upgoing or downgoing or leftgoing plane waves. See Keys (1985) for a generalization of these absorbing boundary conditions.

4. Make a movie of waves emanating from a buried point source in a 300x200 grid model with a Ricker wavelet time history for the point source. Let c=5000 ft/s and choose the dx and the peak frequency of the Ricker source wavelet so that there are about 15 points/wavelength, where the minimum wavelength is twice the peak frequency of the Ricker wavelet. The code for the zero-phase Ricker wavelet is given below, and the wavelet is delayed in time to insure causality of the source wavelet.

```
%%%%%%%%%%%%%%%%%%%%%%%%%%%%%%%%%%%%%%%%%%%%%%%%%%%%%%%%%%%
% NT     - input- # points Ricker wavelet
% FR     - input- Peak frequency of Ricker wavelet
% dt     - input- Temporal sampling interval
% RICKER -output- Time delayed Ricker wavelet
%%%%%%%%%%%%%%%%%%%%%%%%%%%%%%%%%%%%%%%%%%%%%%%%%%%%%%%%%

t=[0:1:NT-1]*dt-0.95/FR;RICKER=zeros(length(t));
RICKER= (1-t .*t * FR^2 *pi^2  ) .*exp(- t.^2 * pi^2 * FR^2 ) ;
```

Exercise 1 *Apply a 40-point sponge zone to the 2-2 FD code. Find the value of α that optimizes absorption of waves that enter the sponge zone.*

1.5 Absorbing Boundary Conditions

An important absorbing boundary condition (ABC) is obtained by factoring the wave equation into leftgoing and rightgoing component PDEs that are a weighted sum of 1st-order space and time derivatives. That is, the 1D wave equation can be recast into the following form:

$$\overbrace{(\frac{\partial}{\partial x}+\frac{1}{c}\frac{\partial}{\partial t})}^{rightgoing\ waves}\ \overbrace{(\frac{\partial}{\partial x}-\frac{1}{c}\frac{\partial}{\partial t})}^{leftgoing\ waves}\ P \quad = \quad 0, \tag{1.7}$$

where a homogeneous velocity c is assumed and P is the solution to the wave equation. The left-bracketed term above is called a rightgoing wave annihilator because a rightgoing plane wave $P^+ = e^{i(kx-\omega t)}$ (for $k > 0,\ \omega > 0$) exactly satisfies this equation. That is,

$$\overbrace{(\frac{\partial}{\partial x}+\frac{1}{c}\frac{\partial}{\partial t})}^{rightgoing}P^+ \quad = \quad i(k-\omega/c)P^+ = 0. \tag{1.8}$$

In a similar fashion, the other bracketed term in equation 1.7 exactly annihilates leftgoing waves $P^- = e^{i(kx+\omega t)}$ such that

$$\overbrace{(\frac{\partial}{\partial x}-\frac{1}{c}\frac{\partial}{\partial t})}^{leftgoing}P^- \quad = \quad i(k-\omega/c)P^- = 0. \tag{1.9}$$

Therefore, we can apply the 1st-order rightgoing wave operator to the rightside boundary of the computational grid and expect perfect annihilation of a plane wave that is purely rightgoing. A similar procedure can be used for the leftside boundary except we use a FD approximation to the leftgoing annihilation operator[1]. These operators can be approximated by one-sided FD approximations to the first-order spatial derivative. The one-sided nature

---

[1] For the bottom of the model the dowgoing wave annihilator is $(\partial/\partial x - 1/c\partial/\partial t)$ for decreasing z in the depth directions.

of the FD approximation insures that the FD stencil does not need field values outside the grid.

As an example, the FD approximation to the rightgoing operator in equation 1.7 is

$$(\frac{\partial}{\partial x}+\frac{1}{c}\frac{\partial}{\partial t})P \quad\approx\quad \frac{P^t_{i+1}-P^t_i}{\Delta x}+\frac{1}{c}\frac{P^{t+1}_{i+1}-P^t_{i+1}}{\Delta t}=0 \tag{1.10}$$

where the spatial pivot point is at the $i+1$ gridpoint along the x axis. Here, a 1st-order forward differencing in time (pivoted at time t) is used along with a backward differencing in space (pivoted at spatial gridpoint $i+1$).

The unknown field value P_N^{t+1} at future time $t+1$ can be solved for at the rightside boundary labeled as $i+1=N$ to get

$$P_N^{t+1} \quad=\quad -c\Delta t\frac{P^t_N-P^t_{N-1}}{\Delta x}+P^t_N. \tag{1.11}$$

Note, the field values at time t are assumed to be known everywhere within the computational model. Here, the spatial index numbers increase for points from left to the right with the last computational gridpoint number denoted as N. A similar argument shows that the leftgoing operator applied to the leftside boundary is given by

$$P_1^{t+1} \quad=\quad c\Delta t\frac{P^t_2-P^t_1}{\Delta x}+P^t_1, \tag{1.12}$$

except the 1st-order spatial derivative is replaced by a forward difference approximation pivoted at the number 1 gridpoint.

What happens if the wave, e.g., $P^+=e^{i(k_xx+k_zz-\omega t)}$ is traveling obliquely to the horizontal axis? In this case we see that the rightgoing operator does not exactly satisfy the wave equation:

$$(\frac{\partial}{\partial x}+\frac{1}{c}\frac{\partial}{\partial t})P^+ \quad=\quad i(k_x-\omega/c)P^+\neq 0. \tag{1.13}$$

In this case the only way the equation can be satisfied at the boundary is if a left going wave with reflection strength R is generated at the boundary. That is, at the boundary, a combination of a rightgoing and leftgoing waves

$$P^+ \quad=\quad \overbrace{e^{i(k_xx+k_zz-\omega t)}}^{rightgoing}+\overbrace{Re^{i(-k_xx+k_zz-\omega t)}}^{leftgoing}, \tag{1.14}$$

are superimposed to exactly satisfy the rightgoing wave operator. The value of R increases with increasingly oblique angles of incidence. This can be shown analytically by plugging equation 1.14 into equation 1.8 and solving for R.

To annihilate waves at several incidence angles Keys (1985) showed that the wave equation could be decomposed into

$$\overbrace{(\nabla+\frac{\mathbf{a}}{c}\frac{\partial}{\partial t})}^{rightgoing\ waves}\quad\cdot\quad\overbrace{(\nabla-\frac{\mathbf{a}}{c}\frac{\partial}{\partial t})}^{leftgoing\ waves}\quad P \quad=\quad 0, \tag{1.15}$$

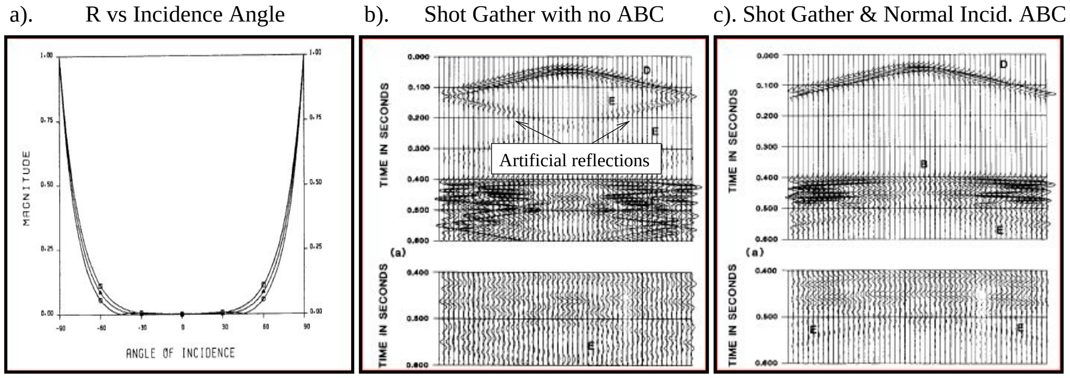
a). R vs Incidence Angle b). Shot Gather with no ABC c). Shot Gather & Normal Incid. ABC

Figure 1.6: a). R vs incidence angle graph for incidence angles $|\theta|$ equal to 15 degrees and 45 using the ABC in equation 1.17, b). shot gather using no ABC along left and right sides of model, and c). shot gather using an ABC tuned to annihilate plane waves normally incident on the boundary.

where $\mathbf{a}$ is selected to absorb waves at several incidence angles. In this case the rightgoing wave operator will annihilate a rightgoing plane wave $P^+ = e^{i(k_x x + k_z z - \omega t)}$ if $\mathbf{a}/c$ is equal to $\mathbf{k} = (k_x, k_z)$, which is parallel to the oblique direction of $\mathbf{k}$. This can easily be seen since $\nabla P^+ = i\mathbf{k}P^+$, which when plugged into the rightgoing operator in equation 1.15 gives

$$\nabla P^+ - \frac{\mathbf{a}}{c}\frac{\partial P^+}{\partial t} = i(\mathbf{k} - \frac{\mathbf{a}}{c}) = 0, \tag{1.16}$$

if $\mathbf{a}/c = \mathbf{k}$. A slight adjustment of this ABC increases its capability to absorb plane waves in two directions parallel to either $\mathbf{k_1}$ and $\mathbf{k_2}$. This adjusted ABC is given by

$$\mathbf{a_1} \cdot (\nabla P^+ - \frac{\mathbf{a_2}}{c}\frac{\partial P^+}{\partial t}) = 0, \tag{1.17}$$

where one of the perfect absorption directions is parallel to $\mathbf{a}_2$ and the other is at $(\mathbf{a}_1 + \mathbf{a}_2)/|\mathbf{a}_1 + \mathbf{a}_2|^2$. Figure 1.6a depicts the reflection strength $|R|$ vs incidence angle for waves reflecting from a boundary with the equation 1.17 ABC. Here, the ABC is designed to perfectly annihilate waves incident at angles of plus/minus 15 and 30 degrees. Figures 1.6b-c depict shot gathers before and after application of ABCs along the side boundaries. Note the improvement in reducing artifacts from the model boundaries after application of the ABC.

Since waves are typically traveling in all directions at a model boundary then some artificial reflections are generated for non-normal incidence angles, even for the equation 1.6 ABC. Thus we get artificial unwanted reflections generated at the boundaries that propagate into the interior part of the grid. If such artificial reflections are strong then they can spoil the accuracy of the simulation. For this reason a combination of 1st-order ABC's and absorbing sponges are used in some FD codes.

---

[2] Note, a rogue plane wave traveling in a direction not parallel to $\mathbf{a_2}$ will not zero out the term in parentheses in equation 1.17; instead it will leave a predictable residual vector denoted by $\mathbf{r}$. In this case we can choose $\mathbf{a_1}$ to be perpendicular to $\mathbf{r}$ so this rogue plane wave will be annihilated.

1.6 Summary

A 2-2 finite difference scheme is used to simulate wave propagation in an arbitrary velocity model of constant density. The method can be used to migrate reflected arrivals in RTM, or estimate the velocity distribution for waveform inversion. Stability and accuracy conditions are described, and absorbing boundaries should be applied to the model to minimize spurious reflections. The more modern approach is to use much higher order finite-difference stencils, with recommendations of up to 8th-order in space and 4th-order in time. This will enhance the accuracy but slow down the computation time.

Chapter 2

Traveltime Calculation by Solution of Eikonal Equation

This chapter introduces the eikonal equation, and shows how to solve it by a finite-difference method. The output is the first-arrival traveltime field for a smoothly varying inhomogeneous velocity model. These traveltimes are used for both traveltime tomography and reflection migration.

Section 1 describes the derivation of the eikonal equation, followed by section 2 which presents the algorithm for computing traveltimes by a finite-difference solution to the eikonal equation.

2.1 Eikonal Equation

The acoustic isotropic wave equation from chapter 1 can be expressed in terms of the particle displacement vector $\mathbf{u}$:

$$\rho \frac{\partial^2 \mathbf{u}}{\partial t^2} = \nabla(\kappa \nabla \cdot \mathbf{u}), \tag{2.1}$$

where κ is the bulk modulus.

For a harmonic plane wave source oscillating at angular frequency ω and a scatterer embedded in a medium with smoothly varying velocity, it is reasonable to assume that scattered far-field first arrivals can be approximated by a free-space Green's function, i.e,

$$\mathbf{u}(\mathbf{r}, \omega) \sim \mathbf{A}(\mathbf{r}) e^{i\omega\tau}, \tag{2.2}$$

where the scatterer is at the origin, τ is the traveltime from the scatterer to the interrogation point $\mathbf{r}$, and $\mathbf{A}(\mathbf{r})$ is a displacement vector that accounts for scattering and geometrical spreading losses. This displacement vector is parallel to the direction of wave propagation, as a P body wave should behave.

Equation 2.2 can be used as an *ansatz* or trial solution to the wave equation. The unknowns $\mathbf{A}$ and τ can be found by plugging equation 2.2 into equation 2.1 to yield a quadratic equation in ω. At high frequencies, the geometrical spreading term is governed by the transport equation:

$$-\rho \mathbf{A} + \kappa(\mathbf{A} \cdot \nabla\tau)\nabla\tau = 0. \tag{2.3}$$

This equation is true by choosing $\nabla\tau$ to be parallel to $\mathbf{A}$ to give

$$|\nabla\tau|^2 = \rho/\kappa = {v_P}^{-2}, \tag{2.4}$$

where v_P is the P-wave velocity. This equation is valid for smoothly varying velocities where the dominant wavelength of the velocity medium is at least 3 times larger than that of the source wavelength (Bleistein, 1993).

Equation 2.4 is the P-wave eikonal equation whose solution can yield the traveltime of the first P- arrival everywhere in an inhomogeneous velocity medium. This equation also leads to the traveltime integral which is used to calculate the traveltimes of rays that traverse the medium. For an elastic medium with both P and S body waves the eikonal equations are derived in the appendix.

2.1.1 Finite Difference Solution To The Eikonal Equation

The traveltime field can be computed by a finite-difference solution to the eikonal equation (Qin et al., 1992). For the refraction tomography example in Figure **??**, the finite difference algorithm is given in the following steps:

1. Project the slowness field $s(\mathbf{x})$ onto a rectangular grid of nodes as shown in Figure **??**, and assume a constant slowness value s_i in the i^{th} cell.

2. Calculate the first arrival traveltime from the source point to its nearest eight neighboring nodes by simple ray tracing or a simple finite-difference approximation to the eikonal equation. In the Figure 2.1a example, the traveltime t_{B1} at point B1 is calculated by $t_{B1} = \Delta x \ s(\vec{B1})$, where Δx is the distance between the source and the point B1. The other seven gridpoints are timed in a similar fashion. The outer ring of timed gridpoints represents the computational wavefront at a particular iteration; and the computational wavefront expands along with the physical first arrival wavefront. Ray tracing is used until the computational wavefront is at least 5 points from the source point (see Qin et al., 1992).

3. Approximate the eikonal equation by a finite difference formula (Vidale, 1990); e.g., in Figure 2.1b the finite-difference approximation centered at point c becomes

   $$((t_e - t_w)/2h)^2 + ((t_n - t_s)/2h)^2 = s(\vec{c})^2 \tag{2.5}$$

   If the known traveltimes are at points w, n, and s then the unknown traveltime at point e can be found from the above equation to give

   $$t_e = t_w + 2h\sqrt{(\bar{s}^2 - (t_n - t_s)^2/4h^2)}. \tag{2.6}$$

   The gridpoints at or next to the corner points are timed by the stencils shown in Figure 2.1b.

4. Search for the minimum traveltime point along the computational wavefront and, from this minimum traveltime point, expand the solution to its nearest outer neighbor. For

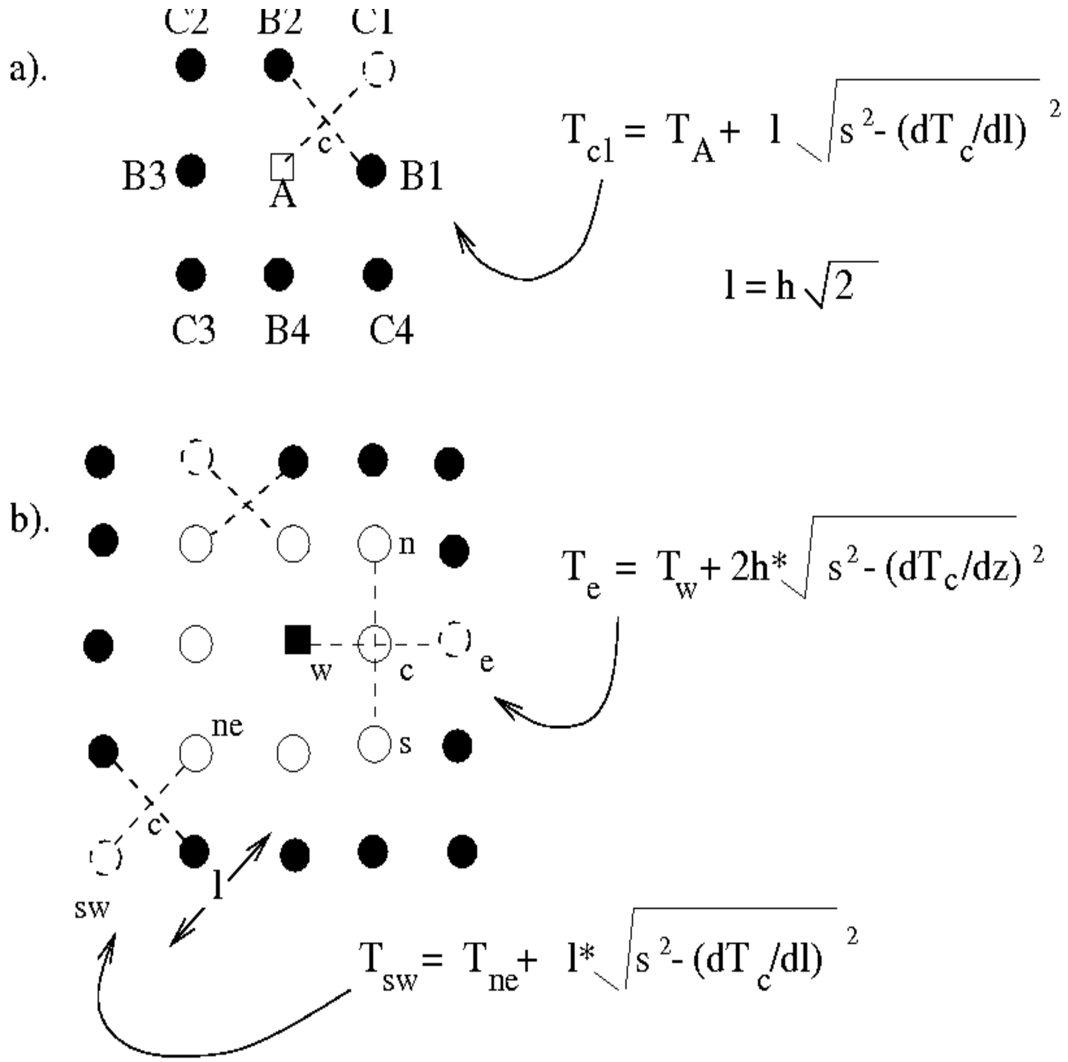

Figure 2.1: The finite-difference grid and differencing stencils associated with the discrete approximation to the eikonal equation. The stencils are shown for the (a). source point region and (b). away from the source point region. In Figure (a), point A is the source point and the points shown as filled or dashed circles are about to be timed. In Figure (b), the dashed circles are about to be timed.

example, the dotted circle in Figure 2.2 is assumed to belong to the minimum traveltime so the solution is expanded (using a formula similar to that in equation 2.6) from X to its nearest neighbors (open circles along perimeter in Figure 2.2b) . Update the computational wavefront by including the 3 newly timed points shown in Figure 2.2c.

5. Step 4 is repeated until all of the gridpoints in the model have been timed. Expanding outward from the minimum traveltime point insures that the computational wavefront stays nearly coincident with the physical wavefront of first arrivals. This prevents violation of causality (Qin et al., 1992).

Note that the above procedure times new points along and "expanding wavefront". This is superior to that of an "expanding square" because an "expanding square" solution will violate causality, as shown in Figure 2.3. The problem with this "expanding square" strategy is that it is invalid for models with moderate to large velocity contrasts. It is because causality, that is "the time for the part of the ray path leading to a point must be known before the time of the point can be found" (Vidale, 1990), is violated in some cases. This can lead to negative values inside the square root resulting in completely erroneous traveltimes. Figure 2.3 is a sketch to show the difference between the actual wavefronts and those calculated by the "expanding square" method. The miscalculation of the head waves is clearly seen. The above procedure can be quite expensive because each gridpoint will initiate a minimum traveltime search along its associated computational wavefront of $O(N)$ points. Thus, the computational cost to time the entire grid will be $O(N^3)$ operations for a square model of NxN gridpoints. To reduce this cost to $O(N^2)$ operations, Qin et al. (1992) suggest that the perimeter search for the minimum traveltime point be reinitiated only after the computational wavefront expands over some fixed time interval, say δt. Prior to the next perimeter search at, say $t + \delta t$, the solution is expanded in the same pointwise order as determined by the previous perimeter search at t. Larger δt values will lead to less traveltime accuracy, so there is a tradeoff between accuracy and computational efficiency.

The advantages of the calculating traveltimes by a finite-difference method compared to raytracing are (Vidale, 1990) that traveltime fields can be computed in shadow zones, some multipathing events are included and the entire grid is efficiently timed. Knowing the traveltimes at all gridpoints can facilitate applying traveltime tomography to the data (Nolet, 1987). The disadvantage is that only first arrivals can easily be computed. See Figure 2.4 for an example of traveltime contours computed by a finite difference solution of the eikonal equation for a low velocity cylinder model.

Raypaths are computed by either tracing rays normal to a wavefront, or by invoking the traveltime reciprocity equation

$$\tau_{rs} = \tau_{rx} + \tau_{xs}, \tag{2.7}$$

where τ_{xs}, τ_{rx} and τ_{rs} are the first arrival traveltimes, respectively, from the source point $\mathbf{s}$ to $\mathbf{x}$, from the receiver point $\mathbf{r}$ to $\mathbf{x}$, and from the source point to the receiver point. The first arrival raypath between $\mathbf{s}$ and $\mathbf{r}$ is described by the locus of points $\mathbf{x}$ that satisfy equation 2.7.

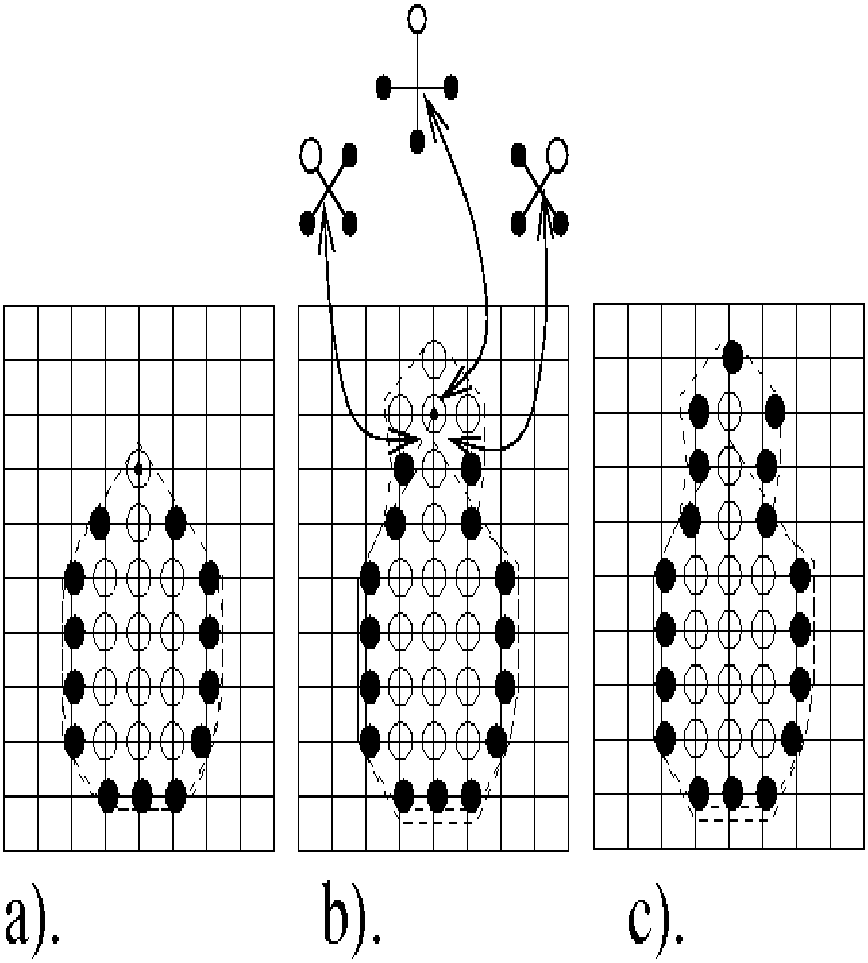

Figure 2.2: Figure illustrating the "expanding wavefront" method. (a) The solution region and the minimum traveltime point (filled dot inside an open circle). The dashed curve represents the actual wavefront. (b) The solution region is expanded to the points (open circles along perimeter) adjacent to the minimum traveltime point. The finite-difference stencils used to time the new points are shown above the solution region. (c) New solution region and new minimum traveltime point among the new perimeter points.

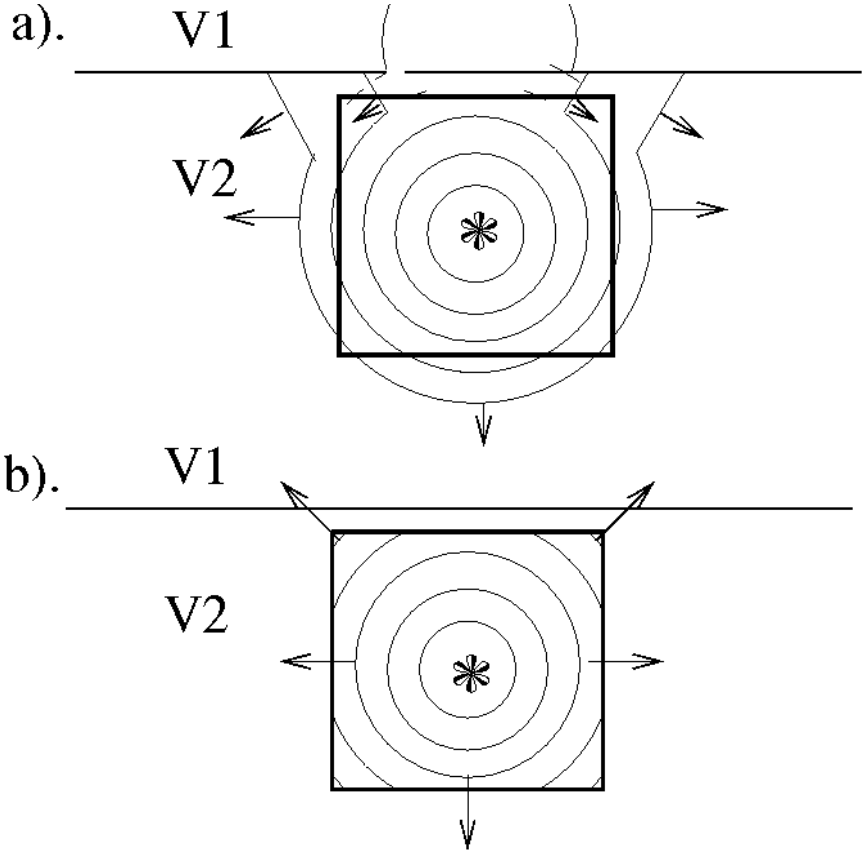

Figure 2.3: A sketch to show the differences between (a) the actual wavefront and (b) the wavefront calculated by the *expanding square* method for a 2 layer model. Note that the *expanding square* wavefront is incorrect if the critical angle θ_c is less than $\sin^{-1}(V_1/V_2) = 45°$ (or $V_1/V_2 < 0.7071$).

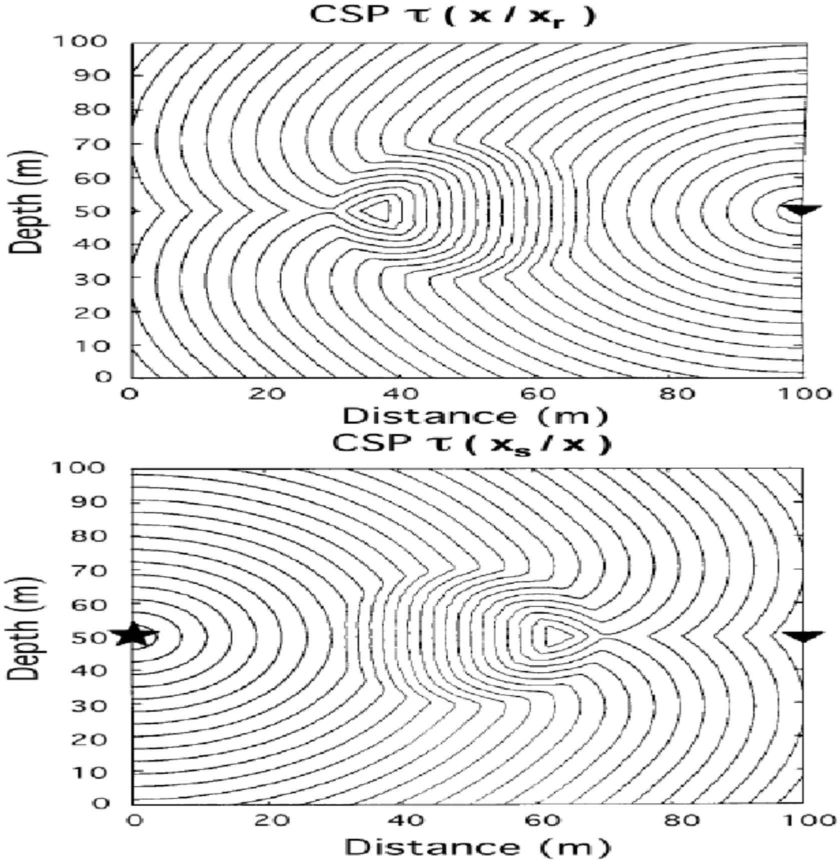

Figure 2.4: (Top) First arrival traveltime contours for a source located on the left side of a low velocity cylinder. (Bottom) First arrival traveltime contours for a source located at the star position on left side of the cylinder. All traveltimes computed by a Finite Difference solution to the eikonal equation.

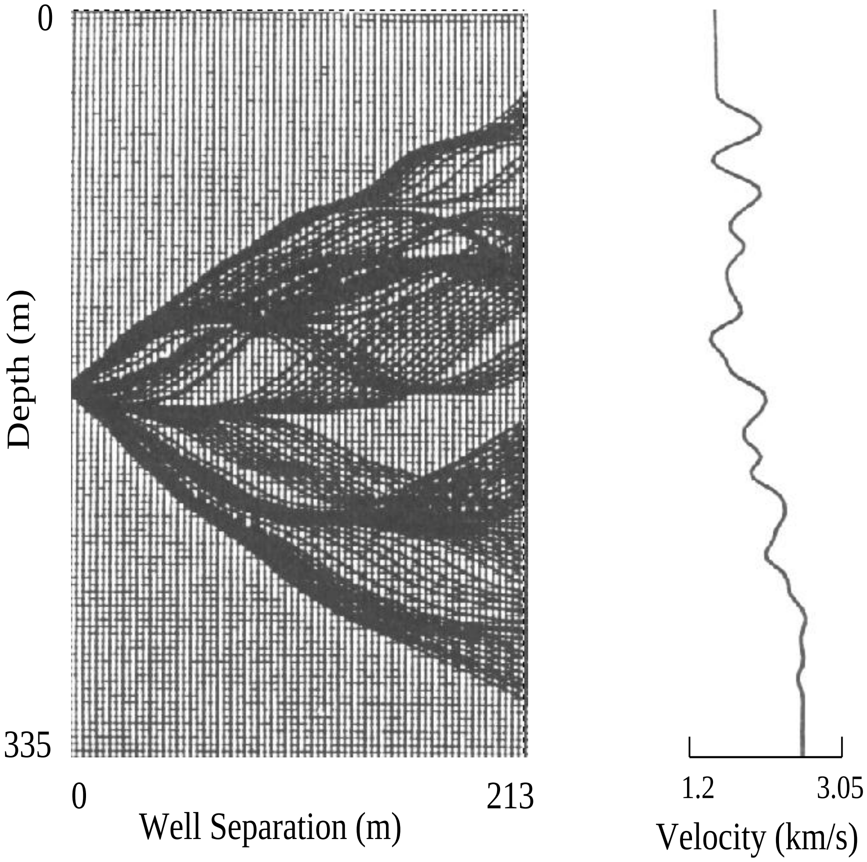

Figure 2.5: Langan velocity model adapted from a Southern California well log and rays computed by a shooting method. Note the failure of rays to penetrate into the shadow zones.

2.2 Traveltime Integral

The traditional means for solving the eikonal equation is by a shooting ray trace method (Aki and Richards, 1978). While useful, the shooting method can be expensive when the entire grid of traveltimes is needed, and can be difficult to implement when there are numerous shadow zones as shown in Figure 2.5. Here we describe a simple algorithm for tracing rays via the shooting method.

The first step is to pound the eikonal equation into a traveltime integral. We do this by defining the unit direction vector $\hat{\mathbf{dl}} = \nabla\tau(\mathbf{x})/|\nabla\tau(\mathbf{x})|$ which depends on the slowness medium $s(\mathbf{x})$. Therefore the eikonal equation can be cast into the form

$$\hat{\mathbf{dl}} \cdot \nabla\tau(\mathbf{x}) \quad = \quad s^2(\mathbf{x}), \tag{2.8}$$

or rearranging and defining $d\tau(\mathbf{x})/dl = \nabla\tau(\mathbf{x}) \cdot \hat{\mathbf{dl}}$ we get

$$\frac{d\tau(\mathbf{x})}{dl} \quad = \quad s(\mathbf{x})^2/|\nabla\tau(\mathbf{x})| = s(\mathbf{x}). \tag{2.9}$$

Integrating this one-dimensional ODE with respect to the raypath differential length we get the traveltime integral

$$\tau(\mathbf{x}|\mathbf{s}) \quad = \quad \int_{raypath} s(\mathbf{x})dl, \tag{2.10}$$

where we have introduced the traveltime notation $\tau(\mathbf{x}|\mathbf{s})$ to account for the initial conditions that the ray starts out at the source coordinates $\mathbf{s}$ and ends at the observer point $\mathbf{x}$. The traveltime computed by the above integral is the time it takes for energy to follow Snell's law and propagate from $\mathbf{s}$ to $\mathbf{x}$ given some starting ray angle at $\mathbf{s}$. It is a high frequency approximation valid for a slowness medium whose dominant wavelength (take a 2D spatial Fourier transform of model and highest wavenumbers k_x and k_y in the model spectrum define the shortest wavelengths in the slowness mdoel) is about 3 or more times longer than the dominant frequency in the source wavelet (Bleistein, 1984). The problem with the traveltime integral is that it is non linear with respect to the slowness field because both the raypath and the integrand depend on the slowness field. The next section will show how to linearize this modeling equation so that we can invert traveltime data for the slowness field. This inversion procedure is often refered to as traveltime tomography.

The procedure for solving the traveltime integral is sketched in rough psuedo-code.

```
[x(1),z(1)]=[1,1]*dx;angle=pi/6;m=sin(angle)/cos(angle);
z(2)=z(1)+m*(dx+x(1));
for i=2:L
[gradx,gradz]=grad(s,x(i),z(i)); % Find gradient of
                                 % slowness field s at [x,z].
[dlx,dlz]=[gradx,gradz]/(sqrt(gradx^2+gradz^2));
% [dlx,dlz] is the unit  vector perpendicular to flat interface
% Write a subroutine that finds angle of transmitted ray across this
% flat interface that satisfies Snell's law for incident ray with
% slope=[z(i)-z(i-1)]/(x(i)-x(i-1)]. This transmitted ray has a new
```

```
% slope we define as m, which is used in next calculation statement.
z(i+1)=z(i)+m*(dx+x(i));
x(i+1)=x(i)+dx;
end
```

The above pseudo code needs to be regularized to avoid zeros in the denominators, e.g., the slowness gradient calculation, and assumes a ray that monotonically moves to the right.

2.3 Perturbed Traveltime Integral

The eikonal equation can be used to derive the traveltime integral associated with a perturbed slowness medium. This integral is the keystone equation by which the slowness model can be efficiently updated in traveltime tomography.

Let the slowness perturbation from a background slowness field $s(\mathbf{x})$ be given by $\delta s(\mathbf{x})$, and let the corresponding perturbed traveltime field be given by $t(\mathbf{x}) + \delta t(\mathbf{x})$. Here, $t(\mathbf{x})$ is the unperturbed traveltime field and $\delta t(\mathbf{x})$ is the traveltime perturbation. The perturbed traveltime field honors the eikonal equation

$$\begin{aligned} |\nabla t(\mathbf{x}) + \nabla \delta t(\mathbf{x})|^2 &= |\nabla t(\mathbf{x})|^2 + 2\nabla \delta t(\mathbf{x}) \cdot \nabla t(\mathbf{x}) + |\delta t(\mathbf{x})|^2 \\ &= s(\mathbf{x})^2 + 2\delta s(\mathbf{x}) s(\mathbf{x}) + \delta s(\mathbf{x})^2. \end{aligned} \tag{2.11}$$

Subtracting equation 2.11 from the unperturbed eikonal equation we get

$$2\ \nabla t(\mathbf{x}) \cdot \nabla \delta t(\mathbf{x}) + |\delta t(\mathbf{x})|^2 = 2\delta s(\mathbf{x}) s(\mathbf{x}) + \delta s(\mathbf{x})^2, \tag{2.12}$$

and neglecting the terms second order in the perturbation parameters this becomes

$$\begin{aligned} \nabla t(\mathbf{x}) \cdot \nabla \delta t(\mathbf{x}) &= |\nabla t(\mathbf{x})|\ d\hat{l} \cdot \nabla \delta t(\mathbf{x}) \\ &= \delta s(\mathbf{x}) s(\mathbf{x}), \end{aligned} \tag{2.13}$$

where $d\hat{l}$ is defined to be the unit vector parallel to the unperturbed ray direction, so that $\nabla t(\mathbf{x}) = |\nabla t(\mathbf{x})|\ d\hat{l}$.

Defining the directional derivative along $d\hat{l}$ to be $d/dl = d\hat{l} \cdot \nabla$ (note, this directional derivative is determined by the background slowness distribution, not the perturbed medium), and dividing equation 2.13 by $|\nabla t(\mathbf{x})| = s(\mathbf{x})$ gives

$$d\delta t(\mathbf{x})/dl = \delta s(\mathbf{x}). \tag{2.14}$$

Multiplying both sides by dl and integrating along the old raypath finally yields the perturbed traveltime integral

$$\delta t(\mathbf{x}) = \int_{raypath} \delta s(\mathbf{x}')\mathbf{dl}', \tag{2.15}$$

which is correct to first order in the perturbation parameters. Equation 2.15 says that the traveltime perturbation due to a slowness perturbation is given by an integration over the old raypath weighted by the slowness perturbation. This can be quite cost efficient because the traveltime perturbation calculation uses the old raypaths and does not require the retracing of rays through the perturbed slowness model.

Replacing the perturbation parameters in equation 2.15 by the unperturbed traveltimes and slownesses gives the traveltime integral

$$t(\mathbf{x}) = \int_{raypath} s(\mathbf{x}')\mathbf{dl}'. \tag{2.16}$$

The traveltime integral represents the integral equation solution to the unperturbed eikonal equation.
This is a non-linear equation because both the raypath and integrand depend on the slowness model $s(x')$.
Parameterization of Slowness Model. The slowness perturbation field $s(\mathbf{x})$ can be discretized into N cells of constant slowness so that the j^{th} cell has slowness perturbation δs_j. Equation 2.15 then reduces to a summation

$$\delta t_i = \sum_j^N l_{ij}\delta s_j \tag{2.17}$$

where δt_i is the i^{th} traveltime perturbation and l_{ij} is the segment length of the i^{th} ray in the j^{th} cell. If there are M equations then these form a system of equations represented by

$$\vec{\delta t} = L\vec{\delta s}, \tag{2.18}$$

where L is the MxN raypath matrix with elements l_{ij}, $\vec{\delta s}$ is the $Nx1$ slowness vector, and $\vec{\delta t}$ is the $Mx1$ traveltime perturbation vector. If the slowness perturbations are zero everywhere except in the k^{th} cell, then equation 2.17 becomes

$$\delta t_i = l_{ik}\delta s_k,$$

or dividing by the segment length

$$\delta t_i / \delta s_k = l_{ik}. \tag{2.19}$$

$\delta t(\mathbf{x})_i/\delta s_k$ is known as the Frechet derivative, or the change in the i^{th} traveltime data with respect to a change in the k^{th} model parameter. When convenient, the perturbation symbol δ will be replaced by the partial derivative symbol ∂. Smoother parameterizations can be used such as piecewise continuous spline functions.

2.4 Traveltime Tomography

To solve for the slowness distribution from the observed traveltimes in the non-linear equation 2.16 we first linearize it to get equation 2.15, solve this equation and update the slowness model. We then repeat this process until convergence.

1. Set initial model $\mathbf{s^{(0)}}$ and find predicted times $\mathbf{t^{(0)}} = \mathbf{Ls^{(0)}}$. Set $nit = 0$.

2. Find traveltime residual $\delta\mathbf{t}^{(nit)}$, which is the difference between predicted and observed traveltimes. Find perturbed slowness $\delta\mathbf{s}^{(nit)} = \mathbf{L}^{\mathbf{T}}\mathbf{L}^{-1}\mathbf{L}^{\mathbf{T}}\delta\mathbf{t}^{(nit)}$. The matrix inversion is sometimes too expensive so we solve for $\delta\mathbf{s}^{(nit)}$ by some type of iterative method such as a limited number of iterations in a conjugate gradient method or steepest descent method.

3. Update slowness $\mathbf{s}^{(nit+1)} = \mathbf{s}^{(nit)} + \delta s^{(nit)}$ and then find updated predicted traveltimes $\mathbf{t}^{(nit+1)} = \mathbf{L}\mathbf{s}^{(nit+1)}$.

4. Set $nit = nit + 1$ and repeat steps 2-4 until convergence.

2.5 Summary

The eikonal equation is derived from the wave equation, and is used to compute both rays and traveltimes for high frequency waves propagating through a smooth velocity medium. In practice, this means that the characteristic wavelength of the velocity fluctuations must be more than three times longer than the source wavelength (Bleistein, 1984). The finite-difference solutions to the eikonal equations are computed and used to compute traveltimes and rays for traveltime tomography. Computing the traveltimes for every grid point is very convenient for refraction tomography where there is dense source-receiver coverage in exploration surveys.

2.6 Exercises

1. Prove equation 2.23. State the conditions under which it provides a correct kinematic description of wavefield propagation.

2. Sketch out a rough MATLAB code that solves the 2-D eikonal equation for an arbitrary velocity model.

2.7 Appendix: Eikonal equations for elastic wave equation

The elastic isotropic wave equation is given by

$$\rho\frac{\partial^2 u_i}{\partial t^2} = \frac{\partial \tau_{ij}}{\partial x_j}, \tag{2.20}$$

where

$$\tau_{ij} = \lambda\delta_{ij}\frac{\partial u_k}{\partial x_k} + \mu(\frac{\partial u_i}{\partial x_j} + \frac{\partial u_j}{\partial x_i}), \tag{2.21}$$

where τ_{ij} represents the stress tensor (see chapter on elastic wave propagation). Here, repeated indices indicate summation from 1 to 3, u_k corresponds to the k^{th} particle displacement, ρ is density, and λ and μ are the Lame's constants.

For a harmonic plane wave source oscillating at angular frequency ω and a scatterer embedded in a homogeneous medium, it is reasonable to assume that scattered far-field first arrivals can be approximated by a free-space Green's function, i.e,

$$\vec{u}(\mathbf{r},\omega) \sim \vec{A}(\mathbf{r})e^{i\omega\tau_{ro}}, \tag{2.22}$$

where the scatterer is at the origin, τ_{so} is the traveltime from the scatterer to the interrogation point $\mathbf{r}$, and $\vec{A}(\mathbf{r})$ is a displacement vector that accounts for scattering and geometrical spreading losses.

Equation 2.22 can be used as an *ansatz* or trial solution to the wave equation. The unknowns $\mathbf{A}$ and τ can be found by plugging equation 2.22 into equation 2.20 to yield a quadratic equation in ω. At high frequencies, the geometrical spreading term is governed by the transport equation:

$$-\rho\vec{A} + (\lambda+\mu)(\mathbf{A}\cdot\nabla\tau)\nabla\tau + \mu|\nabla\tau|^2\mathbf{A} = 0. \tag{2.23}$$

This equation is true either by:

1. choosing $\mathbf{A}\cdot\nabla\tau = 0$ which implies

$$\begin{aligned} |\nabla\tau|^2 &= \rho/\mu \\ &= {v_S}^{-2}, \end{aligned} \tag{2.24}$$

2. or choosing $\nabla\tau$ to be parallel to $\mathbf{A}$ to give

$$\begin{aligned} |\nabla\tau|^2 &= \rho/(\lambda+2\mu) \\ &= {v_P}^{-2}, \end{aligned} \tag{2.25}$$

   where v_P and v_S are the P- and S-wave velocities, respectively.

Equations 2.24 and 2.25 are the S- and P-wave eikonal equations, respectively, whose solutions yield the traveltimes of the first P- and S-wave arrivals everywhere in an inhomogeneous velocity medium.

Part III

Traveltime Tomography

Chapter 1

Least Squares Optimization and Traveltime Tomography

1.1 Introduction

Sometimes the best way to quickly understand a topic is to use an example, particularly one that is both simple and practically interesting. Here I present the example of traveltime tomography. Many of the key ideas in this simple example reinforce the central principles of seismic optimization, where other books provide greater details and depth of analysis.

We will introduce a special type of optimization, least squares inversion (Nolet, 1987; Gill et al., 1981;Fletcher, 1987; Nemeth et al., 1997). In this case, a misfit function is formed by summing the squared traveltime residuals and the solution is the one that minimizes the misfit function. The traveltime residual is the difference between the observed and predicted traveltimes. The obtained solution is the starting model for the next iteration because typical geophysical problems are strongly non-linear.

We will first review the main characteristics of an overconstrained system of equations, and then show how such systems characterize traveltime tomography problems. This example will illustrate the three features of a well-posed inverse problem: existence of a solution, uniqueness, and stability (Groetsch, 1993).

1.2 Least Squares Minimization

An overconstrained system of linear equations has more equations than unknowns. For example, the 3x2 system of equations symbolized by $L\mathbf{s} = \mathbf{t}$ is given by

$$\begin{bmatrix} 1 & 0 \\ 1 & 1 \\ 0.7 & 0.7 \end{bmatrix} \cdot \begin{pmatrix} s_1 \\ s_2 \end{pmatrix} = \begin{pmatrix} 1 \\ 2 \\ 2 \end{pmatrix}. \tag{1.1}$$

Note, these equations are *inconsistent*, i.e., no one solution can simultaneously satisfy all of the equations. For example, the second and third equations conflict with one another.

A physical example related to equation 1 is the tomographic imaging experiment shown

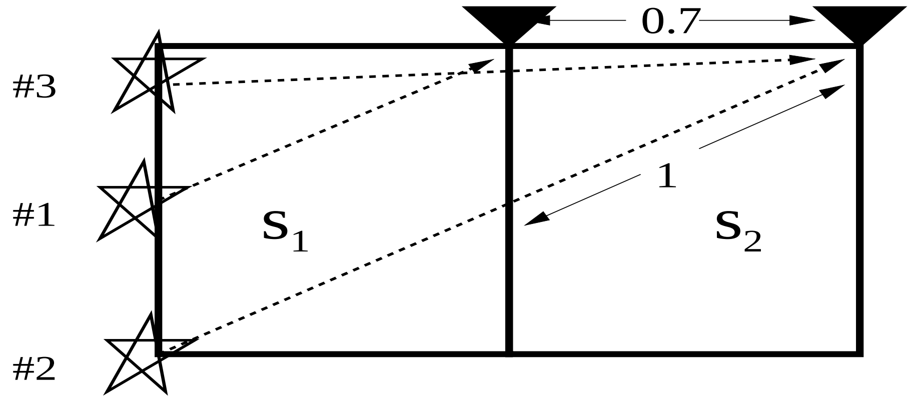

Figure 1.1: Imaging experiment related to equation 1. The data are the measured traveltimes, the segment lengths are denoted next to the segment, and the goal is to reconstruct the slowness value in each cell. Note, the total traveltime is the sum of the segment traveltimes (i.e., (segment length)xslowness) in a ray.

in Figure 1.1. The traveltime for each curved ray is governed by the traveltime integral:

$$t(x,y) \quad = \quad \int_{raypath} s(x,y)dl, \tag{1.2}$$

where $t(x,y)$ is the traveltime for waves to propagate from the source along the raypath to the observer point at (x,y), $s(x,y) = 1/c(x,y)$ is the slowness and dl is the incremental change in distance along the raypath. The velocity model is discretized into N cells of unknown constant slowness, the traveltime integral becomes approximated by a summation

$$t_i \quad = \quad \sum l_{ij} s_j \tag{1.3}$$

over the subsegment lengths l_{ij} of the ith ray that intersect the jth cell, and there are M equations. This results in a MxN system of equations, denoted as $\mathbf{Ls} = \mathbf{t}$, where $\mathbf{t}$ represents the measured $Mx1$ traveltime data vector, and $\mathbf{s}$ is the $Nx1$ vector of unknown slownesses in the cells. The MxN matrix $\mathbf{L}$ contains the segment lengths of the rays. The Appendix derives this integral starting from the wave equation.

The goal is to solve the system of equations 1.3 and find the unknown slowness values s_i in each cell. The solution to this overconstrained system of equations gives the slowness tomogram $\mathbf{s}$. Physically, the traveltime equations are inconsistent because the data contain traveltime picking errors and/or because the physics used to model the data is incomplete.

Geometrically, the three equations in 1.1 plot as straight lines shown in Figure 1.2a, and no common intersection point means that the equations are inconsistent. Although

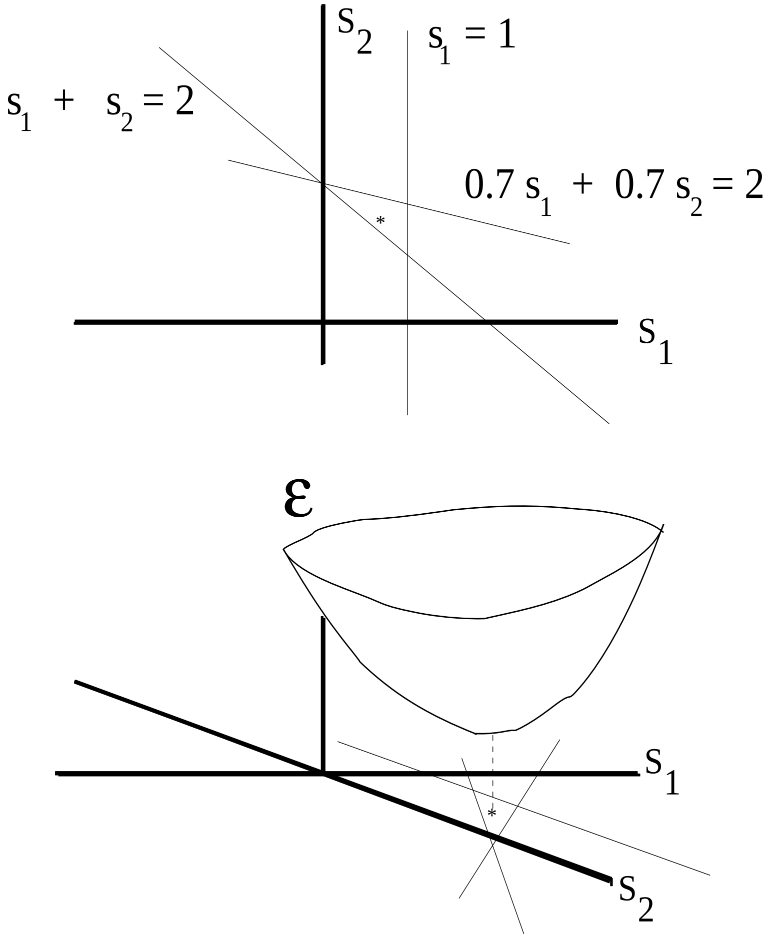

Figure 1.2: (a). Lines associated with equation 1, where the equations are inconsistent so there is no common intersection point. (b). Error surface associated with misfit function.

there is no *exact* solution to equation 1.1, we would be happy with an approximate solution "close" to the points of intersection. Such a compromise is the least squares solution which minimizes the following misfit functional:

$$
\begin{aligned}
\epsilon &= 1/2\ [\mathbf{Ls} - \mathbf{t}\ ]^T \cdot [\mathbf{Ls} - \mathbf{t}\ ], \\
&= 1/2 \sum_{i=1}^{3} \sum_{j=1}^{2} (l_{ij} s_j - t_i)^2, \\
&= 1/2 \sum_{i=1}^{3} r_i^2, \qquad (1.4)
\end{aligned}
$$

where r_i is the *ith* residual, i.e., the difference between the *ith* component of the predicted $\mathbf{t}$ and the actual RHS vector $\mathbf{t}$. If the rays bend then the matrix components in equation 1.1 depend on the unknowns $\mathbf{s}$. This means that the above system of equations should be replaced by their linearized approximation represented by $\mathbf{L_o}\delta\mathbf{s} = \delta\mathbf{t}$, as discussed in a later section. Here, $\delta\mathbf{s} = \mathbf{s_o} - \mathbf{s}$, where $\mathbf{s_o}$ is the background slowness model.

Plotting the misfit value against s_1 and s_2 yields the error bowl shown in Figure 1.2b. It is obvious that the bottom of this error bowl is directly over the optimal solution $\mathbf{s}^*$, which will also be considered the least squares solution. There is a bottom to the error bowl, so we now know there *exists* a least squares solution.

Plotting out the error surface to find the optimal solution may be convenient for systems of equations with just a few unknowns, but is impractical for many unknowns. A more systematic approach is to recognize that at the bottom of the error bowl the partial derivatives $\partial\epsilon/\partial s_i = 0$ are simultaneously zero. That is,

$$
\begin{aligned}
\partial\epsilon/\partial s_k &= \sum_{i=1}^{3} \sum_{j=1}^{2} [(l_{ij} s_j - t_i) l_{ij} \partial s_j/\partial s_k + (l_{ij} s_j - t_i) s_j \partial l_{ij}/\partial s_k], \\
&\approx \sum_{i=1}^{3} \sum_{j=1}^{2} (l_{ij} s_j - t_i) l_{ij} \delta_{jk}, \qquad (1.5)
\end{aligned}
$$

where $\delta_{jk} = 1$ if $j = k$, otherwise it is equal to zero. The far-right term $s_j \partial l_{ij}/\partial s_k (\sum_j l_{ij} s_j - t_i)$ is often neglected partly because it is too expensive to compute and partly because $\partial l_{ij}/\partial s_k$ is really small when the background slowness model is sufficiently close to the actual model. Of course, if the rays were straight then T_{ik} is identically zero because straight rays do not change with slowness perturbations. Therefore,

$$
\begin{aligned}
\partial\epsilon/\partial s_k &= \sum_{i=1}^{3} (l_{ik} s_k - t_i) l_{ik}, \\
&= [\mathbf{L}^T(\mathbf{Ls} - \mathbf{t})]_k \ = 0 \qquad k = 1, 2. \qquad (1.6)
\end{aligned}
$$

This is exactly the gradient for the small residual Gauss-Newton method derived in Fletcher (1987) or Gill (1981). The extra term of second derivatives is not present because the starting equations were assumed to be linear.

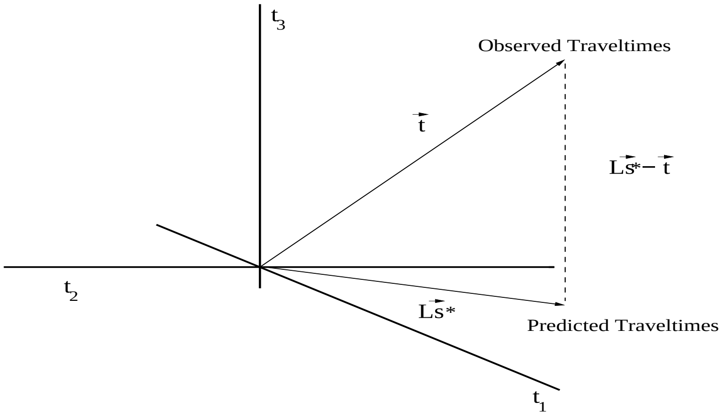

Figure 1.3: The least squares solution finds the optimal $\mathbf{s}^*$ so that the residual $\mathbf{Ls}^* - \mathbf{t}$ is orthogonal to the predicted traveltimes given by $\mathbf{Ls}^*$.

1.2.1 Normal Equations

Equation 1.6 can be more compactly written as

$$\mathbf{L}^T\mathbf{L}\mathbf{s}^* \quad = \quad \mathbf{L}^T\mathbf{t}^*, \tag{1.7}$$

and are called the normal equations. In this case, $\mathbf{L}^T\mathbf{L}$ is a symmetric $2x2$ matrix and the two unknowns s_1 and s_2 can be solved by inverting the above matrix to give the least squares solution denoted as $\mathbf{s}^*$. These two constraint equations were obtained by setting to zero the misfit derivative along each of the s_i coordinates. Note, we assume a system of linear equations, otherwise the derivative w/r to s_i would also be applied to the l_{ij} terms.

For a general MxN system of linear equations, equation 1.7 is used to solve for the least squares solution that minimizes the sum of the squared residuals. These are called the normal equations because equation 1.7 can be rearranged and multiplied by $\mathbf{s}^T$ to give

$$(\mathbf{Ls}, \mathbf{Ls} - \mathbf{t}) \quad = \quad 0, \tag{1.8}$$

which says that the residual vector $\mathbf{r} = \mathbf{Ls} - \mathbf{t}$ is normal to the predicted RHS vector $\mathbf{Ls}$, as shown in Figure 1.3.

What kind of matrix $\mathbf{L}$ is associated with the diagram in Figure 1.3? The answer is $\mathbf{L}= [a\ b; c\ d; 0\ 0]$, because $\mathbf{Ls} = \mathbf{t}$ can be expressed as a sum of column vectors

$$\begin{bmatrix} a \\ c \\ 0 \end{bmatrix} s_1 + \begin{bmatrix} b \\ d \\ 0 \end{bmatrix} s_2 \quad = \quad \begin{pmatrix} t_1 \\ t_2 \\ t_3 \end{pmatrix}, \tag{1.9}$$

where each column vector is one of the column vectors in $\mathbf{L}$. The last component of these column vectors is zero, so no weighted linear combination of them can create a component that lives in the t_3 dimension shown in Figure 1.3. In other words, the columns of $\mathbf{L}$ only span the horizontal plane formed by the t_1 and t_2 basis vectors. This is another interpretation of inconsistent traveltime equations: they predict data vectors $\mathbf{t}$ that cannot live in the same space as the observed data vector.

Exercises

1. The column span of the MxN matrix $\mathbf{L}$ is the ensemble of $Mx1$ vectors that are linear combinations of the $\mathbf{L}$ column vectors. What plane is spanned by the $3x1$ column vectors in $\mathbf{L} = [1\ 1; 1\ 0; 1\ 0]$? Is that plane closer to the observed 3x1 vector $\mathbf{t}$ than the t_1xt_2 plane in Figure 1.3? The $Mx1$ $\mathbf{t}$ vector represents data, so the column vectors of $\mathbf{L}$ are said to span a region of data space.
2. Can every region in three-dimensional space be spanned by the column vectors in $\mathbf{L} = [1\ 1; 1\ 0; 1\ 0]$?.
3. What geometrical object, line or plane, is spanned by the column vectors in $\mathbf{L} = [1\ 2; 1\ 2; 1\ 2]$? Are these two column vectors in data space linearly independent?
4. Linear combinations of slowness vectors span a *model* space. For the example $\mathbf{L} = [1\ 2; 1\ 2; 1\ 2]$, show that there is more than one $2x1$ slowness vector $\mathbf{s}$ that yields the same predicted traveltime equations. This means that the solution is non-unique.
5. The vector$\mathbf{s_o}$ such that $\mathbf{Ls_o} = (\mathbf{0\ 0\ 0})^{\mathbf{T}}$ is known as a null space vector. Any null space vector added to a solution of $\mathbf{L}(\mathbf{s}+\mathbf{s_0}) = \mathbf{t}$ will also satisfy the traveltime equations. In other words, there are non-unique solutions. The space spanned by these null vectors define the model null space. What geometrical object is spanned by the model null space vectors for $\mathbf{L} = [1\ 2; 1\ 2; 1\ 2]$? This space is known as the model null space, and is characterized by zero eigenvalues of $\mathbf{L^TL}$.
6. Show that the model null space vector for $\mathbf{L} = [1\ 2; 1\ 2; 1\ 2]$ is the same as the eigenvector of $\mathbf{L^TL}$ associated with a zero eigenvalue.
7. Insert a new ray that is parallel to ray 3 in Figure 1.1, and call it ray 4. Show that the three traveltime equations associated with rays 2, 3 and 4 in Figure 1.1 give rise to a non-empty null space. What does this say about the ability of a straight ray crosswell experiment to resolve lateral velocity variations? A crosswell experiment is one in which the receivers are along a vertical well and the sources are along another vertical well offset from the receiver well.

1.2.2 Poorly Conditioned Equations and Regularization

The condition number of $\mathbf{L^TL}$ can be large and therefore many different solutions can give rise to nearly the same value of ϵ. This is an example of an *unstable* or ill-conditioned inverse problem. To clarify this statement, we define a system of equations as

$$\begin{bmatrix} \kappa_1 & 0 \\ 0 & \kappa_2 \\ \kappa_1 & 0. \end{bmatrix} \cdot \begin{pmatrix} s_1 \\ s_2 \end{pmatrix} = \begin{pmatrix} 1 \\ 1 \\ 3 \end{pmatrix}, \tag{1.10}$$

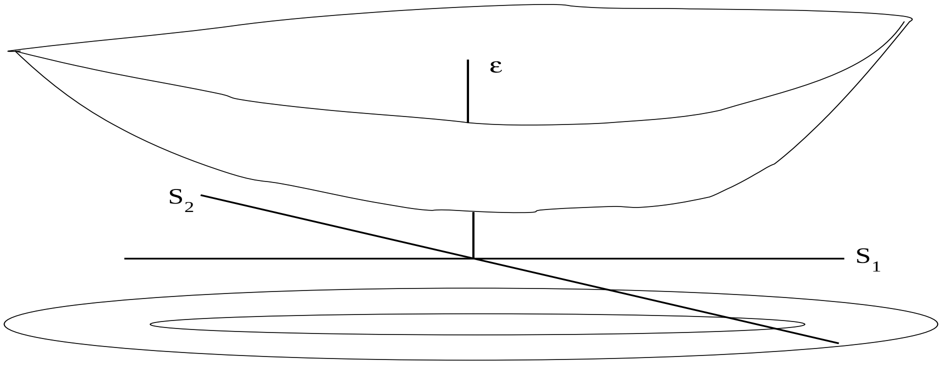

Figure 1.4: Poorly conditioned $\mathbf{L^T L}$ leads to long valleys in the contoured misfit function. Equivalently, many different models can equally account for the data.

where $\kappa_1 >> \kappa_2$. The corresponding normal equations are

$$\left[\begin{array}{cc} 2\kappa_1^2 & 0 \\ 0 & \kappa_2^2 \end{array} \right] \cdot \left(\begin{array}{c} s_1 \\ s_2 \end{array} \right) = \mathbf{L^T t}. \tag{1.11}$$

It is clear that if $\kappa_1 >> \kappa_2$ then the condition number (ie., maximum eigenvalue/minimum eigenvalue or $cond = 2\kappa_1^2/\kappa_2^2$) is very large. This means that quite different values of s_2 give about the same value of ϵ. Equivalently, the misfit function shown in Figure 1.4 is characterized by the long narrow valley along the s_2 axis where ϵ is somewhat insensitive to large changes in the parameter value of s_2.

In fact, if $\kappa_2 = 0$ then the null space of $\mathbf{L}^T\mathbf{L}$ is non-empty and is spanned by the null space vector $(0 \quad 1)^T$. Any scaled value of this null space vector will not change the residual value and therefore contaminate the solution with unrealistic model features. This is an example of $non-uniqueness$ in the inverse problem. To avoid non-uniqueness we introduce an extra constraint in the misfit function, i.e.,

$$\epsilon \quad = \quad 1/2||\mathbf{Ls} - \mathbf{t}||^2 + 0.5\lambda||\mathbf{s} - \mathbf{s}^0||^2, \tag{1.12}$$

where λ is a small damping parameter and $\mathbf{s}^0$ is an a priori guess to the solution. The constraint says that we wish to find $\mathbf{s}$ that minimizes the sum of the squared residuals and is also close to the a priori guess at $\mathbf{s}^0$. The degree of closeness is determined by the value of λ.

The normal equations associated with this constrained misfit function is obtained by differentiating ϵ to give

$$\partial\epsilon/\partial s_k \quad = \quad \sum_{i=1}^{3}\sum_{j=1}^{2}(l_{ij}s_j - t_i)l_{ij}\partial s_j/\partial s_k + 0.5\lambda\partial||\mathbf{s} - \mathbf{s}^0||^2/\partial s_k,$$

$$= \sum_{i=1}^{3}\sum_{j=1}^{2}(l_{ij}s_j - t_i)l_{ij}\delta_{jk} + \lambda(s_k - s_k^o) = 0, \qquad (1.13)$$

or more compactly

$$[\mathbf{L}^T\mathbf{L} + \lambda\mathbf{I}]\mathbf{s} \quad = \quad \mathbf{L}\mathbf{t} + \lambda\mathbf{s}^0, \qquad (1.14)$$

and is sometimes known as the Levenberg-Marquardt solution. In the case of equation 1.11, the solution becomes $s_1 = [\mathbf{L}^T\mathbf{t}]_1/(2\kappa_1^2 + \lambda)$ and $s_2 = [L^T\mathbf{t}]_2/(\kappa_2^2 + \lambda)$ if $\mathbf{s}^0 = 0$. Note, the condition number is improved with damping where $cond = (2\kappa_1^2 + \lambda)/(\kappa_2^2 + \lambda)$, at the cost of somewhat diminished accuracy.

Other constraint equations include a smoothness constraint which incorporates the gradient raised to the nth power $||\nabla^n\mathbf{s}||^2$. Zhang and Toksoz (1998) compare the performance of these roughness constraints and show that $n = 2$ or $n = 4$ provide superior performance compared to $n = 0$.

1.2.3 Synthetic Traveltime Tomography Example

We will now apply the Gauss-Newton method with small residuals to the traveltime tomography problem. The example is that of a transmission experiment where the model is gridded into a 20 by 20 grid of cells with unknown slowness. There are 20 sources evenly distributed along the bottom boundary of the model, and each source shoots a straight ray into each of the 20 evenly distributed receivers along the top boundary of the model. This gives rise to 400 traveltimes that are used as input data into the least squares Gauss-Newton method. The model and data are linearly related because straight rays are employed.

The damped least squares solution resulted in the reconstructed models shown Figure 1.5. In this case the vertical-layered model was best resolved while the horizontal layered model was least resolved. This is because the best resolution is achieved for rays that are perpendicular to the direction of velocity variations, so that the nearly vertical rays are best at resolving nearly vertical interfaces.

For example, simply dividing the raypath length by the traveltime for a vertical ray passing through one vertical layer will yield the exact velocity of that layer. Hence, a sequence of vertical layers (i.e., model with strictly horizontal velocity variations) can be uniquely reconstructed by inverting traveltimes associated with vertical rays. Conversely, if the model were purely horizontal layers then the lengths divided by the traveltimes will only yield the average velocity of the layers.

If errors are added to the data, then least squares inversion can adequately handle Gaussian noise. As an example, Figure 1.6 depicts the Gauss-Newton solutions for standard and reweighted least squares inversion (Bube and Langan, 1994) when the traveltime data are contaminated with zero-mean 1 percent Gaussian noise. Reweighted least squares becomes important when large non-Gaussian outliers are added to the noise, as shown in in Figure 1.7. The top figure is the image from damped least squares while the bottom figure is from a reweighted least squares method (Bube and Langan, 1995). It is obvious that the large outliers have been suppressed by the reweighted least squares method.

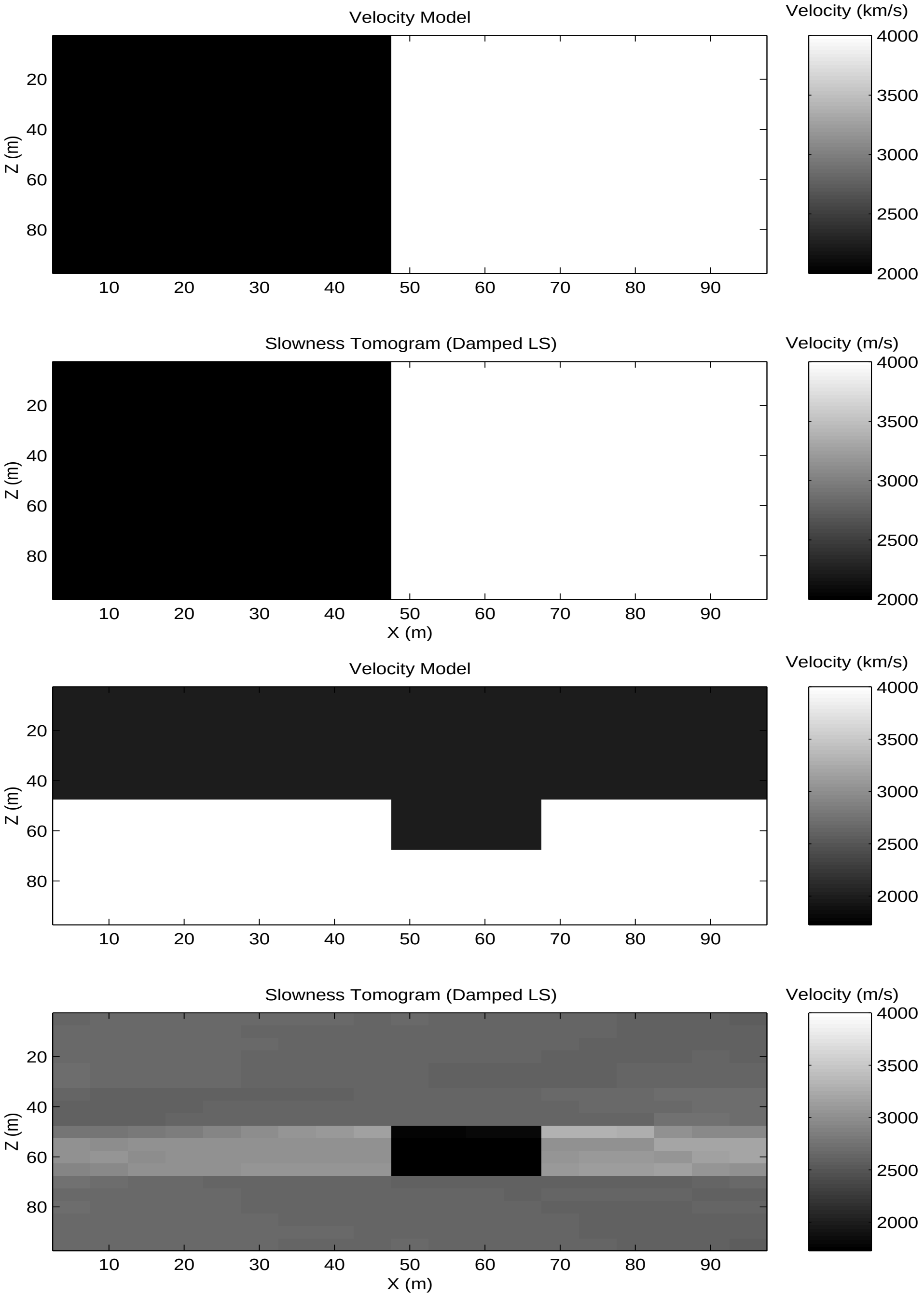

Figure 1.5: Top two figures depict the two-layer vertical model and its damped least squares reconstruction. Bottom two figures are the same except the model is a two-horizontal layer model with a graben along the interface. Note, the ray directions are mostly oriented along the vertical axis, so the vertical-layer model with layering parrallel to the rays is best resolved (courtesy of Min Zhou).

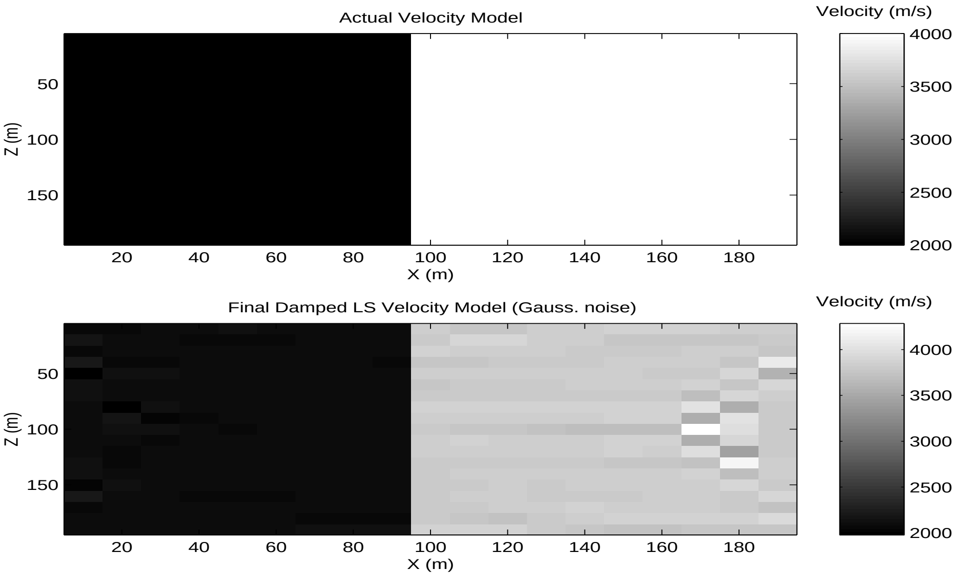

Figure 1.6: Reconstructed models for (top) standard and (bottom) reweighted least squares inversion for the vertical-layer model in Figure 1.5. The traveltime data are contaminated with 1 percent zero-mean Gaussian (courtesy of G. Waite).

Student Version of MATLAB

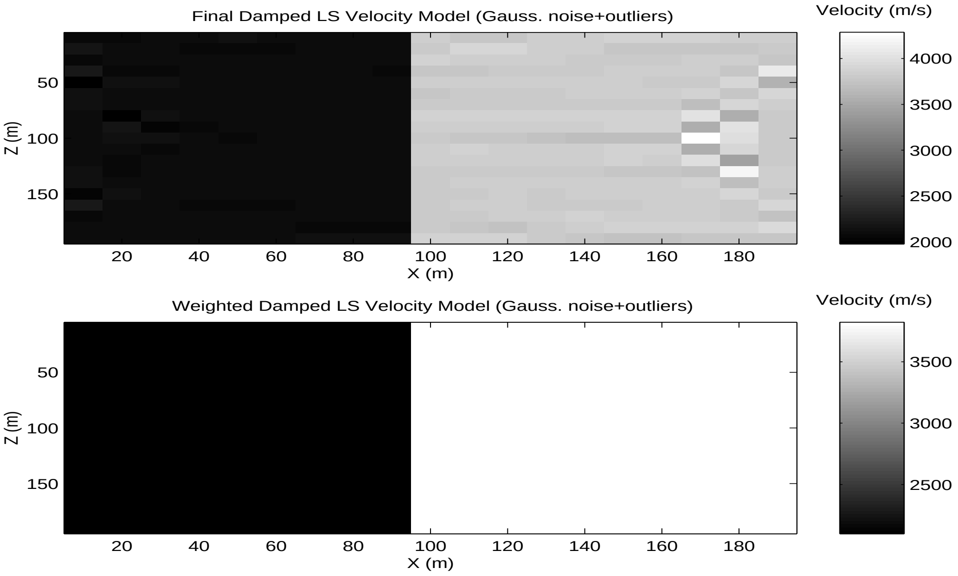

Figure 1.7: Same as previous figure except large outlier errors (about >500 percent) have been added to six of the traveltime picks (courtesy of G. Waite).

Student Version of MATLAB

Linearization

The earth's velocity distribution varies in space, so the shortest traveltime path between a source and receiver is not a straight line. The ray is curved, as shown in Figure 1.8. Consequently, the raypath geometry depends on the slowness model so the raypath lengths in equation 2 also depend on the slowness model. Thus, the traveltimes in equation 2 depend non-linearly on the slownesses. To linearize this equation, we choose a background slowness model $\mathbf{s_o}$ that is very close to the actual model $\mathbf{s}$. "Close" means that the raypaths for $\mathbf{s_o}$ are nearly the same as those for $\mathbf{s}$. In this case, we have the background traveltime equation given as $\mathbf{t_o} = \mathbf{L_o s_o}$ so that $\mathbf{L_o} \approx \mathbf{L}$. The original traveltime equation is $\mathbf{t} = \mathbf{Ls}$, and subtracting it from the background traveltime equations give:

$$\begin{aligned} \mathbf{t} - \mathbf{t_o} &= \mathbf{Ls} - \mathbf{L_o s_o}, \\ &= \mathbf{L_o}(\mathbf{s} - \mathbf{s_o}). \end{aligned} \tag{1.15}$$

Setting $\delta\mathbf{s} = \mathbf{s} - \mathbf{s_o}$ and $\delta\mathbf{t} = \mathbf{t} - \mathbf{t_o}$, we get the linearized traveltime equations:

$$\delta\mathbf{t} = \mathbf{L_o}\delta\mathbf{s}, \tag{1.16}$$

where $\delta\mathbf{s}$ is known as the traveltime residual and $\delta\mathbf{s}$ is slowness perturbation. Often we will not use the subscript in $\mathbf{L_o}$. The strategy is to solve for $\delta s = [\mathbf{L^T L}]^{-\mathbf{1}}\mathbf{L^T}\delta\mathbf{t}$, and find the new update for the slowness field by

$$\mathbf{s}' = \mathbf{s_o} + \alpha[\mathbf{L^T L}]^{-\mathbf{1}}\mathbf{L^T}\delta\mathbf{t}, \tag{1.17}$$

where α is a scalar quantity $0 < \alpha \leq 1$ known as the step length. It is selected by trial and error to insure that the misfit function decreases after each iteration. The slowness field $\mathbf{s}'$ is used as the new background slowness, and a new traveltime residual is found $\delta\mathbf{t}' = \mathbf{t} - \mathbf{Ls}'$. Here, $\mathbf{Ls}'$ is the predicted traveltimes using the updated slowness and $\mathbf{t}$ is the observed traveltime vector.

More generally, a regularization parameter is introduced (see equation 1.14 and set $\mathbf{s^0} = 0$) and the updating is repeated in an iterative manner:

$$\mathbf{s}^{(k+1)} = \mathbf{s}^{(k)} + \alpha[\mathbf{L^T L} + \lambda\mathbf{I}]^{-1}\mathbf{L^T}\delta\mathbf{t}, \tag{1.18}$$

where k is the iteration index and it is assumed that the $[\mathbf{L^T L} + \lambda\mathbf{I}]^{-1}\mathbf{L^T}\delta\mathbf{t}$ is computed using the kth slowness model.

1.2.4 Steepest Descent

In real applications, the earth model is gridded so that there can be anywhere from several thousand unknowns to more than a million unknown slownesses. This means that the cost of storing and direct inversion of $[\mathbf{L^T L}]$ is prohibitive. Thus, an indirect iterative method such as conjugate gradients is used, where only matrix-vector multiplication is needed. A simpler cousin of the conjugate gradient method is steepest descent, and has proven useful in a multigrid mode (Nemeth et al., 1997).

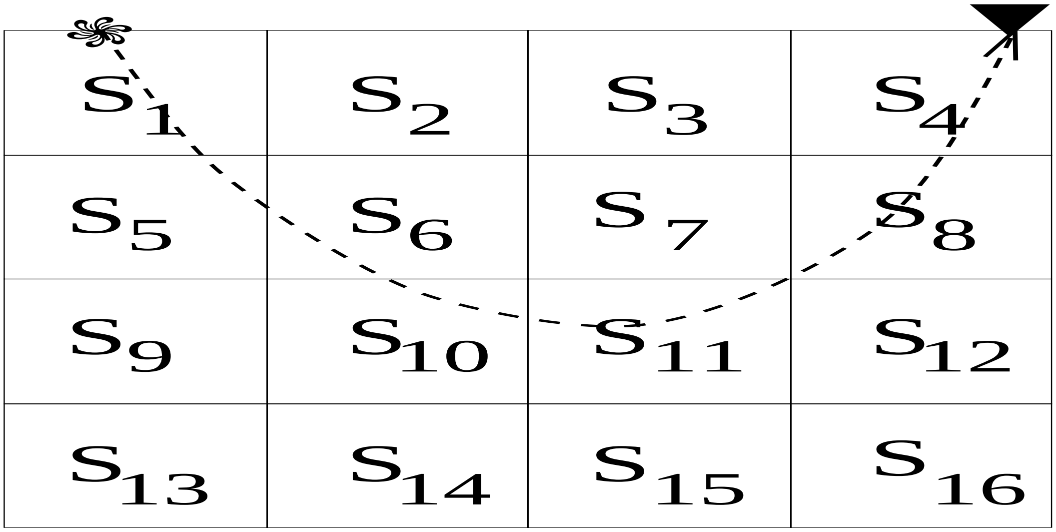

Figure 1.8: Diagram of jth ray through a discretized earth model, where the ith cell has a constant slowness s_i. For this ray, the segment length in the ith cell is given by l_{ij}.

The regularized steepest descent formula is obtained by approximating the inverse to $[\mathbf{L^TL}]$ by the recipricol of its diagonal elements:

$$[\mathbf{L^TL} + \lambda\mathbf{I}]^{-1} \approx 1/[\mathbf{L^TL} + \lambda\mathbf{I}]_{ii}\delta_{ij}, \tag{1.19}$$

where δ_{ij} is the Kronecker delta function. Substituting this approximation into equation 1.18 yields the steepest descent formula

$$s_i^{(k+1)} \quad = \quad s_i^{(k)} + \alpha/[\mathbf{L^TL} + \lambda\mathbf{I}]_{ii}[\mathbf{L^T}\delta\mathbf{t}]_i, \tag{1.20}$$

where s_i denotes the constant slonwness in the ith cell. Note, only matrix-vector multiplication is needed (cost=$O(N^2)$) compared to direct inversion which costs $O(N^3)$ algebraic operations. Equation 1.20 is sometimes called a preconditioned regularized steepest descent because of the diagonal matrix approximation. It is closely related to the SIRT method (Nolet, 1987).

The $1/[\mathbf{L^TL}]_{ii} = 1/\sum_j l_{ij}^2$ term is the squared sum of the segment lengths of rays that visit the ith cell. Thus cells that do not get visited frequently are given roughly the same weight as frequently visited cells.

Example: One ray and only one slowness perturbation. Assume a single jth ray and a single slowness anomaly in the ith cell that leads to the traveltime residual δt_j. Equation 1.18 reduces to

$$s_i^{(k+1)} \quad = \quad s_i^{(k)} + \alpha l_{ij}\delta t_j/({l_{ij}}^2 + \lambda). \tag{1.21}$$

This says that the slowness in the ith cell is updated by smearing the weighted jth residual δt_j into the ith cell visited by the jth ray, where the weight is $\alpha l_{ij}/({l_{ij}}^2+\lambda) \approx 1/l_{ij}$ for small λ and $\alpha = 1$. Thus, the slowness update $\delta s_i = \delta t_j/l_{ij}$ makes sense because it accounts for the traveltime residual strictly caused by the slowness anomaly in this *ith* cell. However, this residual is erroneously smeared along other cells visited by the *jth* ray, which had the correct slowness. Further iterations and more data (i.e., rays) are needed to correct for these errors, and if we are lucky then the regularized preconditoned steepest descent method should converge to the correct answer.

1.3 Summary

For most overconstrained systems of equations in seismic imaging no exact solution exists. The usual remedy is that seek a least squares solution that minimizes the sum of the squared residuals denoted by $\epsilon = 0.5\sum_i r_i^2$. In this case, the non-linear GN solution $\mathbf{s}^{(k+1)} = \mathbf{s}^k - H^{-1}\mathbf{g}^{(k)}$, yields the Hessian given by $H = \sum_{i=1}^{M} T_i r_i + \mathbf{L^T}\,\mathbf{L}$, where T_i contains second derivatives of the residuals and $\mathbf{L}$ contains the first derivatives of the residuals. Invoking a small residual assumption, the second derivative term is neglected, so that $\mathbf{s}^{(k+1)} = \mathbf{s}^k - [\mathbf{L}^T\mathbf{L}]^{-1}\mathbf{L}^T\delta\mathbf{t}$.

If the $\mathbf{L}^T\mathbf{L}$ are poorly conditioned then many different models can account for the data, i.e., the solution is *unstable.* The partial remedy is to impose equations of constraint to regularize the system of equations. If the system of equations is highly inconsistent because of outlier errors in the traveltime picks then an l^1 method can be used, otherwise known as reweighted least squares. In practice, the system of equations is usually too large to find the direct inverse to $\mathbf{L}^T\mathbf{L}$, so iterative solution methods are used, as discussed in Fletcher (1987), Gill (1981) and Nolet (1987).

1.4 Appendix

A microscopic view of the bent raypath in Figure 1.8 would reveal a straight ray, where the associated wavefronts are straight and perpendicular to this straight ray. In this microscopic zone, a small peeble or velocity inhomeogeneity appears as a limitless ocean of homogeneous velcoity. Consequently, for really small wavelengths the wave equation is solved by the plane wave solution $e^{i\omega(k_x x + k_y y - \omega t)}$. At the point (x, y) and its small neighborhood the medium is effectively constant $c(x, y) = \omega/k$ for very high frequencies f, i.e., small wavelengths $\lambda = c/f$. Thus, the following dispersion relationship is true in this neighborhood:

$$k_x^2 + k_y^2 \;\; = \;\; (2\pi/cT)^2, \qquad (1.22)$$

where T is the period of the source wavelet. Recalling that $k_x = 2\pi/\lambda_x$ and $k_y = 2\pi/\lambda_y$, where λ_x and λ_y are the horizontal and vertical apparent wavelenths, respectivey, equation 1.22 becomes after multiplying by $(.5T/\pi)^2$:

$$(T/\lambda_x)^2 + (T/\lambda_y)^2 \;\; = \;\; (1/c)^2. \qquad (1.23)$$

But, for a plane wave, $T/\lambda_x = \partial t(x, y)/\partial x$ and $T/\lambda_y = \partial t(x, y)/\partial y$ so that the above equation reduces to the eikonal equation:

$$(\partial t(x, y)/\partial x)^2 + (\partial t(x, y)/\partial y)^2 \;\; = \;\; (1/c)^2. \qquad (1.24)$$

The eikonal equation is more compactly expressed as $|\nabla t(x,y)| = 1/c(x,y)$, where $\nabla t(x,y)$ is the gradient of the traveltime field, which points perpendicular to the wavefront. We can replace this compact representation by the directional derivative

$$|\nabla t(x,y)| \quad = \quad dt(x,y)/dl = 1/c(x,y), \tag{1.25}$$

where the direction perpendicular to the wavefront is denoted by $\hat{l}$ and a small incremental change of raypath length along this direction is denoted by dl. Multiplying through by dl and integrating the raypath length from the source to the observation point (x,y) yields the traveltime integral:

$$\begin{aligned} t(x,y) &= \int_{raypath} dl/c(x,y), \\ &= \int_{raypath} s(x,y)dl, \end{aligned} \tag{1.26}$$

which is the modeling equation for traveltime tomography, a high frequency method for inverting the earth's velocity distribution from measured traveltime data. Note that this is a non-linear integral equation with respect to slowness $s(x,y)$ because both the integrand and raypath geometry depend on $s(x,y)$.

Chapter 2

Case History: 3D Refraction Tomography

To demonstrate the capabilities of traveltime tomography, researchers at the University of Utah carried out seismic experiments over the Washington fault in southern Utah. The goal of these 2D and 3D seismic experiments in 2008 was to provide a good estimate of the location of faults and colluvial wedges buried beneath the Washington fault escarpment; such information could be used to optimize the design and placement of a trench survey that would take place in the spring of 2009. Figure 2.1 shows the seismic survey site and the proposed trench site and the next two sections describe the details of these experiments.

2.0.1 2-D Seismic Survey

In March 2008, UTAM researchers carried out a 2-D high resolution seismic survey perpendicular to the Washington fault scarp near the Arizona-Utah border (see Figure 2.1). The 2-D seismic data were collected using 96 vertical-component geophones spaced 1 m apart for a total line length of 95 m (see Figure 2.1). Figure 2.2 shows the source and receiver lines, and the fault strike direction. Seismic sources, using a 16-lb sledgehammer striking a small metal plate, were initiated at every second geophone and stacked five times for each hammer (i.e., shot) position to improve the signal-to-noise ratio of each record. Recording of traces was carried out with a 120-channel Bison data recorder. Table 2.1 summarizes the acquisition and source-receiver parameters of the 2-D and 3-D seismic surveys.

2.0.2 3-D Seismic Survey

A 3-D seismic survey was carried out at the same location as the 2-D survey in October 2008 in order to obtain higher resolution images of the subsurface. The 3-D acquisition geometry consisted of six parallel lines, where there were 80 in-line receivers with a 1 m spacing near the fault scarp and a 2 m spacing far away from the fault scarp. The cross-line spacing was 1.5 m. Shots were also activated at every other geophone, and the experiment geometry is shown in Figure 2.3.

Table 2.1: Parameters for the 2-D and 3-D seismic surveys.

Survey	2-D	3-D
Source	16-lb sledgehammer	10-lb sledgehammer
Recording instruments	one 120-channel BISON	two 120-channel BISONs
No. of shots	48	40/line (6 lines)
No. of receivers	96	80/line (6 lines)
Shot spacing	2 m	(Figure 2.3)
Receiver spacing	1 m	(Figure 2.3)
Survey length	95 m	119 m
No. of traces	4,608	115,200
Sampling interval	0.25 ms	0.25 ms
Record length	1.0 sec	1.0 sec

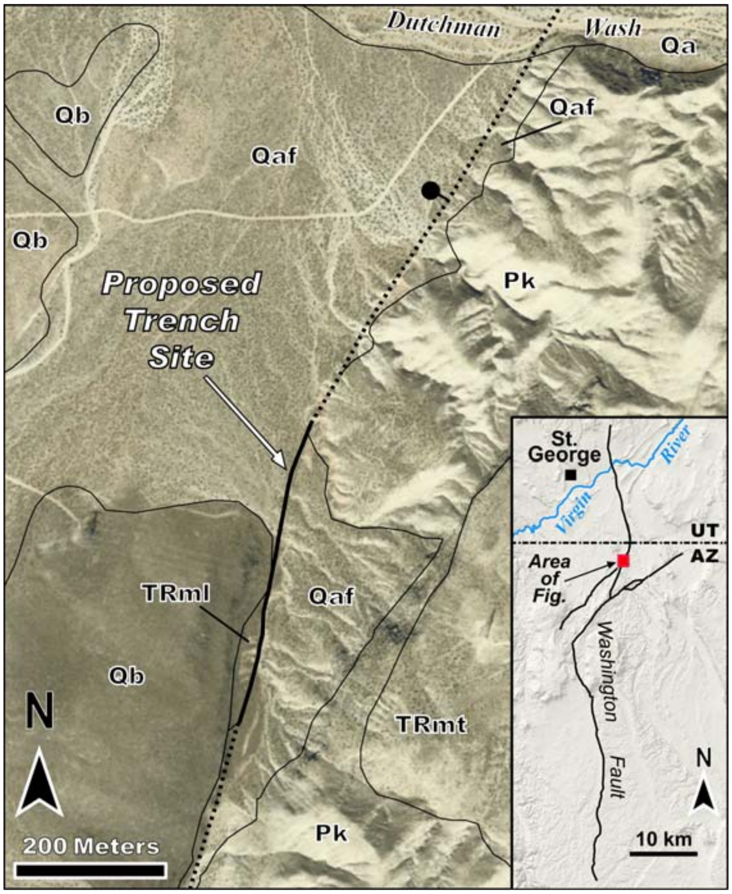

Figure 2.1: The map of the Washington fault and the survey site. The location of the survey site is 5 km south of the Utah-Arizona border. A trench will be excavated by UGS personnel in the same location, marked on the map, sometime in the late spring of 2009.

Figure 2.2: View of the Washington fault scarp and 2-D seismic survey line. The yellow line represents the fault strike direction, and the green line represents the 2-D seismic survey line.

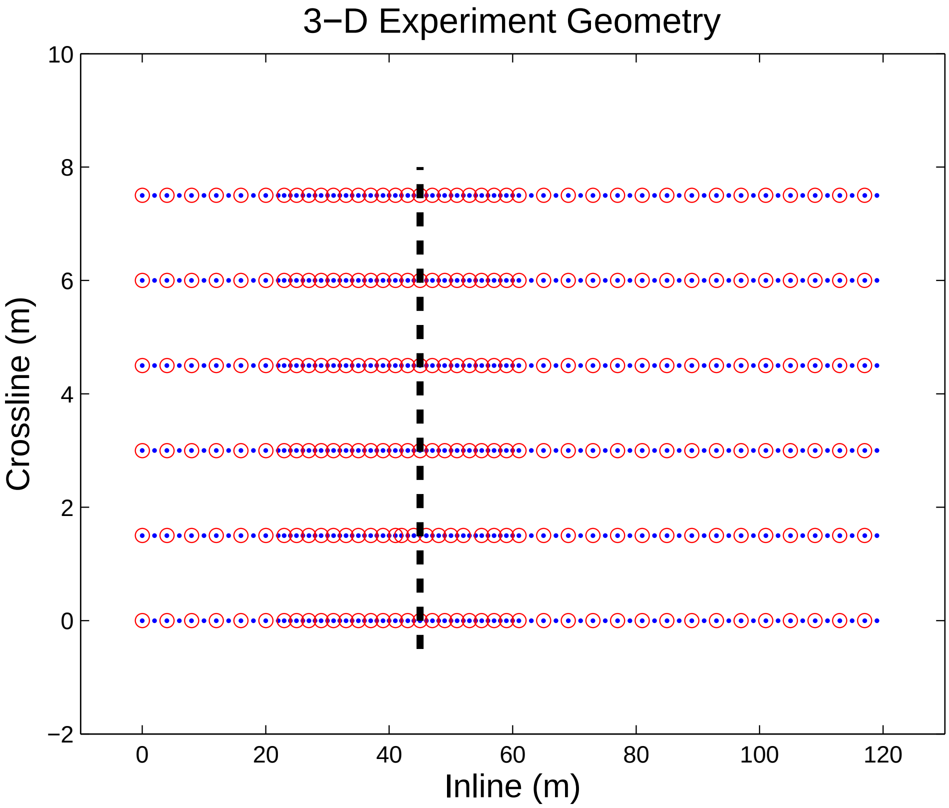

Figure 2.3: Survey geometry for the 3-D experiment. The open circles denote the locations of sources, the solid dots denote the locations of receivers, and the dashed black line denotes the location of the fault scarp. The crossline spacing is 1.5 m, the inline spacing of coarsely spaced receivers (far from the fault scarp) is 2 m, and that of finely spaced receivers (near the fault scarp) is 1 m. The sources are activated at every other receiver.

2.1 Traveltime Tomography

Traveltime tomography is a standard methodology for reconstructing the subsurface velocity distribution from first-arrival traveltimes (Nolet, 1987; Lutter et al., 1990; Aldridge and Oldenburg, 1993; Ammon and Vidale, 1993; Nemeth et al., 1997 and many others), where velocities are updated by an iterative method such as the SIRT technique (Gilbert, 1972). The tomography method consists of a number of steps. First, an initial velocity model is estimated from the x-t slope of the first-arrival in the seismograms. The traveltimes are then computed from the starting model by a finite-difference solution to the eikonal equation (Qin et al., 1992). The result is a velocity model of the P-wave velocity, where smaller velocities correspond to more unconsolidated; experiments along the Wasatch fault show that colluvial wedges are typically characterized by 10 to 20 percent slower velocities (Morey and Schuster, 1989) than the surrounding soil, and faults can sometimes be indicated by sharp horizontal changes in velocity (Ann+Bruhn, 19??; Sheley et al, 19??; Buddensiek et al., 2008). A more definitive indicator of faults is the reflection section (Morey and Schuster, 1998).

2.1.1 Methodology

Traveltime tomography is a standard methodology for reconstructing the subsurface velocity distribution from first-arrival traveltimes (Nolet, 1987; Lutter et al., 1990; Aldridge and Oldenburg, 1993; Ammon and Vidale, 1993; Nemeth et al., 1997 and many others), where velocities are updated by an iterative method such as the SIRT technique (Gilbert, 1972). The tomography method consists of a number of steps. First, an initial velocity model is estimated from the x-t slope of the first-arrival in the seismograms. The traveltimes are then computed from the starting model by a finite-difference solution to the eikonal equation (Qin et al., 1992). In this case, the data misfit function can be defined as:

$$\epsilon = \frac{1}{2}\sum_i (t_i^{obs} - t_i^{cal})^2, \tag{2.1}$$

where the summation is over the i_{th} raypaths, t_i^{obs} is the associated first-arrival traveltime pick, and t_i^{cal} is the calculated traveltime. The j_{th} gradient γ_j of the misfit function is defined as:

$$\gamma_j = \frac{\delta\epsilon}{\delta s_j} = \sum_i \delta t_i \frac{\delta t_i}{\delta s_j} = \sum \delta t_i l_{ij}, \tag{2.2}$$

where δt_i is the traveltime residual, δs_j is the slowness in the jth cell and l_{ij} is the segment length of the i_{th} ray that visits the j_{th} cell. The slowness model is iteratively updated by a gradient optimization method (e.g., steepest descent).

2.1.2 Traveltime Picking and Quality Control

The first step in tomography processing is to pick first-arrival traveltimes. Approximately 4,608 and 115,200 traveltimes are picked, respectively, from the original 2-D and 3-D Washington fault data using ProMAX software. A shot gather of the 2-D data with the picked first-arrival traveltime is shown in Figure 2.4.

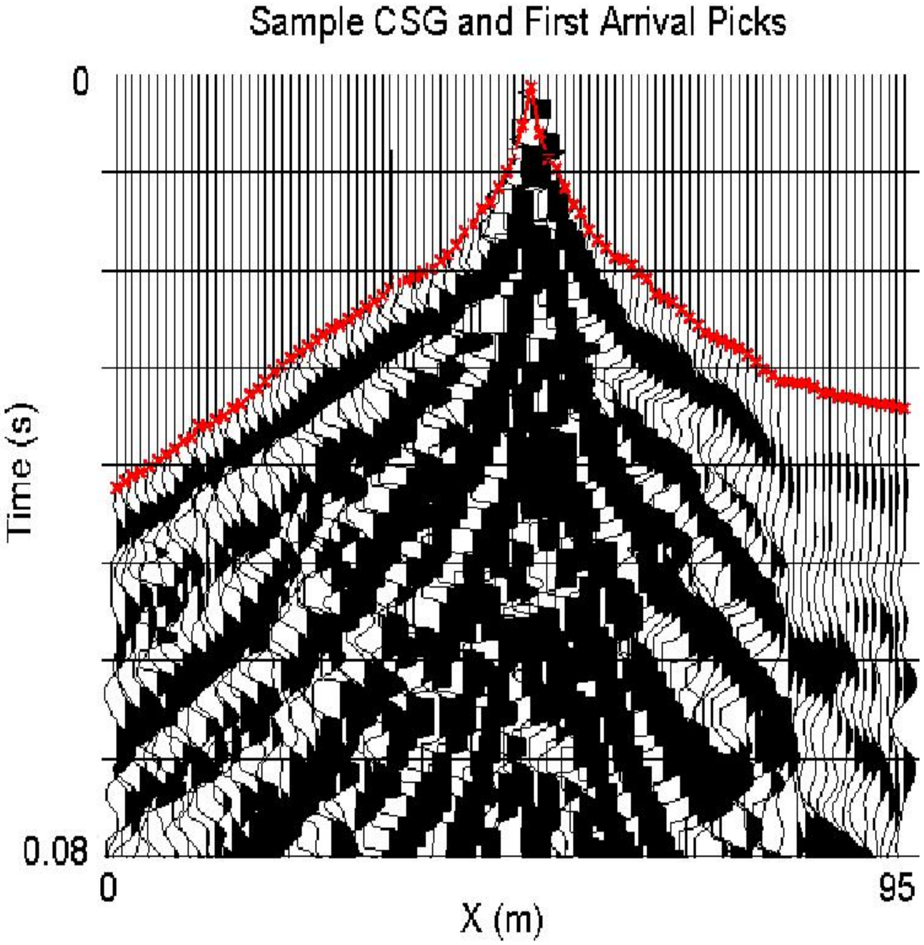

Figure 2.4: A common shot gather from 2-D Washington fault data set and first-arrival traveltime picks are denoted by the red star.

Before computing the traveltime tomogram, a quality control of the traveltime picks is required for a reliable inversion. An important method for the quality control of traveltime picks is a reciprocity test. For traveltime pairs t_{ij} and t_{ji}, where t_{ij} represents the first-arrival traveltime pick for a source at the ith position and a receiver at the jth position, and t_{ji} represents the reciprocal traveltime pick of t_{ij}, if the reciprocity condition $t_{ij} = t_{ji}$ is not satisfied to within a tolerance of 3 milliseconds, the traveltime pairs are rejected. For the 3-D data, 29,750 traveltime picks are rejected by failing the reciprocity test. The remaining traveltimes are inverted using the SIRT algorithm described in 2.2.1.

2.1.3 Smoothing Filter

Due to irregular raypath coverage in some parts of the velocity model, a rectangular smoothing filter is applied after each iteration in the inversion process (Nemeth et al., 1997). Table 2.2 gives a listing of smoothing schedules for the synthetic data and field data in this paper. The reconstructed velocity model is initially smoothed with a 10 m x 5 m x 5 m smoothing filter. After six iterations the smoothing filter size is halved, which results in a better spatial resolution. The final smoothing filter is iteratively reduced to a volume of 2 m x 1 m x 1 m.

Table 2.2: Smoothing schedule for synthetic and field data. The smoothing sizes are given in number of cells. The iteration number is 6 for each schedule.

Experiment	2-D synthetic test	3-D synthetic test	2-D actual data	3-D actual data
Grid size	0.5 m	0.5 m	0.5 m	0.5 m
No. of effective unknowns	4,800	72,000	4,800	72,000
No. of traveltimes	3,200	115,200	2,687	85,450
Smoothing size 1	20 x 10	20 x 10 x 10	20 x 10	20 x 10 x 10
Smoothing size 2	12 x 6	12 x 6 x 6	12 x 6	12 x 6 x 6
Smoothing size 3	8 x 4	8 x 4 x 4	8 x 4	8 x 4 x 4
Smoothing size 4	4 x 2	4 x 2 x 2	4 x 2	4 x 2 x 2

2.2 2-D CDP Reflection Processing

The goal of common depth point (CDP) reflection processing is to transform the seismic reflection data into an approximate reflectivity image of the subsurface. Because near-surface scattering, statics, and surface waves are dominant in the shallow seismic data, the following processing flow (Figure 2.5) is required to obtain reflectivity images (Yilmaz, 1987).

2.2.1 Data Sorting and Geometry Defining

The first step in CDP data processing is to convert the data format from Bison seismograph format to SEG-Y format so processing can be performed with ProMAX. Then the survey geometry is defined according to the field survey, including the shot and receiver locations, shot and receiver offsets, CDP locations, and other known parameters that affect the data processing.

2.2.2 Elevation Statics

The statics problem is defined to be static time shifts introduced into the traces by, e.g., near-surface velocity anomalies and/or topography. These time shifts distort the true geometry of deep reflectors. For the Washington experiment, large static time shifts are introduced by the large elevation changes in the topography. Thus, an elevation statics correction is applied to the data, so that the data appear to have been collected on a flat datum plane. The final datum elevation is the same as the highest topographic point, and the replacement velocity is 500 m/s for correcting the traces to the new datum.

2.2.3 Bandpass Filter

To remove the low-frequency noise (such as surface waves), 40-200 Hz bandpass filtering was applied to the traces. The low frequency surface waves are mostly suppressed by this filter.

2.2.4 NMO and Stacked Section

The seismic data are sort into 190 common midpoint gathers (CMG) with 0.5 meter spacing. Two or three near zero-offset traces of each CMG were selected for stacking.

2.2.5 Poststack Migration

In order to move dipping reflectors into their correct positions and collapse diffractions, poststack migration was applied to the stacked data, where the maximum dip angle is limited to be no more than 30 degrees. The migration method selected was Kirchhoff migration.

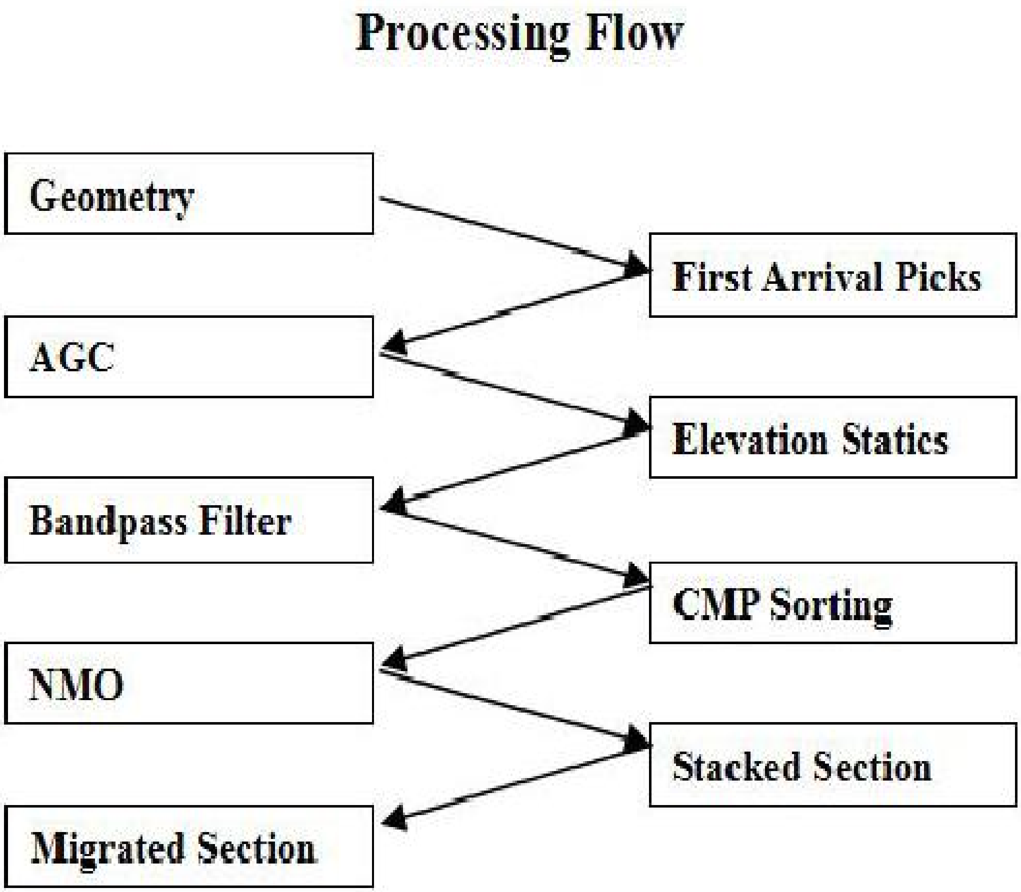

Figure 2.5: Chart for reflection processing of the 2-D Washington fault data set. Here, AGC = automatic gain control, NMO = normal moveout correction, CMP = common midpoint.

2.3 NUMERICAL RESULTS FOR SYNTHETIC DATA

Typically a series of synthetic tests are used to assess the tomogram accuracy for any specific field geometry of sources and receivers. Towards this goal synthetic tests were carried out for 2D and 3D traveltime tomography of synthetic traveltime data with source-receiver geometries similar to that of the Washington fault experiments. The results suggest that the faults and LVZs can be clearly imaged by seismic methods, and 3-D tomograms are more accurate and have fewer artifacts than 2-D tomograms in delineating fault structures.

2.4 Traveltime Tomography of the Synthetic Data

To understand the sensitivity of the tomography method in delineating fault structures, both 2-D and 3-D synthetic tests are carried out. The input model is a 3-D fault model, and has the same dimension as the area investigated with the 3-D Washington fault experiment. The model was constructed by defining the background velocity to be similar to that of the actual 3-D Washington fault tomogram. The velocity at the ground surface is defined to be 500 m/s and the vertical velocity gradient is assigned as 110 m/s/m, and the depth of bedrock is about 15 m below the surface with the velocity 2400 m/s. There is no variation of velocity in the Y direction. An X-Z velocity slice of the fault model is shown in Figure 3.1a. The source and receiver geometry for the synthetic test are identical to that of the 3-D Washington fault experiment, shown in Figure 2.3. Approximately 115,200 first-arrival traveltimes are generated by solving the 3-D eikonal equation with a finite-difference method (Qin et al. 1992), and the traveltimes taken from the 1st source line and receiver line (Y=0 m) are used for 2-D traveltime inversion. Table 2.1 summarizes the model and acquisition parameters for the synthetic tests.

Table 2.3: Model and acquisition parameters for the synthetic tests.

Survey	2-D	3-D
Model size	117 m x 30 m	117 m x 7.5 m x 30 m
Grid size	0.5 m	0.5 m
No. of shots	40	40 x 6
No. of receivers	80	80 x 6
Shot/receiver spacing	(Figure 2.3)	(Figure 2.3)
Survey length	117 m	117 m
No. of traveltimes	3,200	115,200

The first-arrival traveltimes are inverted to obtain the P-wave velocity distribution, and a gradient model with velocities ranging from 500 m/s at shallow depths to 2,400 m/s at depth are used for the initial model. The reconstructed velocity model is initially smoothed with a 10 m x 5 m x 5 m smoothing filter, and the smoothing filter is iteratively reduced to a volume of 2 m x 1 m x 1 m. Table 2.2 gives the inversion and smoothing filter parameters (Nemeth et al., 1997).

A comparison between the 2-D and 3-D tomograms is shown in Figures 3.1b and 3.1c. Both of the tomograms are along the 1st receiver line (Y=0 m), and the images obtained from 2-D and 3-D tomography are comparable at low wavenumbers. The fault surfaces in the model are characterized by a smooth down drop of the velocity contours in both of the tomograms. This is not surprising since previous studies (Buddenseik, et al., 2007) empirically showed that the tomogram is a smoothed version of the actual velocity, where faults are characterized by a smooth downdrop in tomographic velocities. Another observation is that the 3-D tomogram seems to have fewer artifacts than the 2-D tomogram. This should not be too surprising because rays in the the 3-D survey are characterized by a greater diversity of ray angles, which leads to better model resolution. In addition, the radio of unknowns to traveltime equations (see Table 2.2) is smaller for the 3-D tomogram and suggests a more stable and overdetermined solution. In Figure 3.2, the velocity and gradient profiles at X=26 m (Fault 1), X=48 m (Fault 2) and X=74 m (Fault 3) are compared. The faults are identified as large positive gradient values of velocity, and the fault structures delineated in the 3-D tomogram are more accurate than those in the 2-D tomograms. Figure 3.1d depicts the 2-D raypath density image, which displays the number of rays visiting each cell of the tomogram. For the normal-slip fault (F1, F2 and F3), the rays focus near the fault plane, which results in fewer raypaths visiting the hanging wall side, and the LVZ (48 m< X <75 m) has lower raypath coverage than other regions.

To assess the convergence of the iterative solution, a plot of RMS traveltime residual vs. iteration number is shown in Figure 3.3. It demonstrates that the iterative solutions converge within ten iterations. The final traveltime residual is about 0.3 ms, which is close to 0, since no picking errors are added.

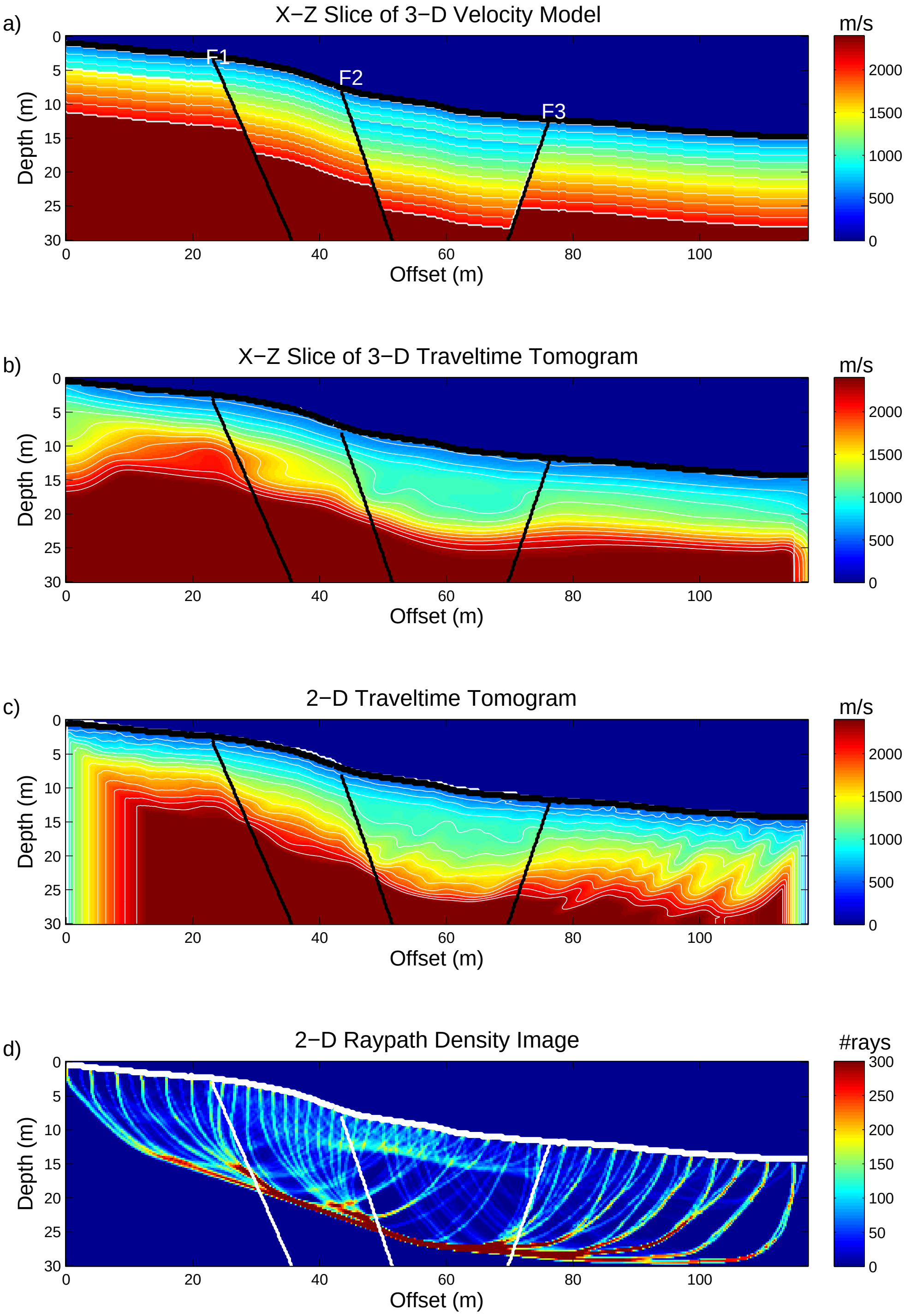

Figure 2.6: Results of 2-D and 3-D traveltime tomography test. a): an X-Z slice of the linear gradient velocity model with 3 normal faults. b): an X-Z slice of the 3-D tomogram along the first receiver line (Y = 0 m). c): 2-D traveltime tomogram along the first receiver line (Y = 0 m). d): raypath density image obtained from 2-D traveltime inversion.

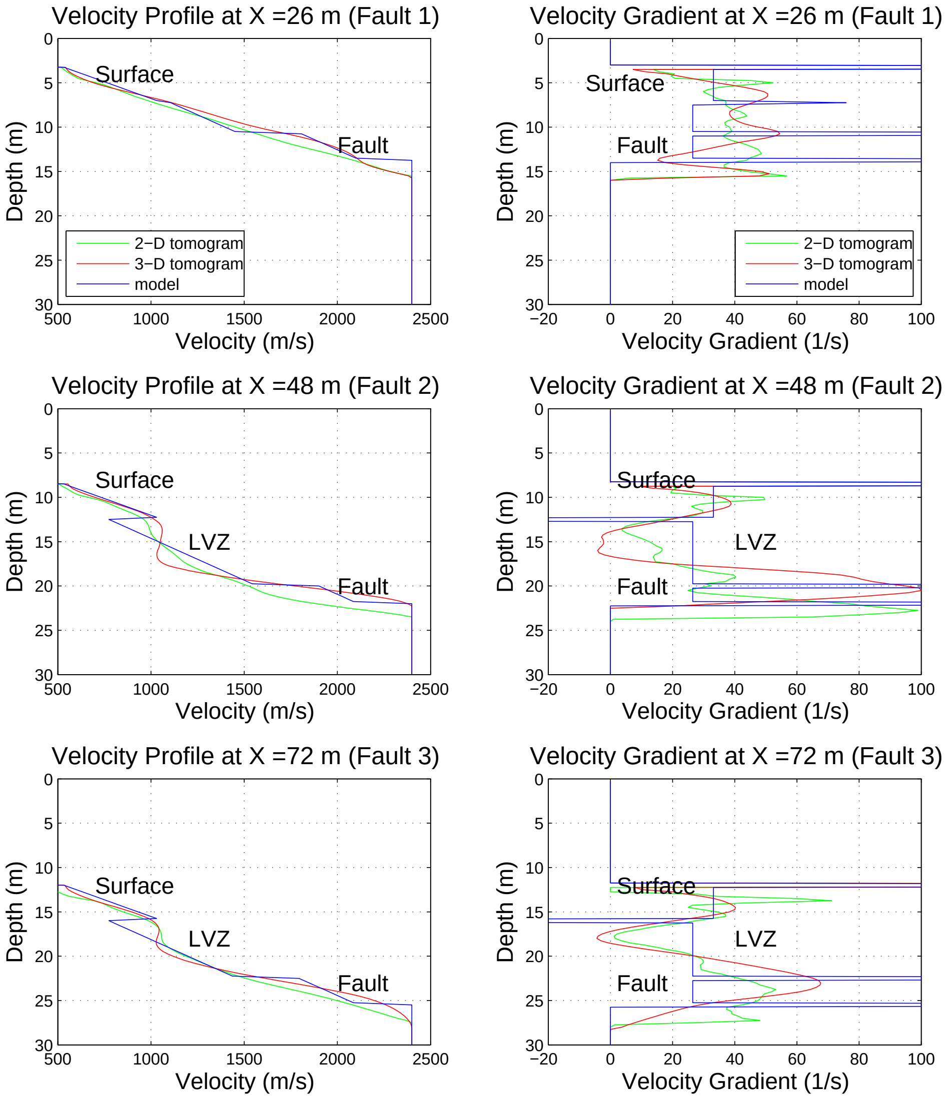

Figure 2.7: Velocity and gradient profile comparison at 3 different locations for the synthetic test . Left panels are the velocity profiles, and right panels are the velocity gradient profiles. In the velocity gradient profiles, the faults are identified by large positive gradient values and LVZs are identified by large negative gradient values.

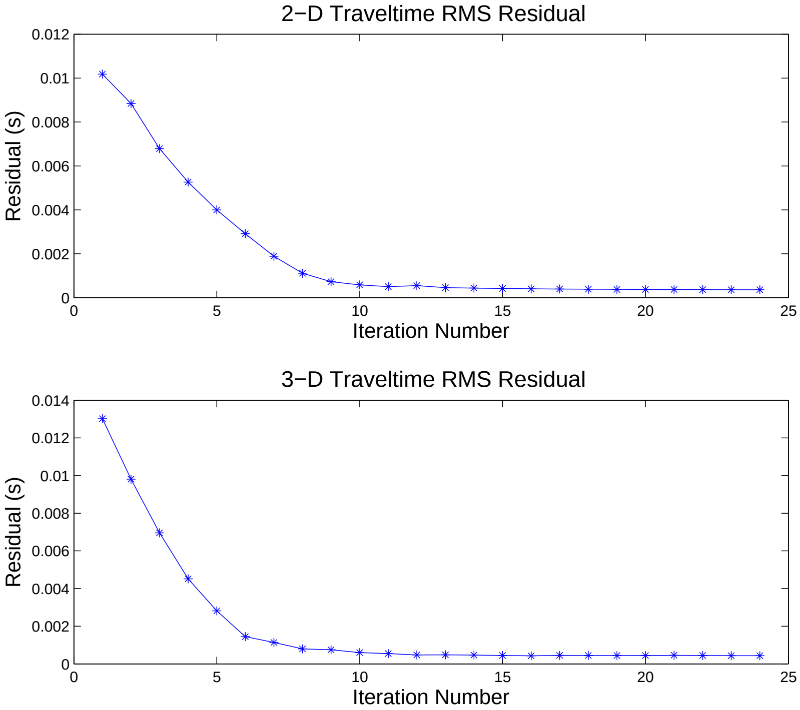

Figure 2.8: 2-D and 3-D RMS traveltime residual vs. iteration number. The iterative solutions converge after about ten iterations. The final traveltime residual is about 0.3 ms, which is close to 0, since no picking errors are added.

2.5 CDP Reflection Processing of the Synthetic Data

To locate the fault positions, CDP reflection processing is carried out. The velocity model is the same as the 2-D model in Section 3.1, and Figure 3.4a shows the reflectivity image computed from the velocity model. To make the processing simple, the sources and receivers are distributed evenly at 1 m spacing for a total line length of 117 m. A 2-4 finite-difference solution to the acoustic wave equation is used to generate the zero-offset seismograms, and Table 3.2 gives the model and acquisition parameters for the synthetic tests. Figure 3.4b shows the stacked seismic section with the horizontal axis in offset and the vertical axis in time. Figures 3.4c and 3.4d show the migration images using the true velocity and the velocity obtained from the tomogram, respectively. Although there are some artifacts in the migration image using the tomographic velocity, where the layers around X $<$ 15 m are tilted and the layers around X $>$ 90 m undulate, the fault locations are clearly identified with the correct dip angles.

Table 2.4: Model and acquisition parameters for the synthetic tests.

Model size	117 m x 30 m
Grid size	0.25 m
No. of shots	118
No. of receivers	118
Shot/receiver spacing	1 m
Source	100 Hz Ricker wavelet
Recording length	0.2 s
Sampling interval	0.02 ms

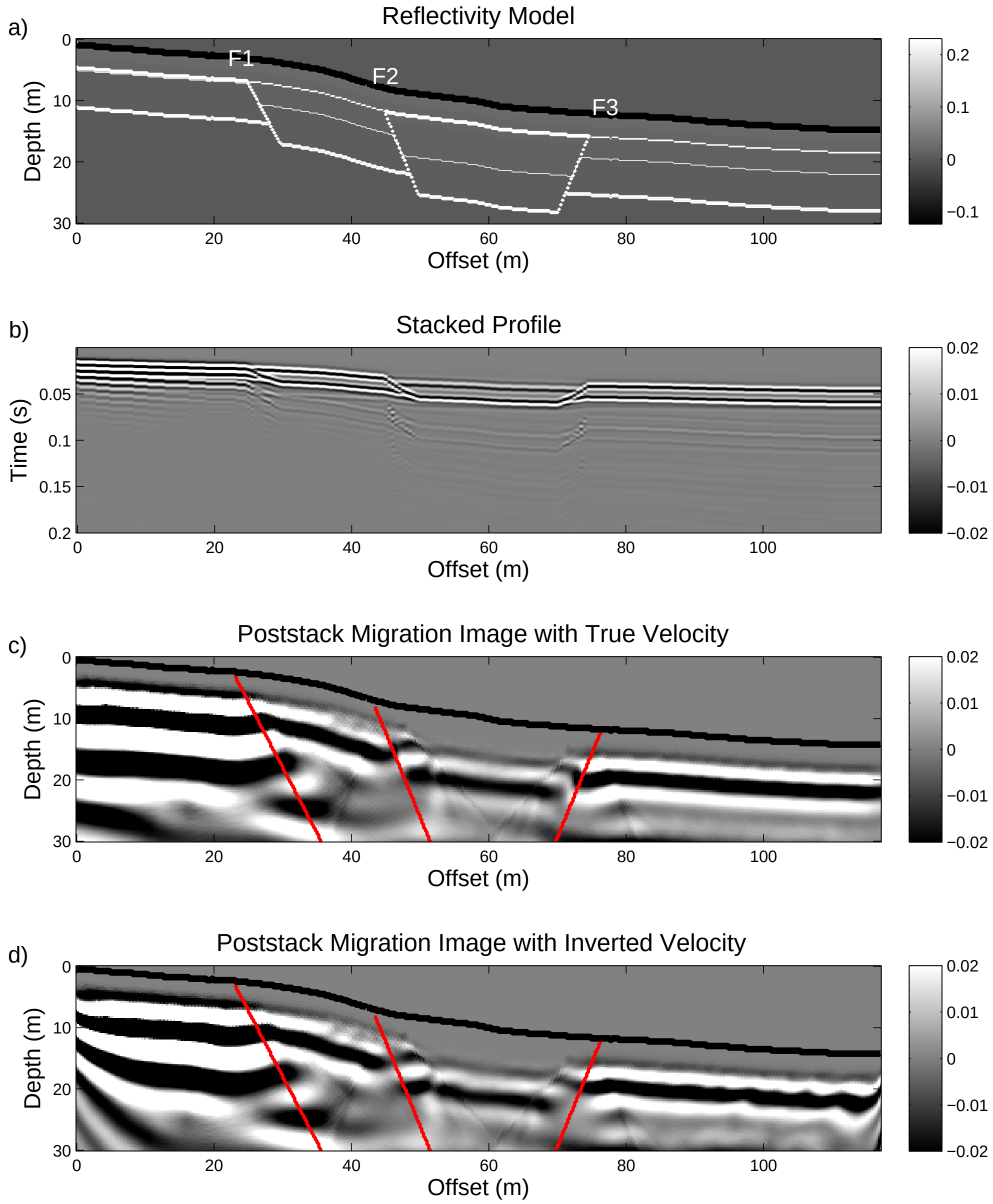

Figure 2.9: Stack and migration images. (a): the reflectivity image computed from the velocity model. (b): the stacked seismic section with the horizontal axis in offset and the vertical axis in time. (c): the migration images using the true velocity. (d): the migration images using the inverted velocity from tomography.

2.6 NUMERICAL RESULTS FOR FIELD DATA

The 2-D and 3-D tomographic results and the 2-D migration images are computed for data recorded from the Washington fault experiment and analyzed in this section. My interpretation suggests that there are four faults and two large LVZs. These LVZs are likely to be colluvial wedge packages, as they appear to be associated with the faulting.

2.6.1 2-D Tomographic Results

One 2-D survey line is taken from the original 3-D data. The first-arrival traveltimes are picked from 3,200 traces, where 513 traveltime picks were rejected because they did not satisfy the reciprocity condition within a tolerance of 3 milliseconds. The remaining traveltimes are inverted to obtain the P-wave velocity distribution. Figures 4.1a depicts the velocity tomogram presented as contours of seismic velocity in depth along the profile, and Figure 4.1b displays the raypath density through each cell in the tomogram. Based on the synthetic tests in section 3.1, two criteria are used to identify a fault in the tomogram: (1) Focusing of rays in the raypath density image (the fault is not exactly located at the greatest raypath density area, but is located at the low-density side near the plane, (see Figure 3.1). (2) a sharp change in the velocity gradient (see Figure 3.2). Combining the tomogram, velocity gradient profile, raypath density distribution and migration image (discussed in Section 4.2) together, four faults are interpreted, numbered from F1 to F4. Four LVZs are outlined with ellipses in the traveltime tomogram. In the raypath density, the LVZs correspond to the zones of low raypath density, marked with ellipses as well. A plot of RMS traveltime residual vs. iteration number is shown in Figure 4.2. The final RMS traveltime residual is about 2.4 ms, which is slightly smaller than the estimated picking error of 3 ms.

2.6.2 3-D Tomographic Results

The first-arrival traveltimes are picked from 115200 traces in the original data set, where 29750 traveltime picks are rejected because they failed the reciprocity test or were deemed unpickable. The 3-D velocity tomogram is inverted from these picks and is shown in Figure 4.3. Four X-Z slices spaced every 2 m along the Y direction are shown in Figure 4.4. This tomogram clearly delineates three large LVZs. The one denoted as LVZ1 is located at X=20-35 m, LVZ2 is located at about X=50-65 m, and LVZ3 is located along the near surface at X= 35-65 m. All of the LVZs are parallel to the fault scarp. The main fault (F3, see Figure 4.8) interpreted from the migration image and the raypath density image, is located at the offset of 45 m, and suggests that LVZ2 is possibly the colluvial wedge generated by surface rupture events on the Washington fault. The LVZ 3 is possibly another colluvial wedge package and is the youngest of the LVZs.Comparing the 2-D tomogram with the 3-D tomogram, both have similar structures at low wavenumbers; but, the 3-D tomogram has fewer artifacts than the 2-D tomogram. To access the accuracy of the predicted traveltimes, a plot of RMS traveltime residual vs. iteration number is shown in Figure 4.5. The final RMS traveltime residual is about 3.2 ms, which is almost the same as the estimated picking error of 3 ms.

2.7 Reflection Results

The 3-D Washington fault data has less observable reflection energy seen in the seismogram. This is because only a 10-lb sledgehammer was used in the 3-D experiment compared to the 16-lb sledgehammer in the 2-D experiment; and the 2-D experiment had a shorter survey length. Here, only the 2-D seismic data are used for reflection stacking. The common shot gathers (CSG) are sorted into 190 common midpoint gathers (CMG) with 0.5 meter spacing, and two or three near zero-offset traces of each CMG were selected for stacking. Figure 4.6 shows the stacked seismic section with the horizontal axis in offset and the vertical axis in time. It shows more than two shallow horizons, which are mostly continuous, except for the region around X = 14 m. From the stacked profile, it is difficult to determine the locations of the fault planes. To delineate the fault structures clearly, the stacked data are migrated. Figure 4.7 shows the final migration image, and using the migration images of the synthetic data as a guide, the layered horizons are discontinuous at the fault plane. Here, four faults (F1-F4) are interpreted, combined with the tomogram and raypath density image, where F3 is possibly the main fault, and F4 is the antithetic fault. The dip angles of the four faults are estimated from the migration image to be about 80+/-10 degree. This is consistent with the description of the Washington fault by Higgins, 1998.

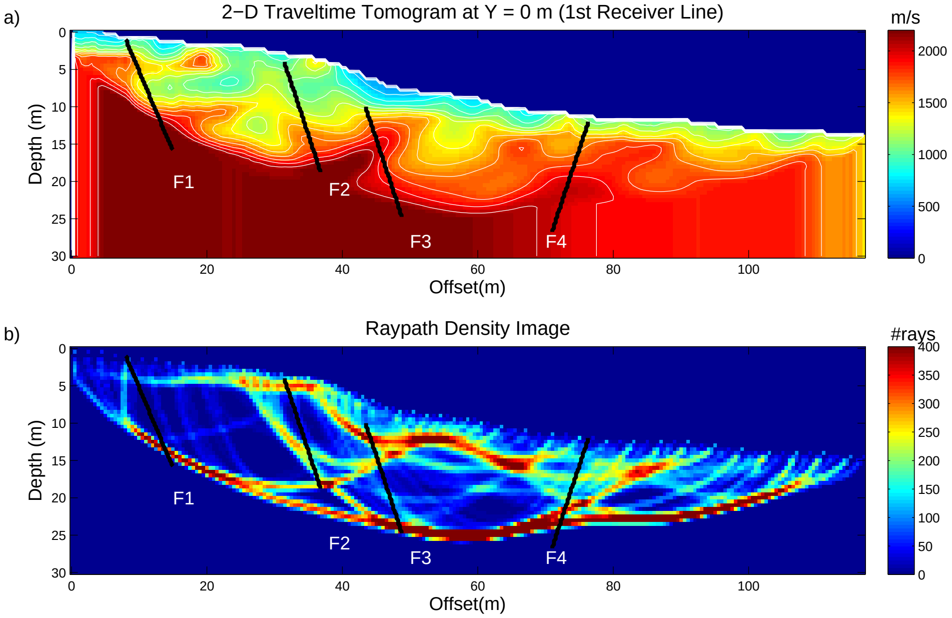

Figure 2.10: 2-D traveltime tomogram and raypath density image. (a): the 2-D traveltime tomogram with the fault interpretation. (b): the raypath density image.

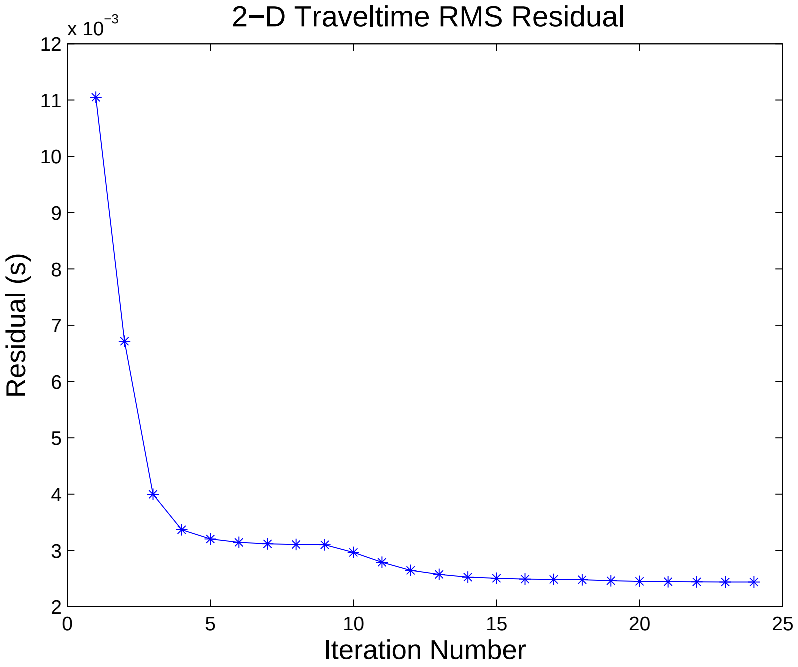

Figure 2.11: RMS traveltime residual vs. iteration number. The solution converges after about twenty iterations, and final RMS traveltime residual is about 2.4 ms.

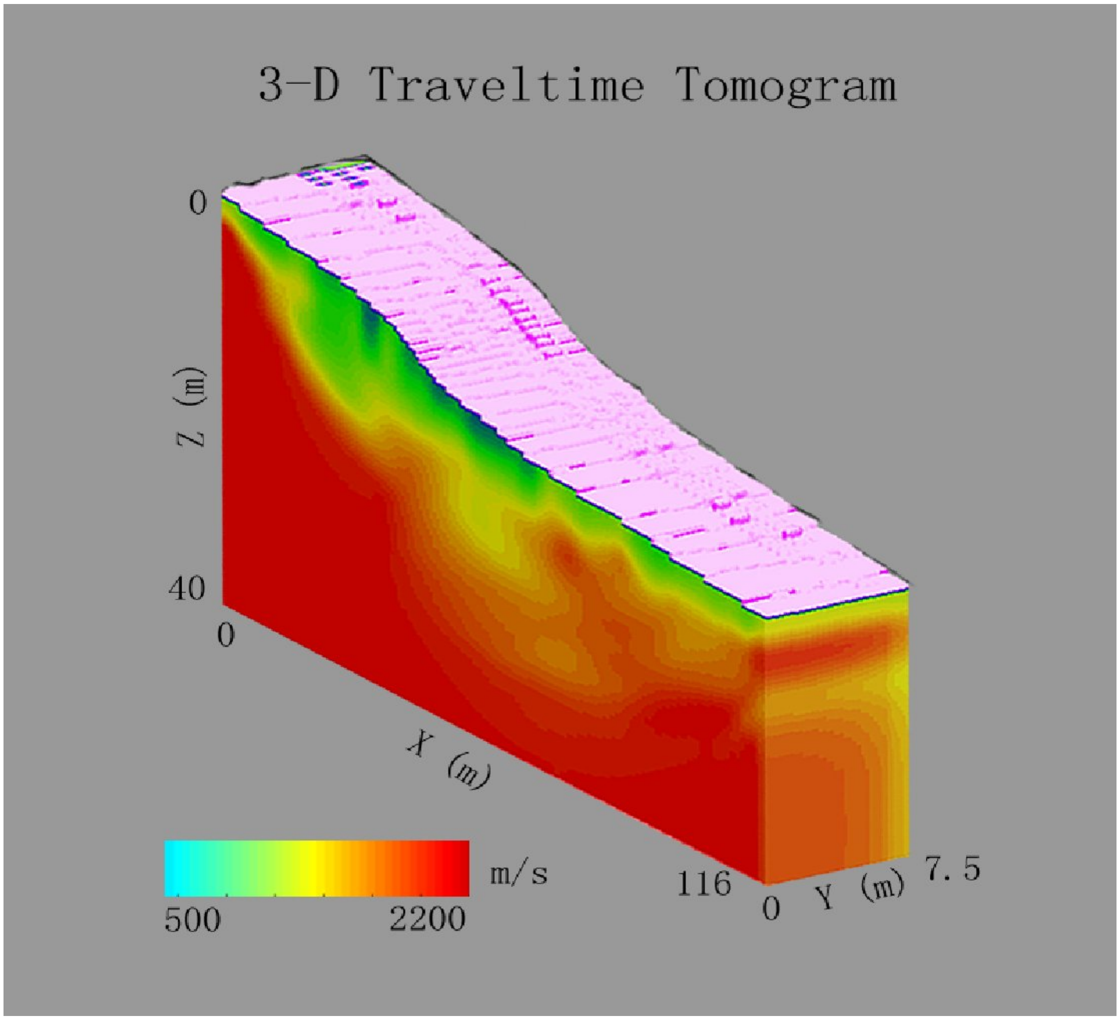

Figure 2.12: The volume of the 3-D velocity tomogram. Two large LVZs are clearly delineated in the tomogram.

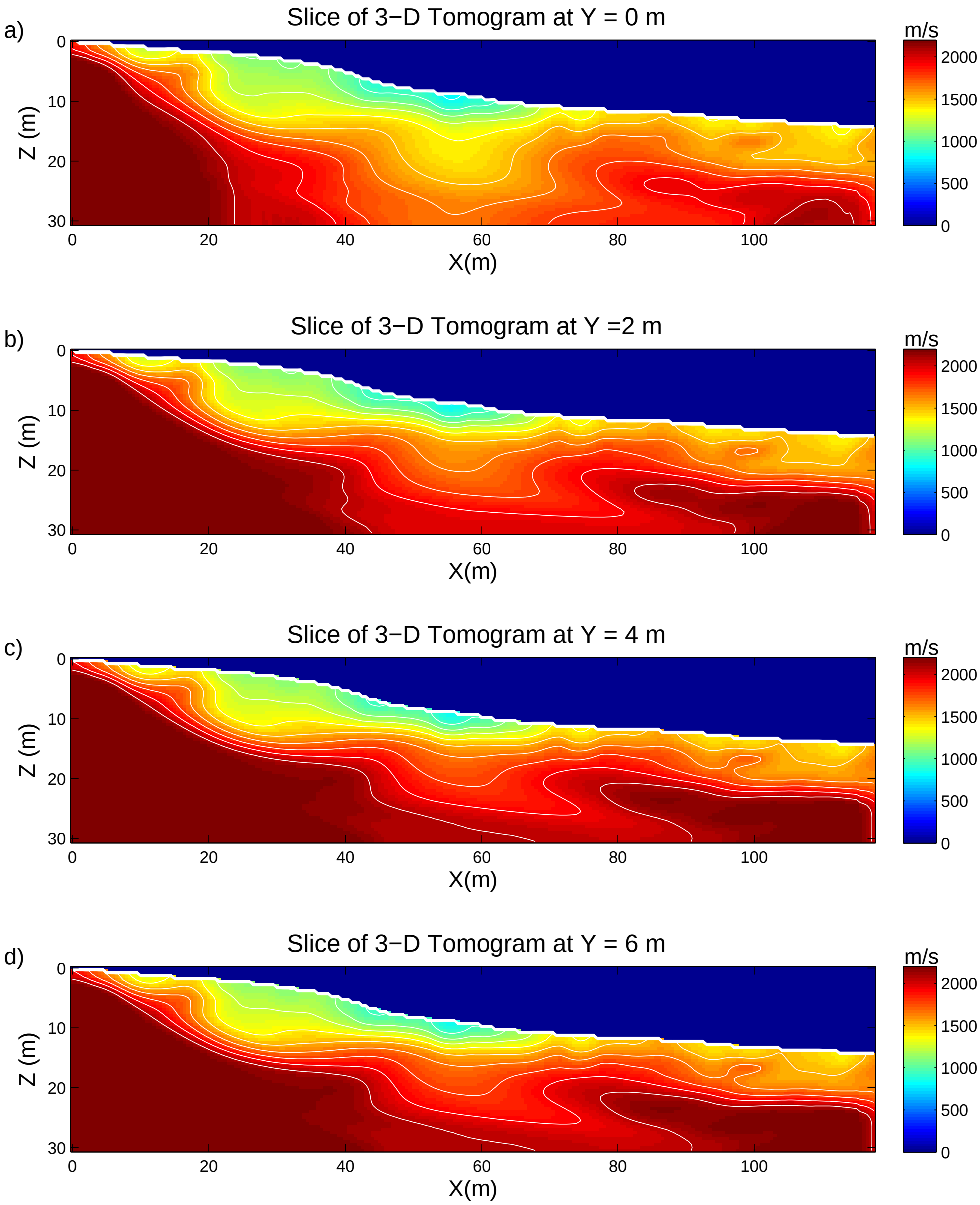

Figure 2.13: X-Z slice of 3-D velocity tomogram. (a): slice at Y = 0 m. (b): slice at Y = 2 m. (c): slice at Y = 4 m. (d): slice at Y = 6 m.

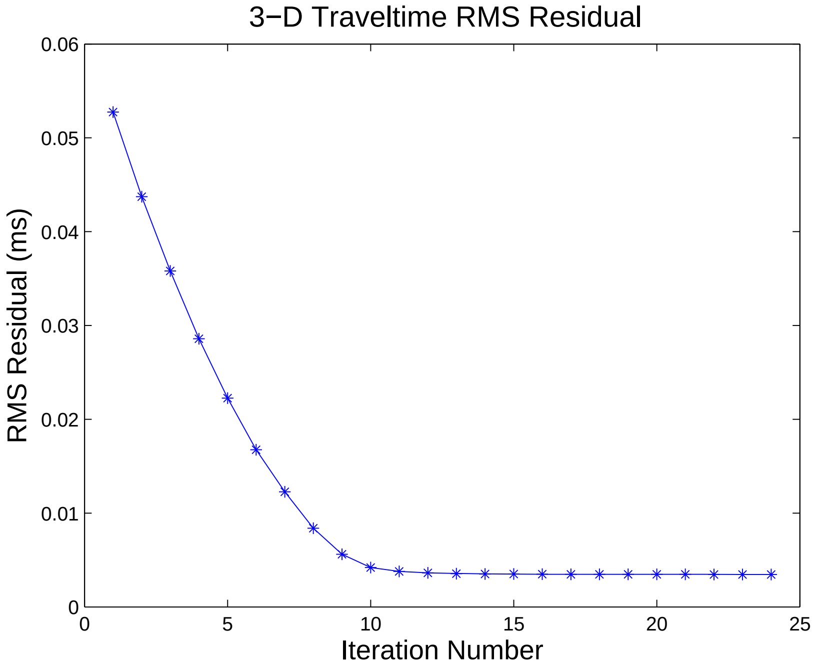

Figure 2.14: RMS traveltime residual vs. iteration number. The solution converges after about fifteen iterations, and the final traveltime residual is about 3.2 ms.

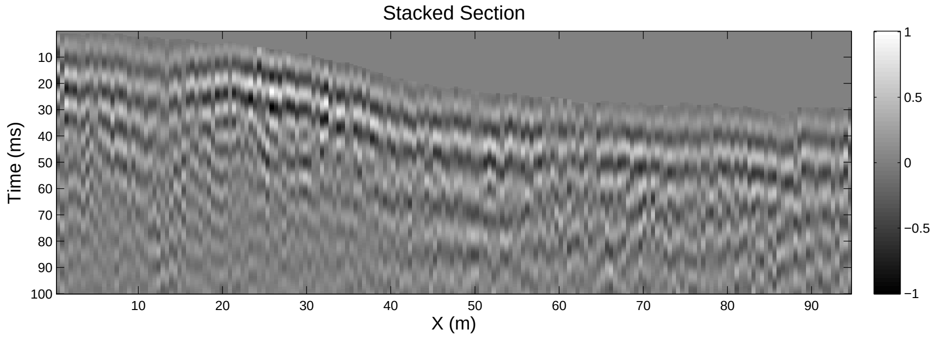

Figure 2.15: Stacked seismic section.

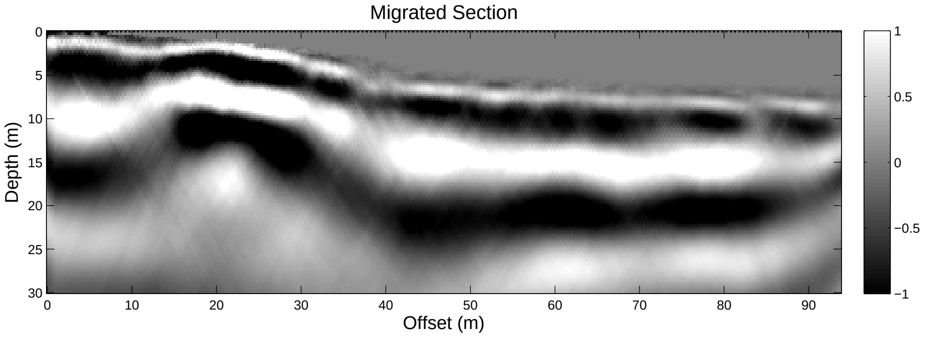

Figure 2.16: Migrated seismic section.

2.8 Interpretations

Figure 4.8 presents a summary of the tomographic results and the migration image. From the 2-D and 3-D traveltime tomogram and 2-D migration images, we can identify the following features:

(1) Three LVZs (LVZ1, LVZ2 and LVZ3) have been imaged with both 2-D and 3-D traveltime tomography. To establish their identity, age, and the estimated frequency of past earthquake occurrence, a much cheaper alternative than trenching is to drill a well over the areas (20 m< X <35 m and 50 m< X <65 m).

(2) F3 is likely to be the main fault, which is consistent with geomorphology data, and F4 is a possible antithetic fault.

(3) The depth of the bedrock is estimated to be about 15 m with the velocity larger than 2200 m/s.

(4) The four faults have an apparent dip of approximately 70-80 degrees.

(5) From the 3-D tomogram, the thickness of the LVZ1 and LVZ2 is about 5 m, and the thickness of LVZ3 is about 2 m.

Four faults and three LVZs are interpreted in Figure 4.9, and Table 4.1 summarizes the features interpreted from Figures 4.8 and 4.9. The thickness of LVZs can be considered as an approximation of the fault vertical slip. Combining the fault slip rate from paleoseismic data with the fault slip inferred by tomography, the age of the fault can be speculatively estimated. Earth Sciences Associates (1982) state that the slip rates for the Washington fault are 0.003 mm/yr for the past 1.5 kyr, and a minimum slip rate of 0.03-0.12 mm/yr for the past 10 to 25 kyr. If these estimates are correct, then I estimate that the fault activity started later than 16 kyr.

Table 2.5: List of the features from the interpretation of Figure 4.8 and 4.9. The letters 'h', 'd', 'w' indicate the thickness, depth and width of the LVZs, respectively.

	Location	Features
F1	15 m	80 degrees
F2	35 m	80 degrees (possibly not exist)
F3	42 m	80 degrees (main fault)
F4	76 m	70 degrees (antithetic fault)
LVZ1	20-35 m	h= 5 m, d= 3 m, w= 15 m
LVZ2	50-65 m	h= 5 m, d= 7 m, w= 15 m
LVZ3	35-65 m	h= 2 m, d= 0 m, w= 30 m

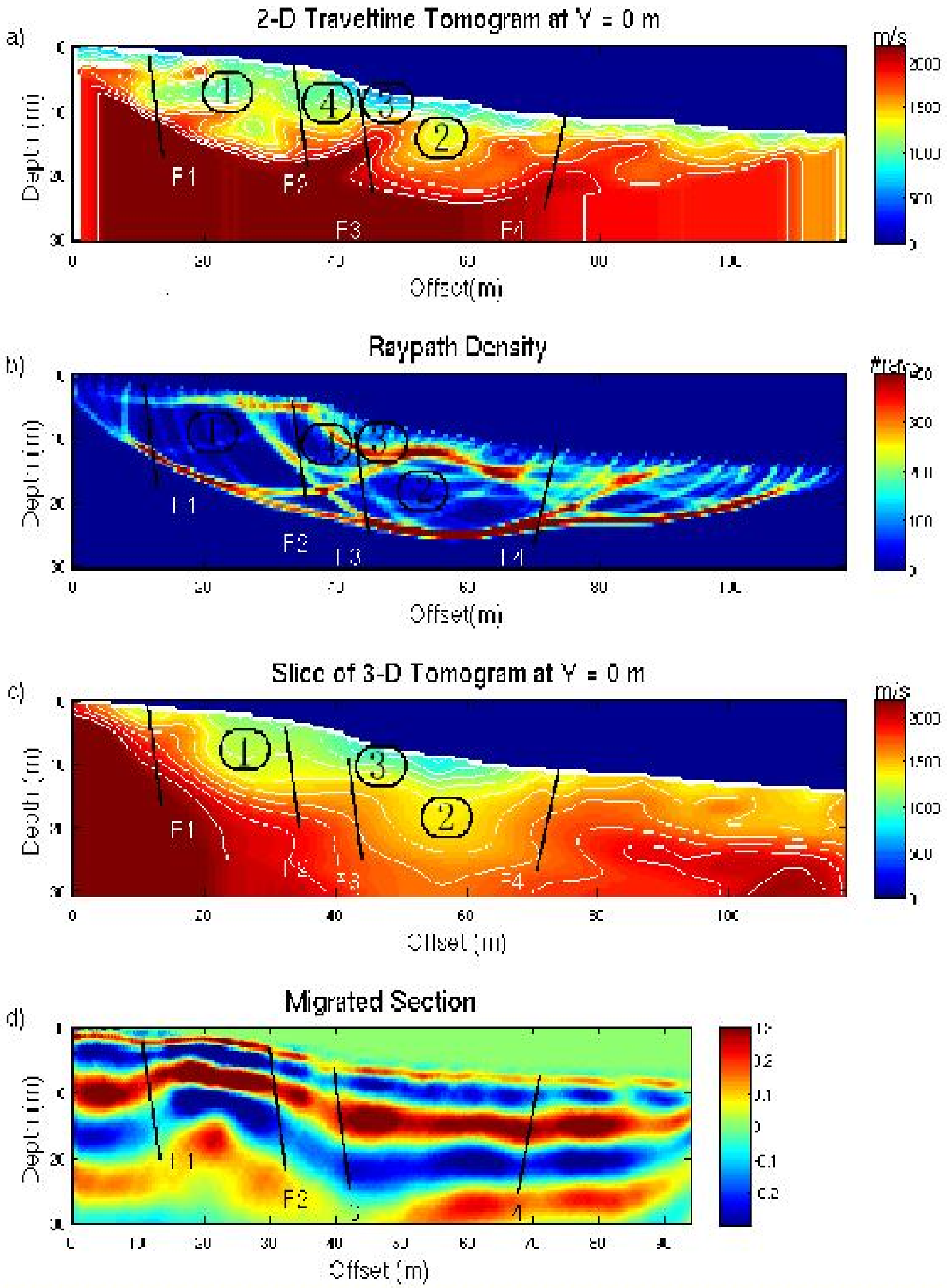

Figure 2.17: Summary of tomographic results and migration image, and interpretation.

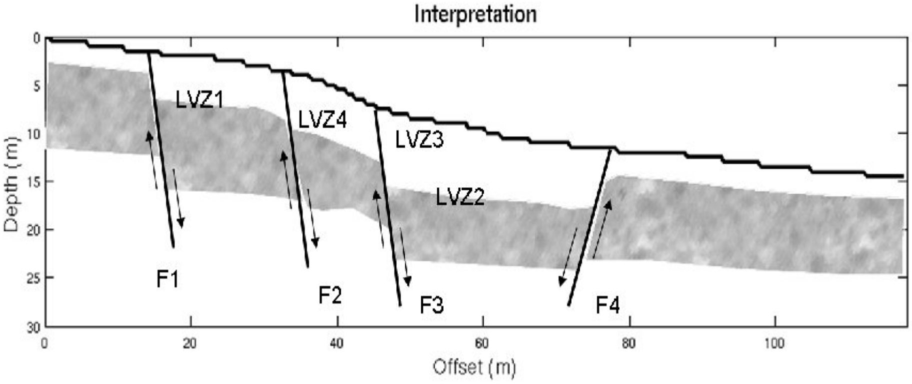

Figure 2.18: Final interpretation.

2.9 Summary

To demonstrate the ability of 3D tomography in imaging colluvial wedges, seismic experiments were conducted across the Washington fault with the goal of imaging the shape and location of colluvial wedges. The 3-D data consisted of 115,200 traces of which 85,450 traveltimes were picked and inverted to estimate the 3-D velocity structure of the Washington fault over a volume of 116 m x 7.5 m x 30 m. Reflectivity images from the 2-D seismic data provided information on the fault zone that was used, in conjunction with information from the 3-D tomogram, to estimate fault and colluvial wedge package locations associated with a prehistoric earthquake along the Washington fault.

The results of processing the 2-D and 3-D seismic surveys over the Washington fault show consistent images that appear to be faults and LVZs to a depth of about 30 m. From the 2-D and 3-D traveltime tomograms and the 2-D migration images, we can identify the following consistent features:

(1) Three LVZs (LVZ1, LVZ2 and LVZ3) are imaged with both 2-D and 3-D traveltime tomography.

(2) F3 is likely to be the main fault, which is consistent with geomorphology data, and F4 is the possible antithetic fault.

(3) The depth of the bedrock is estimated to be about 15 m, the velocity of which is larger than 2200 m/s.

(4) The four faults have an apparent dip of approximately 70-80 degrees.

(5) From the 3-D tomogram, the thickness of the LVZ1 and LVZ2 is about 5 m, and the thickness of LVZ3 is about 2 m.

(6) Combining the fault slip rate from paleoseismic data with the fault slip inferred by tomography, the age of the fault is estimated to be younger than 16 kyr.

I have demonstrated that seismic tomographic images can reveal the shape and depth of LVZs, which are possibly colluvial wedge packages associated with normal-fault earthquakes. This result is now used by UGS personnel to optimally design a trenching survey over this area. A much cheaper alternative is to drill into the LVZs to establish their identity, age, and the estimate the frequency of past earthquake occurrence. A future task is to compare the tomogram with the trench log (soon to be recorded by UGS in 2009), and analyze the accuracy of my interpretation.

Part IV

Migration Methods

Chapter 1

Overview of Exploration Seismology and Imaging

This chapter presents an overview of the basic goals and procedures for seismic exploration, and defines the seismic migration operation sometimes known as linearized seismic inversion. It is the main imaging tool for hydrocarbon mapping, and is increasingly being used for medical, earthquake, and engineering applications. We also review some fundamental mathematics associated with seismic imaging, such as the Fourier transform and convolution.

1.1 Exploration Seismology

The principal goal of exploration seismology is to map out oil and gas reservoirs by seismically imaging the earth's reflectivity distribution. Exploration geophysicists perform seismic experiments ideally equivalent to that shown in Figure 1.1, where the source excites seismic waves, and the resulting primary reflections are recorded by a geophone located at the source position. For this ideal zero-offset (ZO) experiment we assume only primary reflections in the records and that waves only travel in the vertical direction.

After recording at one location, the source and receiver are laterally moved by about 1/2 source wavelength and the experiment is iteratively repeated at different ground positions. All recorded traces are lined up next to one another and the resulting section is defined as the zero-offset (ZO) or poststack seismic section, as shown by the traces in Figure 1.1. This section resembles the actual geology, where one side of the signal is colored black to help enhance visual identification of the interface. Note that the depth z of the first reflector can be calculated by multiplying the 2-way reflection time t by half the P-wave velocity v of the first layer, i.e. $z = tv/2$.

Seismic images of the subsurface are used to understand the geology of the earth. For example, Figure 1.2 shows both optical and seismic pictures of faults[1]. These images provide an understanding of the fault's characteristics and so aid geologists in deciphering the

---

[1] Faults are high angle planar breaks in the subsurface rock. Rocks on one side of the fault slide apart from the rocks on the other side. If this sliding is mostly along the vertical direction then this is a normal fault as shown in Figure 1.2; if the sliding is along the horizontal direction then this is a transverse fault.

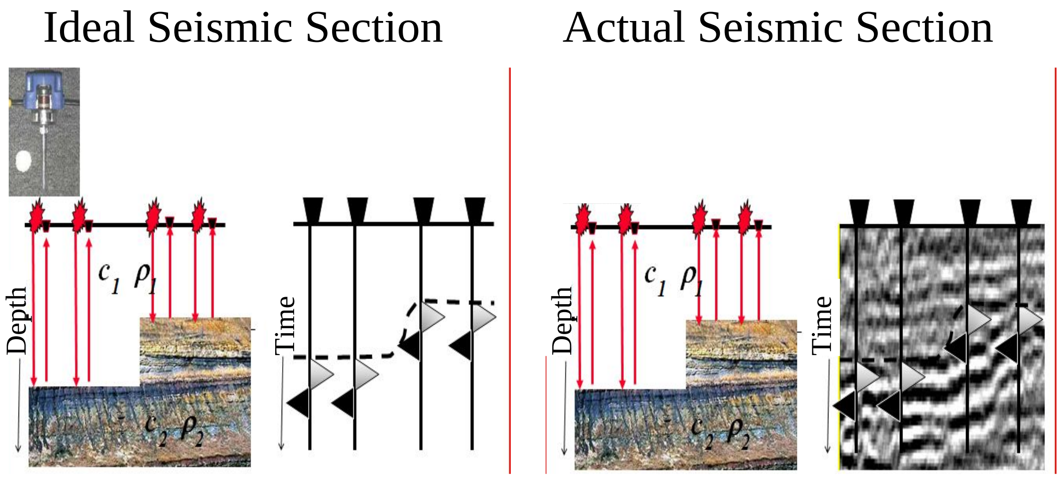

Figure 1.1: Earth model and idealized zero-offset (ZO) seismic section in time. Each trace is recorded by a geophone coincident with the source position; and the light (dark) colored amplitudes correspond to the particle velocity of the ground in the upward (downward) direction. The background image on the far right is an actual seismic section.

tectonic forces that shaped the earth. Faults also serve as impermeable traps for oil and gas deposits, waiting to be found by the explorationist with the most capable seismic camera. Other views of the earth using seismic data are shown in Figure 1.3.

1.1.1 Seismic sources

A land seismic source consists of a mechanical device or explosive located at $\mathbf{s}$ that thumps the earth (see Figure 1.4a) at time $t = 0$, and a geophone (see Figure 1.4b) at $\mathbf{g}$ records the time history of the earth's vertical particle velocity; the resulting seismogram is denoted as a seismic trace $d(\mathbf{g}, t|\mathbf{s}, 0)$. A marine source is usually an array of air guns. Larger amplitudes on the Figure 1.1 traces correspond to a faster particle velocity and the up-going (down-going) motion is denoted here by the unblackened (blackened) lobes. The lobe amplitude is roughly proportional to the reflectivity strength $m(\mathbf{x})$ of the corresponding reflector at $\mathbf{x} = (x, y, z)$. Assuming a constant density and a layered medium, the normal-incidence reflectivity model $m(\mathbf{x})$ is sometimes approximated as

$$m(\mathbf{x}) \quad = \quad \frac{v(z+dz)-v(z)}{v(z+dz)+v(z)} \approx \frac{1}{v(z)}\frac{dv(z)}{dz}, \tag{1.1}$$

where $v(z)$ is the P-wave propagation velocity at depth z and the depth interval $0.5dz$ is normalized to the value 1.

1.1.2 Non-zero offset seismic experiment

In practice, a ZO experiment cannot generate the ideal seismic section because the source also generates strong coherent noise and near-source scattering energy that drowns out

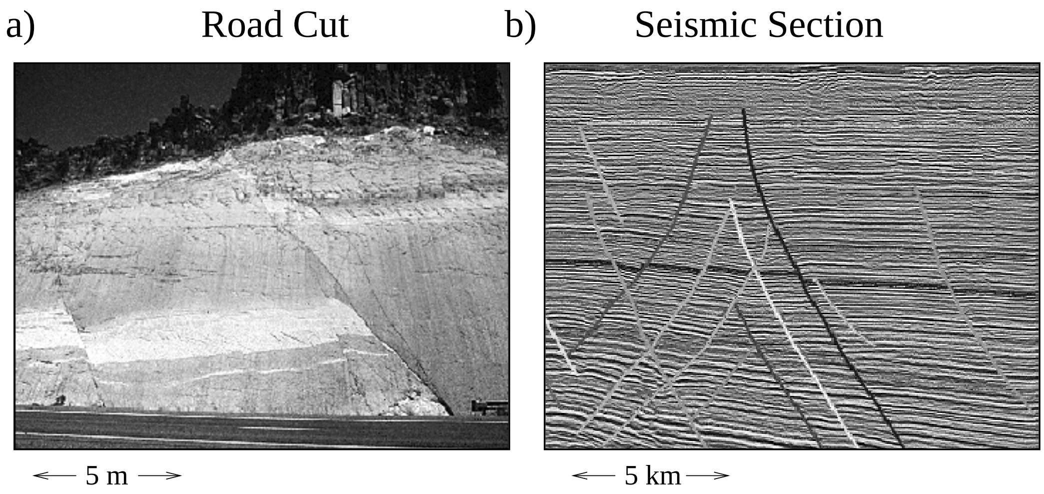

Figure 1.2: Geologic faults revealed by a) road cut and b) marine seismic section. The length scales above are roughly estimated.

the weak reflections. In addition, the waves are propagating in all directions and contain distracting noise such as multiples, surface waves, scattered arrivals, out-of-the plane reflections, and converted waves. To account for these complexities, geophysicists perform non-zero offset experiments where the vibrations are recorded by many receivers as shown in Figure 1.5b. As before, each experiment consists of a shot at a different location except hundreds of active receivers are spread out over a long line for a 2D survey and a large area for a 3D survey[2].

1.1.3 Seismic processing

For surveys over a mostly layered medium, data processing consists of the following steps: 1). filtering of noise and near-surface statics corrections, 2). reassembly of common shot gather (CSG) traces in Figure 1.6a into common midpoint gathers (CMG) in Figure 1.6b where the source-receiver pair of each trace has the same midpoint location, 3). the traces in the CMG are time shifted to align the CMP reflections with the ZO reflection event in Figure 1.6c, 4) stack the traces in the time-shifted CMG to form a single trace (see Figure 1.6d) at the common midpoint position[3]. This stacked trace approximates a ZO trace with a high signal-to-noise at that position, and 5). repeat steps 3-4 for all midpoint gathers to give the seismic section shown in Figure 1.7. If the subsurface reflectivity is complex then steps 2-5 are skipped and instead the algorithm known as *seismic migration* is used, which is the subject of this book.

---

[2] Some surveys activate anywhere from 3,000 to 10,000 receivers per shot.

[3] The ensemble of traces from a surface seismic experiment is also known as surface seismic profile (SSP).

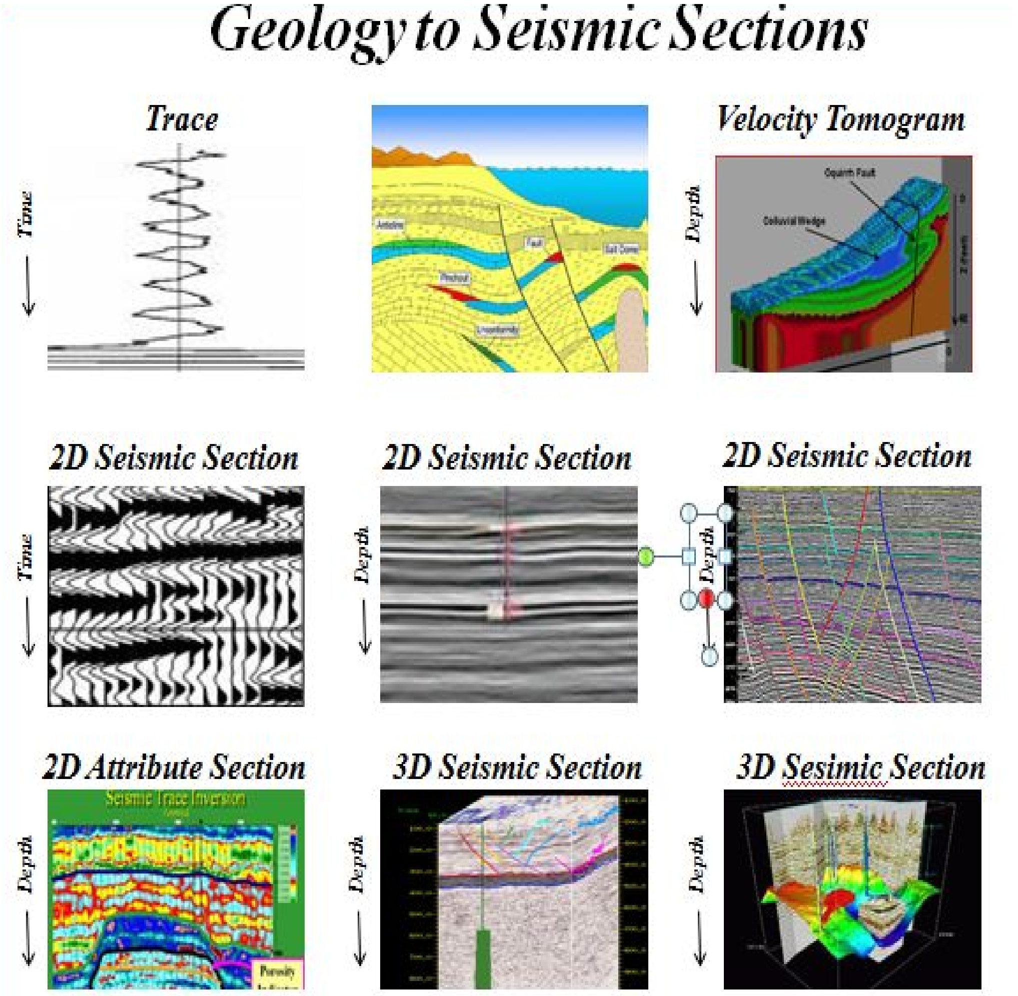

Figure 1.3: Different views of the earth extracted from seismic data. The single trace on the top left is the basic element of seismic recording, and after certain operations an ensemble of such traces can be transformed, e.g., into the 3D migration cube in the lower right or inverted to give the 3D velocity tomogram in the upper right.

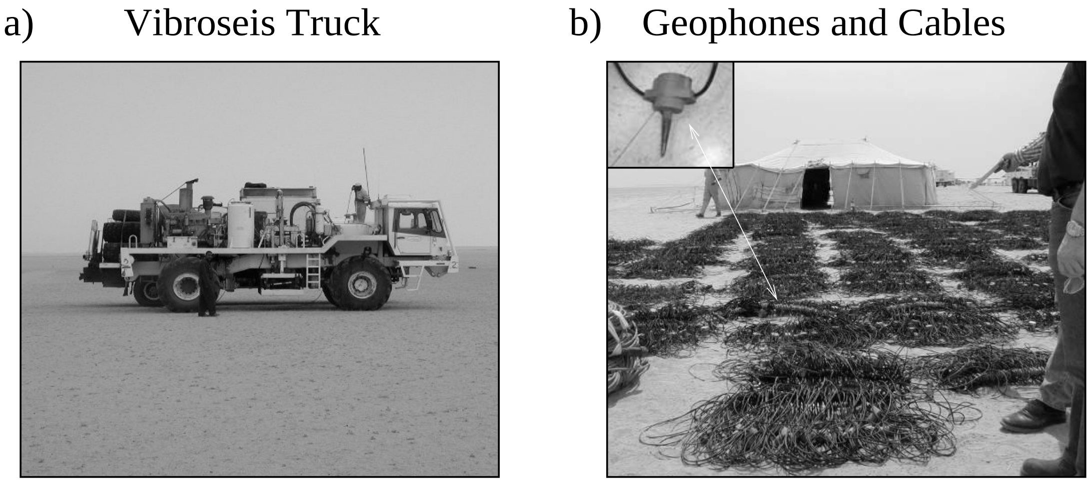

Figure 1.4: a) Vibroseis truck and b) geophones attached to cables at a desert base camp. Inset is a particle velocity geophone about 12 cm long.

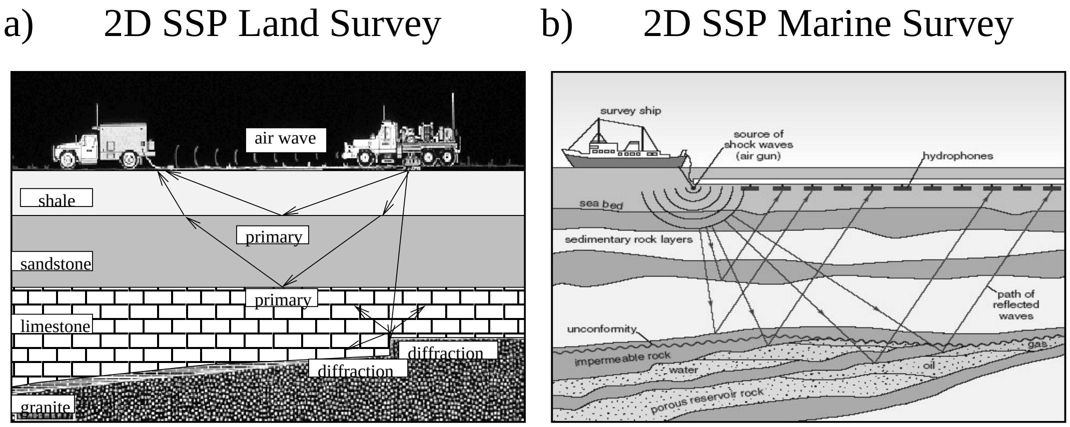

Figure 1.5: a) Land (courtesy of ConocoPhillips) and b) marine (courtesy of openlearn.open.ac.uk) survey geometries to record surface seismic profiles. The hydrophone cable for a marine survey can be as long as 12 km with a 30 m hydrophone spacing.

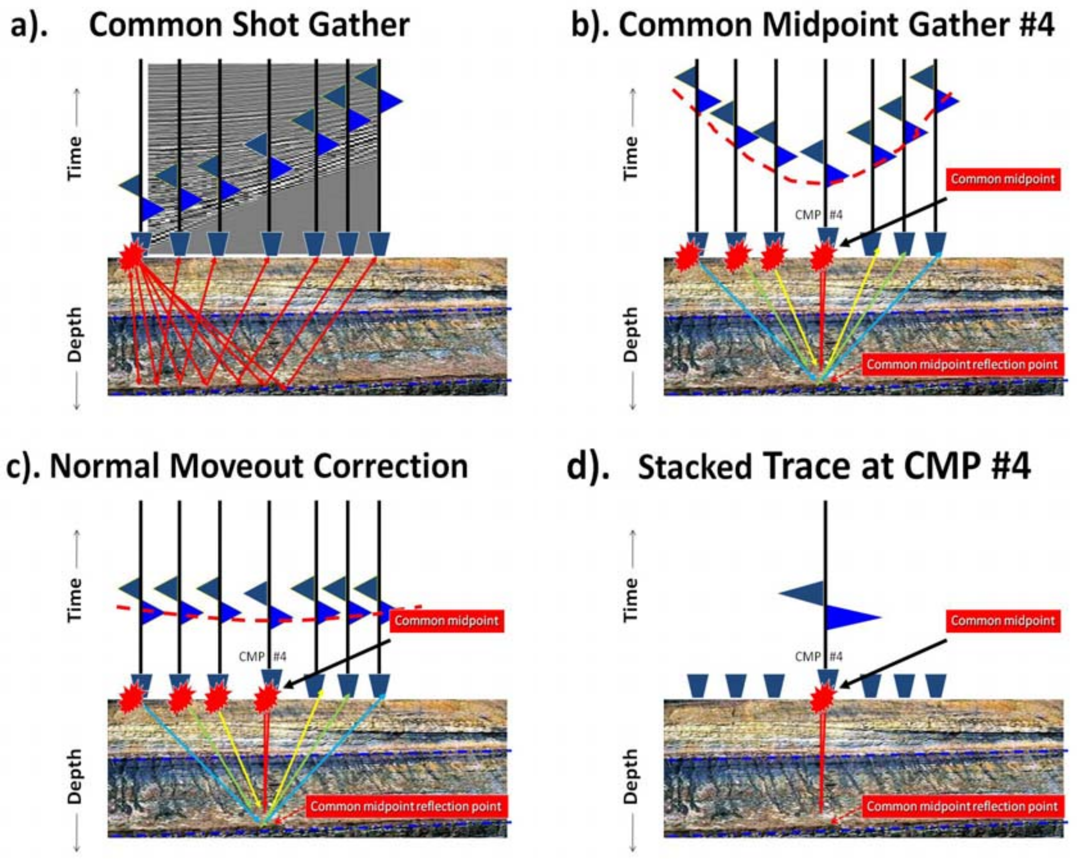

a). Common Shot Gather

b). Common Midpoint Gather #4

c). Normal Moveout Correction

d). Stacked Trace at CMP #4

Figure 1.6: Different types of seismic trace formats. a). common shot gather where a single source is recorded by all of the geophones to form a CSG of traces. b). The traces from many CSGs can be reassembled to form a common midpoint gather (CMG) where a trace associated with each source-receiver pair has the same midpoint position on the surface. The common subsurface reflection point is known as the common reflection point; if the interface is dipping then rays associated with traces in the same CMG do not share a common reflection point. c). Traces after time shifting the CMP traces to align with the zero-offset trace; this time shifting is known as the normal moveout offset correction or NMO. d). The stacked trace is formed by adding the NMO corrected traces. In this case the fold is 7 and the signal/noise is enhanced by a factor of $\sqrt{7}$ if there is additive white noise in the CMG seismograms.

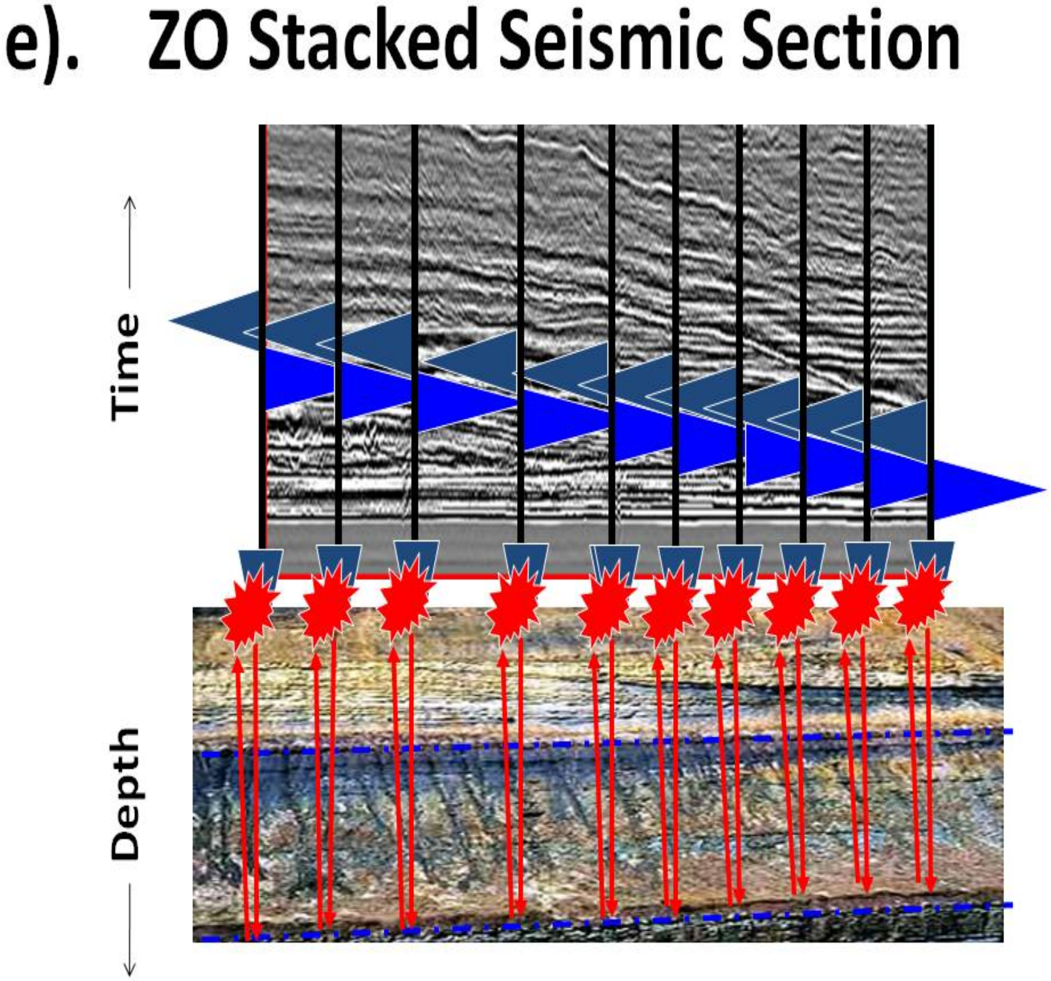

Figure 1.7: Diagram of stacked seismic section with background of an actual stacked seismic section.

1.2 Seismic Migration

For horizontal layers with homogeneous velocity, zero-offset seismic reflections will originate from reflection points directly beneath the geophone as shown in Figure 1.1. In this way the seismic section in time bears an accurate resemblance to the actual interface geometry in the subsurface If the subsurface model strongly violates the layer assumption, then interpretation of the seismic section will be inaccurate. The solution then is to apply migration to the data. Here, *migration is defined as the process which takes the seismic section $d(x, y, t)$ and moves the reflection events back to their origin at the interfaces.* Mathematically, migration maps the data $d(x, y, t)$ into the reflectivity distribution $m(x, y, z)$, denoted as the migration image.

Some departures from a layered model include the following examples.

1. **Dipping layers.** If the interfaces are dipping, as shown in Figure 1.8, then the dip of the seismic section can be noticeably different than the actual dip of the layer interface. Even if the time section were converted to depth z by a $z = v{*}t/2$ correction (where v is the homogeneous velocity of the medium and t is the 2-way time of the reflection event) the apparent dip in the seismic section would still be incorrect. The problem is that the reflection recorded in the trace is assumed to emanate from the interface point directly beneath the ZO geophone, which is an incorrect assumption if the reflector is dipping[4].

2. **Diffractions.** Another problem is that the subsurface interface might change its shape very rapidly with respect to the wavelength, and so strong diffraction energy can emanate from the distorted zone without having to honor Snell's law. An example is the faulted interface in Figure 1.9 that abruptly changes its tangent angle. This abrupt change in angle results in strong scattered energy that appears as a diffraction frown in the Figure 1.9 seismic section. This seismic section can then be incorrectly interpreted as indicating a false dome-like structure in the subsurface. *In this case migration moves the diffraction energy back to its origin at the diffractor point.* A synthetic example that clearly shows the uncollapsed diffraction frowns in the ZO section is shown in Figure 1.10, which are collapsed to points along the fault (dashed white line) in the migration image.

3. **Out-of-plane reflections.** Reflection events can originate outside the vertical plane coincident with the line of sources and receivers. These *out-of-plane reflections* will appear in the seismic section as coming from within the vertical plane, which can lead to falsely interpreted structures in the 2D seismic section. Hence, 3D migration must be applied to the data to map it into the correct reflectivity distribution.

4. **Conflicting dips.** If the geology is complicated then more than one type of reflection event may arrive at nearly the same time, but will be associated with different dip angles in $x - t$ space as shown in Figure 1.10. These dip angles differ from one

---

[4] According to the Snell's law, the transmission and reflection rays must be parallel to one another for a ZO ray, and so they must be perpendicular to the interface at the specular reflection point. This means that, e.g. in a dipping layer model, the ZO green ray in Figure 1.8 is tilted to the left of the geophone rather than being vertical.

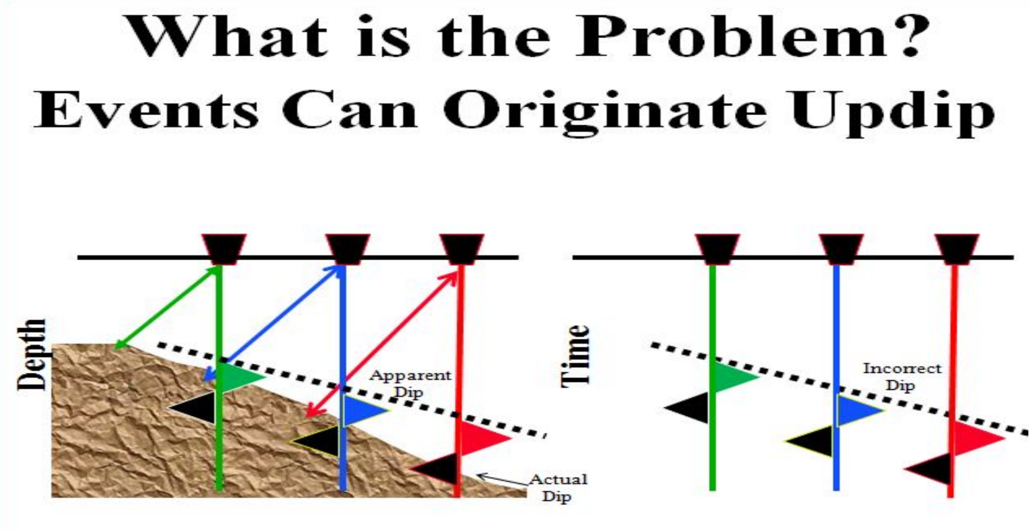

Figure 1.8: Zero-offset (ZO) reflections originate from reflection points updip from the recording geophone. Hence, the resulting seismic section appears to have a shallower dip than the actual seismic section. Two-sided arrows indicate raypaths for the ZO primary reflection events. Also, the migrated section will have a shorter reflector then the one interpreted in the seismic section.

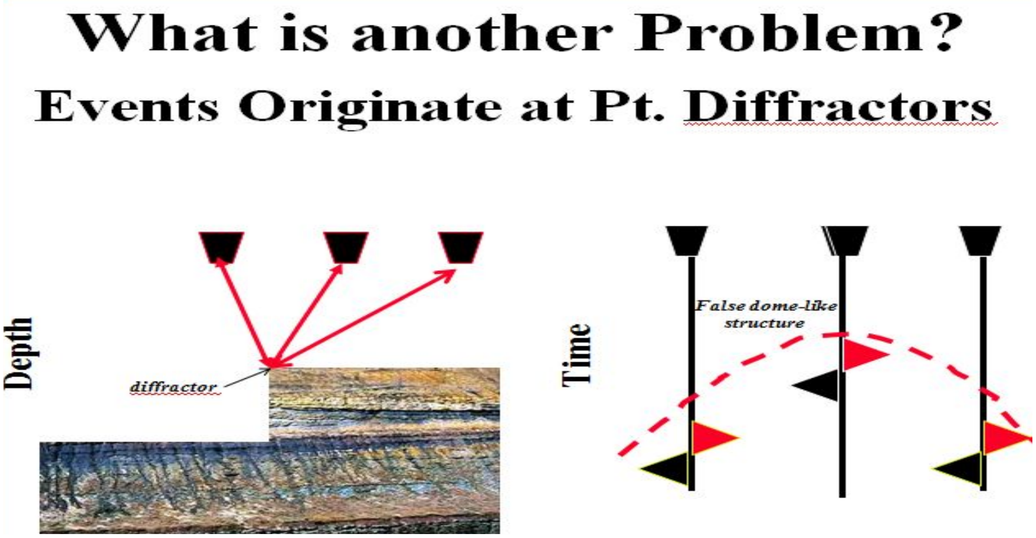

Figure 1.9: Reflectivity models with diffractors produce diffractions that appear as frowns in the seismic section, and can lead to falsely interpreted sections.

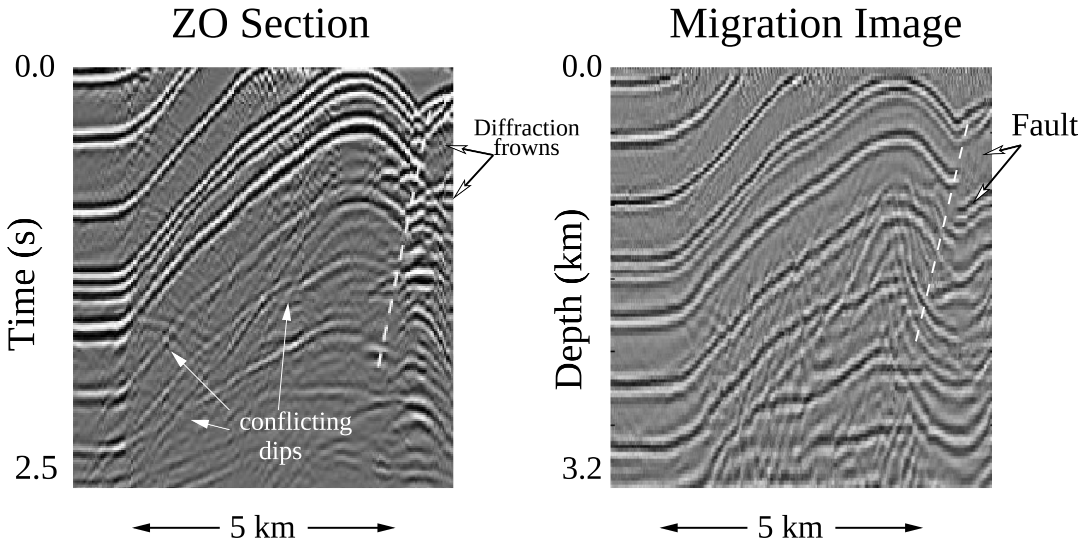

Figure 1.10: (Left) ZO section and (right) migration image of a faulted anticline model. Note, the fault denoted by dashed white lines is characterized by diffraction frowns in the ZO section; also, the dip of the right flank of the anticline is steeper in the migration image than in the ZO section. The conflicting dips seen in the ZO section are mostly eliminated in the migration image.

another because the associated reflections originate from different interfaces, each with a different dip angle in $x - y - z$ space.

Since stacking only assigns one moveout correction curve to each zero-offset time in a CMG, only type of the reflection events will be coherently stacked and the other will be inappropriately ignored. In this case, prestack migration should be used rather than conventional NMO and stacking.

1.2.1 Hand migration

A simple example of migrating traces by hand is described by the following three steps illustrated in Figures 1.11- 1.12.

1. In Figure 1.11a the lone reflection event in the single ZO trace is smeared back into the medium along a circle with radius equal to half the two-way reflectime time. Energy is also smeared within the annulus of width $T_0/2$ to account for the bandlimited source wavelet with period T_0. A point scatterer anywhere within this annulus could have accounted for some of the reflection energy in the single trace.

2. To determine more precisely the location of the reflector, a second trace is migrated (i.e., energy is smeared along the second fat circle in Figure 1.11b) and the intersection of these two annulus' pinpoints the scatterer location that can account for the events in both traces. Mathematically this intersection zone is delineated by summing the two traces and identifying the zone of strongest summed amplitudes.

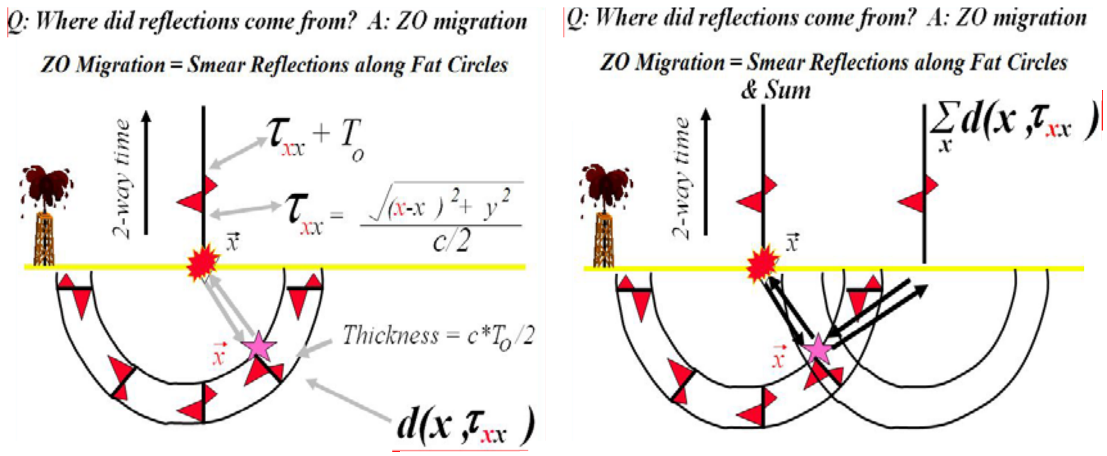

Figure 1.11: Migration images formed from (left) one and (right) two traces.

3. The previous step is repeated for many ZO traces to give the final poststack migration section shown in Figure 1.12.

1.2.2 Key problem with migration images

A *key difficulty in obtaining an accurate migration image is the estimation of a sufficiently accurate velocity model.* An inaccurate velocity model will lead to defocused and sometimes unusable migration images. In this case, the data must be used to estimate not just the reflectivity model but also the migration velocity model. A common velocity model updating method is called traveltime tomography, which uses as input the traveltimes of either reflections or refractions in the data and inverts them for the velocity distribution as a function of (x, y, z). The upper right picture in Figure 1.3 depicts a velocity tomogram estimated by inverting refraction traveltimes[5]. A more expensive and complicated means for updating the velocity model is by full wavefield inversion, which is briefly discussed in the next section.

1.2.3 Algebraic description of migration

We are now ready to represent the seismic imaging operation in terms of matrix-vector algebra. The seismic trace (see upper left image in Figure 1.3) can be represented with the notation $d(\mathbf{g}, t|\mathbf{s}, 0)$, where $\mathbf{g}$ denotes the geophone location and $\mathbf{s}$ denotes the location of the source excited at time zero. Typically the trace might be about 10^3 samples long and so can be represented as a 10^3x1 vector. But many traces can be collected for thousands of different source and receiver positions. For example, an experiment with 10^4 shot positions, where 10^3 receivers record traces for each shot, gives rise to 10^7 traces, each with 10^3 samples. If these trace vectors are sequentially aligned on top of one other into a composite data vector then the input data can be denoted by the $10^{10}x1$ vector $\mathbf{d}$.

---

[5] Hotter colors in this case correspond to faster velocities.

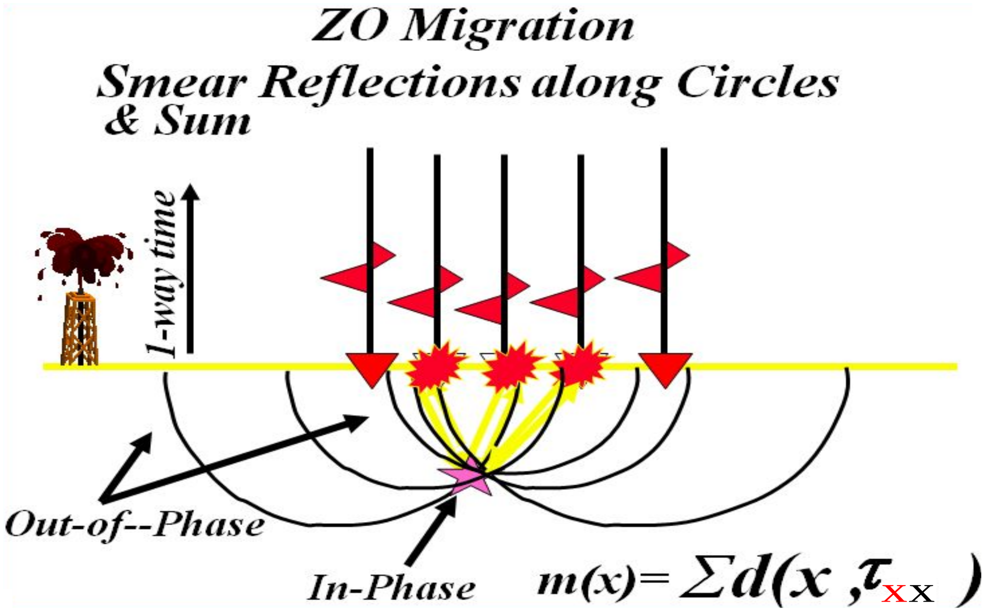

Figure 1.12: Migration image formed from many traces.

Similiarly, the reflectivity distribution can be approximated on a, for example, $10^3x10^3x10^3$ grid and reassembled as a 10^9x1 reflectivity vector $\mathbf{m}$. The mathematical operation $\mathbf{L}$ of forward modeling uses the input earth's reflectivity distribution as $\mathbf{m}$ to give the data $\mathbf{d}$, i.e.,

$$\mathbf{d} \quad = \quad \mathbf{L}(\mathbf{m}), \tag{1.2}$$

so in our example, $\mathbf{L}$ must be a $10^{10}x10^9$ matrix. Mother earth implicitly represents the forward modeling operation $\mathbf{L}$ as exact solutions to the anisotropic poro-viscoelastic wave equation, and so the actual seismic data can be very expensive to model in today's computers. To avoid this expense and only model the important primary reflections, the explorationist typically *assumes that the data are acoustic*, and so approximates $\mathbf{L}$ by solutions to the acoustic wave equation. This approximation was adequate for most processing in the 20th century, although taking into account anisotropic effects is becoming increasingly important if we wish to achieve more accurate images.

As we saw in the previous section, the seismic section $\mathbf{d}$ (e.g., ZO section in Figure 1.10) is not an accurate representation of the reflectivity distribution for complicated earth models. To estimate the actual reflectivity distribution, we migrate the reflection events to their place of origin along the interfaces. Mathematically, this is done by assuming a linearity approximation so equation 1.2 becomes $\mathbf{d} = \mathbf{Lm}$, and then solve it by finding the least squares solution:

$$\mathbf{m} \quad = \quad \overbrace{[\mathbf{L^TL}]^{-1}\mathbf{L^T}\mathbf{d},}^{least\ squares\ migration} \tag{1.3}$$

where $\mathbf{L^T}$ is the adjoint of the forward modeling operator. In this case we implicitly assume that we know how to compute the adjoint of the actual forward modeling operation of mother earth[6]. The above equation describes the *least squares migration* algorithm (Nemeth et al., 1998) and is carried out using a regularized conjugate gradient algorithm.

If the normal equation matrix $[\mathbf{L^T L}]$ is diagonally dominant, then the $[\mathbf{L^T L}]^{-1}$ can be approximated by a weighted diagonal matrix to get the *compensated illumination migration* equation:

$$\mathbf{m} \;\approx\; \overbrace{\mathbf{C L^T d}}^{migration}\,, \tag{1.4}$$

where the illumination compensation matrix $\mathbf{C}$ is a diagonal matrix with components $\mathbf{C}_{ij} = \delta_{ij}/[\mathbf{L^T L}]_{ii}$. Here $\mathbf{C}_{ij}$ compensates primarily for weakening of the signal due to geometric spreading in the reflected field and δ_{ij} is the Kronecker delta function that is equal to one if $i = j$, otherwise it is zero.

The above equations assume that $\mathbf{L}$ is independent of the reflectivity structure and only depends on the accurate smooth background velocity model; this means that the resulting forward modeling and inverse modeling equations are linear. If the background velocity is not accurately known and the reflectivity model contains large reflection coefficient values[7], then we should seek iterative updates to the velocity model. Such updates can be inexpensively obtained by traveltime tomography, or more accurately by the expensive means of waveform inversion. Due to the relentless increase in computational capabilities, it is now becoming possible to update the background velocity model in this way. The most common means for doing this is by an iterative non-linear gradient formula known as full wavefield inversion:

$$\mathbf{m}^{(k+1)} \;=\; \mathbf{m}^{(k)} + \overbrace{[\mathbf{L}^T_{(k)}\mathbf{L}_{(k)}]^{-1}\mathbf{L}^T_{(k)}\mathbf{d}^{(k)}}^{full-wave\ inversion}, \tag{1.5}$$

where $\mathbf{d}^{(k)}$ represents the data residual[8] at the k^{th} iteration and $\mathbf{m}^{(k)}$ represents the velocity model at the k^{th} iteration. The modeling $\mathbf{L}_{(k)}$ and adjoint $\mathbf{L}^T_{(k)}$ operators depend on the iteration index because they are both updated with the new velocity model at each iteration. *Full wave inversion can be described as an iterative sequence of migrations, where the data residuals updated and migrated at each iteration to give the new model update. Moreover,* $\mathbf{L}$ *is updated at each iteration.*

Full wavefield inversion is a broad subject that will not be covered much in this book. Instead we we will mostly concentrate on showing the many ways of applying the adjoint approximation in equation 1.4 to seismic data, otherwise known as seismic migration. It is method that is used for the vast majority of seismic processing today, and so we will concentrate on its most popular implementations.

---

[6] We never know how to do this exactly because 1). it is too expensive and 2). we do not know the rock parameters with high precision.

[7] Reflection coefficients with absolute values much larger than 0.05 cause problems in the validity of the Born approximation, which will be discussed in later chapters.

[8] The data residual is computed by taking the difference between the observed seismic trace vector and the predicted trace vector. The predicted traces are obtained by forward modeling synthetic seismograms for the k^{th} velocity model.

1.3 Summary

This chapter describes the goals and key procedures of seismic exploration, where seismic data are collected and the goal is to invert it for the subsurface reflectivity and velocity distributions. In the early days of exploration (1960s) the ZO seismic section was mostly used to deduce the subsurface reflectivity structure, with the understanding that the interpreted geology became increasingly erroneous with increasing complexity in the subsurface geology. Some examples of complicated geology include dipping layers that produce conflicting dips, sharp changes in impedance that cause diffractions, and 3D geology that produces out-of-plane reflections. The remedy to these problems is to avoid NMO corrections and stacking, and directly map the primary reflections recorded in (x, y, t) data space onto their origin at the reflecting interfaces in (x, y, z) model space; this procedure is known today as migration and widely practiced since the 1960s. Migration should almost always be applied to prestack data. If the smooth background velocity model is well known, migration applies the adjoint operator $\mathbf{L}^T$ to the data $\mathbf{d}$ to get an estimate of the reflectivity distribution $\mathbf{m}$. This and accurate estimation of velocity models are the keystone tools for mapping oil and gas deposits by every oil company in the world today. The detailed study of seismic migration methods is the primary focus of this book.

1.4 Exercises

1. Appendix 1 defines the forward and inverse Fourier transforms as

$$F(\omega) \quad = \mathcal{F}[f(t)] = \frac{1}{2\pi}\int_{-\infty}^{\infty} f(t)e^{i\omega t}dt, \tag{1.6}$$

$$f(t) \quad = \mathcal{F}^{-1}[F(\omega)] = \int_{-\infty}^{\infty} F(\omega)e^{-i\omega t}d\omega. \tag{1.7}$$

   Show that $cos(\omega\tau) = [e^{i\omega\tau} + e^{-i\omega\tau}]/2$ has an inverse Fourier transform equal to $\pi\delta(t+\tau) + \pi\delta(t-\tau)$, where $\int e^{i\omega(t-\tau)}d\omega = 2\pi\delta(t-\tau)$.

2. The discrete convolution of the real N-point vectors $\mathbf{f} = [f[0]\ f[1]\ ...f[N-1]]$ and $\mathbf{g} = [g[0]\ g[1]...g[N-1]]$ is given by

$$h[i] \quad = \quad \sum_{i'=0}^{N-1} f[i-i']g[i'] = \sum_{i'=0}^{N-1} f[i']g[i-i']. \tag{1.8}$$

   The argument values refer to the time values of each element. Validate the above expression by computing the time series $h[t]$ for $\mathbf{f} = [1\ -2]$ and $\mathbf{g} = [-1\ 3]$.

3. The discrete correlation of two N-point vectors is given by

$$h[i] \quad = \quad \sum_{i'=0}^{N-1} f[i'-i]g[i'] = \sum_{i'=0}^{N-1} f[i']g[i+i'], \tag{1.9}$$

where the coefficients are assumed to be real. Compute the time series $h[t]$ for $\mathbf{f} = [1\ -2]$ and $\mathbf{g} = [0\ 1]$ and validate this equation (assume the elements in each vector are ordered from time zero for the 1st element and have increasing time indices for the other elements). Does the filter $\mathbf{g}$ shift $\mathbf{f}$ forward or backward in time?

4. For $f(t) = \delta(t-2) + \delta(t-4)$ and $g(t) = \delta(t-1)$, find $f(t) \otimes g(t)$ and $g(t) \otimes f(t)$. Is the cross-correlation operation commutative, i.e., is $f(t) \otimes g(t) = g(t) \otimes f(t)$?

5. Is convolution commutative? Mathematically prove your answer and test it in MATLAB.

```
f=[1 0 0 0 -2 0 0 0 0 4];
g=[0 0 -2 0 0 0 0 0 0 0];
h=conv(f,g);subplot(121);stem(h)
h=conv(g,f);subplot(122);stem(h)
```

   Convolution of two M-length vectors produces a $2M-1$ length vector. Which is the zero-lag position in the MATLAB plot? The procedure for plotting the correct time axis labels is demonstrated in the next exercise.

6. The cross-correlation operation is equivalent to a reversed time convolution, i.e., $f(t) \otimes g(t) = f(-t) \star g(t)$ (see Appendix 1). The MATLAB program for cross-correlating two length M vectors $f(t)$ and $g(t)$ is

```
f=[1 0 0 0 -2 0 0 0 0 4];
g=[0 0 -2 0 0 0 0 0 0 0];M=length(g);
h=xcorr(f,g);
TMm1=length(h);
t=[1:TMm1];t=t-M;stem(t,h);
```

   The result is a $2M-1$ length vector where the amplitude at lag zero is at the Mth element. Is this equal to $f(-t) \star g(t)$

```
h=conv(fliplr(f),g);subplot(121);stem(h)
```

   or $g(-t) \star f(t)$?

```
h=conv(fliplr(g),f);subplot(122);stem(h)
```

   Note that $fliplr(g)$ reverses the order of the vector g.

7. To create synthetic seismograms geophysicists often use a Ricker wavelet (Yilmaz, 2001) as their source wavelet. The formula in MATLAB script is given as

```
np=100;fr=20;dt=.001;
npt=np*dt;t=(-npt/2):dt:npt/2;
out=(1-t .*t * fr^2 *pi^2  ) .*exp(- t.^2 * pi^2 * fr^2 ) ;
plot(t,out);xlabel('Time (s)')
```

   where (np, fr, dt) are equal to the number of samples, peak frequency (Hz), and time interval dt in seconds. The operation $t = (-npt/2) : dt : npt/2$ creates a vector of time units from time $-npt/2$ to $npt/2$, sampled at the time interval of dt. Plot out this wavelet using the above script except adjust the plotting code so the time units are in seconds, not samples. Repeat this exercise except choose (np, fr) so that a 5 Hz Ricker wavelet is plotted.

8. The Ricker wavelet from the previous question is acausal if there are non-zero amplitudes prior to $t = 0$. Implement a time shift to make it causal and plot it. One can create a subroutine by the following command

```
function [rick]=ricker(np,dt,fr)
% Computes acausal\index{acausal} Ricker wavelet\index{Ricker wavelet} with peak frequency fr
% sampled at dt with a total of np points. Make
% sure you choose np to be longer than T/dt , where
% T=1/fr.
npt=np*dt;t=(-npt/2):dt:npt/2;
rick=(1-t .*t * fr^2 *pi^2  ) .*exp(- t.^2 * pi^2 * fr^2 ) ;
z=rick(np/2:np);
%rick=rick*0;rick(1:np/2+1)=z;% Causal\index{causal} 1/2 Ricker
```

   and typing $np = 100; dt = .002; fr = 20; rick = ricker(np, dt, fr)$ to create a vector $rick$ that represents a Ricker wavelet with a peak frequency of 20 Hz.

9. A two-layer velocity model consists of a 500 m thick layer with velocity v_1 =1 km/s and an underlying layer of velocity v_2 =2 km/s; here density is assigned a unit value everywhere and the top interface is a free surface. For a zero-offset acquisition geometry with source and receiver at **A** just below the free surface, the synthetic seismogram that contains only a primary reflection is given by $s(t) = r\delta(t - \tau_{AyA})$, where the reflection coefficient is $r = (v_2 - v_1)/(v_2 + v_1)$ and τ_{AyA} is the two-way normal incidence reflection time for a source at **A** and reflection point at **y**. For a sampling interval of 0.001 s, plot the impulse $I(t)$ response that only consists of primaries and upgoing waves. Use MATLAB to plot the response of a Ricker wavelet that only consists of primaries. That is, if the impulse response and Ricker wavelet are respectively defined in MATLAB by the vectors I and R then the Ricker response is given by

```
s=conv(I,R);plot(s);
```

10. A more elaborate modeling program for a 2-layer model that generates the primary reflection, and the 1st- and 2nd-order multiples is given by

```
function [seismo,ntime]=forward(v1,v2,dx,nx,d,dt,np,rick,x)
% (v1,v2,d) -input- velocity of 1st & 2nd layer of thickness d
% (dx,nx,dt)-input- (phone interval, # of phones, time interval)
% (np,rick) -input- (# of samples Ricker, Ricker wavelet)
%  x        -input- Nx1 vector of x values of  phone at z=0
%seismo(i,j,k)-output- Shot gather at ith src, jth phone, kth time
r=(v2-v1)/(v2+v1);r1=r*r;r2=r1*r;
for ixs=1:nx  % Loop over sources
  xs=(ixs-1)*dx;
  t=round(sqrt((xs-x).^2+(2*d)^2)/v1/dt)+1;  %Primary Time
  t1=round(sqrt((xs-x).^2+(4*d)^2)/v1/dt)+1; %1st Multiple Time
  t2=round(sqrt((xs-x).^2+(6*d)^2)/v1/dt)+1; %2nd Multiple Time
if ixs==1; ntime=max(t2)+np; seismo=zeros(nx,nx,ntime); end;
  s=zeros(nx,ntime);
 for i=1:nx; % Loop over  receivers
   s(i,round(t(i)))=r/t(i);   %Primary
   s(i,round(t1(i)))=-r1/t1(i); % 1st-order Multiple
   s(i,round(t2(i)))=r2/t2(i); % 2nd-order Multiple
   ss=conv(s(i,:),rick); % Convolve Ricker & Trace
   s(i,:)=ss(1:ntime);   % Synthetic Seismograms
   seismo(ixs,i,1:ntime)=ss(1:ntime);
 end
```

```
  c=seismo(ixs,:,:);c=reshape(c,nx,ntime);
  imagesc([1:nx]*dx,[1:ntime]*dt,c');xlabel('X(km)');ylabel('Time (s)')
  title('Shot Gather for Two-Layer Model'); pause(.1)
end
```

Run this program to generate synthetic seismograms for a two-layer model. Adjust the frequency content of the Ricker wavelet. If the Nyquist sampling criterion says that you need more than two samples per period, how should you adjust dt as you increase the wavelet frequency fr? How should you adjust dx as you decrease the velocity of the 1st layer $v1$, where wavelength is $v1/fr$?

11. Generate seismograms s that only contain primary reflections; convolve s with s to generate the 1st-order free-surface multiple. Does it have the correct arrival time for a 1st-order multiple? Does it have the correct magnitude for the reflection coefficient?

12. This is the same question as the previous one, except generate the 2nd-order free-surface multiple by two sequential convolutions of the primary trace.

13. The free-surface reflection coefficient for an incident pressure field is -1. What adjustment should you make to the previous convolutions in order to correctly model the polarity of the reflections?

14. In MATLAB, use $forward.m$ in problem 10 to generate the synthetic seismograms that contain the direct wave, primary and free-surface multiples up to the 2nd order. Assume a 20-Hz Ricker wavelet for the source time history and a two-later model. Write down the mathematical expression for this seismogram in terms of delta functions.

Appendix 1: Fourier Identities

The forward and inverse Fourier transforms are respectively given by (Bracewell, 2000)

$$F(\omega) \quad = \mathcal{F}[f(t)] = \quad \frac{1}{2\pi}\int_{-\infty}^{\infty} f(t)e^{i\omega t}dt, \tag{1.10}$$

$$f(t) \quad = \mathcal{F}^{-1}[F(\omega)] = \quad \int_{-\infty}^{\infty} F(\omega)e^{-i\omega t}d\omega, \tag{1.11}$$

where we adopt the following convention throughout the book: a lower case letter indicates a time- or space-domain function and its capitalized version indicates the Fourier transform. The following are Fourier identities, where the double-sided arrows indicate the functions are Fourier pairs and $\mathcal{F}$ indicates the forward Fourier transform.

1. **Differentiation:** $\partial^n/\partial t^n \leftrightarrow (-i\omega)^n$. This property is proved by differentiating equation 1.11 w/r to t.

2. **Convolution Theorem:** $f(t)*g(t) = \int f(\tau)g(t-\tau)d\tau \leftrightarrow 2\pi F(\omega)G(\omega)$. This property is proved by applying the Fourier transform to the convolution equation

$$\begin{aligned} \mathcal{F}[f*g] &= \mathcal{F}[\int_{-\infty}^{\infty} f(\tau)g(t-\tau)d\tau], \\ &= \frac{1}{2\pi}\int_{-\infty}^{\infty} e^{i\omega t}[\int_{-\infty}^{\infty} f(\tau)g(t-\tau)d\tau]dt. \qquad (1.12) \end{aligned}$$

Interchanging the order of integration we get

$$\mathcal{F}[f*g] = \frac{1}{2\pi}\int_{-\infty}^{\infty} f(\tau)[\int_{-\infty}^{\infty} e^{i\omega t}g(t-\tau)dt]d\tau, \qquad (1.13)$$

and defining the integration variable as $t' = t-\tau$

$$= \frac{1}{2\pi}\int_{-\infty}^{\infty} f(\tau)[\int_{-\infty}^{\infty} e^{i\omega(t'+\tau)}g(t')dt']d\tau, \qquad (1.14)$$

and using the definitions of the Fourier transform of $g(t)$ and $f(t)$ we get

$$= G(\omega)\int_{-\infty}^{\infty} f(\tau)e^{i\omega\tau}d\tau, \qquad (1.15)$$

$$= 2\pi F(\omega)G(\omega). \qquad (1.16)$$

We will often denote the convolution of two functions $f(t)*g(t)$ by the $*$ symbol.

3. **For real $f(t)$: $f(-t) \leftrightarrow F(\omega)^*$.** This property is easily proven by taking the complex conjugate of equation 1.11 to get $f(t)^* = f(t) = \int F(\omega)^* e^{i\omega t}d\omega$ and then apply the transform $t = -t'$.

4. **Correlation.** $f(-t)*g(t) = f(t)\otimes g(t)$**:** By definition $f(-t)*g(t) = \int f(-\tau)g(t-\tau)d\tau$. By changing the dummy integration variable $\tau \rightarrow -\tau'$ we get $f(-t)*g(t) = \int f(\tau')g(t+\tau')d\tau' = f(t)\otimes g(t)$, where $\otimes$ represents correlation. By identities 2 and 3 we conclude $\mathcal{F}[f(t)\otimes g(t)] = \mathcal{F}[f(-t)\star g(t)] = 2\pi F(\omega)^* G(\omega)$.

Appendix 2: Glossary

The following is a glossary of acronyms and terms commonly used in this book. A more detailed description of such terms can be found in Yilmaz (2001).

- AGC - Automatic gain control. An amplitude gain procedure applied to the trace that equalizes the trace energy over a contiguous sequence of specified time windows. After application of AGC, attenuation and geometrical spreading effects can be roughly corrected for and reflection amplitudes are normalized to be about the same value.

- Autocorrelation - $\phi(\tau)_{gg} = g(t)\otimes g(t) = \int_{-\infty}^{\infty} g(t+\tau)g(t)dt$. If $g(t)$ is a vector then the autocorrelation function $\phi(\tau)$ can be interpreted as the dot product of $g(t)$ with shifted copies of itself. Large positive values of $\phi(\tau)$ indicate a high degree of positive similarity between $g(t)$ and $g(\tau+t)$, large negative values indicate a high degree of negative similarity, and zero values mean no similarity.

- Cross-correlation - $\phi(\tau)_{gf} = g(t) \otimes f(t) = \int_{-\infty}^{\infty} g(t-\tau)f(t)dt = \int_{-\infty}^{\infty} g(t)f(t+\tau)dt = g(-t) \star f(t)$.

- CMG - Common midpoint gather. A collection of traces all having the same midpoint location between the source and geophone.

- COG - Common offset gather. A collection of traces all having the same offset displacement between the source and geophone.

- CRG - Common receiver gather. A collection of traces all recorded with the same geophone but generated by different shots.

- CSG - Common shot gather. Vibrations from a shot (e.g., an explosion, air gun, or vibroseis truck) are recorded by a number of geophones, and the collection of these traces is known as a CSG.

- Fold - The number of traces that are summed together to enhance coherent signal. For example, a common midpoint gather of N traces is time shifted to align the common reflection events with one another and the traces are stacked to give a single trace with fold N.

- IVSP data - Inverse vertical seismic profile data, where the sources are in the well and the receivers are on the surface. This is the opposite to the VSP geometry where the sources are on the surface and the receivers are in the well (see Figure 1.13). An IVSP trace will sometimes be referred to as a VSP trace or reverse vertical seismic profile (RVSP) seismogram.

- OBS survey - Ocean bottom seismic survey. Recording devices are placed along an areal grid on the ocean floor and record the seismic response of the earth for marine sources, such as air guns towed behind a boat. The OBS trace will be classified as a VSP-like trace.

- Reflection coefficient. A flat acoustic layer interface that separates two homogeneous isotropic media with densities ρ_1 and ρ_2 and compressional velocities v_1 and v_2 has the pressure reflection coefficient $(\rho_2 v_2 - \rho_1 v_1)/(\rho_2 v_2 + \rho_1 v_1)$. This assumes that the source plane wave is normally incident on the interface from the medium indexed by the number 1.

- RTM - Reverse Time Migration. A migration method where the reflection traces are reversed in time as the source-time history at each geophone. These geophones now act as sources of seismic energy and the fields are backpropagated into the medium (Yilmaz, 2001).

- PDE - Partial differential equation.

- Stacking - Stacking traces together is equivalent to summation of traces. This is usually done with traces in a common midpoint gather after aligning events from a common reflection point.

- S/N - Signal-to-noise ratio. There are many practical ways to compute the S/N ratio. Gerstoft et al. (2006) estimates the S/N of seismic traces by taking the strongest amplitude of a coherent event and divides it by the standard deviation of a long noise segment in the trace.
- SSF - Split step Fourier migration. A migration method performed in the frequency, depth, and spatial wavenumber domains along the lateral coordinates (Yilmaz, 2001).
- SSP data - Surface seismic profile data. Data collected by locating both shots and receivers on or near the free surface (see Figure 1.13).
- SWD data - Seismic-while-drilling (SWD) data. Passive traces recorded by receivers on the free surface with the source as a moving drill bit. Drillers desire knowledge about the rock environment ahead of the bit, so they sometimes record the vibrations that are excited by the drill bit. These records can be used to estimate the subsurface properties, such as reflectivity (Poletto and Miranda, 2004).
- SWP data - Single well profile data with the shooting geometry shown in Figure 1.13. Data are collected by placing both shots and receivers along a well.
- VSP data - Vertical seismic profile data. Data collected by firing shots at or near the free surface and recorded by receivers in a nearby well. The well can be either vertical, deviated, or horizontal (see Figure 1.13).
- Xwell data - Crosswell data. Data collected by firing shots along one well and recording the resulting seismic vibrations by receivers along an adjacent well (see Figure 1.13).
- ZO data - Zero-offset data where the geophone is at the same location as the source.

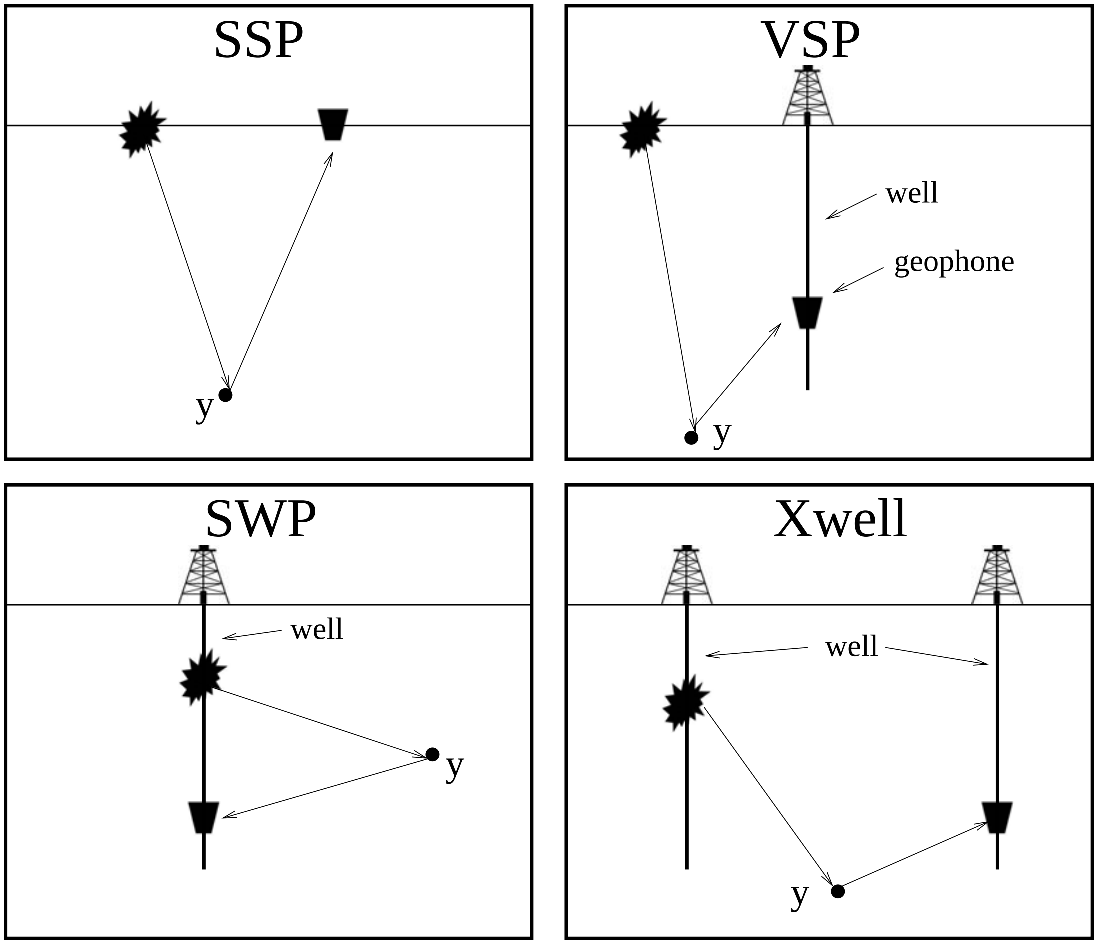

Figure 1.13: Source-receiver configurations for four different experiments: SSP=surface seismic profile, VSP=vertical seismic profile, SWP=single well profile, and Xwell=Crosswell. Each experiment can have many sources or receivers at the indicated boundaries (horizontal solid line is the free surface, vertical thick line is a well). The derrick indicates a surface well location, **y** denotes the reflection point, and the stars indicate sources.

Chapter 2

Practical Aspects of Diffraction Stack Migration

The basic assumption in resorting shot gathers into common midpoint gathers, applying NMO and stacking is that the reflectors are flat. If true, the origin of the stacked reflection energy originates somewhere directly beneath the trace, as shown in Figure 2.1. However, layering that departs from the horizontal, such as the dipping layers shown in Figure 2.2-2.3, violates this assumption. The consequence is that the reflection energy in a trace could have originated along a reflector point horizontally offset from the trace. Thus we need to "migrate" the reflection to its point or origin, a process commonly known as migration. Not doing so will lead to mispositioning errors in estimating oil location and result in many dry holes.

Another reason for "migration" is that sharp changes in the interface geometry give rise to diffractions. Examples are a point scatterer and a synclinal model giving rise to the ZO sections shown in Figure 2.4. Without migration, the point scatterer traces appear as if they were generated by a synclinal structure.

2.1 Poststack Migration

The goal in seismic imaging is to use seismic data to create reflectivity sections of the earth in either (x, z) or (x, y, z) space. If the reflection traces are all we have, how do we identify in (x, z) the origin point of reflections and migrate them to their reflection point of origin? The answer to this question for a dipping layer is shown in Figure 2.3. The reflection energy at time t in trace C could have originated anywhere along a circle of radius vt centered at C, where v is the homogeneous velocity of the medium. Any reflector located along this circle could have contributed energy to trace C at time t. However, this ambiguity in location is not acceptable, so we improve our answer by asking the question: what kind of reflector could account for *all* the traces? The answer is found by drawing circles of radius vt centered at all trace positions, where t is the reflection time at that particular trace. The *common* tangent to these circles defines the reflector that could account for energy seen in all of the traces.

2.1.1 Poststack Migration = Smear $d(x_g, t)$ along Semicircle(x, z)

Rather than drawing circles, the migration procedure can be automated by smearing reflection energy along fat circles where each donut is filled with the reflection wavelet $w(t)$, as shown in Figure 2.5. The areas where the adjacent donuts cross are likely to be out of phase, so that if the reflection energy is smeared and *summed* in model space coordinates (x, z) then destructive interference is likely to result within the intersections. However, along the common tangent (i.e., the actual reflector) the energy is in phase and so summation is coherent. Thus, migration can be described as smearing and summing the reflections along the appropriate donuts (Stolt and Benson, 1986; Claerbout, 1992).

Mathematically, ZO migration is given by the formula (see previous chapter on Green's functions):

$$\begin{aligned} m(x,z) &= \sum_{g=1}^{ntraces} \ddot{data}(x_g, t(x_g,x,z))/||(x-x_g)^2+z^2||^2, \\ &\quad where \\ t(x_g,x,z) &= \sqrt{(x-x_g)^2+z^2}/c, \end{aligned} \tag{2.1}$$

where $t(x_g, x, z)$ is the one-way time for energy to go from the surface point $(x_g, 0)$ to the model point (x, z), and $data(x_g, t)$ is the reflection ZO trace in one-way time at position $(x_g, 0)$. The double dot denotes second-order differentiation with respect to time, which is to undo the smoothing effects of integration in the data-space x' coordinate. Since phase changes mainly determine the constructive/destructive interference of energy, I will usually ignore the geometrical spreading factor in my later formulations.

This procedure can be automated with the following MATLAB fragment for ZO migration;

```
for ixtrace=1:ntrace;       Loop over ZO trace indicies
for xs=istart:iend;         Loop over model space indicies (xs,zs)
for zs=1:nz;
   r = sqrt((ixtrace*dx-xs*dx)^2+(zs*dx)^2);      compute radius of semi-circle
   time = round( 1 +  r/c/dt );                   compute 1-way time to circle
   m(xs,zs) = m(xs,zs) + data(ixtrace,time)/r;    Smear and sum data reflections into (x,z)
 end;
 end;
end
```

Note, the data in $data(ixtrace, time)$ are assumed to be in one-way time, otherwise the velocity v would have to be halved.

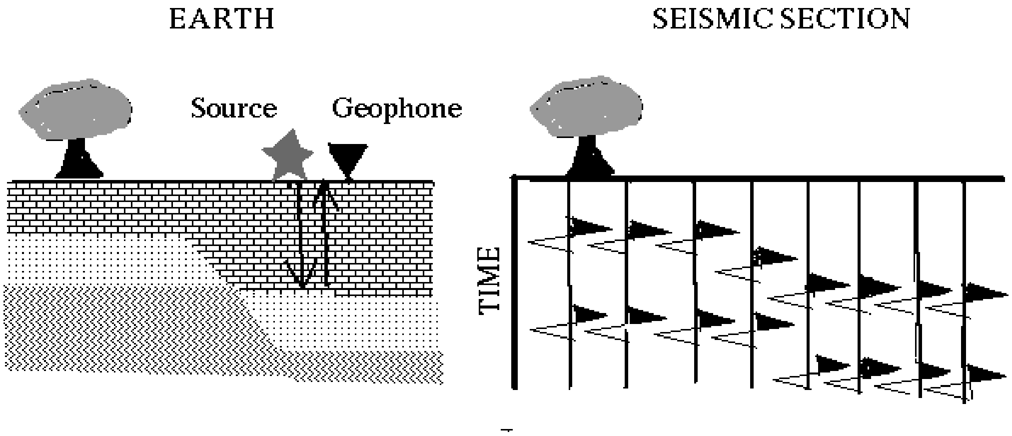

Figure 2.1: Earth model on top left and idealized zero-offset (ZO) seismic section on top right, where each trace was recorded by an experiment where the source has zero offset from the geophone. The above ZO seismic section represented by $data(x, z = 0, t)$ roughly resembles the earth's reflectivity model $m(x, z)$ because we unrealistically assume it contains only the primary reflections and the reflections in the data originate directly beneath the trace.

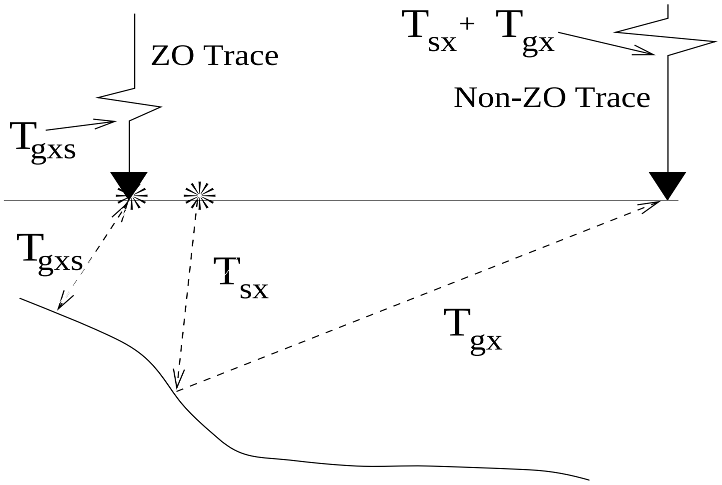

Figure 2.2: Raypaths and associated CMP traces for a 2-layer medium. Note that there is no common reflection point associated with these rays, and so the 1D NMO formula incorrectly predicts the moveout of the reflection data. The subsequent stack will not produce the correct ZO trace illustrated on the left.

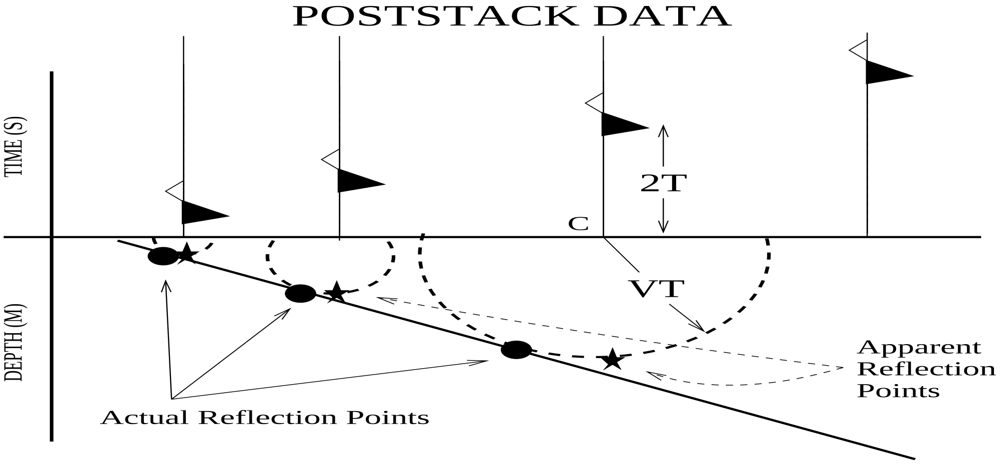

Figure 2.3: Where could the reflection energy in trace C have originated from? Answer: Along the semi-circle with radius $c \cdot t$ centered at C. Where could the reflection energy have originated for all of the traces? Common Answer: the tangent to the semi-circles which is the dipping interface. Note, migrated energy always moves *updip* of the reflection energy seen in the seismic section and actual dip is steeper than apparent dip seen in seismic section.

2.1.2 Inhomogeneous Velocity

An implicit assumption in the above procedure is that the velocity medium is homogeneous so that possible reflector positions fall along a semi-circle. More realistically, the earth has a heterogeneous velocity distribution so that energy should fall along a irregular circle shown at the bottom of Figure 2.5. The quasi-circles can be computed by first using ray tracing to construct the traveltime table $t(x, z, ixtrace)$ for a source at $(ixtrace, 0)$; that is, find the 3D matrix $t(x, z, ixtrace)$ for all model coordinates (x, z) and trace offsets $(ixtrace, 0)$. Then, replace $time = round(1 + r/c/dt)$ in the above MATLAB code by $t(x, z, ixtrace)$.

2.1.3 3D Poststack Migration = Smear $d(x_g, t)$ along Hemisphere(x, z)

Instead of a line of ZO traces, a 3D section will contain an areal patch of ZO traces. The motivation for 3D recording is that the reflection energy could have originated anywhere in the subsurface, even away from the vertical plane along the 2D recording line. That is, out-of-the-plane reflections could have been recorded. To migrate these out-of-the-plane reflections to their origin point we should smear+sum reflection energy along semispheres rather than semicircles (see Figure 2.6). The change to the MATLAB code is to include extra loops over the model- and data-space y-axes.

```
3D MATLAB Poststack Migration Code

for ixtrace=1:ntrace;    % Loop over ZO trace indicies
for IYTRACE=1:ntrace;
 for xs=istart:iend; % Loop over model space indicies (xs,ys,zs)
```

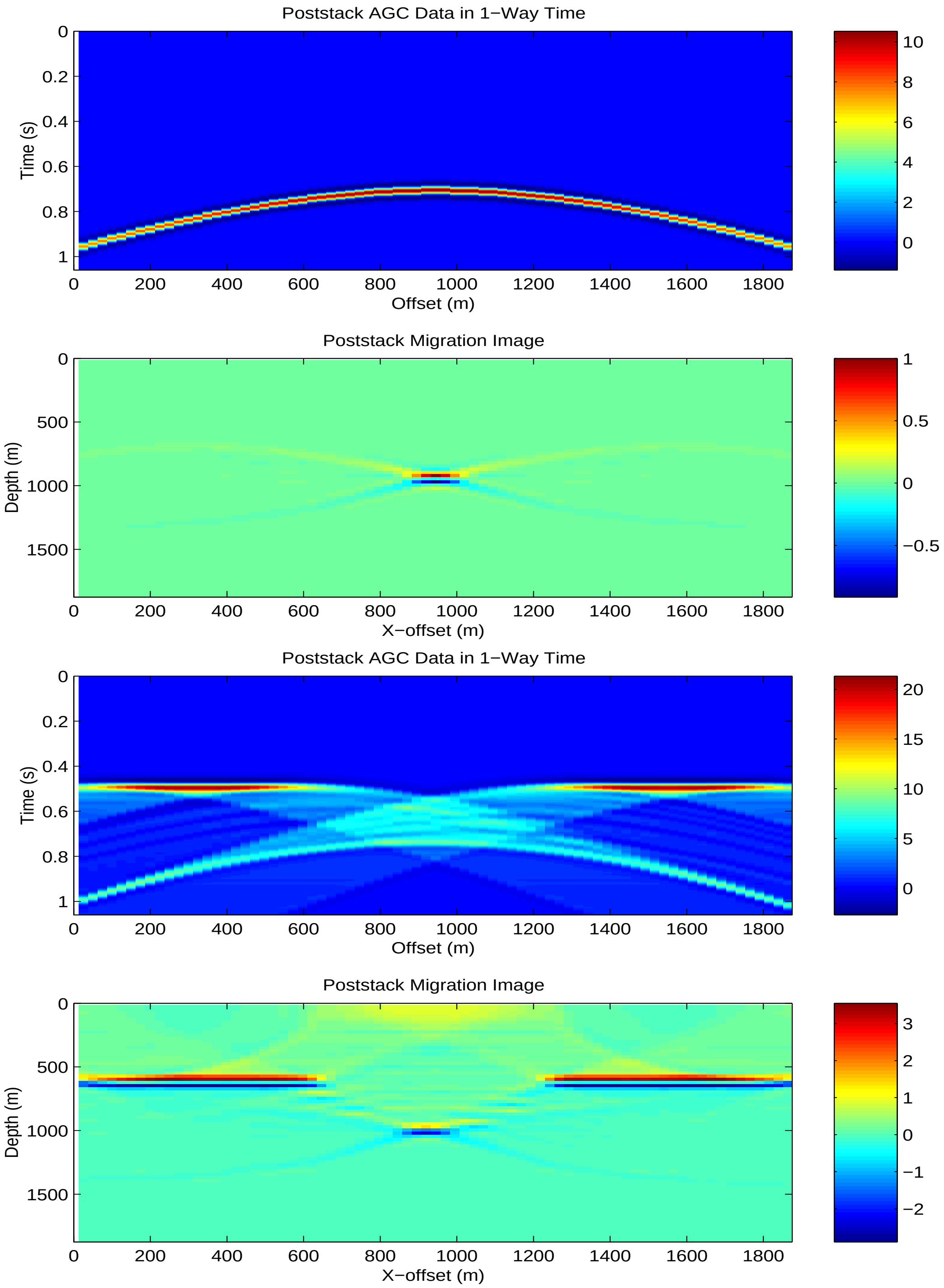

Figure 2.4: ZO traces and model generated by reflections from a (top 2 images) point scatterer and (bottom 2 images) synclinal model denoted by white dashed lines. Migration image in red and blue colors is shown as well.

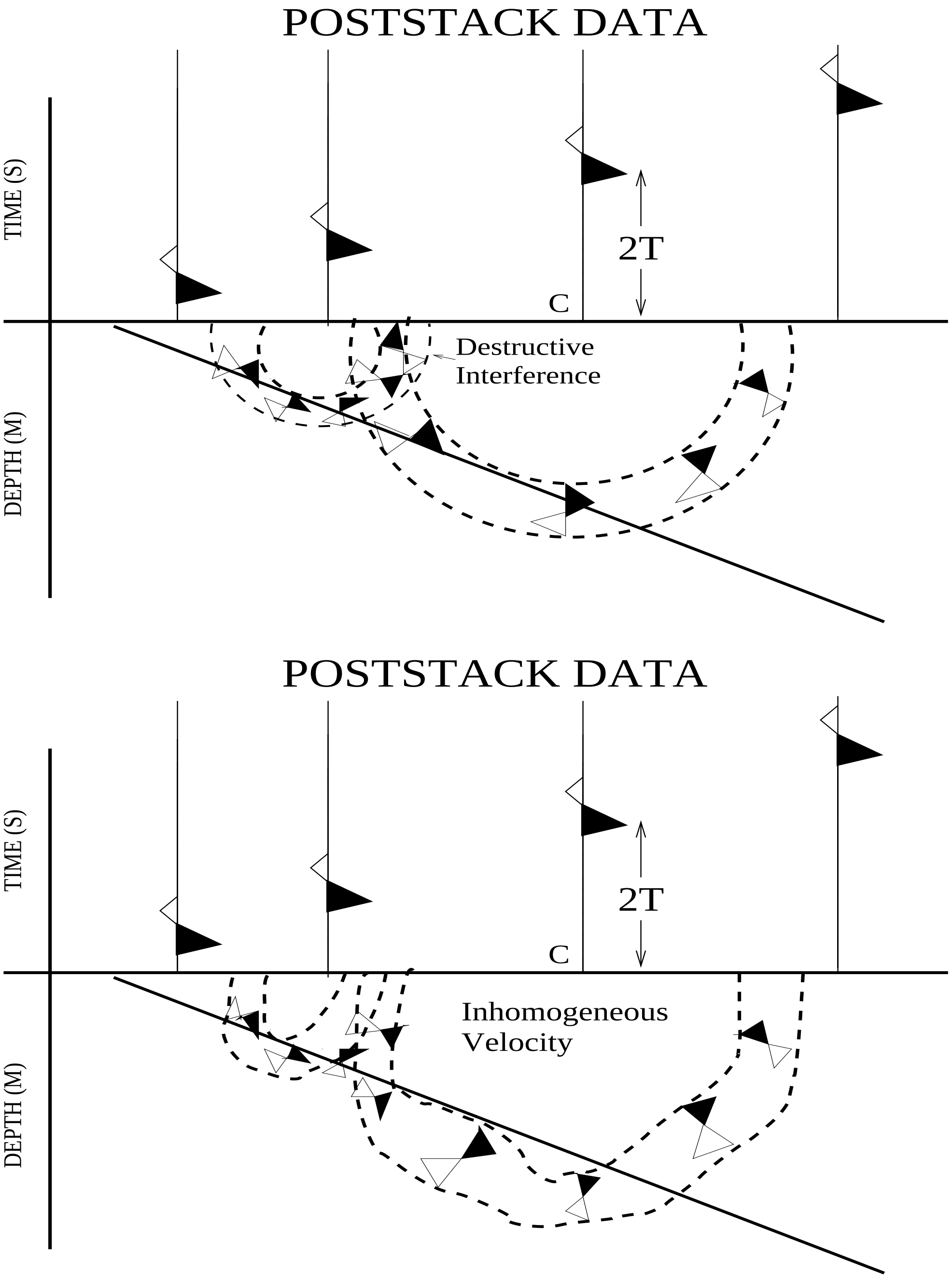

Figure 2.5: Fat migration "circles" for a (top) homogeneous and (bottom) an inhomogeneous velocity medium. The source wavelet fills in the fat "circles".

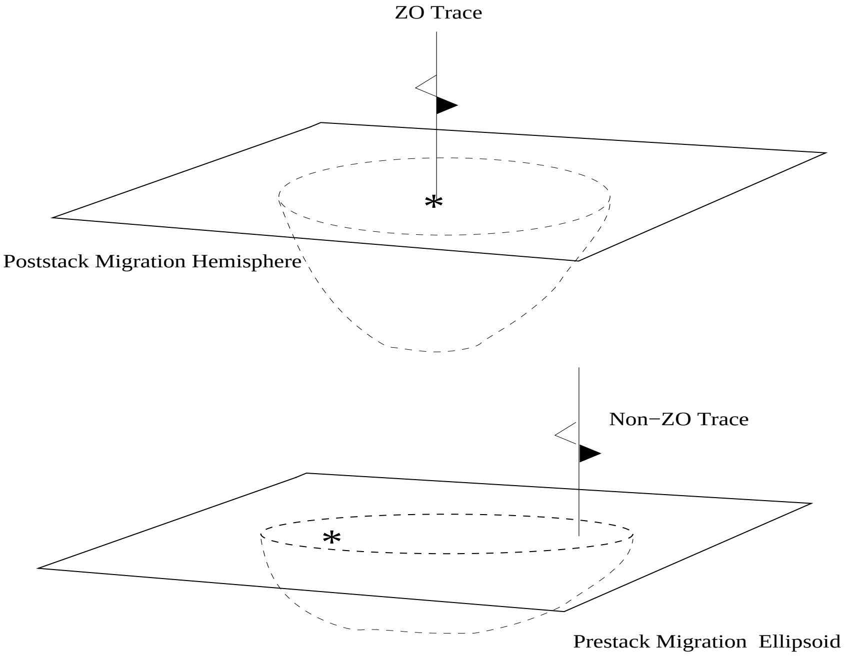

Figure 2.6: (Top) Poststack and (bottom) prestack migration impulse responses for 3D data.

```
 for zs=1:nz; for YS=1:ny;
  r = sqrt((ixtrace*dx-xs*dx)^2+(IYTRACE*dy-YS*dy)^2+(zs*dx)^2); % compute radius of
                                                                 % hemi-sphere
  time = round( 1 +  r/c/dt );                % compute 1-way time to circle
  m(xs,YS,zs) = m(xs,YS,zs) + data(ixtrace,IYTRACE,time)/r; % Smear and sum data
 end                                                         % reflections into (x,z)
 end;
 end;
end
end
```

Note that there are almost twice as many *end* statements in the 3D code compared to the 2D code, which means that 3D ZO migration is several orders of magnitude more expensive than 2D ZO migration.

2.1.4 Obliquity Factor

An improved poststack image can be obtained by including an obliquity factor in the diffrcation stack equation:

$$m(x,z) \quad = \quad \sum_{g=1}^{ntraces} \ddot{data}(x_g, t(x_g,x,z))\hat{\mathbf{n}} \cdot \hat{\mathbf{r}}/||(x-x_g)^2 + z^2||^2, \qquad (2.2)$$

where $\hat{\mathbf{n}}$ is the unit normal at the surface and $\hat{\mathbf{r}}$ is the unit vector at the surface that is the incidence angle of the reflection ray between the trial image point and the geophone.

2.2 Prestack Migration

In a complex medium, such as beneath a salt dome, the NMO and stacking assumption is inappropriate so that the stacked section is too blurry to focus by poststack migration. The cure to this problem is to eliminate the NMO and stacking steps and perform prestack migration on the shot gather $d(x_g, 0, t_g|x_s, 0, t_s)$, where x_g and x_s denote the source and geophone x-coordinates for a shot gather; and t_g and t_s denote the listening time and source excitation time, respectively. Typically, the source is assumed to be excited at time $t_s = 0$.

2.2.1 Prestack Migration = Smear $d(x_g, t)$ along Ellipse(x, z)

Which parts of the model could the reflection energy at time τ originate from? Similar to the poststack migration example, the answer is that the (x, z) parts of the model that satisfy the moveout equation for a fixed t, x_g and x_s. This equation defines an ellipse in model space with foci at $(x_g, 0)$ and $(x_s, 0)$.

Similar to the poststack migration formula, prestack migration smears a reflection sample into model space, but along the appropriate ellipse rather than a semi-circle. The formula for prestack migration is given by

$$m(x,z) \quad = \quad \sum_{x_g}\sum_{x_s}\ddot{d}(x_g,0,\tau(x_g,x_s,x,z)|x_s,0,t_s)/A(x,z,x_g,x_s), \tag{2.3}$$

Examples of stacked data, poststack migration and prestack migration are given in Figures 2.7-2.8.

2.3 Spatial Sampling Issues

How does one choose the trace and shot intervals as well as the total recording aperture? The trace interval is selected so that the discrete representation of the data still contains unambiguous information about dips. Steeper data dips and higher source frequencies will demand finer trace spacing. Also, steeper dips in the model will give rise to ZO reflection rays that are almost horizontal, so will demand wider recording apertures.

2.3.1 Aliased Data

If the trace spacing is too coarse, the ”wings” of the hyperbolas will not completely cancel and so leave ugly smiles or frowns in the shot gather or the migration image, as shown in Figure 2.9. We say that the coarse trace spacing results in migration aliasing artifacts. Another point of view is that steep dips in the data appear more shallow if the trace spacing is too coarse; i.e., the data are aliased..

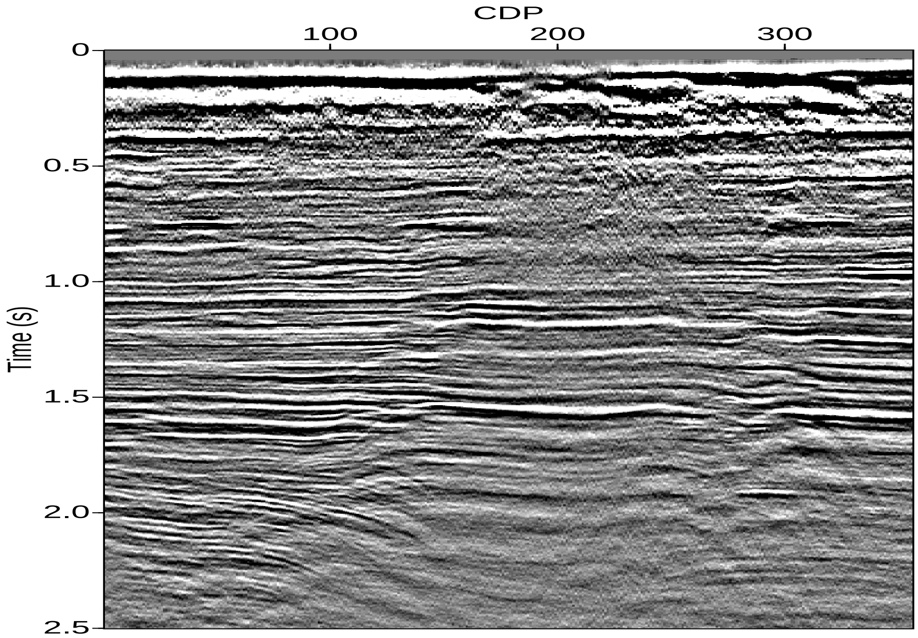

Stack

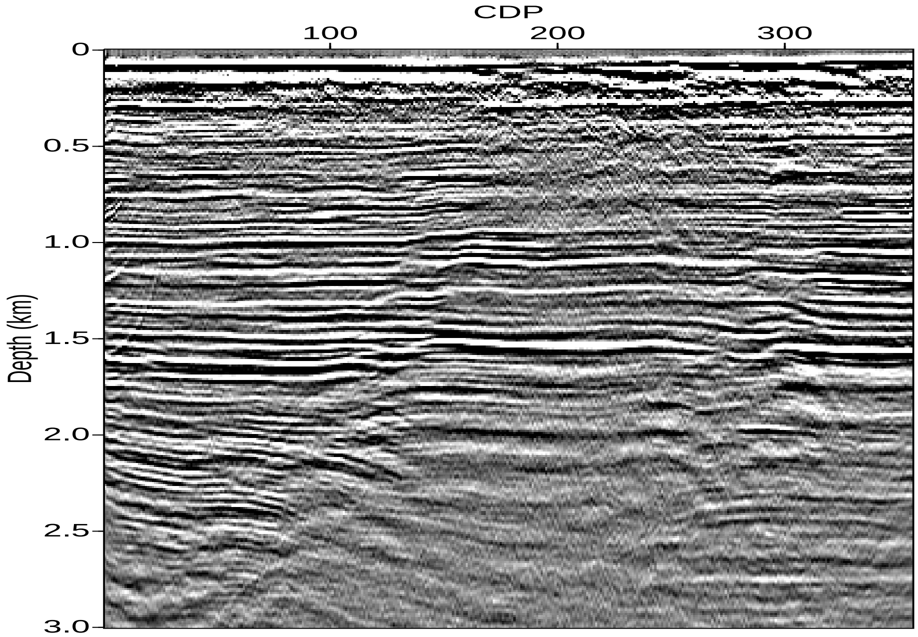

Poststack Depth Mig

Figure 2.7: (Top) Stacked section and (bottom) poststack depth migration sections (courtesy of Jianhua Yu and Unocal). Notice how truncated reflectors have been shortened and diffractions frowns have been reduced by migration.

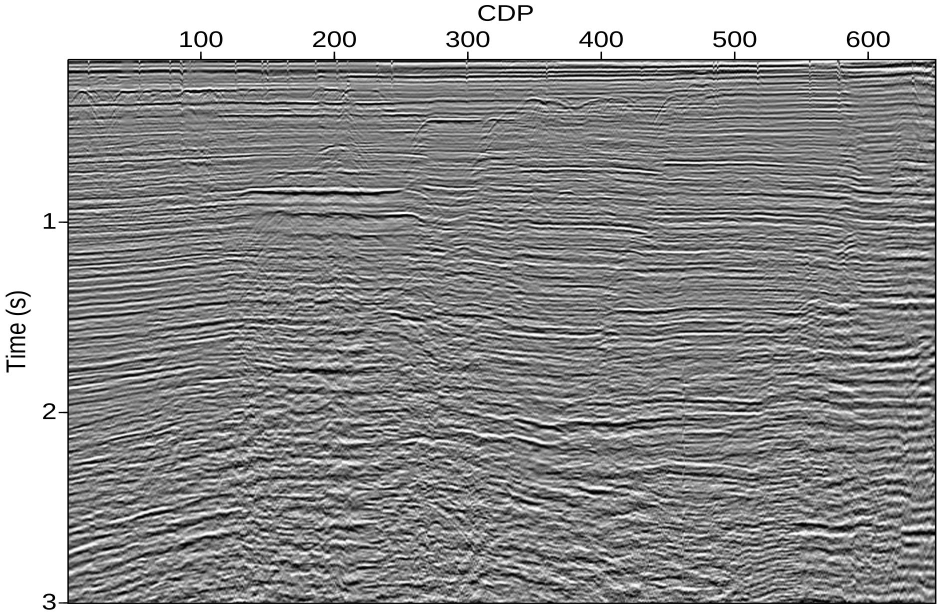

Stack section with AGC window of 400 ms

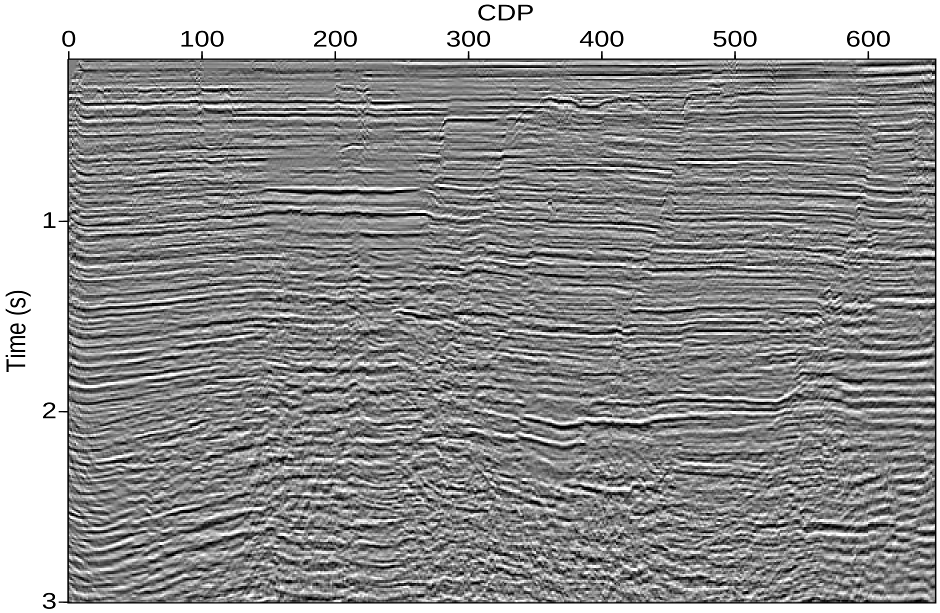

PSTM section with AGC window of 400 ms

Figure 2.8: (Top) Stacked section and (bottom) prestack time migration (courtesy of Jianhua Yu and Unocal).

Aliasing can be cured by making sure that the shortest apparent wavelength in the data $(\lambda_x)_{min}$ is greater than 1/2 the trace spacing Δx. By definition $min(\lambda_x) = T_{min}(dx/dt)_{min}$ so that the anti-aliasing condition is

$$2\Delta x \quad < \quad min(\lambda_x) = (dx/dt)_{min} T_{min}, \tag{2.4}$$

where $min(\lambda_x)$ is the minimum apparent wavelength along the x-direction in the hyperbolas. This is known as the Nyquist sampling criterion, and its violation means that neighboring traces undergo more than 1/2 period of time shift. This assumes that the model grid is discretized finely enough to avoid problems in discretely sampling a continuous interface.

A visual example of aliased data is given in Figure 2.10. The bottom image is a snapshot of a horizontally propagating plane wave. The top and middle figures show the seismograms recorded on the horizontal surface, except the top section is aliased while the middle section is well sampled in space. The dip of the events in the middle section show the true propagation velocity (dx/dt=v) while the apparent velocity of the dip in the top section is slower because the data are aliased. Try running the MATLAB code below to see how aliasing affects recorded data.

```
colormap(’gray’); subplot(311); plot(1:2,1:2); subplot(312);
plot(1:2,1:2); subplot(313); plot(1:3,1:3);
nangle=3;nt=50;nsnap=nt*nangle;itt=0;c=.2;
%%%%%%%%%%%%%%%%%%%%%%%%%%%%%%%%%%%%%%%%%%%%%%%%%%%%%

rect=get(gcf,’Position’);
rect(1:2)=[0 0];
M=moviein(nsnap,gcf,rect);

%%%%%%%%%%%%%%%%%%%%%%%%%%%%%%%%%%%%%%%%%%%%%%%%%%%%%
for iangle=1:nangle; lam=6;angle=pi/4.2*(iangle-1);
kx=2*pi*cos(angle)/lam;ky=sin(angle)*2*pi/lam;
nx=100;k=sqrt(kx^2+ky^2);w=k*c; r=1:1:nx;i=ones(nx,1);
dx=i*r; dy=dx’;tt=.001*[nt:-1:1];sei1=ones(nt,nx/4);
sei=ones(nt,nx);

for it=1:nt; itt=itt+1; pw=cos(dx*kx+dy*ky+w*it);pw=fliplr(pw);
for iii=1:25; sei1(it,iii)=pw(1,1+(iii-1)*4); end;
sei(it,:)=pw(1,:);
%%%%%%%%%%%%%%%%
subplot(311);
imagesc(r,tt,sei1);
if iangle==1;title(’Seismograms: Angle = 0 deg’);end;
if iangle==2;title(’Seismograms: Angle = 40 deg’);end;
if iangle==3;title(’Seismograms: Angle = 80 deg’);end;
ylabel(’Time (s)’); pause(.2)
%%%%%%%%%%%%%%%%
```

```
subplot(312);
imagesc(r,tt,sei);
if iangle==1;title('Seismograms: Angle = 0 deg');end;
if iangle==2;title('Seismograms: Angle = 40 deg');end;
if iangle==3;title('Seismograms: Angle = 80 deg');end;
ylabel('Time (s)'); pause(.2)
%%%%%%%%%%%%%%
subplot(313);
imagesc(pw);xlabel('Horizontal Offset (m)');
ylabel('Depth (m)');
if iangle==1;title('Snapshots: Angle = 0 deg');end;
if iangle==2;title('Snapshots: Angle = 40 deg');end;
if iangle==3;title('Snapshots: Angle = 80 deg');end;
pause(.2)
%%%%%%%%%%%%%%
M(:,itt)=getframe(gcf,rect); end; end; N=1 ;
FPS=1 ;
movie(gcf,M,N,FPS,rect);
%mpgwrite(M, hot, 'filename', [1, 0, 1, 0, 10, 8, 10, 25]);
```

2.3.2 Migration Operator Aliasing

Even if the data are sampled properly, the migration operator can be aliased. That is, migration can be viewed as either "smearing a time sample of data along the corresponding migration circle (or ellipse)", or equivalently it can be viewed as "summing energy along the appropriate hyperbola (for a fixed trial image point at **x** and source-receiver pair) and dumping it into the pixel centered at **x**". The latter view is illustrated in Figure 2.11, where shallower trial image ponts lead to more steeply dipping wings of the hyperbola. Since we are summing amplitudes along these hyperbola we must ensure that the dip along the migration hyperbola is not as steep as the trace spacing allows; otherwise the data are aliased.

$$2\Delta x < {\lambda_x}^{operator} = \frac{dx}{dt^{mig.\ op.}} T^{min}. \tag{2.5}$$

Violation of this operator anti-aliasing condition will lead to migration artifacts in the migration image. A simple cure is to low pass filter the trace so the righthand side of the above equation becomes larger. More sophisticated cures are also possible (Biondi, 2001).

For the simple cure of migration operator aliase, we apply a low pass filter to the traces to eliminate the frequency components for which the anti-aliasing condition is violated. According to the anti-aliase condition in equation 2.5, the maximum unaliased frequency can be represented as:

$$\overbrace{f_{max}}^{unaliased} < \frac{1}{2\Delta x \frac{dt^{mig.\ op.}}{dx}}. \tag{2.6}$$

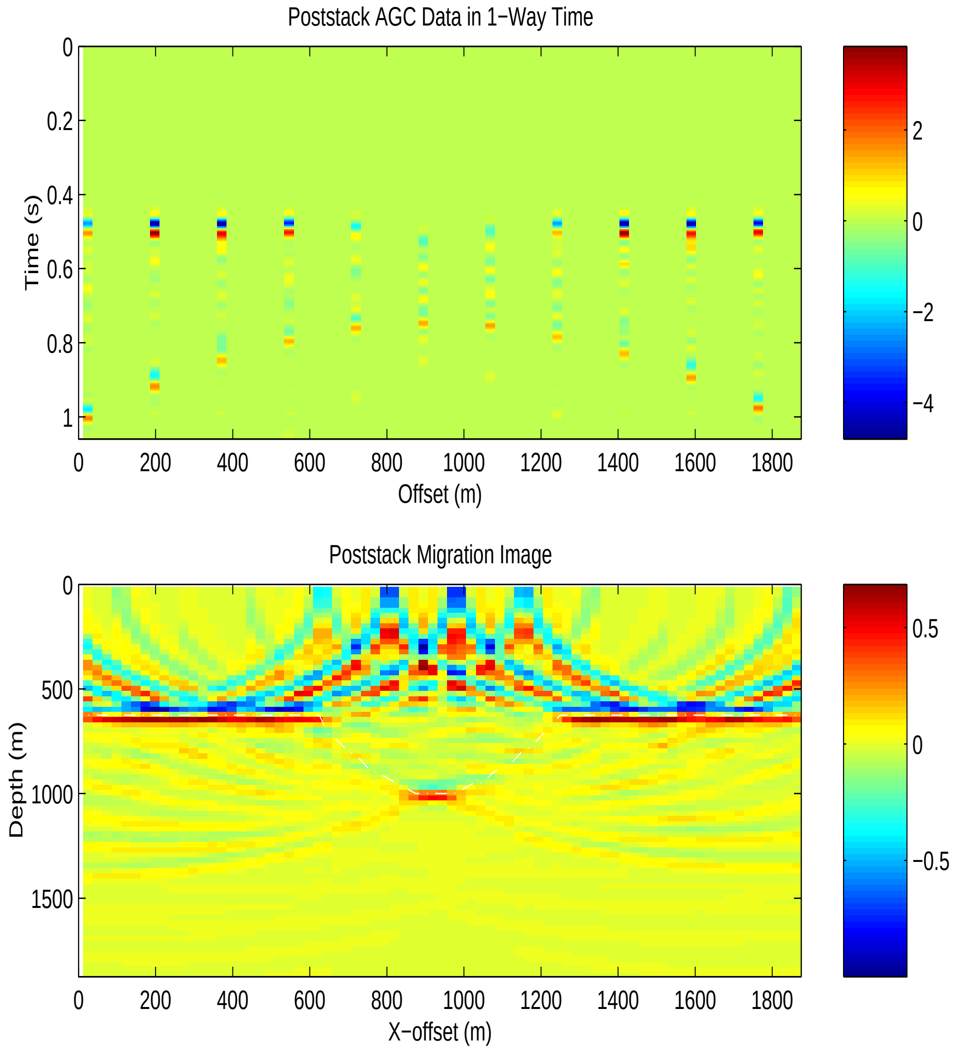

Figure 2.9: Same as synclinal model results except a coarse grid of data are the input to give rise to an aliased migration section with smiley artifacts. Note, the flat reflector data is not aliased but the steeply dipping part of data (syncline reflections) is aliased.

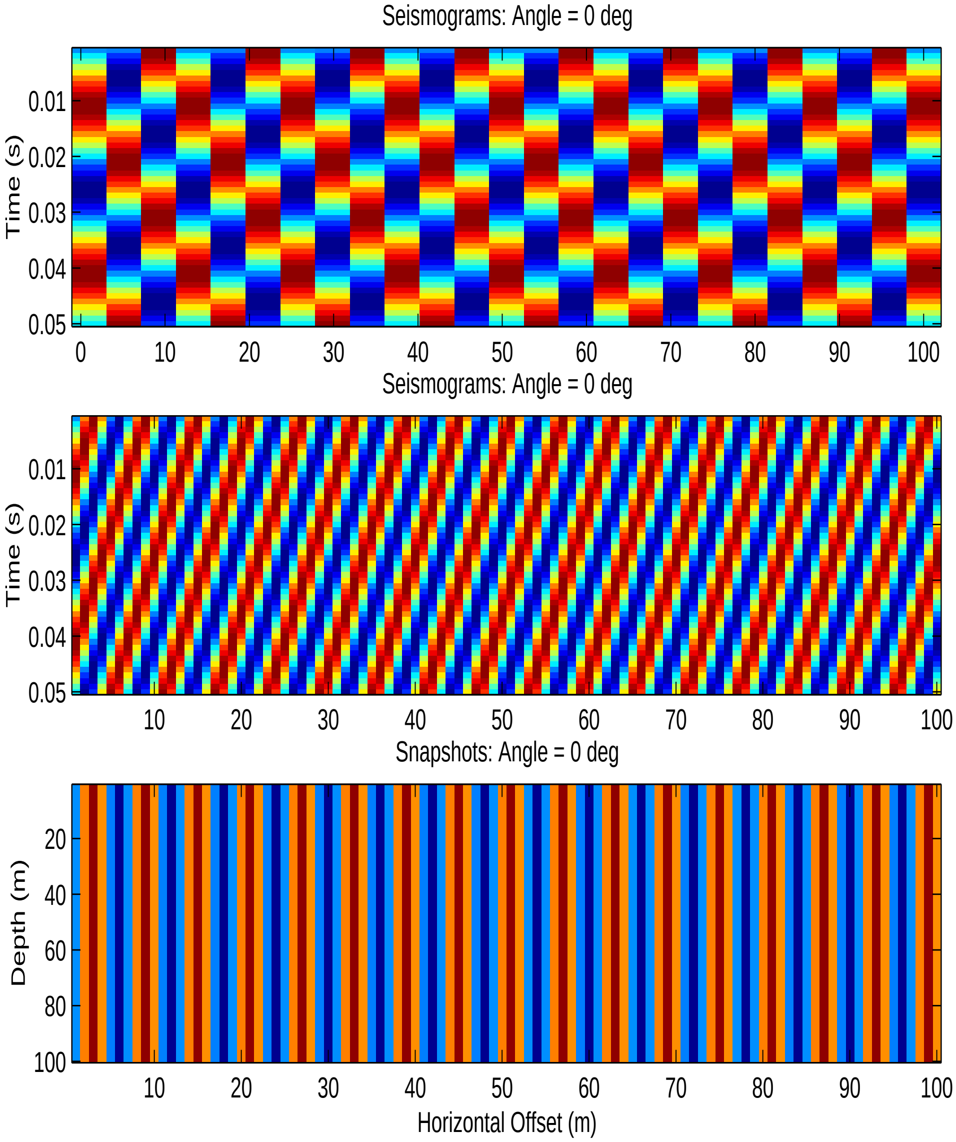

Figure 2.10: (Top) Aliased and (middle) well-sampled seismograms for the horizontally propagating wave seen in the bottom snapshot. Aliased data appears to have slower moving waves, just like a fan that appears to spin backward in a strobe light.

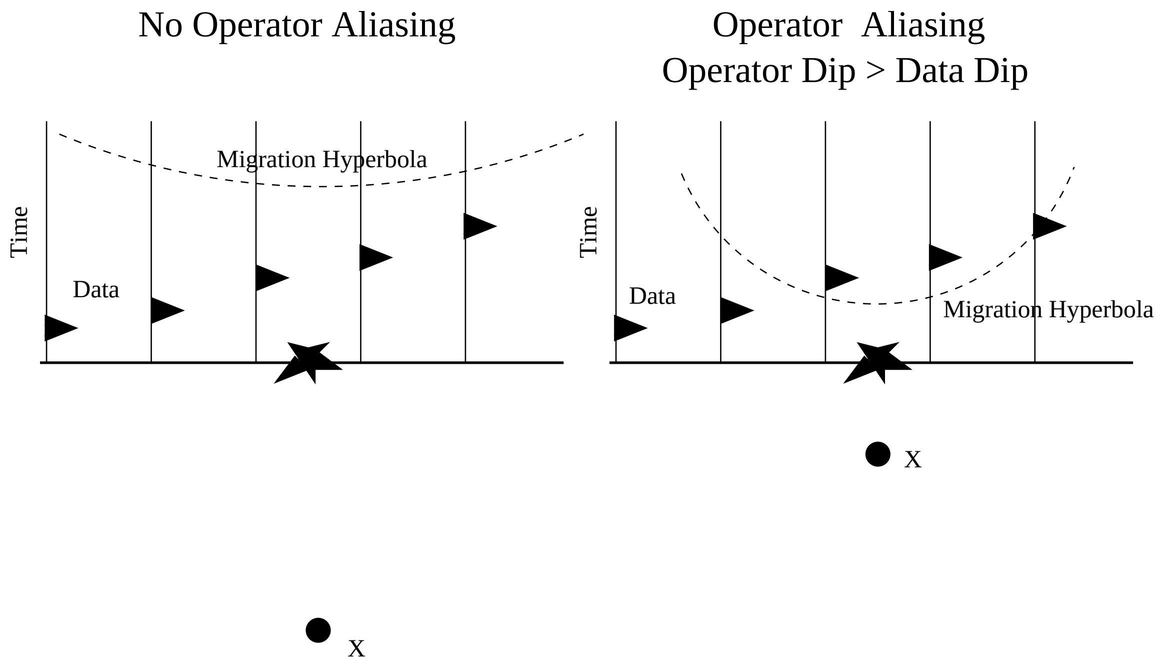

Figure 2.11: (Left) Migration hyperbola associated with a fixed trial image point at (left) deep and (right) shallow depths. The shallow depth migration operator has a dip angle steeper than that for the data, so it is aliased.

For 2D poststack Kirchhoff time migration, $t^{mig.\ op.}$ is the two way traveltime from the shot/geophone position to the image point in the model, $\frac{2\sqrt{(x-x_{image})^2+z_{image}{}^2}}{c}$. Substitute the traveltime for 2D poststack migration operator into equation 2.6, and we obtain the maximum unaliased frequency for the migration operator:

$$\overbrace{f_{max}}^{unaliased} < \frac{c\sqrt{(x-x_{image})^2+z_{image}{}^2}}{4x\cdot\Delta x}. \tag{2.7}$$

The maximum unaliased frequency for 3D and prestack migration operator can be obtained in a similar way.

Then we design a low pass filter to eliminate the components in the traces with frequencies higher than the corresponding maximum unaliased frequencies. A triangle filter is introduced by Lumley et al. (1994) to eliminate the aliased frequencies. The Z transformed formulation of this triangle filter is:

$$g(z) = \frac{-z^{-k-1}+2-z^{k+1}}{\alpha(1-z)(1-z^{-1})}, \tag{2.8}$$

where the filter scaling coefficient $\alpha = (k+1)^2$ and the length of the filter is $N = 2k+3$. The magnitude spectrum of the triangle filter can be derived as:

$$A(\omega) = \frac{\sin^2(\omega\Delta t(k+1)/2)}{\alpha\sin^2(\omega\Delta t/2)}, \tag{2.9}$$

and has spectral notches at the frequencies

$$f^n = \frac{\omega_n}{2\pi} = \frac{n}{(k+1)\Delta t}; n = 1, 2, 3, ... \tag{2.10}$$

The length of the filter is decided such that f_1, the first notch frequency at the magnitude spectrum, is equal to the maximum unaliased frequency $\overbrace{f_{max}}^{unaliased}$. Then we have

$$k = \frac{1}{f^1} - 1 = \frac{1}{\overbrace{f_{max}}^{unaliased}} - 1 = \frac{4(x-x_{image})\Delta x}{\sqrt{(x-x_{image})^2+z_{image}{}^2}\Delta t\cdot c} - 1. \tag{2.11}$$

Figure 2.12 shows the magnitude spectrum of a triangle filter with $\Delta t = .01$ sec and k=5.

Note that $1/(1-z)$ in the denominator of the filter $g(z)$ can be expanded as a geometrical series $1+z+z^2+z^3+z^4+\cdots$, which represents a causal filter with unit values at and after time point 0 in time domain. Convolving an input trace $f(n)$ with this filter gives $\sum_{-\infty}^{n} f(i)$, the causal integration of the input trace. Similarly, $1/(1-z^{-1})$ in the denominator of $g(z)$ represents an acausal filter with unit values at and before time point 0, and convolving the input $f(n)$ with this acausal filter gives the acausal integration of the input $\sum_{i=n}^{\infty} f(i)$. The numerator of the filter $g(z)$ is a gapped three-point difference operator and the gap length $k+1$ determines the high cut frequency of the filter. Therefore, after the causal and acausal integration of the input trace, we need only to implement a three-point difference to the integrated series and can obtain the low pass output for the local time points.

The effect of the triangle anti-aliased filter on migration results is shown in Figure 2.13, where two sections migrated with and without the triangle anti-aliase filter for the same data set are demonstrated. This comparison indicates that the anti-aliase filter effectively precludes the migration artifacts due to migration operator aliasing. This improvement is more much obvious in the shallow part of the section than in the deep part because the migration operator is easier to get aliased with small image point depth, which is also implied in equation 2.7.

A latent problem of using this triangle filter to preclude migration operator aliases is the possible loss of numerical precision, which might lead to amplitude distortion in migrated sections (Abma, 2006). Since a causal and an acausal integrations of the values along traces are involved in the filtering process, the amplitude of the integration output may increase dramatically in some occasions. If the computation precision is not high enough the numerical precision will be lost when we sum some low amplitude values during the integrations, especially when there are significant amplitude difference in input traces. This loss of numerical precision may result in serious distortions of migrated images. Figure 2.14 shows an exaggerated example of the effect of numerical precision on migration results. In this example two sections migrated with triangle filter done in single and double precision are demonstrated for a synthetic data set with spikes having magnitude of about 100 000 and of about 1.0. There are apparent loss of weak events in the migrated section done in single precision (Abma, 2006).

One solutions to this problem is using double precision float numbers during the whole computation processes, which demands twice computer memory as single precision computation does. When twice memory can not be easily accessed, we can do the integration in double precision, and store the result in single precision after removing the linear trends from the integrated data, because the three-point difference in the filter ignores any linear trend.

Following code is an application of the triangle anti-aliase filter to 2D poststack time migration, and it is the function to implement the anti-aliasing migration.

```
function [migi]=migrate1(cdp1,nx,ntime,dt,app,rick,dx,c,zbottom,fwavelet)
dz=dx*.1; izbottom=round(zbottom/dz);
x=dx*nx;nxx=round(x/dz);
migi=zeros(nxx,izbottom);
for ixtrace=1:nx;
    ixtrace;xtrace=round(dx*ixtrace);

  % Apply causal integration to the trace
    trace_int1=cumsum(cdp1(ixtrace,:));
  % Apply acausal integration to the trace
    temp=fliplr(trace_int1);trace_int2=fliplr(cumsum(temp));

    istart=max(1,1 + round(dx/dz*((ixtrace-1)-app)));
    iend=min(nxx,1+ round(dx/dz*((ixtrace-1)+app)));
```

```
    for ixs=istart:iend;
        for izs=2:izbottom;
            r = sqrt((ixtrace*dx-ixs*dz)^2+(izs*dz)^2);
     % Determine the maximun unaliased frequency fmax
            if (ixtrace*dx-ixs*dz==0)
                fmax=10000;
            else
                fmax=r*c/2/dx/abs(ixtrace*dx-ixs*dz);
            end

            obliquity=abs(izs*dz)/r;
            time = round( 1 +  r/c/dt );time=min(ntime,time);r=1;
  % if fmax is greater than 3 times of the wavelet dominana frequency,
  % all frequency components in the trace is unaliased and we apply
  % the migration operator to the original traces.
  % Otherwise, we low pass filter the traces and then migrate them.
       if (fmax>3*fwavelet)
        migi(ixs,izs) = migi(ixs,izs) + cdp1(ixtrace,time)*obliquity/r;
       else
   % Determine the filter length according to
   % the maximum unaliased frequency fmax
        k=max(round(1/fmax/dt-1),0);
t1=max(time-k-1,1);t2=min(time+k+1,ntime);
filt_output=-trace_int2(t1)-trace_int2(t2)+2*trace_int2(time);
filt_output=filt_output/(k+1)^2;
        migi(ixs,izs) = migi(ixs,izs) + filt_output*obliquity/r;
        end
        end;
    end;
end;
subplot(212);
imagesc([1:izbottom]*dz,[1:nx]*dx,migi');colormap(gray)
title(['Partial Migration Section at Iteration ',num2str(ixtrace)])
subplot(211);imagesc([1:ntime]*dt,[1:nx]*dx,cdp1');
title('Radar Section');pause(.05)
```

2.3.3 Aperture Limitation.

Wider apertures will lead to better horizontal resolution, and also allow for recording of events with nearly horizontal raypaths. The aperture width should be estimated by using the formula given in Figure 2.15.

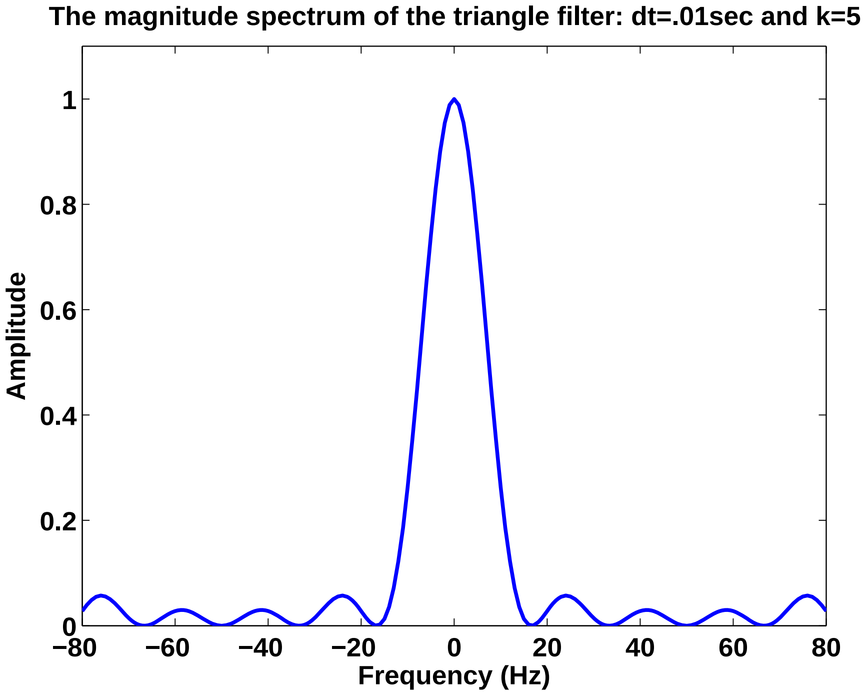

Figure 2.12: The magnitude spectrum of the triangle low pass filter with $\Delta t = .01$ sec and k=5. The spectrum notches are at the frequencies $f^n = \frac{n}{(k+1)\Delta t}$. The frequencies between the two first notches are preserved and the other frequency components are suppressed after the filtering.

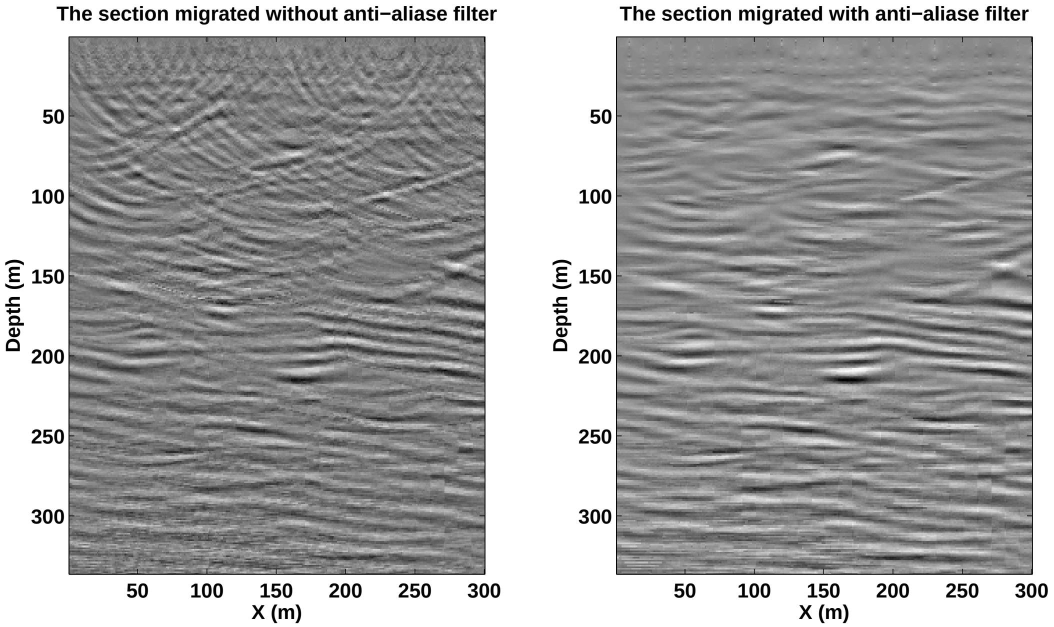

Figure 2.13: The sections migrated without (left) and with (right) anti-aliase filter. After applying an anti-aliase filter to the migration operator, the migration artifacts due to migration operator aliasing are effectively eliminated.

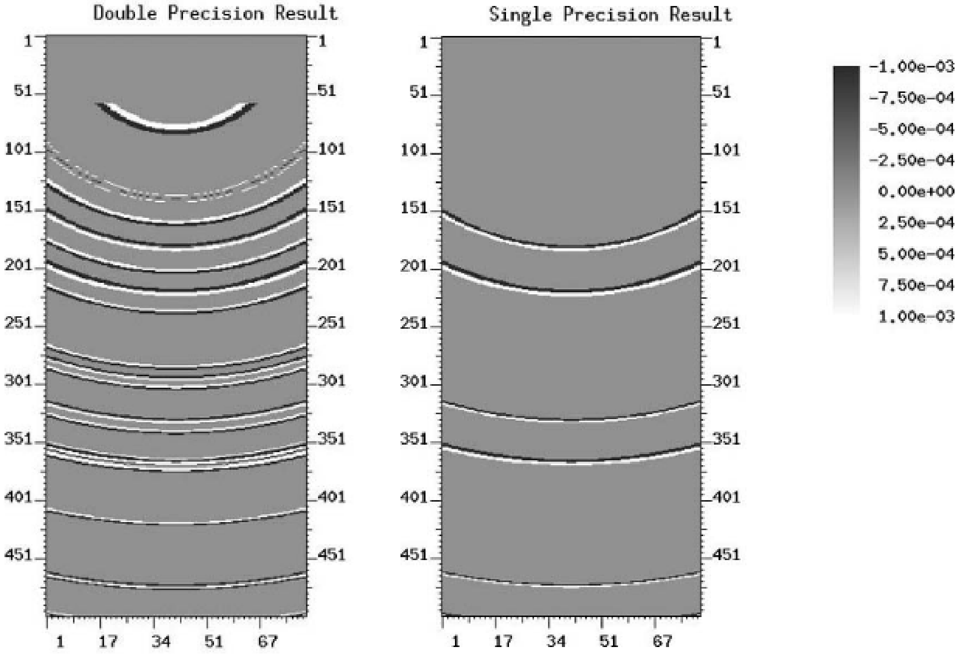

Figure 2.14: The migrated sections done in double precision (left) and single (right) for an identical synthetic data set with large amplitude difference (Ray Abma, 2006).

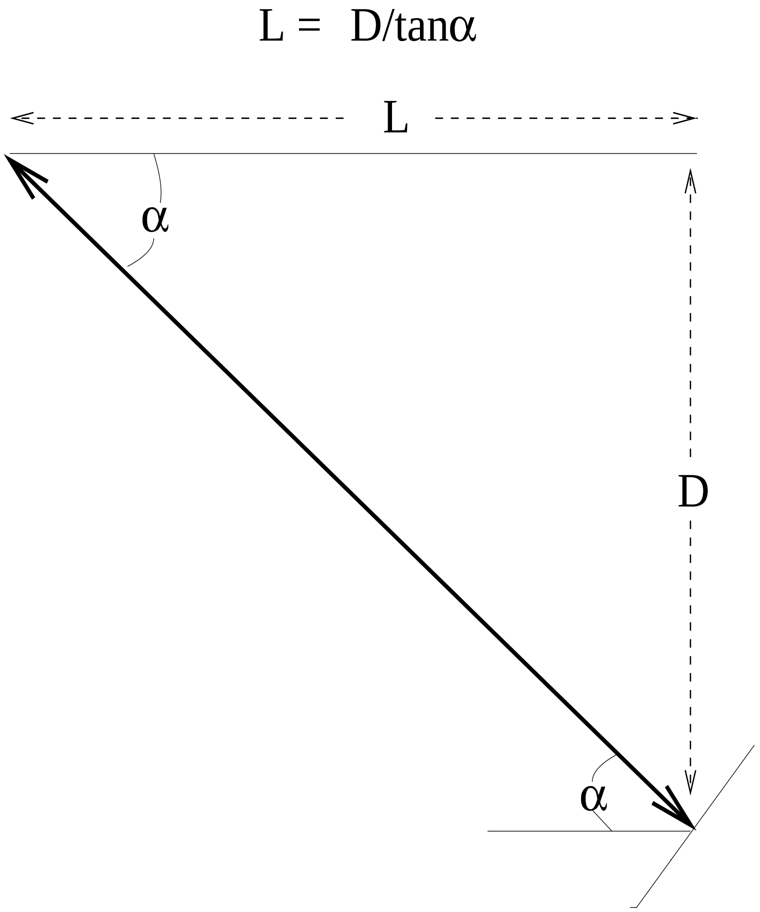

Figure 2.15: Aperture width L should be computed by estimating the maximum dip angle α of a reflector and its depth D, so that $L = D/tan\alpha$.

2.4 Time Migration vs Depth Migration

Depth migration in a variable velocity medium can be effected by replacing the $t = r/c$ statement in the MATLAB script by the traveltime obtained from ray tracing seismic energy from the trace position to the migrated image point. This is the correct procedure for downward continuing recorded energy to its place of origin, and such traveltimes can computed by a finite-difference solution to the eikonal equation.

Sometimes the velocity is not known very well so that the depth migration results do not look very good. In this case the geophysicists try to use a degraded form of migration known as time migration. Time migration is effected by replacing the $t = r/c$ statement in the MATLAB script by the NMO traveltime computed from the RMS velocity. The depth loop is replaced by a loop over the zero-offset traveltimes. This replacement automatically assumes an earth model with vertically varying velocity, negligible ray bending, and no lateral velocity variations. The reflection event is smeared along a circle, as shown in Figure 3.1. Note that this type of migration does not require ray tracing so it is faster than depth migration. The problem is that it still smears energy along circles, which is incorrect if there is significant ray bending across interfaces. This leads to the mispositioning of the lateral positions of irregular reflectors. As an example, the migration of the field data clearly images the dipping layer while the time migrated Kirchhoff migration smeared the reflector position. Below is a time-migration MATLAB code.

```
for ixtrace=1:ntrace;        Loop over ZO trace indicies
 for xs=istart:iend;         Loop over model space indicies (xs,t0)
 for t0=1:nt0;
  r = vnmo(t0)*t0           Compute geometrical-spreading radius
  time = sqrt( (t0/dt)^2 +  (x/vnmo(t0)/dt)^2 ); Compute 1-way time to circle
  m(xs,t0) = m(xs,t0) + data(ixtrace,time)/r; Smear/sum reflections into (x,t0)
 end;
 end;
end
```

One effect of time migration is that the time migration images sometimes looks better than depth migration images. This is because the images are plotted in offset vs two-way vertical time space, so there will be no wavelet stretch due to a faster velocity medium. That is, in depth migration the wavelet is smeared within the fat semicircle, but if the velocity of the semicircle is faster at depth (longer wavelength for a given period) then the upper part of donut is thin and lower part of donut is fat. Compare the stretching effect in Figure 2.7 to the no-stretch time migration section in Figure 2.8. Thankfully, time migration looks like it is becoming less common because of the inaccuracies in positioning events.

However, time migration is preferred if the velocity model is not very well known. Why? Because the NMO velocity is obtained by looking for the best hyperbola that most coherently stacks reflections. Thus, time migration focuses energy as well as any summation along hyperbolas can hope to achieve. Compare this to depth migration with a crummy velocity model. For a crummy velocity model we are summing energy along a correspondingly crummy quasi-hyperbola, resulting in a crummy focused image. Crumbs in, crumbs out.

2.5 Spatial Resolution

What is the minimum separation between two point scatterers that can be resolved in a migrated section? This minimum distance is known as the spatial resolution of the migrated section, where the horizontal resolution will differ from the vertical resolution. The spatial resolution will largely be a function of the wavelength λ, recording aperture L and/or depth of the scatterer.

The spatial resolution is quantitatively estimated by using the idea of a Fresnel zone (Elmore and Heald, 1969), where the first Fresnel zones makes the largest contribution to the recorded reflection signal, with a negligible contribution from the higher-order Fresnel zones. The definition of the 1st reflection Fresnel zone is the area on the reflector such that any reflection ray path (see Figure 3.5) from source-to-reflector-geophone differs in total path length by no more than a $\lambda/2$ (or arrival time difference of $T/2$). Therefore, two point scatterers located within each others first Fresnel zone will not be clearly distinguishable from one another on a migrated section because of interference effects. An example of imaging data for several neighboring point scatterers at different depths is given in Figure 3.3. Here, the lateral resolution becomes worse with depth because the migration circles become flatter with depth, so that the deepest pair of scatterers is not resolvable in the migration image. The migration ellipses interfere such that only one bump rather than two appear in the sideview image (Schuster, 1996; Chen and Schuster, 1999).

An intuitive picture of resolution limits is given in Figure 3.2. Here, two traces are used to resolve the location of a scatterer, where the intersection of the migration donuts determines the approximate location of the point scatterer. Note, the width (i.e., horizontal resolution limit) of the intersection zone is controlled by the width of the far-trace donut at the scatterer point, while vertical height (i.e., vertical resolution limit) of the intersection zone is controlled by the thickness of the near-trace donut at the scatterer point. More generally, vertical resolution limits are controlled by the near-offset traces and the horizontal resolution limit is controlled by the far-offset traces. The next two sections quantify these resolution limits with analytic formulas.

Poststack Migration Resolution. As shown in Figure 3.5, a Fresnel zone encompasses a spatial region in which the length difference between the shortest and longest reflection ray is $1/2\lambda$. For the ZO trace in Figure 3.5, the 1st horizontal Fresnel zone has a radius of

$$\begin{aligned} T/2 &= T_{ACA} - T_{ABA}, \\ &= 2AB\sqrt{1+BC^2/AB^2}/c - 2*AB/c, \end{aligned}$$

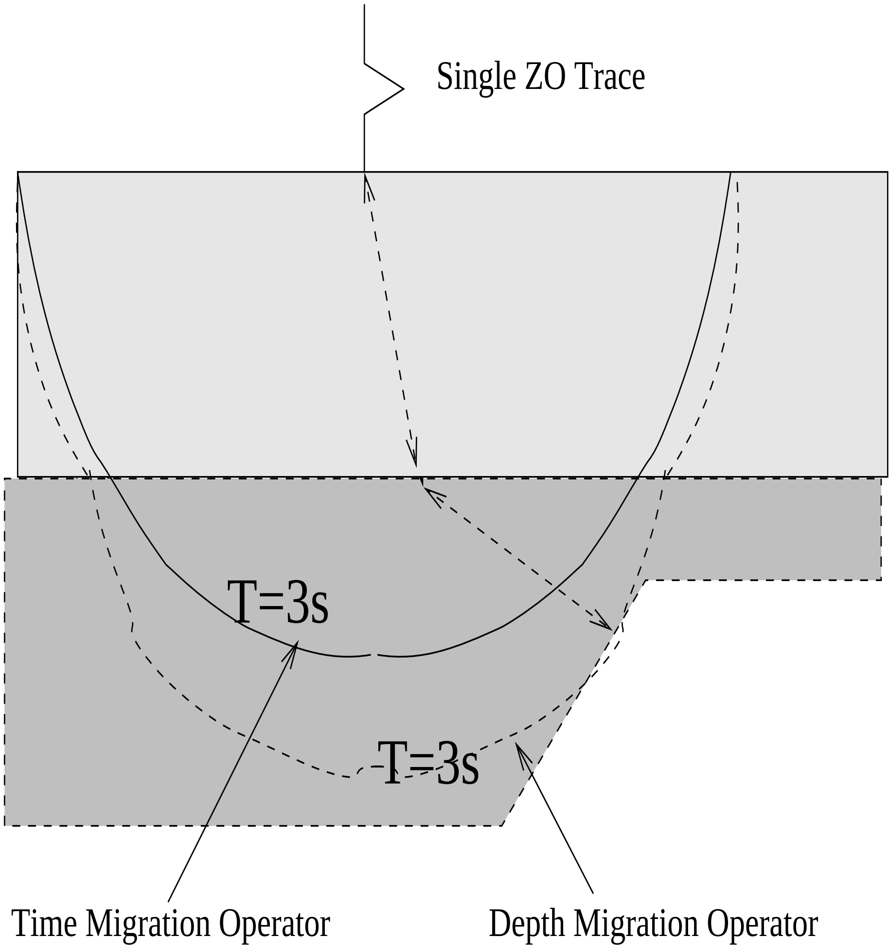

Figure 2.16: ZO time migration circles do not take into account raybending effects, so the result is that time migration laterally mispositions the events. Depth migration takes into account raybending across interfaces as well as lateral velocity variations, and so will correctly image the ZO reflection energy. The problem is that the ZO trace is formed by stacking CMP traces using a 1D NMO formula, which can be inappropriate for earth models with strong lateral velocity variations. The solution is prestack depth migration

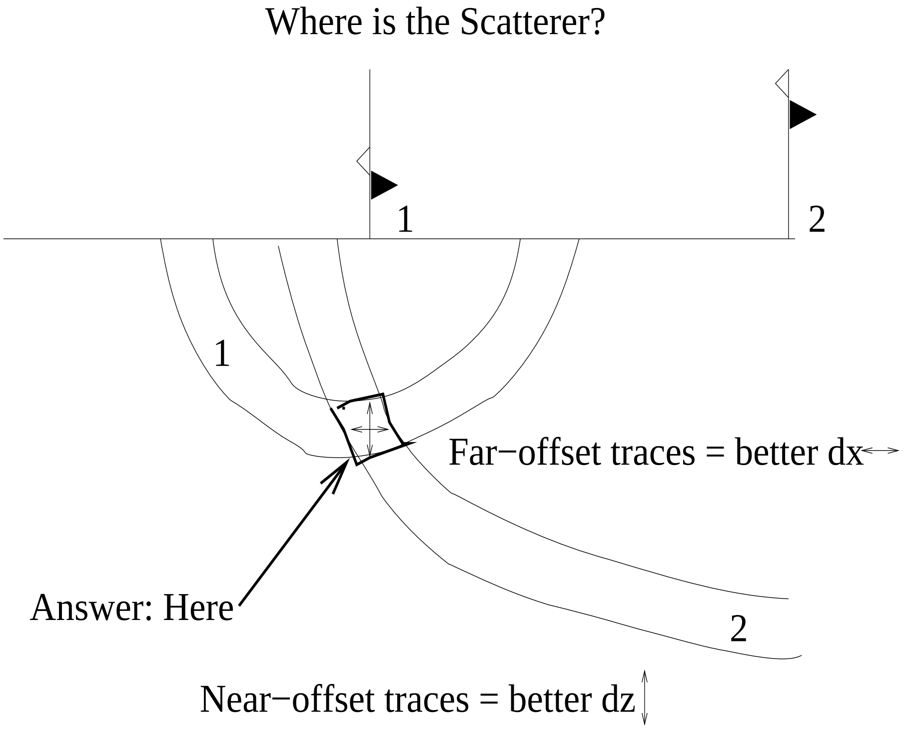

Figure 2.17: Where is the scatterer located that explains the reflections in the near- and far-offset ZO traces? Answer: The quadrilateral intersection zone. The width of the intersection zone is controlled by the far-offset (i.e., farthest from the scatterer) trace while its height is controlled by the near-offset (i.e., nearest to scatterer) trace.

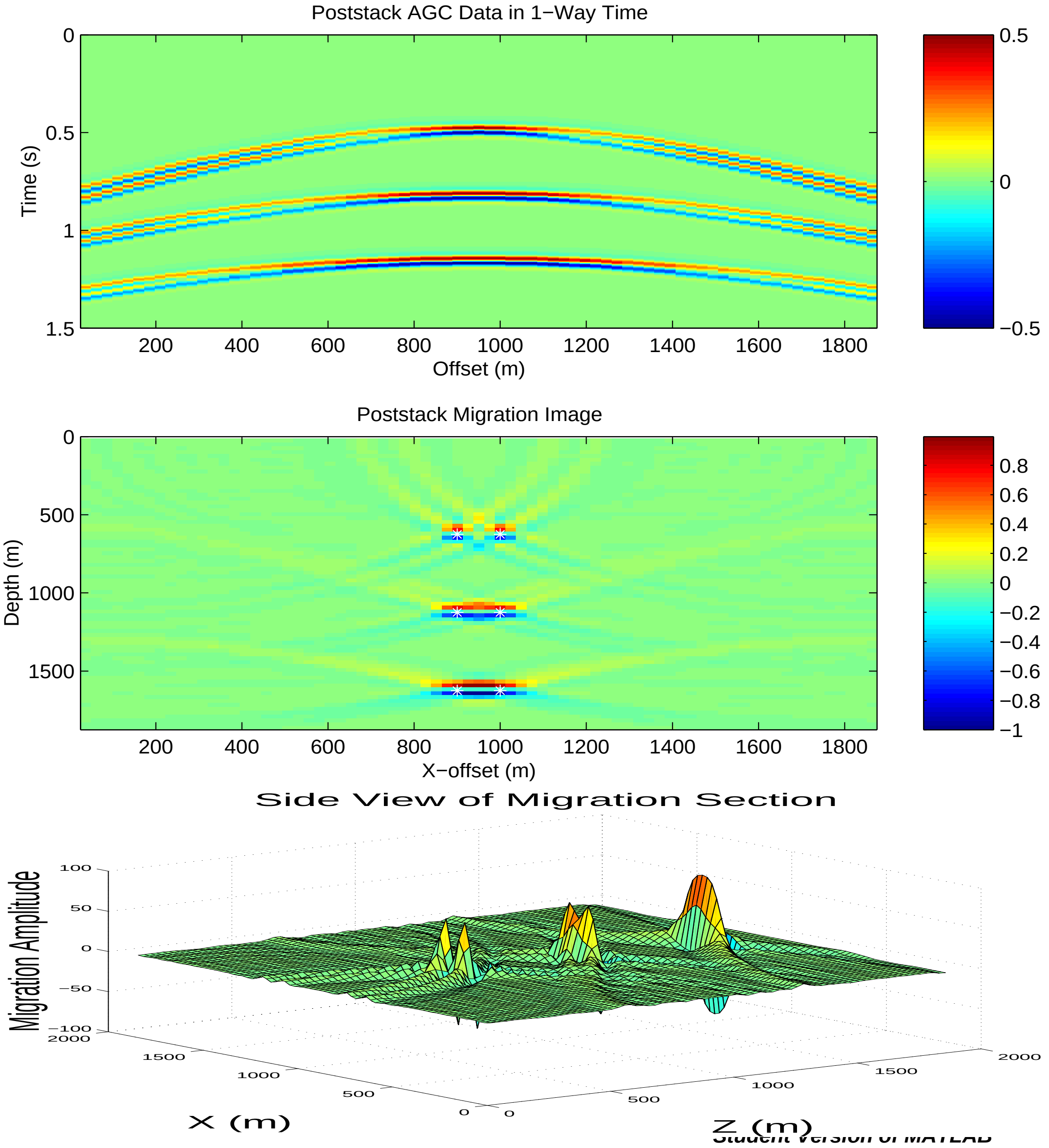

Figure 2.18: (Top) ZO data (middle and bottom) migration images for a model with 3 pairs of neighboring scatterers (white stars). Lateral resolution becomes worse with depth because the migration circles become less tilted and Fresnel zones become wider. The pair of scatterers separated by 125 m at $z = 1700$ m are not resolvable, where the central frequency of wavelet is 15 Hz, velocity is 1500 m/s, and the aperture width is 1875 m.

$$\begin{aligned}
&\approx && 2AB(1+0.5BC^2/AB^2)/c - 2*AB/c,\\
&= && BC^2/(AB*c),
\end{aligned} \tag{2.12}$$

and rearranging, noting that $cT=\lambda$, setting $AB = z_{depth}$ and solving for BC gives

$$BC \quad = dx = \quad \sqrt{\lambda * z_{depth}/2}. \tag{2.13}$$

where $AB = z_{depth}$ is the depth of the scatterer directly beneath the ZO trace. The length BC is proportional to the horizontal resolution directly below a ZO trace, and so horizontal resolution becomes better for smaller wavelengths and shallower scatterers.

But what is the horizontal resolution of a ZO trace for a scatterer laterally offset from the ZO trace? We can cook up an analytic formula similar to the above, except now we use a short cut. That is, differentiate the traveltime equation 2.1 w/r to x to get

$$dt/dx \quad = \quad 2*(x-x_g)/(\sqrt{(x-x_g)^2+z^2}*c), \tag{2.14}$$

where the factor 2 comes about because we are using the two-way traveltime equation. Setting $dt = T/2$ and solving for dx gives

$$\begin{aligned}
dx &= (cT\sqrt{(x-x_g)^2+z^2})/(4(x-x_g)),\\
&= \lambda\sqrt{(x-x_g)^2+z^2}/(4*(x-x_g)).
\end{aligned} \tag{2.15}$$

We seek the parameters that give the minimum resolution value dx and denote this as $\Delta x = min\ dx$. If the scatterer depth z is much larger than the aperture $L = max(x-x_g)$, then equation 3.4 becomes

$$\begin{aligned}
\Delta x \quad = min(dx) = &\quad .25T\sqrt{L^2+z^2}*c/L,\\
= &\quad .25\lambda z\sqrt{1+L^2/z^2}/L.\\
\approx &\quad .25\lambda z/L,
\end{aligned} \tag{2.16}$$

for $z >> L$. Thus larger apertures, shallower scatterers, and smaller wavelengths lead to better horizontal resolution.

Similar considerations show that the vertical resolution can be obtained by subtracting $T_{ABA} - T_{ACA}$ for the vertical raypath shown in the right plot of Figure 3.5:

$$\begin{aligned}
T/2 &= T_{ACA} - T_{ABA},\\
&= 2*ABA/c - 2*ACA/c,\\
&= 2*BC/c.
\end{aligned} \tag{2.17}$$

Solving for BC gives

$$BC = \quad \Delta z \quad = \lambda/4. \tag{2.18}$$

Figure 3.4 shows the depth migrated traces for reflections from a thinning bed, and suggests that we can distinguish the there are two reflectors from the migration section if their thickness is greater than or equal to $1/4\lambda$.

Equation 3.7 says that vertical resolution does not depend on the recording aperture. In designing a recording array, the horizontal and vertical resolution limits can be estimated (see Figure 3.5) for ZO migrated sections by the formulas 3.5 and 3.7. In fact, equation 3.5 can be used to validate that the deepest pair of scatterers in Figure 3.3 are not laterally resolvable.

Prestack Migration Resolution. Similar considerations define the resolution limits for migrating a prestack gather of CMP traces, as shown in Figure 3.6. Here, the minimum vertical resolution of the migrated gather is governed by the migrated ZO trace, which is $\Delta z = \lambda/4$. On the other hand, the far-offset trace will govern the minimum horizontal resolution, which is $dx = \lambda * z/(4L)$, where L is the recording aperture.

A formula for Δx can be derived by a procedure similar to that of the ZO trace resolution; or by differentiating the traveltime equation

$$\begin{aligned}\tau &= \tau_{sx} + \tau_{xg},\\ &= \overbrace{\sqrt{(x_s-x)^2+(y_s-y)^2+(z_s-z)^2}/c}^{downgoing\ time} + \overbrace{\sqrt{(x_g-x)^2+(y_g-y)^2+(z_g-z)^2}/c}^{upgoing\ time},\end{aligned} \tag{2.19}$$

with respect to the x-coordinate x of the trial image point, $\partial\tau/\partial x$, setting $d\tau \rightarrow T/2$, and solving for dx. These are known as migration stretch formula and give both stretch and resolution estimates along the x and z directions.

How does one find the minimum dz and dx at image point (x_0, y_0, z_0) for an entire ensemble of prestack traces? Simply find the source receiver pairs that minimize these resolution estimates.

The above formulas are restricted to homogeneous velocity media, but the real earth is inhomogeneous in velocity. Resolution estimates can be obtained for inhomogeneous media by using the simple idea that the sum of the unit vectors of the downgoing and negative upgoing rays is proportional to the wavenumber $\mathbf{k_{model}}$ of the model that can be reconstructed For example, the ZO vertical rays suggest that the wavenumber of the model that can be reconstructed is proportional to $\vec{k}_{mocel} = (0, 0, 2\pi/\lambda)$. Note, the k_x and k_y components are zero because the ray is perfectly vertical and has no x-y component (Gesbert, 2003). Formally, the model wavenumber that can be reconstructed (see Figure 3.7) is given by

$$\vec{k} = \omega\nabla(\tau_{down}(x) + \tau_{up}(x)). \tag{2.20}$$

Similar considerations can be used to estimate resolution for tomographic images (Sheng and Schuster, 2003).

Is it really important to be concerned about the subtle nuances of improving lateral resolution? Jianhua Yu shows in Figure 3.8 that modest lateral resolution leaves doubt about the existence of fault, but slightly improving this lateral resolution via migration deconvolution leaves no doubt about the existence of a fault.

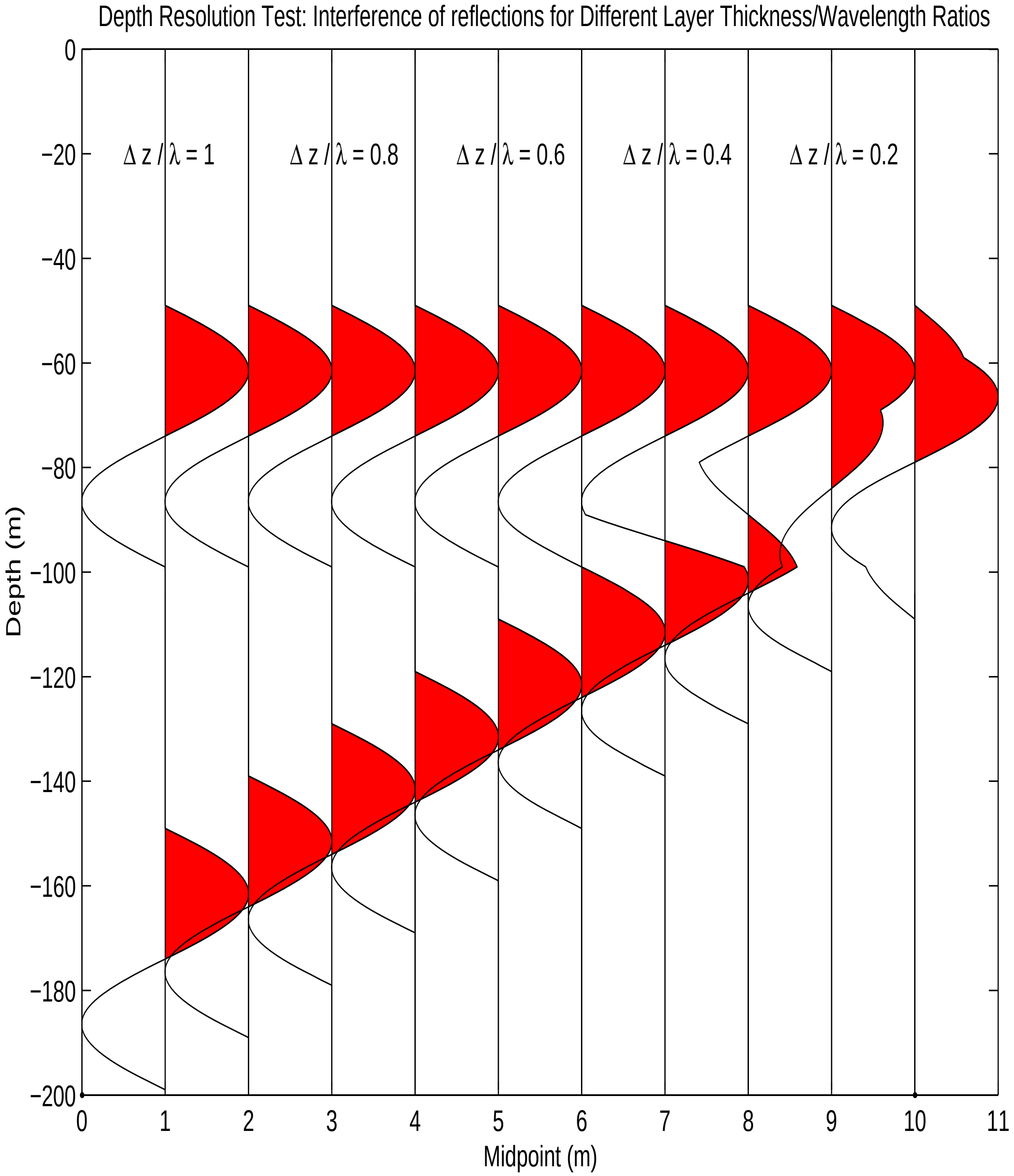

Figure 2.19: Vertical resolution limit is reached when the thickness between two neighboring reflectors $\Delta z = \lambda/4$.

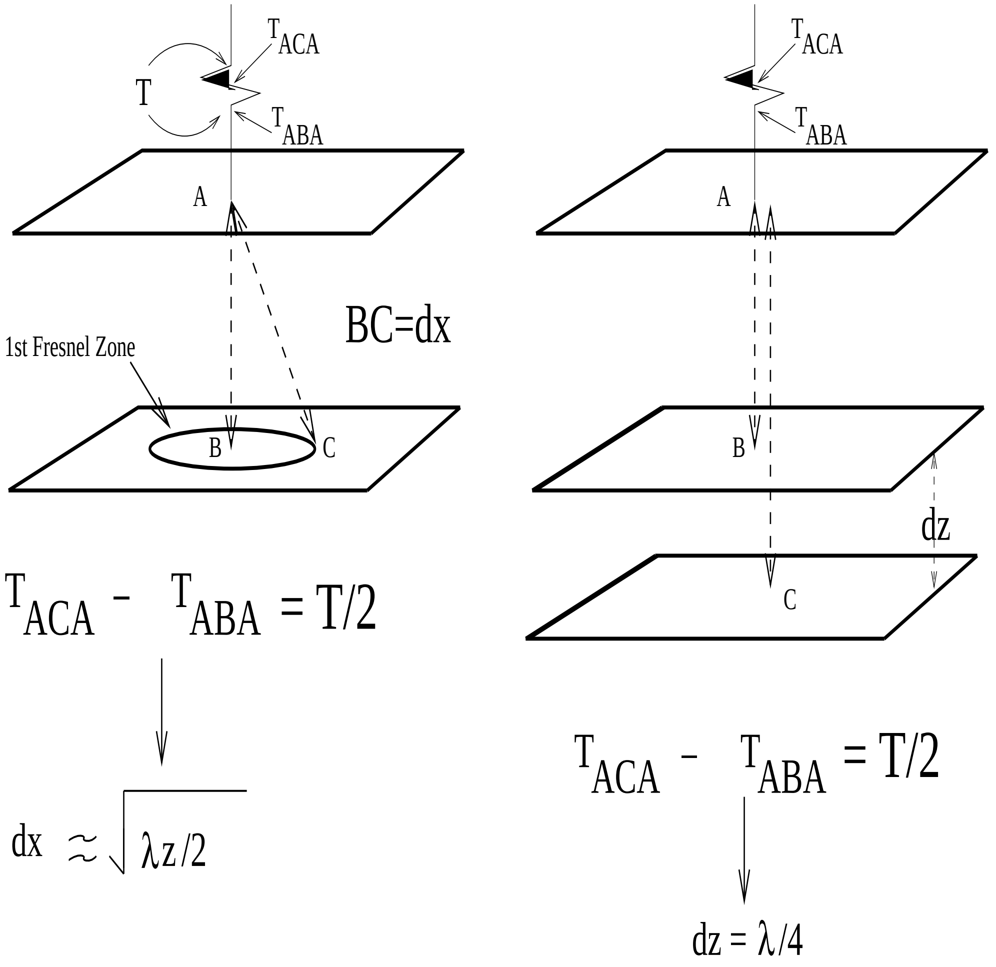

Figure 2.20: Extent of horizontal (left) and vertical (right) Fresnel zones for a ZO trace, where the 1st Fresnel zone defines the area where the difference in the shortest and longest raypath is equal to half the wavelength. The approximation formula for horizontal resolution is valid when AB is much larger than λ.

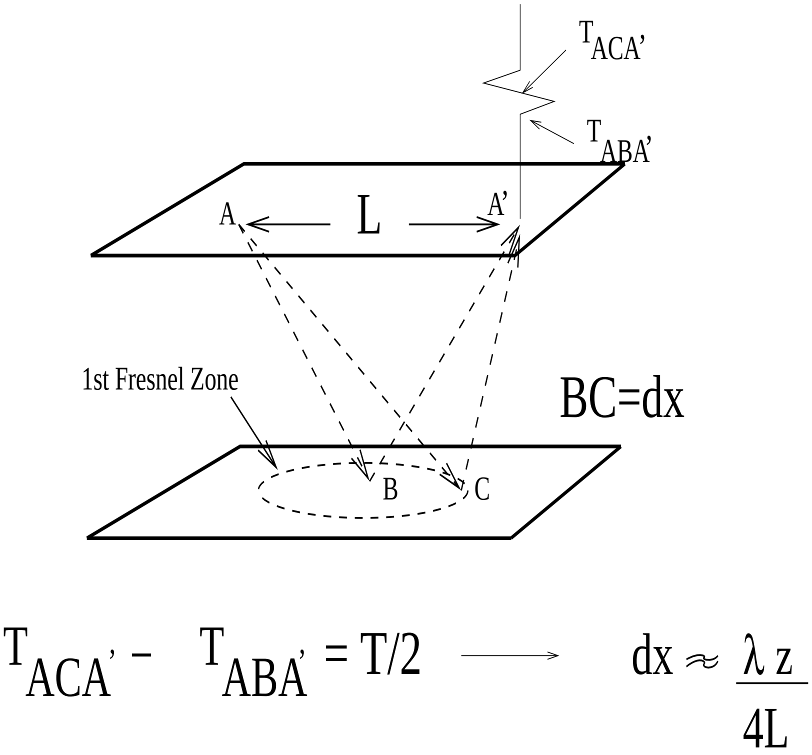

Figure 2.21: Extent of horizontal Fresnel zone for a trace with non-zero offset between the source and receiver. The 1st horizontal Fresnel zone for a reflection defines the area where the difference in the shortest and longest reflection raypaths is equal to half the wavelength.

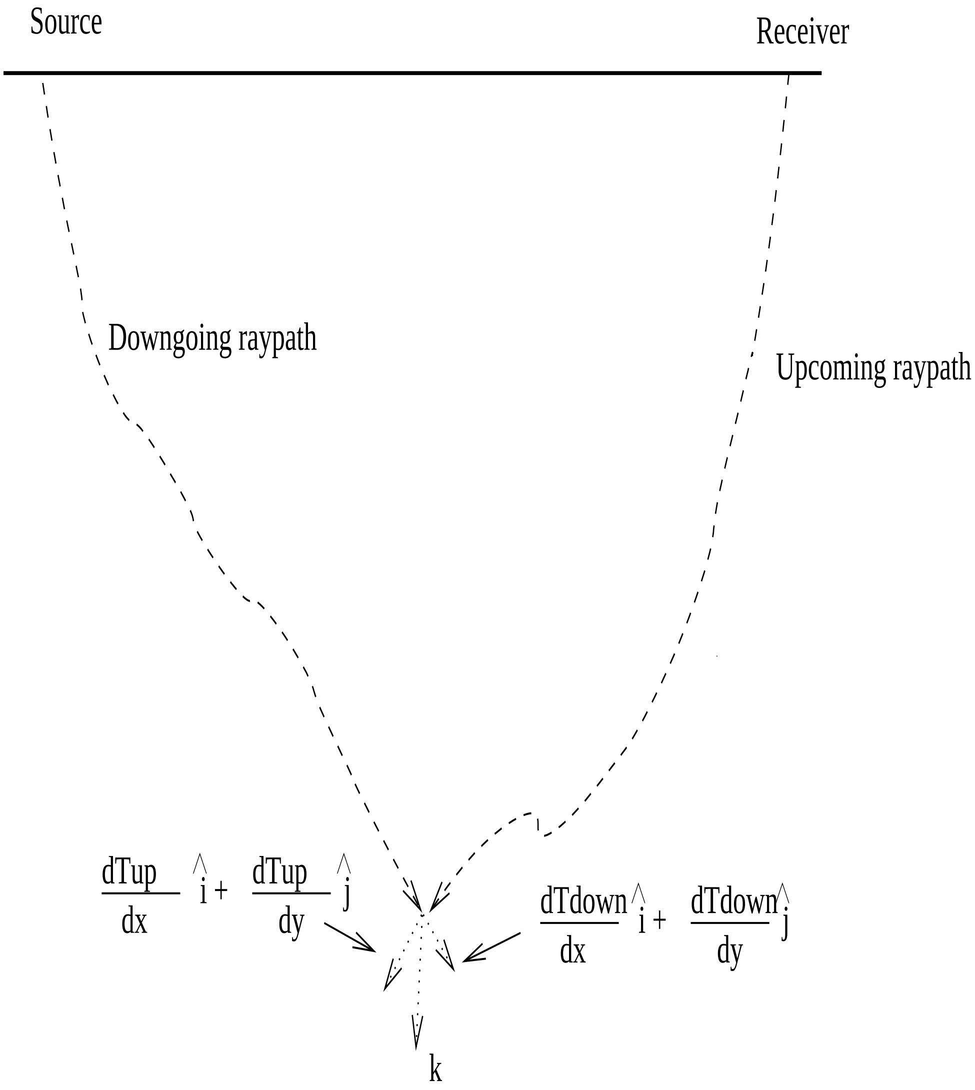

Figure 2.22: Wavenumber **k** of model that can be reconstructed by the downgoing and upgoing rays of the reflection. Here $\mathbf{k} = \omega(\nabla \mathbf{T_{down}} + \nabla \mathbf{T_{up}})$, so that wavenumbers that point sideways (down) indicate good lateral (vertical) resolution.

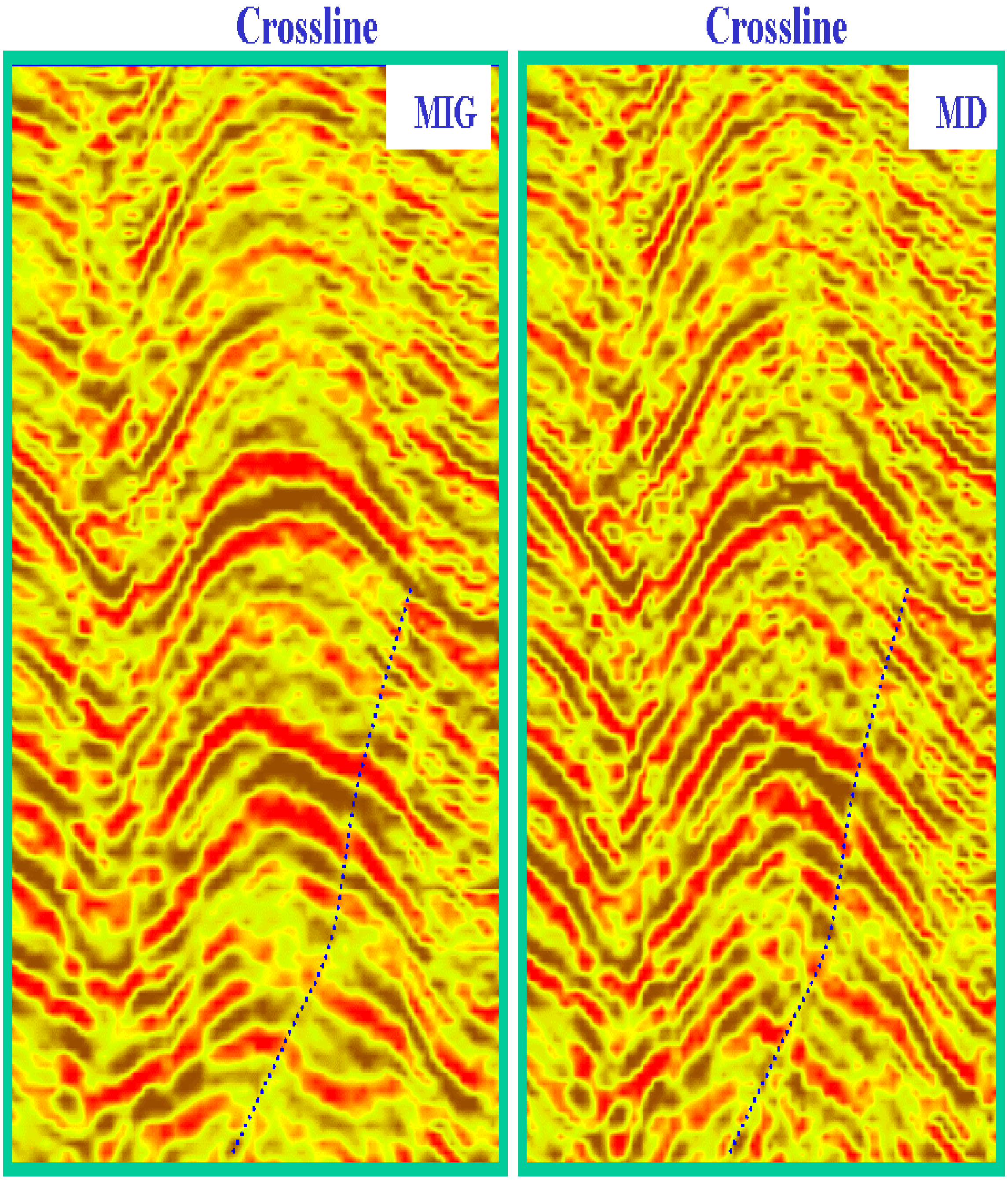

Figure 2.23: 3D prestack migration images (left) before and (right) after migration deconvolution. Lateral resolution improves by about 20 percent so that the right image leaves no doubt about the existence of a fault.

Beylkin Resolution → Migration Stretch. A simple interpretation of equation 3.9 is that it is equivalent to the formula for migration stretch. Specifically, the migration stretch formulas in the different coordinate directions are given by differentiating the traveltime formula 3.8 with respect to the coordinates of the trial image point (x, y, z):

$$\begin{aligned} \partial\tau/\partial x &= \partial\tau_{sx}/\partial x + \partial\tau_{xg}/\partial x, \\ \partial\tau/\partial y &= \partial\tau_{sx}/\partial y + \partial\tau_{xg}/\partial y, \\ \partial\tau/\partial z &= \partial\tau_{sx}/\partial z + \partial\tau_{xg}/\partial z. \end{aligned} \tag{2.21}$$

Using a Fresnel-zone argument, we set $\partial\tau \approx T/2$ and $\partial x \approx \Delta x$, $\partial y \approx \Delta y$ and $\partial z \approx \Delta z$ on the left hand side of the above equation, and rearrange terms to get analytical expressions for the resolution limits $(\Delta x, \Delta y, \Delta z)$, or migration stretch in the three coordinates similar to the expression in Figure 3.6. Here, T is the dominant period of the wavelet. Multiplying the three stretch formula in equation 3.10 by ω yields the components proportional to the Beylkin wavenumber formula in equation 3.9 (e.g., recall $\omega\partial\tau/\partial x = k_x$). This establishes the equivalency between Beylkin's fancy resolution formula and the well known migration stretch formulas.

2.6 Summary

The practical aspects of integral equation migration are reviewed. Migration can be viewed as either "smearing a time sample of data along the corresponding migration circle (or ellipse)", or equivalently it can be viewed as "summing energy along the appropriate hyperbola (for a fixed trial image point at **x** and source-receiver pair) and dumping it into the pixel centered at **x**". The latter view is illustrated in Figure 2.11, where shallower trial image ponts lead to more steeply dipping wings of the hyperbola. Since we are summing amplitudes along these hyperbola we must ensure that the dip along the migration hyperbola is not as steep as the trace spacing allows; otherwise the data are aliased.

A more economical migration can be carried out by ordering the loops so that the outer loops are over data space coordinates (i.e., traces), while the inner loops are over model space coordinates. This is because the data volume is five dimensional while the model volume is 3 dimensional; thus, IO cost is minimized if the trace sample is visited only once by having the outer loop over trace coordinates.

There are three critical parameters that should be selected prior to designing a seismic experiment or migrating seismic data:

- Spatial sampling interval Δx of geophones and sources. The spatial sampling interval is determined by the minimum horizontal wavelength λ_{min} of the seismic data such that $\lambda_{min} > 2\Delta x$. This minimum wavelength is estimated a priori from previous experiments in the area or from a test seismic experiment that spatially oversamples a shot gather and determines from this shot gather the minimum apparent wavelength in the data: $(dx/dt)_{min}T_{min} > 2\Delta x$. Normally, the surface waves are much slower than the body wave reflections (they travel along the surface at about the shear wave velocity at the near surface) so this would require too expensive of a geophone sampling interval. Instead companies will use an array of geophones (up to 70/group in Saudi Arabia!) for each group or channel to cancel out the slow moving surface wave yet retain the long wavelength body wave reflection.

- Aperture width. Wide angle reflections will allow for the capture of steeply dipping specular reflections. Estimation of the aperture width should use the formula given in Figure 2.15. An alternative estimation procedure is the Beylkin stretch formula where the user decides the acceptable resolution at a selected depth region and uses the stretch formulas to estimate aperture width. The best vertical resolution you can achieve is $\lambda_{min}/4$ but the best horizontal resolution is estimated by a complicated stretch formula that is a function of source and receiver coordinates.
- A digital anitaliasing filter should be applied to the data to eliminate operator aliasing.

The diffraction stack formula is acceptable when there is plenty of redundancy in the data (i.e., high fold) but the obliquity factor should be used if fold is low. Experience shows that the obliquity factor suppreses aliasing-like artifacts in the final migration image. Unlike depth migration, time migration does not suffer from migration stretch but does suffer from mispositioning of events in complex geologic areas. Therefore it is rarely used today for subsalt imaging. However, the velocity model must be finely tuned in order to get depth imaging to show a coherent section. This compares to time migration which usually provides a good looking image because the stacking velocity is used to estimate the time-migration velocity. The stacking velocity is robustly estimated by efficient and automatic velocity scans while the velocity model for depth migration is typically estimated by a time-consumming and tedious process (e.g., reflection tomography or migration velocity analysis).

2.7 Exercises

1. The CDP interval in Figure 7 is 50 m. The velocity at $z = 1$ km is 2 km/s and at $z = 2.5$ km it is 4 km/s, and the recording aperture is 350 CDP's wide for any shot point. Calculate the minimum horizontal and vertical resolutions for a prestack migration image at the points $(x, z) = (0\ km, 1\ km)$, $(x, z) = (1\ km, 1\ km)$, $(x, z) = (0\ km, 2.5\ km)$, and $(x, z) = (1\ km, 2.5\ km)$. Same question as before, except calculate minimum horizontal and vertical resolutions for a poststack migration image. Show work.

2. Using fat circles and fat ellipses, compare the vertical and horizontal resolution limits for poststack migration and prestack migration for a point at $(x, z) = (1\ km, 2.5\ km)$ in Figure 7. Assume a homogeneous velocity.

3. Convert your poststack depth migration code into a prestack time migration code. The output should be in the offset-time domain. Show poststack depth and time migration images.

4. Determine the maximum aperture for a seismic experiment in order to image $0 - 40$ degree dips at $z = 5$ km. Assume a homogeneous velocity of 5 km/s. What is

the minimum geophone spacing in order to not spatially alias the data? Assume a minimum wavelet period of 0.01 s. Clearly show steps in your reasoning.

5. Derive and use the Beylkin stretch formulas (starting point for derivation is equation 3.10) to estimate the best horizontal and vertical resolutions for a 12 km wide poststack depth section at the following coordinates: (0,12), (12,12), (6,12), (6,6), (0,6), (3,3), (0,12). Assume the origin of coordinate system is at upper left portion of migration section and positive z is pointing downward. Assume a homogeneous velocity of $v = 3\ km/s$ from 0-3 km, $v = 5\ km/s$ from 3-7 km, and any deeper than 7 km we have a velocity of 6 km/s. Assume a maximum useful frequency of 80 Hz. Assume straight rays everywhere. Why is there better horizontal resolution at shallow depths?

6. Time migrate the radar data from your lab exercise. Choose a suitable time migration velocity by trial and error. Show results. Which results look more coherent, the time migration or depth migration results? Why does depth migration suffer from migration stretch which is avoided by time migration. Wgat are benefits and liabilities of time migration vs depth migration?

7. Apply an antialiasing filter (equation 2.8 to your radar migration images. Select different cutoff frequencies as a function of depth (note, c in equation 2.7 varies as a function of depth).

8. Estimate the horizontal wavelength of surface waves and body wave reflections in the Saudi shot gather (from a previous lab). What is a good array interval that would suppress surface waves but retain body waves ion the data. Test your estimate by applying an N-point spatial averaging filter to the data, where N is length of your estimated filter. Show results.

Chapter 3

Time Migration and Resolution

In this section time migration is defined and its pitfalls and benefits are compared to depth migration. In the far-field approximation the resolution formula for analyzing a migration image is derived and its application to practical problems is analyzed.

3.1 Time Migration vs Depth Migration

Depth migration in a variable velocity medium can be effected by replacing the $t = r/c$ statement in the MATLAB script by the traveltime obtained from ray tracing seismic energy from the trace position to the migrated image point. This is the correct procedure for downward continuing recorded energy to its place of origin, and such traveltimes can computed by a finite-difference solution to the eikonal equation.

Sometimes the velocity is not known very well so that the depth migration results do not look very good. In this case the geophysicists try to use a degraded form of migration known as time migration. Time migration is effected by replacing the $t = r/c$ statement in the MATLAB script by the NMO traveltime computed from the RMS velocity. The depth loop is replaced by a loop over the zero-offset traveltimes. This replacement automatically assumes an earth model with vertically varying velocity, negligible ray bending, and no lateral velocity variations. The reflection event is smeared along a circle, as shown in Figure 3.1. Note that this type of migration does not require ray tracing so it is faster than depth migration. The problem is that it still smears energy along circles, which is incorrect if there is significant ray bending across interfaces. This leads to the mispositioning of the lateral positions of irregular reflectors. As an example, the migration of the field data clearly images the dipping layer while the time migrated Kirchhoff migration smeared the reflector position. Below is a time-migration MATLAB code.

```
for ixtrace=1:ntrace;       Loop over ZO trace indicies
 for xs=istart:iend;        Loop over model space indicies (xs,t0)
 for t0=1:nt0;
  r = vnmo(t0)*t0          Compute geometrical-spreading radius
  time = sqrt( (t0/dt)^2 + (x/vnmo(t0)/dt)^2 ); Compute 1-way time to circle
```

```
  m(xs,t0) = m(xs,t0) + data(ixtrace,time)/r; Smear/sum reflections into (x,t0)
 end;
 end;
end
```

One effect of time migration is that the time migration images sometimes looks better than depth migration images. This is because the images are plotted in offset vs two-way vertical time space, so there will be no wavelet stretch due to a faster velocity medium. That is, in depth migration the wavelet is smeared within the fat semicircle, but if the velocity of the semicircle is faster at depth (longer wavelength for a given period) then the upper part of donut is thin and lower part of donut is fat. Compare the stretching effect in Figure 2.7 to the no-stretch time migration section in Figure 2.8. Thankfully, time migration looks like it is becoming less common because of the inaccuracies in positioning events.

However, time migration is preferred if the velocity model is not very well known. Why? Because the NMO velocity is obtained by looking for the best hyperbola that most coherently stacks reflections. Thus, time migration focuses energy as well as any summation along hyperbolas can hope to achieve. Compare this to depth migration with a crummy velocity model. For a crummy velocity model we are summing energy along a correspondingly crummy quasi-hyperbola, resulting in a crummy focused image. Crumbs in, crumbs out.

3.2 Spatial Resolution

What is the minimum separation between two point scatterers that can be resolved in a migrated section? This minimum distance is known as the spatial resolution of the migrated section, where the horizontal resolution will differ from the vertical resolution. The spatial resolution will largely be a function of the wavelength λ, recording aperture L and/or depth of the scatterer.

The spatial resolution is quantitatively estimated by using the idea of a Fresnel zone (Elmore and Heald, 1969), where the first Fresnel zones makes the largest contribution to the recorded reflection signal, with a negligible contribution from the higher-order Fresnel zones. The definition of the 1st reflection Fresnel zone is the area on the reflector such that any reflection ray path (see Figure 3.5) from source-to-reflector-geophone differs in total path length by no more than a $\lambda/2$ (or arrival time difference of $T/2$). Therefore, two point scatterers located within each others first Fresnel zone will not be clearly distinguishable from one another on a migrated section because of interference effects. An example of imaging data for several neighboring point scatterers at different depths is given in Figure 3.3. Here, the lateral resolution becomes worse with depth because the migration circles become flatter with depth, so that the deepest pair of scatterers is not resolvable in the migration image. The migration ellipses interfere such that only one bump rather than two appear in the sideview image (Schuster, 1996; Chen and Schuster, 1999).

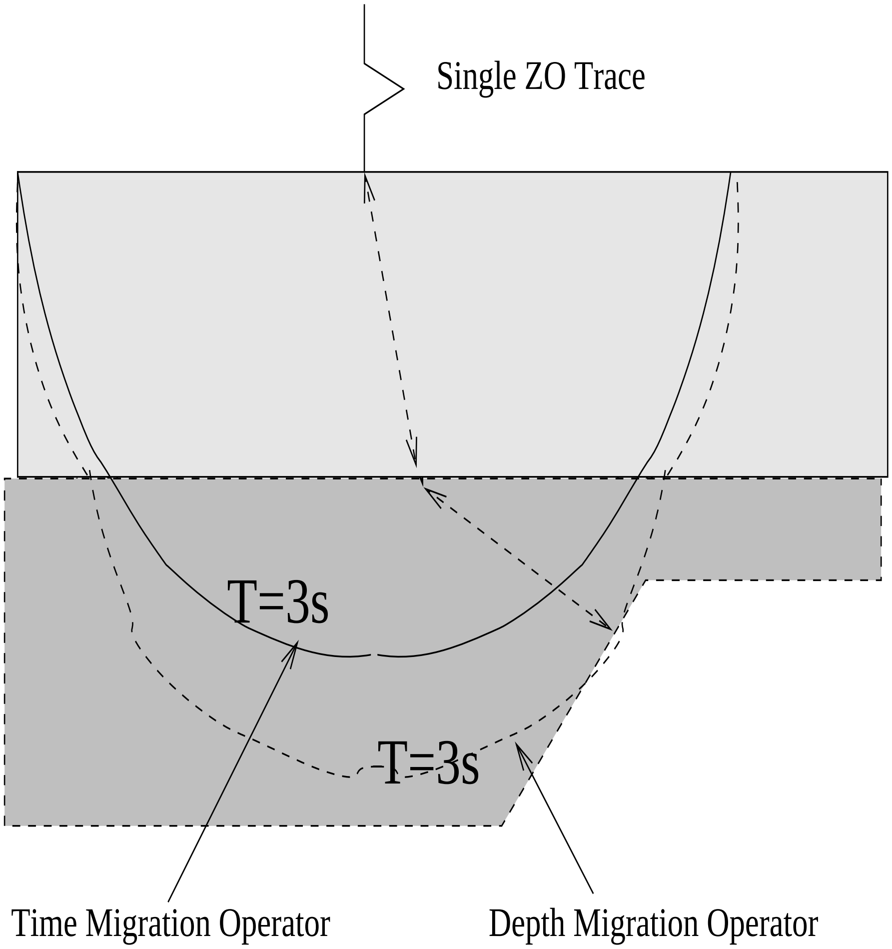

Figure 3.1: ZO time migration circles do not take into account raybending effects, so the result is that time migration laterally mispositions the events. Depth migration takes into account raybending across interfaces as well as lateral velocity variations, and so will correctly image the ZO reflection energy. The problem is that the ZO trace is formed by stacking CMP traces using a 1D NMO formula, which can be inappropriate for earth models with strong lateral velocity variations. The solution is prestack depth migration

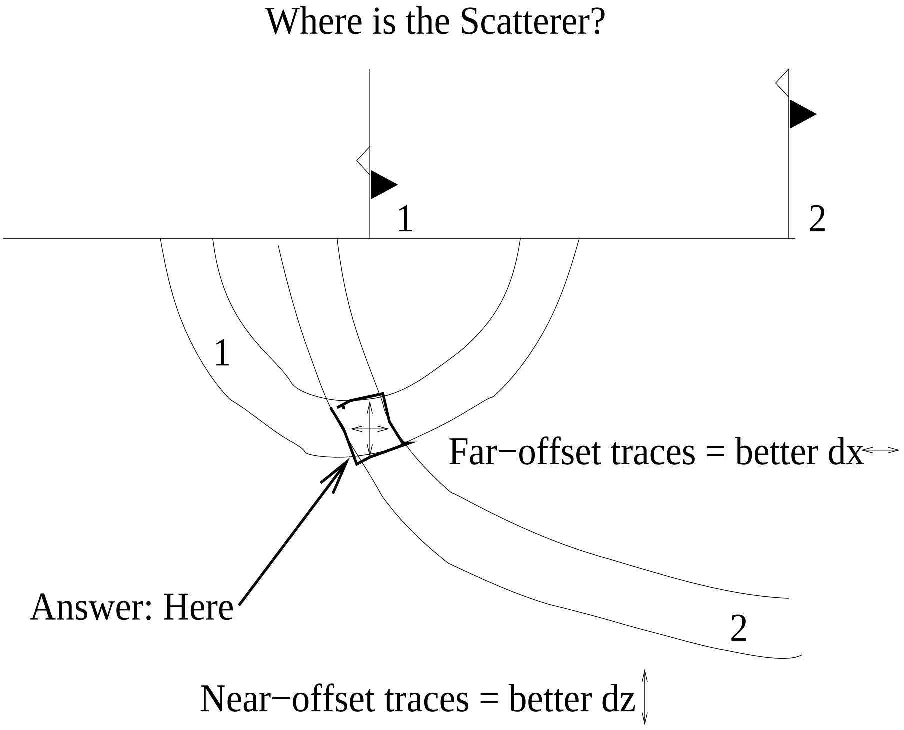

Figure 3.2: Where is the scatterer located that explains the reflections in the near- and far-offset ZO traces? Answer: The quadrilateral intersection zone. The width of the intersection zone is controlled by the far-offset (i.e., farthest from the scatterer) trace while its height is controlled by the near-offset (i.e., nearest to scatterer) trace.

An intuitive picture of resolution limits is given in Figure 3.2. Here, two traces are used to resolve the location of a scatterer, where the intersection of the migration donuts determines the approximate location of the point scatterer. Note, the width (i.e., horizontal resolution limit) of the intersection zone is controlled by the width of the far-trace donut at the scatterer point, while vertical height (i.e., vertical resolution limit) of the intersection zone is controlled by the thickness of the near-trace donut at the scatterer point. More generally, vertical resolution limits are controlled by the near-offset traces and the horizontal resolution limit is controlled by the far-offset traces. The next two sections quantify these resolution limits with analytic formulas.

Poststack Migration Resolution. As shown in Figure 3.5, a Fresnel zone encompasses

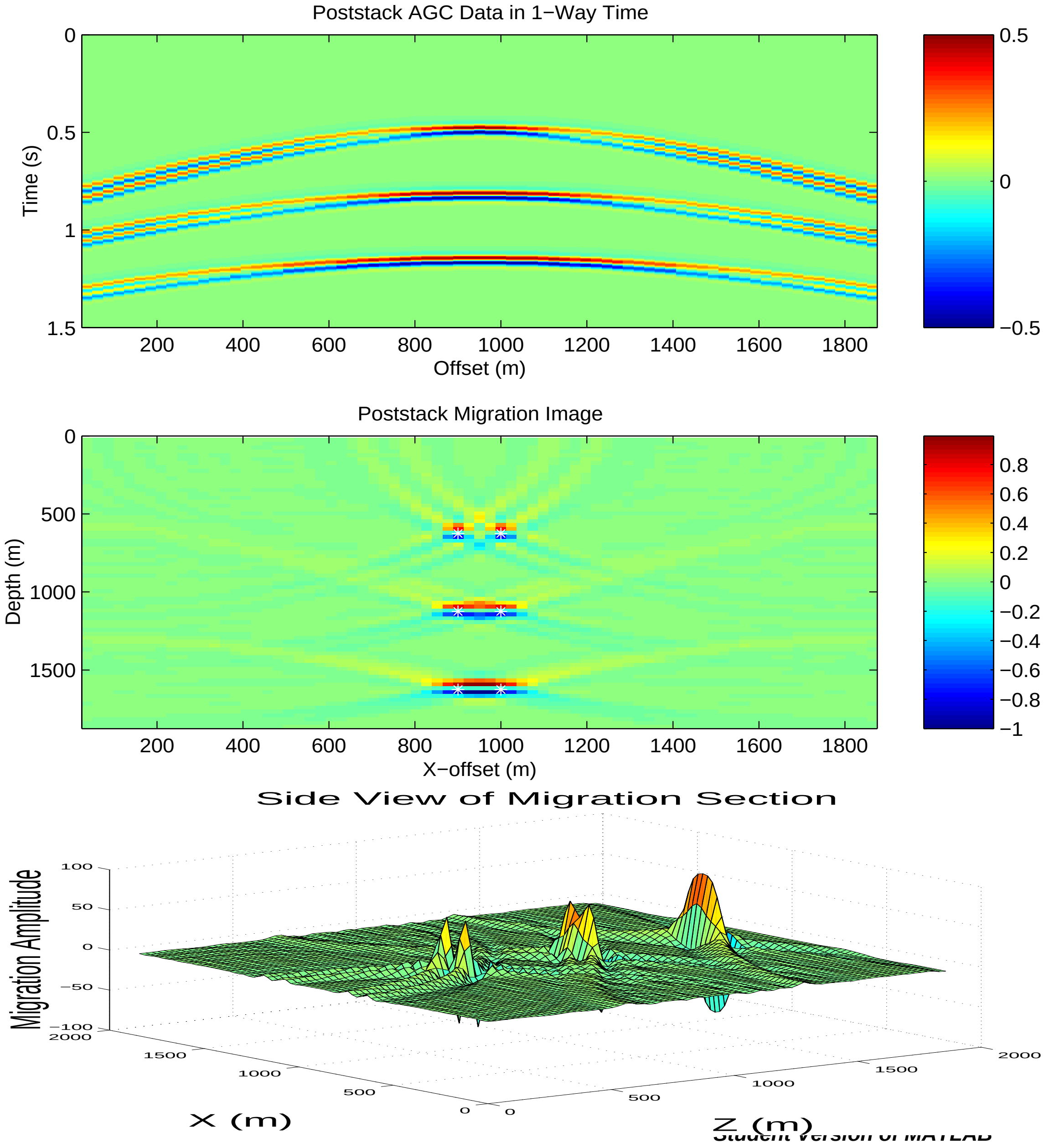

Figure 3.3: (Top) ZO data (middle and bottom) migration images for a model with 3 pairs of neighboring scatterers (white stars). Lateral resolution becomes worse with depth because the migration circles become less tilted and Fresnel zones become wider. The pair of scatterers separated by 125 m at $z = 1700$ m are not resolvable, where the central frequency of wavelet is 15 Hz, velocity is 1500 m/s, and the aperture width is 1875 m.

a spatial region in which the length difference between the shortest and longest reflection ray is $1/2\lambda$. For the ZO trace in Figure 3.5, the 1st horizontal Fresnel zone has a radius of

$$\begin{aligned}
T/2 &= T_{ACA} - T_{ABA}, \\
&= 2AB\sqrt{1 + BC^2/AB^2}/c - 2 * AB/c, \\
&\approx 2AB(1 + 0.5BC^2/AB^2)/c - 2 * AB/c, \\
&= BC^2/(AB * c),
\end{aligned} \tag{3.1}$$

and rearranging, noting that $cT = \lambda$, setting $AB = z_{depth}$ and solving for BC gives

$$BC \quad = dx = \quad \sqrt{\lambda * z_{depth}/2}. \tag{3.2}$$

where $AB = z_{depth}$ is the depth of the scatterer directly beneath the ZO trace. The length BC is proportional to the horizontal resolution directly below a ZO trace, and so horizontal resolution becomes better for smaller wavelengths and shallower scatterers.

But what is the horizontal resolution of a ZO trace for a scatterer laterally offset from the ZO trace? We can cook up an analytic formula similar to the above, except now we use a short cut. That is, differentiate the traveltime equation 2.1 w/r to x to get

$$dt/dx \quad = \quad 2 * (x - x_g)/(\sqrt{(x - x_g)^2 + z^2} * c), \tag{3.3}$$

where the factor 2 comes about because we are using the two-way traveltime equation. Setting $dt = T/2$ and solving for dx gives

$$\begin{aligned}
dx &= (cT\sqrt{(x - x_g)^2 + z^2})/(4(x - x_g)), \\
&= \lambda\sqrt{(x - x_g)^2 + z^2}/(4 * (x - x_g)).
\end{aligned} \tag{3.4}$$

We seek the parameters that give the minimum resolution value dx and denote this as $\Delta x = min\ dx$. If the scatterer depth z is much larger than the aperture $L = max(x - x_g)$, then equation 3.4 becomes

$$\begin{aligned}
\Delta x \quad = min(dx) = &\quad .25T\sqrt{L^2 + z^2} * c/L, \\
= &\quad .25\lambda z\sqrt{1 + L^2/z^2}/L, \\
\approx &\quad .25\lambda z/L,
\end{aligned} \tag{3.5}$$

for $z >> L$. Thus larger apertures, shallower scatterers, and smaller wavelengths lead to better horizontal resolution.

Similar considerations show that the vertical resolution can be obtained by subtracting $T_{ABA} - T_{ACA}$ for the vertical raypath shown in the right plot of Figure 3.5:

$$\begin{aligned}
T/2 &= T_{ACA} - T_{ABA}, \\
&= 2 * ABA/c - 2 * ACA/c, \\
&= 2 * BC/c.
\end{aligned} \tag{3.6}$$

Solving for BC gives

$$BC = \quad \Delta z \quad = \lambda/4. \tag{3.7}$$

Figure 3.4 shows the depth migrated traces for reflections from a thinning bed, and suggests that we can distinguish there are two reflectors from the migration section if their thickness is greater than or equal to $1/4\lambda$.

Equation 3.7 says that vertical resolution does not depend on the recording aperture. In designing a recording array, the horizontal and vertical resolution limits can be estimated (see Figure 3.5) for ZO migrated sections by the formulas 3.5 and 3.7. In fact, equation 3.5 can be used to validate that the deepest pair of scatterers in Figure 3.3 are not laterally resolvable.

Prestack Migration Resolution. Similar considerations define the resolution limits for migrating a prestack gather of CMP traces, as shown in Figure 3.6. Here, the minimum vertical resolution of the migrated gather is governed by the migrated ZO trace, which is $\Delta z = \lambda/4$. On the other hand, the far-offset trace will govern the minimum horizontal resolution, which is $dx = \lambda * z/(4L)$, where L is the recording aperture.

A formula for Δx can be derived by a procedure similar to that of the ZO trace resolution; or by differentiating the traveltime equation

$$\begin{aligned}\tau &= \tau_{sx} + \tau_{xg}, \\ &= \overbrace{\sqrt{(x_s-x)^2+(y_s-y)^2+(z_s-z)^2}/c}^{\textit{downgoing time}} + \overbrace{\sqrt{(x_g-x)^2+(y_g-y)^2+(z_g-z)^2}/c}^{\textit{upgoing time}},\end{aligned} \tag{3.8}$$

with respect to the x-coordinate x of the trial image point, $\partial\tau/\partial x$, setting $d\tau \rightarrow T/2$, and solving for dx. These are known as migration stretch formula and give both stretch and resolution estimates along the x and z directions.

How does one find the minimum dz and dx at image point (x_0, y_0, z_0) for an entire ensemble of prestack traces? Simply find the source receiver pairs that minimize these resolution estimates.

The above formulas are restricted to homogeneous velocity media, but the real earth is inhomogeneous in velocity. Resolution estimates can be obtained for inhomogeneous media by using the simple idea that the sum of the unit vectors of the downgoing and negative upgoing rays is proportional to the wavenumber $\mathbf{k_{model}}$ of the model that can be reconstructed For example, the ZO vertical rays suggest that the wavenumber of the model that can be reconstructed is proportional to $\vec{k}_{model} = (0, 0, 2\pi/\lambda)$. Note, the k_x and k_y components are zero because the ray is perfectly vertical and has no x-y component (Gesbert, 2003). Formally, the model wavenumber that can be reconstructed (see Figure 3.7) is given by

$$\vec{k} \quad = \quad \omega\nabla(\tau_{down}(x) + \tau_{up}(x)). \tag{3.9}$$

Similar considerations can be used to estimate resolution for tomographic images (Sheng and Schuster, 2003).

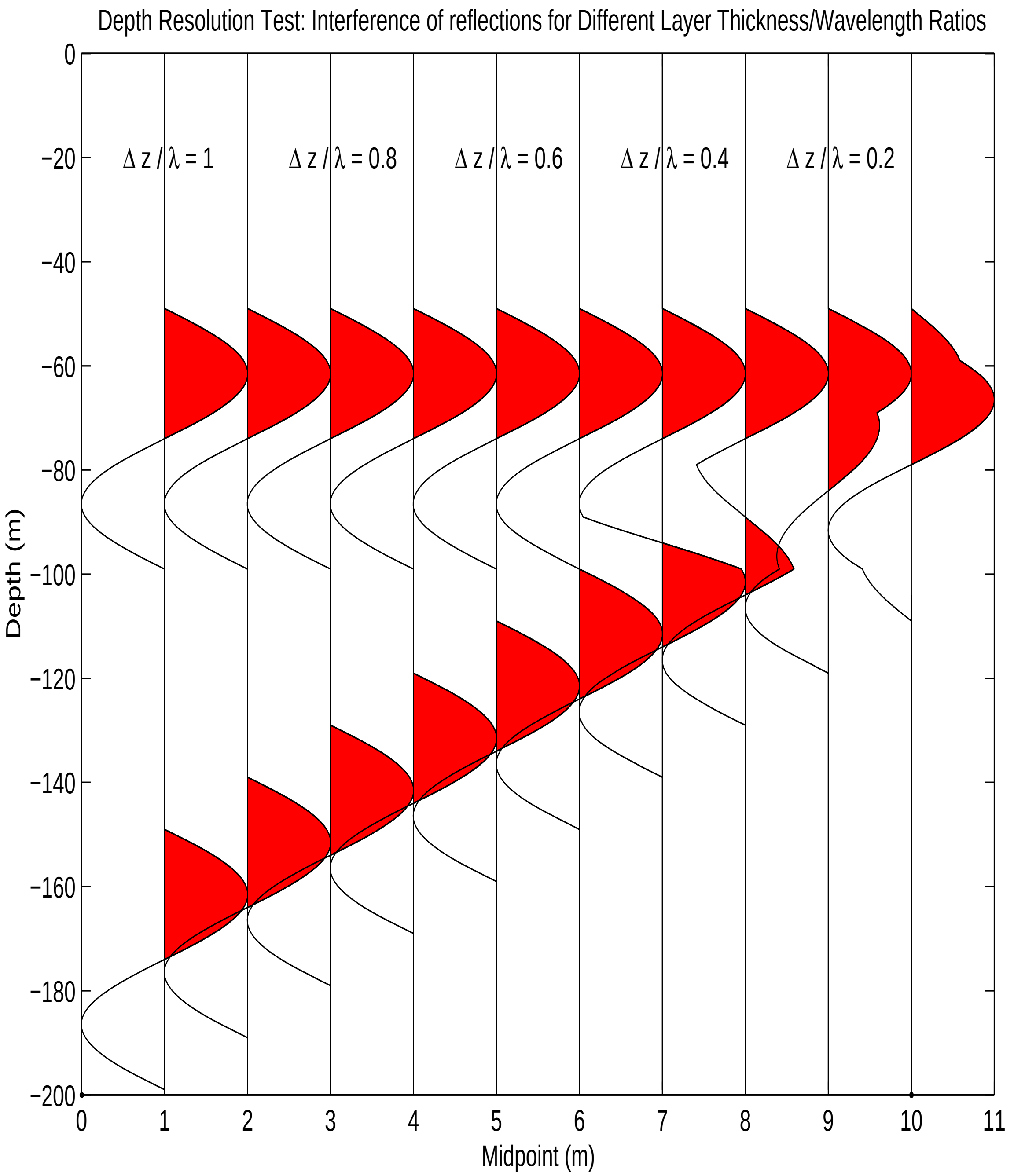

Figure 3.4: Vertical resolution limit is reached when the thickness between two neighboring reflectors $\Delta z = \lambda/4$.

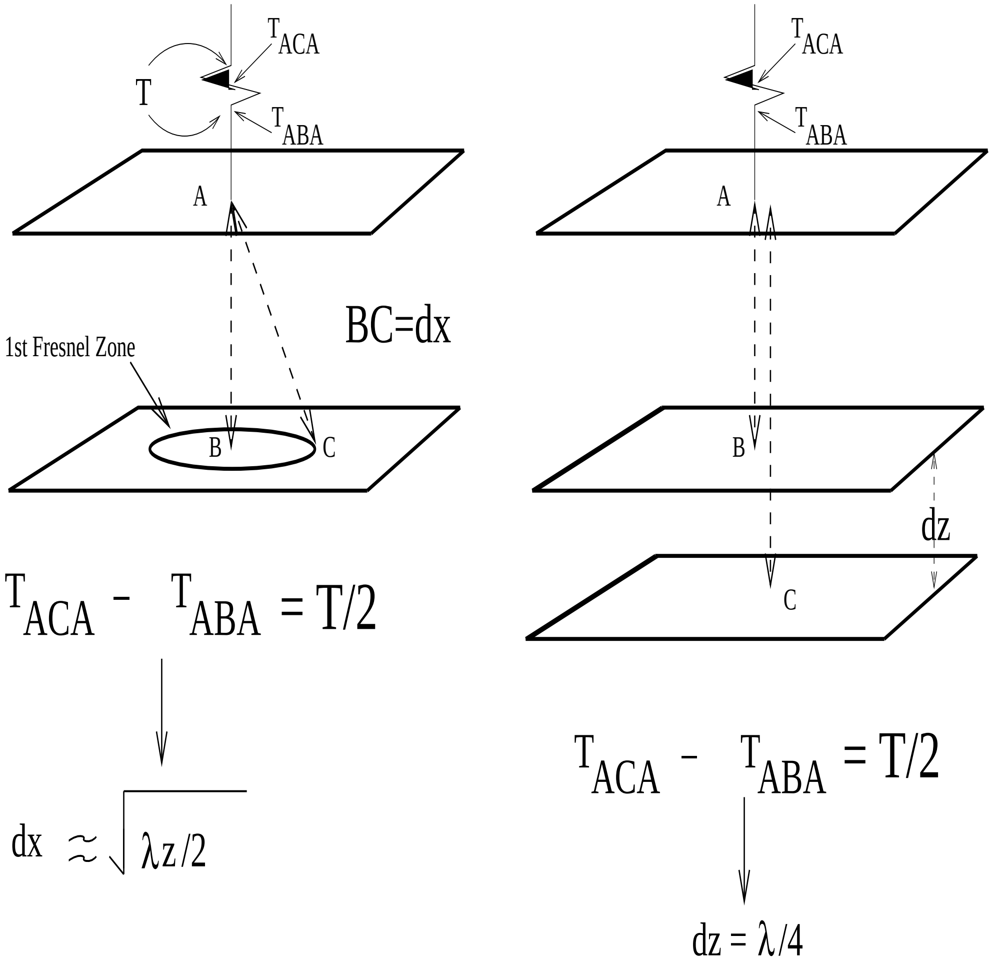

Figure 3.5: Extent of horizontal (left) and vertical (right) Fresnel zones for a ZO trace, where the 1st Fresnel zone defines the area where the difference in the shortest and longest raypath is equal to half the wavelength. The approximation formula $0.25\lambda z/L$ for horizontal resolution is valid when the B point is far to the right of the square and $z >> L$ so points A and A' appear to be coincident, resembling a ZO configuration. In contrast, if B is laterally offset $\approx L/2$ from the center at depth $z >> L$ then $\Delta x \approx 0.5\lambda z/L$ for the prestack configuration. If B is centered below the square then the horizontal resolution is $\approx \sqrt{z\lambda}$.

Is it really important to be concerned about the subtle nuances of improving lateral resolution? Jianhua Yu shows in Figure 3.8 that modest lateral resolution leaves doubt about the existence of fault, but slightly improving this lateral resolution via migration deconvolution leaves no doubt about the existence of a fault.

Beylkin Resolution → Migration Stretch. A simple interpretation of equation 3.9 is that it is equivalent to the formula for migration stretch. Specifically, the migration stretch formulas in the different coordinate directions are given by differentiating the traveltime formula 3.8 with respect to the coordinates of the trial image point (x, y, z):

$$\begin{aligned}\partial\tau/\partial x &= \partial\tau_{sx}/\partial x + \partial\tau_{xg}/\partial x,\\ \partial\tau/\partial y &= \partial\tau_{sx}/\partial y + \partial\tau_{xg}/\partial y,\\ \partial\tau/\partial z &= \partial\tau_{sx}/\partial z + \partial\tau_{xg}/\partial z.\end{aligned} \tag{3.10}$$

Using a Fresnel-zone argument, we set $\partial\tau \approx T/2$ and $\partial x \approx \Delta x$, $\partial y \approx \Delta y$ and $\partial z \approx \Delta z$ on the left hand side of the above equation, and rearrange terms to get analytical expressions for the resolution limits $(\Delta x, \Delta y, \Delta z)$, or migration stretch in the three coordinates similar to the expression in Figure 3.6. Here, T is the dominant period of the wavelet. Multiplying the three stretch formula in equation 3.10 by ω yields the components proportional to the Beylkin wavenumber formula in equation 3.9 (e.g., recall $\omega\partial\tau/\partial x = k_x$). This establishes the equivalency between Beylkin's fancy resolution formula and the well known migration stretch formulas.

3.3 Summary

Both time migration and spatial resolution are defined. The Beylkin stretch formula is used so that the user decides the acceptable horizontal resolution at a selected depth region and uses the stretch formulas to estimate aperture width. The best vertical resolution you can achieve is $\lambda_{min}/4$ but the best horizontal resolution is estimated by a complicated stretch formula that is a function of source and receiver coordinates.

Unlike depth migration, time migration does not suffer from migration stretch but does suffer from mispositioning of events in complex geologic areas. Therefore it is rarely used today for subsalt imaging. However, the velocity model must be finely tuned in order to get depth imaging to show a coherent section. This compares to time migration which usually provides a good looking image because the stacking velocity is used to estimate the time-migration velocity. The stacking velocity is robustly estimated by efficient and automatic velocity scans while the velocity model for depth migration is typically estimated by a time-consumming and tedious process (e.g., reflection tomography or migration velocity analysis).

3.4 Exercises

1. The CDP interval in Figure 3.8 is 50 m, and assume the total depth of 4 km in the image. The velocity at $z = 1$ km is 2 km/s and at $z = 2.5$ km it is 4 km/s, and the recording aperture is 350 CDP's wide for any shot point. Calculate the

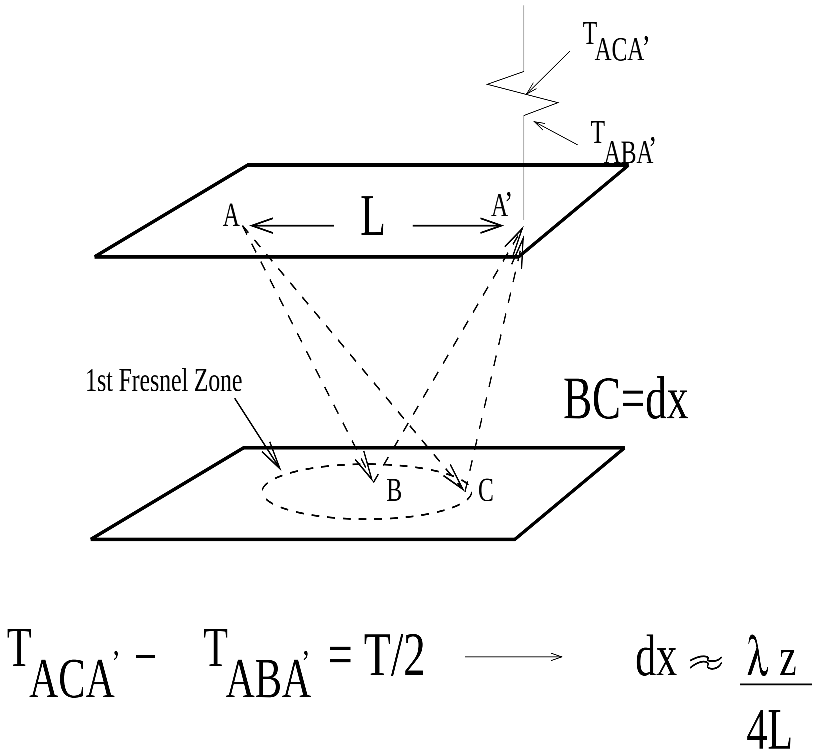

Figure 3.6: Extent of horizontal Fresnel zone for a trace with non-zero offset between the source and receiver. The 1st horizontal Fresnel zone for a reflection defines the area where the difference in the shortest and longest reflection raypaths is equal to half the wavelength.

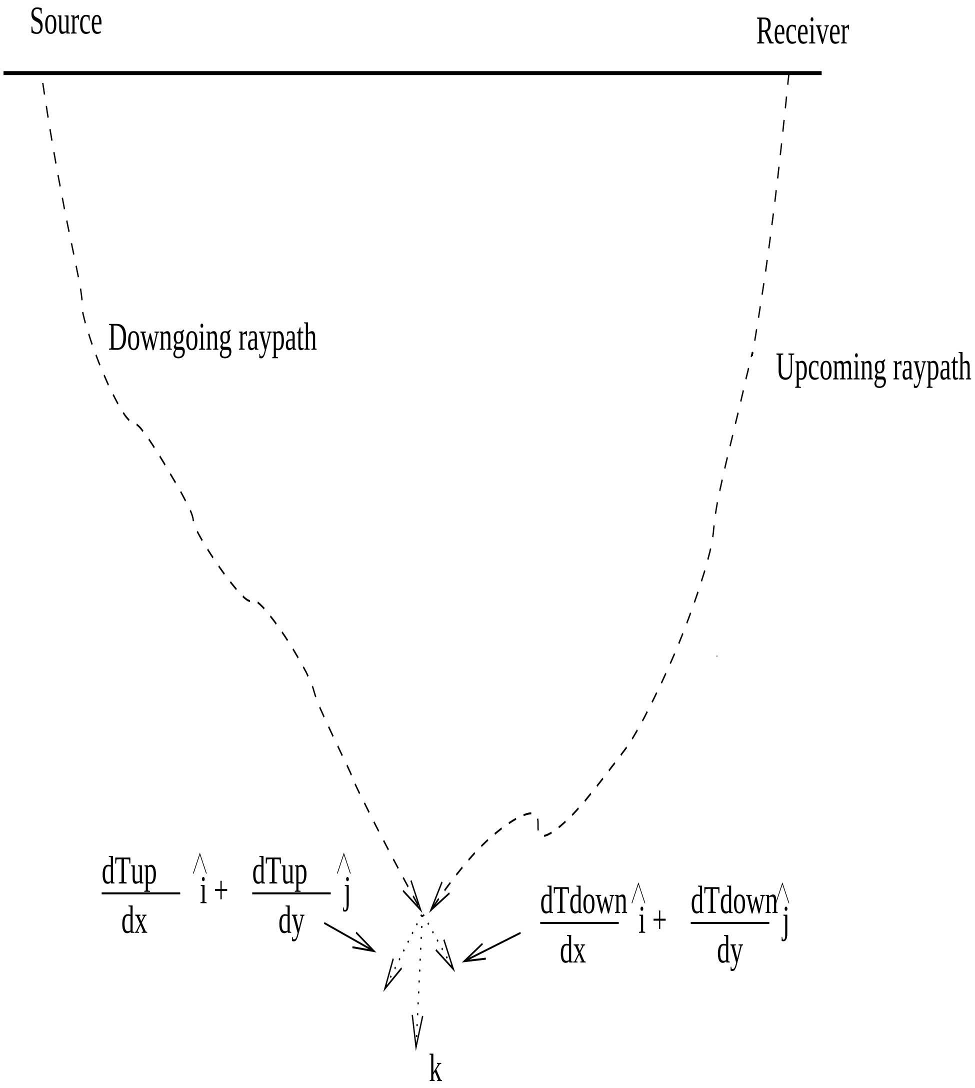

Figure 3.7: Wavenumber **k** of model that can be reconstructed by the downgoing and upgoing rays of the reflection. Here $\mathbf{k} = \omega(\nabla \mathbf{T_{down}} + \nabla \mathbf{T_{up}})$, so that wavenumbers that point sideways (down) indicate good lateral (vertical) resolution.

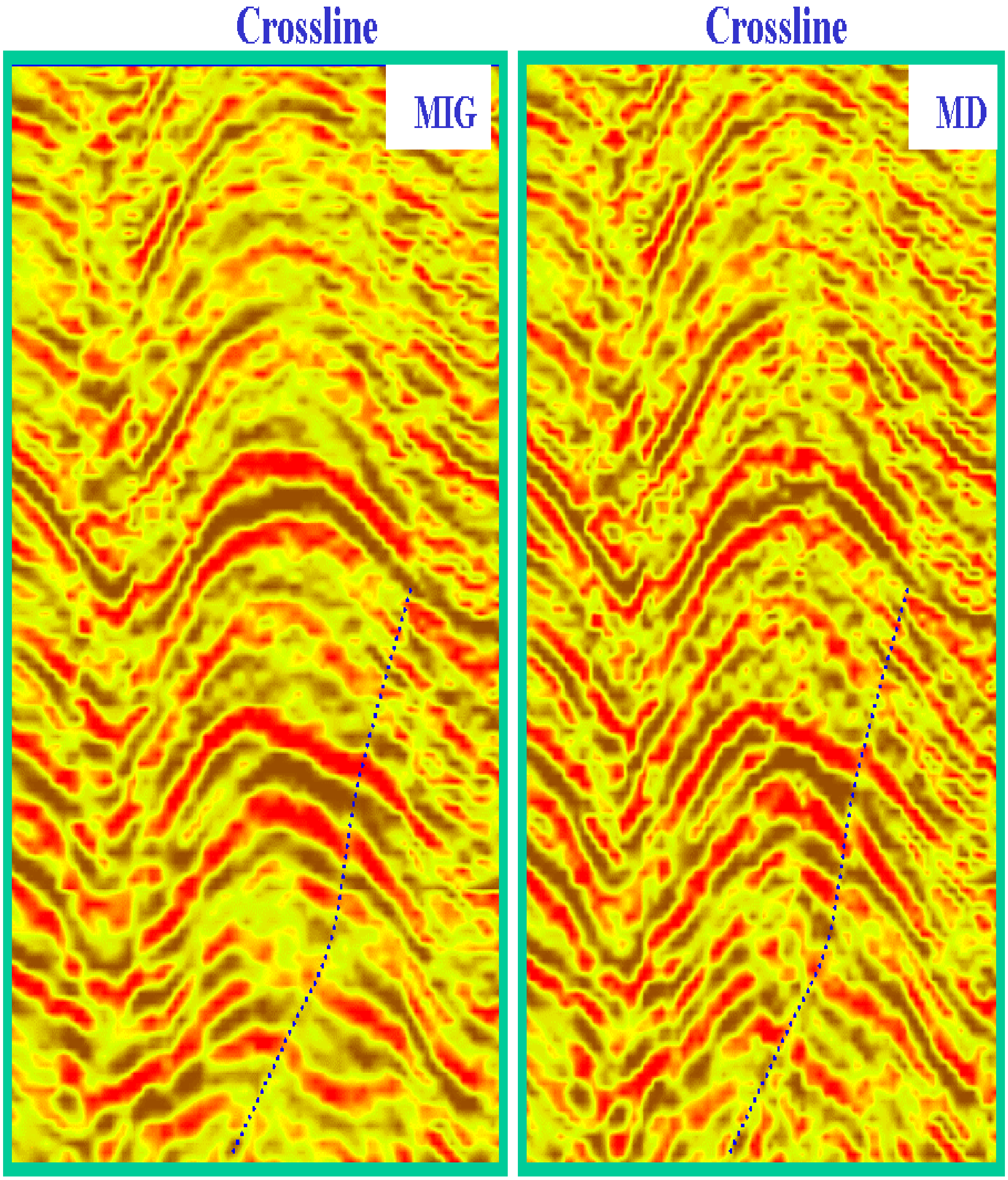

Figure 3.8: 3D prestack migration images (left) before and (right) after migration deconvolution. Lateral resolution improves by about 20 percent so that the right image leaves no doubt about the existence of a fault.

minimum horizontal and vertical resolutions for a prestack migration image at the points $(x, z) = (0\ km, 1\ km)$, $(x, z) = (1\ km, 1\ km)$, $(x, z) = (0\ km, 2.5\ km)$, and $(x, z) = (1\ km, 2.5\ km)$. Same question as before, except calculate minimum horizontal and vertical resolutions for a poststack migration image. Show work. In the above example why would it be better to use $.25\lambda z\sqrt{1 + (L/z)^2}/L$ rather than $.25\lambda z/L$ for the horizontal resolution formula?

2. Using fat circles and fat ellipses, compare the vertical and horizontal resolution limits for poststack migration and prestack migration for a point at $(x, z) = (1\ km, 2.5\ km)$ in Figure 3.8. Assume a homogeneous velocity.

3. Convert your poststack depth migration code into a prestack time migration code. The output should be in the offset-time domain. Show poststack depth and time migration images.

4. Determine the maximum aperture for a seismic experiment in order to image $0 - 40$ degree dips at $z = 5$ km. Assume a homogeneous velocity of 5 km/s. What is the minimum geophone spacing in order to not spatially alias the data? Assume a minimum wavelet period of 0.01 s. Clearly show steps in your reasoning.

5. Derive and use the Beylkin stretch formulas (starting point for derivation is equation 3.10) to estimate the best horizontal and vertical resolutions for a 12 km wide poststack depth section at the following coordinates: (0,12), (12,12), (6,12), (6,6), (0,6), (3,3), (0,12). Assume the origin of coordinate system is at upper left portion of migration section and positive z is pointing downward. Assume a homogeneous velocity of $v = 3\ km/s$ from 0-3 km, $v = 5\ km/s$ from 3-7 km, and any deeper than 7 km we have a velocity of 6 km/s. Assume a maximum useful frequency of 80 Hz. Assume straight rays everywhere. Why is there better horizontal resolution at shallow depths?

6. Time migrate the radar data from your lab exercise. Choose a suitable time migration velocity by trial and error. Show results. Which results look more coherent, the time migration or depth migration results? Why does depth migration suffer from migration stretch which is avoided by time migration. Wgat are benefits and liabilities of time migration vs depth migration?

7. Estimate the horizontal wavelength of surface waves and body wave reflections in the Saudi shot gather (from a previous lab). What is a good array interval that would suppress surface waves but retain body waves ion the data. Test your estimate by applying an N-point spatial averaging filter to the data, where N is length of your estimated filter. Show results.

8. Using Figure 3.3, estimate the maximum trace sampling interval that will avoid aliasing the earliest reflections seen in the seismograms. Same question, except the latest-arriving reflections. Show work.

9. Same as previous question, except find the maximum trace sampling intervals that avoid aliasing of the ZO migration operators? Show work.

10. Assume that Figure 3.4 represents a ZO seismic migration section and that it agrees with the exact earth model. Assume a homogeneous velocity of 500 m/s. What trace spacing in the original stacked data would have been required to just avoid data aliasing for the a). dipping reflector, b). flat reflector? Show work.
11. Same as previous question, except what is the trace spacing that would avoid aliasing for the ZO migration operator? Show work.
12. Same as previous question except what is trace spacing that would just avoid aliasing the prestack migration operator?

Part V

Physics of Elastic Wave Propagation

Chapter 1

Physics of Elastic Wave Propagation

We now introduce the equations of motion for a rock that has non-zero shear strength, i.e., it resists a twisting motion. This is an elastic rock, which is more representative of waves propagating through the earth compared to the acoustic approximation of Chapter 1. The most significant difference is that elastic wave propagation consists of a new type of wave, namely the shear or S wave (see Figure 1.1). Other wave types are now possible, including ground roll which consists of surface waves such as Rayleigh waves and Love waves. The shear wave is a body wave characterized by particle motion perpendicular to the wave propagation direction and has a propagation velocity that is half or less than that of the P wave. Other new modes include the surface Rayleigh wave, which is a strong source of noise in exploration records. See the movie (http://www.ndt-ed.org/EducationResources/CommunityCollege/Ultrasonics/Physics/wavepropagation.htm) of particle motion for a propagating shear wave. Although most of our treatment of exploration seismology will assume the acoustic approximation, we will need to acknowledge the underlying physics of elastic wave propagation when dealing with surface waves and shear waves in our data.

1.1 Elastic Strain and Stress

If the medium has non-zero shear strength then there can be shear strains supported by the rock. This means that the shape of a cube can be distorted into a, e.g., trapezoidal-like shape after application of a shear stress on the cube. Unlike an acoustic cube where, e.g., water molecules do not resist sliding past one another, an elastic cube will resist the shearing of it into a trapezoidal shape so it has *shear strength*. Similar to acoustic rocks, increasing strength of an elastic rock will lead to an increase in the shear velocity speed. We now describe the general theory of stress and strain for an elastic rock, which can be used to derive the elastodynamic equations of motion.

1.1.1 Simple and Pure Shear Strain

It is important to establish the physical meaning of shear strain compared to compressional strain. As discussed in Chapter 1, compressional strain changes the volume of the acoustic

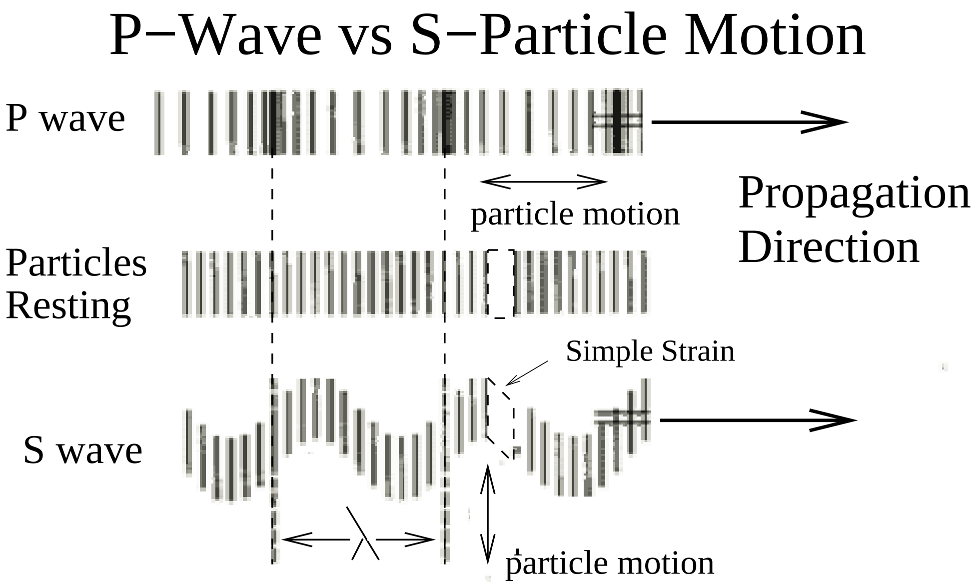

Figure 1.1: Snapshots of particle motions for (top) P and (bottom) S waves, which are parallel and perpendicular, respectively, to the direction of wave propagation from left to right.

cube. This volume change can be estimated by drawing two perpendicular lines within the cube and comparing the change in area (or volume for a 3D deformation) after deformation, as shown in Figure 1.2a. If the angles between the two perpendicular lines change then it is likely that simple shear strain is involved, as shown in Figure 1.2b. If the area (or volume in 3D) does not change but the angles do change as illustrated in Figure 1.2c, then this is denoted as pure shear strain.

To quantify the measure of shear strain we can define the end point vectors of two points (small filled circle and square) of a box as $\mathbf{r}$ and $\mathbf{r}+\mathbf{dz}$ in Figure 1.3a. After shear deformation, these two points have been displaced by the respective displacement vectors $\mathbf{u}(\mathbf{r})$ and $\mathbf{u}(\mathbf{r}+\mathbf{dz})$ shown in Figure 1.3b. The displacement vector $\mathbf{u}$ has components in 3D as $\mathbf{u}=(u,v,w)$, but often we will use the index notation u_i where $u_1=u$, $u_2=v$, and $u_3=w$.

To reduce notational clutter we simplify the Figure 1.3b diagram to that in Figure 1.3c, and see that the deformation vector $\mathbf{du}(\mathbf{r}+\mathbf{dz})$ represents the change of the line's end point (small filled box) location relative to the beginning point (small filled circle). In this example, the ratio du/dz is equal to the tangent of the deformation angle θ, and will increase with increasing shear forces that deform the box. This measure du/dz of shear deformation is defined as the shear strain, and is unitless just like the compressional (or longitudinal) strain defined in Chapter 1. Similar to Hooke's law that linearly related the compressional force that changed the volume of a box, experiments show that that the shear forces can be linearly related to the shear strains as

$$\tau_{xz} \quad = \quad \mu dv/dz, \tag{1.1}$$

as long as the infinitesimal strain limit is satisfied $dv/dz < 10^{-5}$. Here, τ_{xz} is known as the simple shear stress component and has units of force/unit area. The ratio $(shear\ stress)$ $/(shear\ strain)=\mu$ is known as the shear modulus, with stiffer rocks having larger values of μ. For now we will naively define τ_{xz} as the z-component of deformational force the outer media acts on the cube along the face normal to the x-axis.

1.1.2 S Waves Shear Rocks

But what does shear strain have to do with the propagation of S waves seen in Figure 1.1? Figure 1.4 depicts the deformations of boxes associated with a snapshot of propagating P and S waves. Obviously the P waves only change the volume of the boxes while the S wave changes both volume and the angle between two perpendicular lines. Therefore we conclude that shear waves must be strongly associated with shear stains while compressional waves are associated with dilatational strains (i.e., volume changing). The next section describes how to quantify the stress-strain relationship in an elastic medium.

1.1.3 Stress Tensor

Equation 1.1 loosely defined the shear stress as proportional to the shear strain, and it has units of $force/area$. The generalization of this concept is needed because the deformational forces acting on a planar area depends on the orientation of the plane. For example, the building in Figure 1.5 has a large compressional stress τ_{zz} on the horizontal plane at the

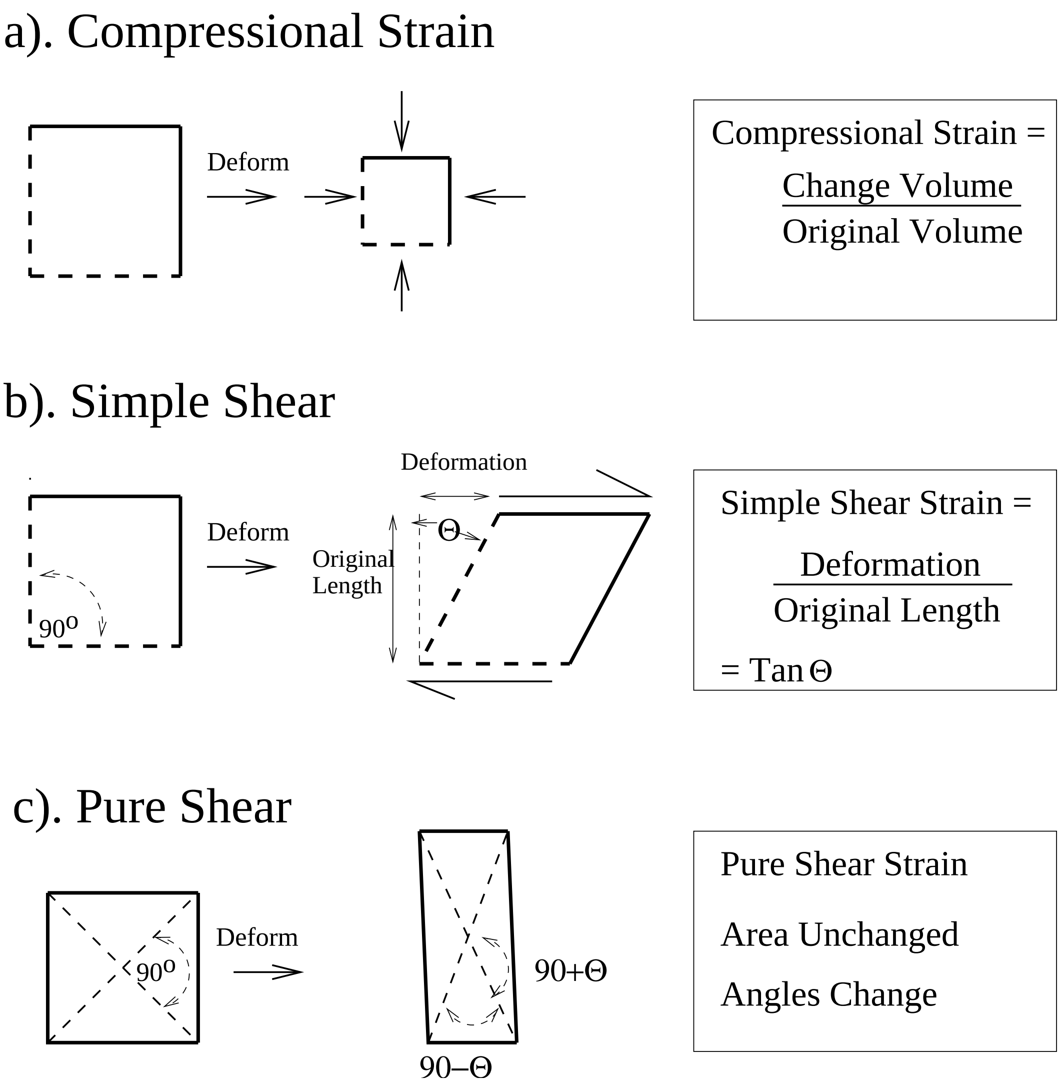

Figure 1.2: Box (left) before and (right) after deformation. Pure shear changes angle between two perpendicular lines but does not change the area of the box.

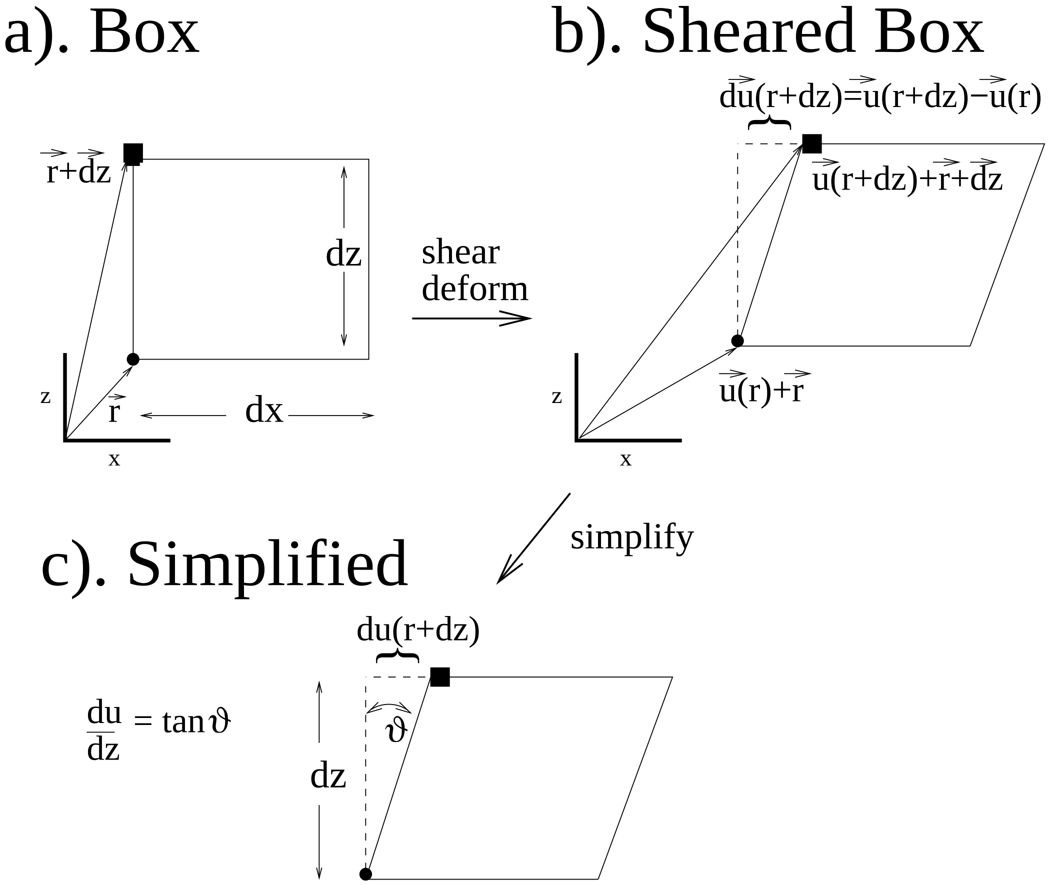

Figure 1.3: a). Undeformed box, b). deformed box after applying a simple strain, and c). deformed box after simplification of notation. The displacement vector $\mathbf{u}(\mathbf{r})$ is defined as the vector that connects the particle at $\mathbf{r}$ (in the undeformed state) with the same particle after deformation.

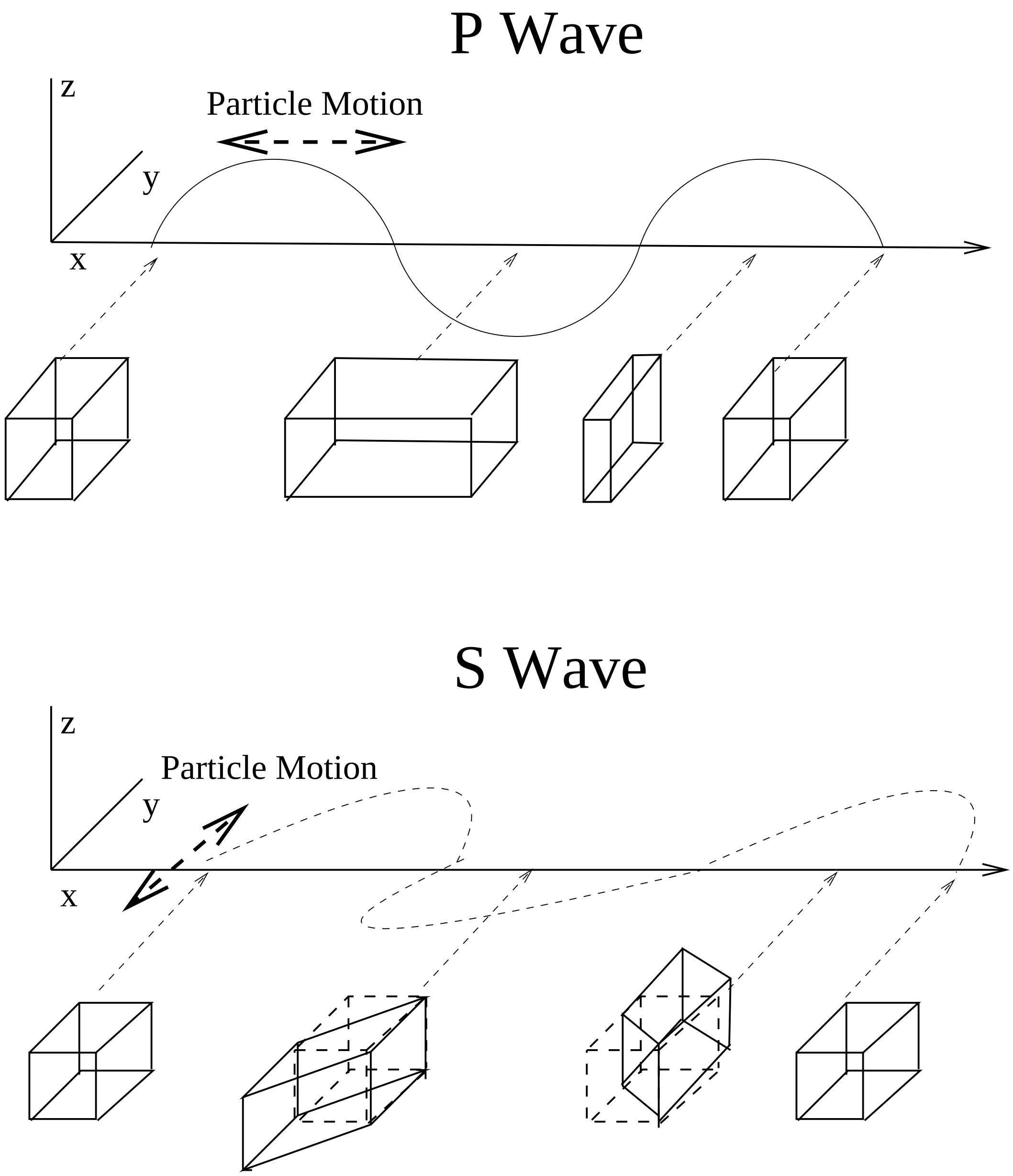

Figure 1.4: Snapshots of particle motions for (top) P and (bottom) S waves, which are parallel and perpendicular, respectively, to the direction of wave propagation. The height of the sinusoidal curve above the x axis represents the amplitude of particle motion.

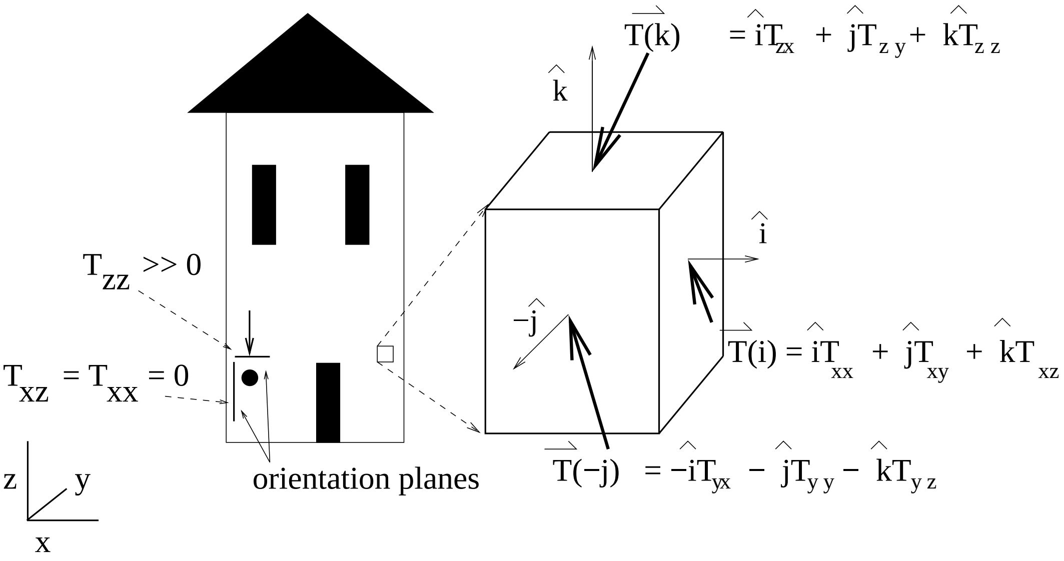

Figure 1.5: Building where the deformation forces depend on the orientation of the plane located at the solid circle. The enlarged infinitesimal cube on the right defines the components of the traction vector as the stress tensor components. For example, τ_{ij} is the *jth* component of the traction vector on the face perpendicular to the *ith* coordinate axis.

solid circle. But if we rotate this plane by 90^o to the vertical (at the solid circle) there are negligible shear and compressional forces $\tau_{xz} = \tau_{xx} = 0$ acting on this vertical plane. This seems strange, the body force at a point remains the same yet the deformation forces depend on the orientation of the plane.

To mathematically describe these deformation forces, an infinitesimally small 3D cube can be extracted from the building as shown and the traction vector $\mathbf{T}(\hat{\mathbf{n}})$ is defined to be the force per unit area exerted by the exterior media (i.e., the contiguous material that lies just outside the small cube) on a plane with normal $\hat{\mathbf{n}}$. The normal points to this source of the exterior force. If this plane is perpendicular to the ith unit vector then the x, y and z traction components are the stresses τ_{ix}, τ_{iy}, and τ_{iz}:

$$\mathbf{T}(\hat{\mathbf{n}}_\mathbf{i}) \quad = \quad \tau_{ix}\hat{\mathbf{i}} + \tau_{iy}\hat{\mathbf{j}} + \tau_{iz}\hat{\mathbf{k}}, \tag{1.2}$$

where $\hat{\mathbf{n}}_\mathbf{i}$ represents the unit vector along the *ith* coordinate axis (e.g., $\hat{\mathbf{n}}_\mathbf{1} = \hat{\mathbf{i}}$). If the cube is in static equilibrium then it makes sense that the sum of the components on the six faces of the cube are zero. As the opposite faces with normals parallel to $\hat{\mathbf{k}}$ become closer this implies that the τ^+_{zz} component on the top face is equal and opposite to τ^-_{zz} along the bottom face. It also says that the τ^+_{zx} component on the top face is equal and opposite to τ^-_{zx} along the bottom face. To prevent rotation of the cube then the shear stress tensors must be symmetrical so that $\tau_{xz} = \tau_{zx}$, as shown in Figure 1.6.

The symmetry argument above was based on a cube in static equilibrium. The same argument can be used for a cube dynamically deformed by a passing wave by noting that the cube's inertial component of force $dx^3\rho\ddot{u}$ along the x direction can be equated to the net sum of the deformational forces $dx^2(\tau^+_{xx} - \tau^-_{xx} + \tau^+_{xy} - \tau^-_{xy} + \tau^+_{xz} - \tau^-_{xz})$. As $dx \rightarrow 0$ the

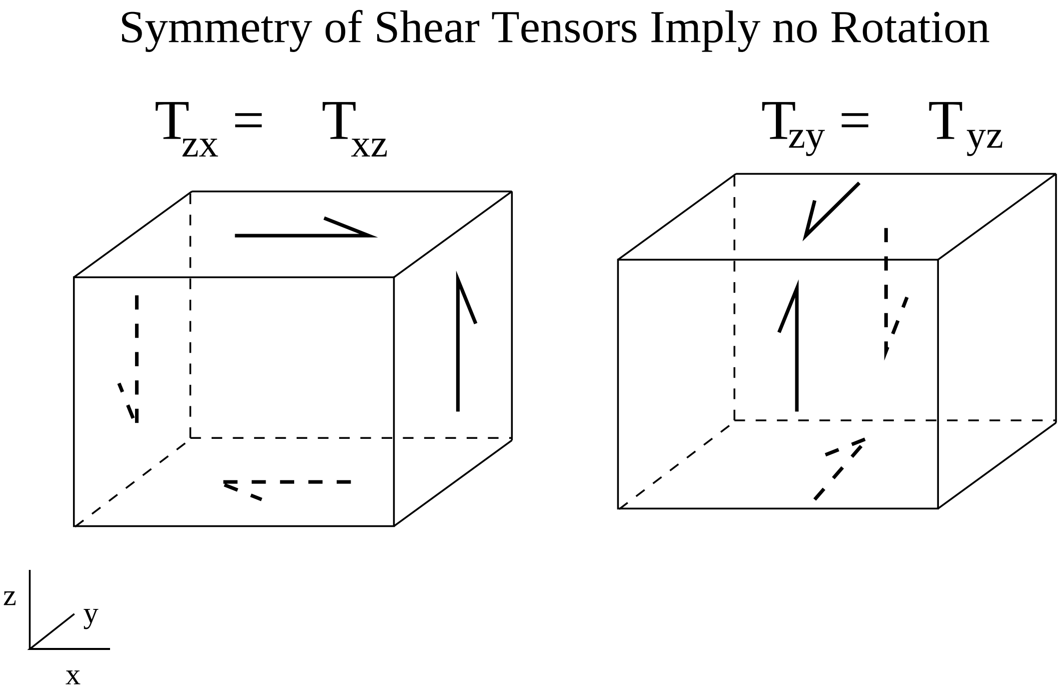

Figure 1.6: No rotation implies symmetry of shear stresses, e.g., $\tau_{xz} = \tau_{zx}$.

inertial force terms shrinks to zero faster (i.e., cubically in dx), compared to the traction terms (i.e., they shrink to zero quadratically in dx). Therefore for small enough dx, we can set the deformational force components to zero, i.e., $\tau^+_{xx} - \tau^-_{xx} + \tau^+_{xy} - \tau^-_{xy} + \tau^+_{xz} - \tau^-_{xz} = 0$. This condition is equivalent to the static equilibrium condition that the sum of traction components on a cube is equal to zero.

We call τ_{ij} a tensor because it is invariant under a coordinate transformation; this means that the deformation forces on any one face are independent of the orientation of the mathematical coordinate system.

1.1.4 Stress and Strain Definitions

We now borrow some intuitive definitions of strain and stress from Steven Dutch's WWW page (http://www.uwgb.edu/DutchS/structge/strsparm.htm). This will help us make the connection between the familiar geological definitions of stress and strain and the geophysicist's definitions.

- **Stress** is defined as force per unit area. It has the same units as pressure, and in fact pressure is one special variety of stress. However, stress is a much more complex quantity than pressure because it varies both with direction and with the surface it acts on.

- **Compression.** Stress that acts to shorten an object.

- **Tension.** Stress that acts to lengthen an object.

- **Normal Stress.** Stress that acts perpendicular to a surface. Can be either compressional or tensional.
- **Shear Stress** that acts parallel to a surface. It can cause one object to slide over another. It also tends to deform originally rectangular objects into parallelograms. The most general definition is that shear acts to change the angles in an object.
- **Hydrostatic Stress** (usually compressional) that is uniform in all directions. A scuba diver experiences hydrostatic stress. Stress in the earth is nearly hydrostatic. The term for uniform stress in the earth is lithostatic.
- **Directed Stress.** Stress that varies with direction. Stress under a stone slab is directed; there is a force in one direction but no counteracting forces perpendicular to it. This is why a person under a thick slab gets squashed but a scuba diver under the same pressure doesn't. The scuba diver feels the same force in all directions.
- **Traction.** Vector of force acting per unit area across an internal interface. It quantifies the *contact* force between particles along one side of the plane acting on the particles on the other side.

In geology we never see stress. We only see the results of stress as it deforms materials. Even if we were to use a strain gauge to measure in-situ stress in the rocks, we would not measure the stress itself. We would measure the deformation of the strain gauge (that's why it's called a "strain gauge") and use that to infer the stress.

Strain is defined as the amount of deformation an object experiences compared to its original size and shape. For example, if a block 10 cm on a side is deformed so that it becomes 9 cm long, the strain is (10-9)/10 or 0.1 (sometimes expressed in percent, in this case 10 percent.) Note that strain is dimensionless.

- **Longitudinal or Linear Strain.** Strain that changes the length of a line without changing its direction. Can be either compressional or tensional.
- **Compression strain.** Longitudinal strain that shortens an object.
- **Tension.** Longitudinal strain that lengthens an object.
- **Shear Strain** that changes the angles of an object. Shear causes lines to rotate.
- **Infinitesimal Strain.** Strain that is tiny, a few fraction of a percent or less. Allows a number of useful mathematical simplifications and approximations. All acoustic and elastodynamic equations of motion in this book assume infinitesimal approximations to linearize the relation between stress and strain.
- **Finite Strain.** Strain larger than a few percent. Requires a more complicated mathematical treatment than infinitesimal strain.
- **Homogeneous Strain.** Uniform strain. Straight lines in the original object remain straight. Parallel lines remain parallel. Circles deform to ellipses. Note that this definition rules out folding, since an originally straight layer has to remain straight.

- **Inhomogeneous Strain.** How real geology behaves. Deformation varies from place to place. Lines may bend and do not necessarily remain parallel.

1.1.5 Strain Tensor

The stress tensor was introduced in the previous section, so it is time to introduce the generalized definition of the strain tensor. The starting point is to recognize that the components of the net deformation vector $\mathbf{du}(\mathbf{r}+\mathbf{dr})$ (for the line segment with end points at $\mathbf{r}$ and $\mathbf{r}+\mathbf{dr}$) can be expanded in a Taylor series about the particle at $\mathbf{r}$:

$$du(\mathbf{r}+\mathbf{dr})_i = u(\mathbf{r}+\mathbf{dr})_i - u(\mathbf{r})_i \quad = \quad \sum_{j=1}^{3} \frac{\partial u_i}{\partial x_j} dx_j + O(dx^2), \tag{1.3}$$

where higher-order terms in dx_j are neglected under the infinitesimal approximation. The above equation can be rearranged into strain and rigid rotation terms to give

$$du(\mathbf{r}+\mathbf{dr})_i \quad = \quad 1/2 \sum_{j=1}^{3} \overbrace{(\frac{\partial u_i}{\partial x_j} + \frac{\partial u_j}{\partial x_i})}^{strain\ tensor} dx_j + 1/2 \sum_{j=1}^{3} \overbrace{(\frac{\partial u_i}{\partial x_j} - \frac{\partial u_j}{\partial x_i})}^{rigid\ rotation} dx_j, \tag{1.4}$$

where it can easily be shown that the rigid rotation term corresponds to $\nabla \times \mathbf{u} \times d\mathbf{x}$. The rigid rotation term can be neglected assuming infinitesimal strains that do not undergo rotations (Aki and Richards, 1980).

The definition of the curl $\nabla\mathbf{u}$ in terms of a line integral is given in Figure 1.7.

The notation for the shear strain is $\epsilon_{ij} = 1/2(\partial u_i/\partial x_j + \partial u_j/\partial x_i)$, which says that a shear strain exists if there is a non-zero gradient of displacement that is perpendicular to the direction of displacement. We can also use Einstein index notation so that $\epsilon_{ij} = 1/2(u_{i,j} + u_{j,i})$, where the index following a comma indicates a partial derivative with respect to that index's coordinate and common index symbols in a term imply summation over the values of the index, i.e., equation 1.4 reduces to

$$\begin{aligned} du(\mathbf{r}+\mathbf{dr})_i &= 1/2(\frac{\partial u_i}{\partial x_j} + \frac{\partial u_j}{\partial x_i})dx_j, \\ &= \epsilon_{ij} dx_j, \end{aligned} \tag{1.5}$$

where the rigid rotation term is assumed to be zero and the strain tensor is defined to be $\epsilon_{ij} = 1/2(\frac{\partial u_i}{\partial x_j} + \frac{\partial u_j}{\partial x_i})$. It is interpreted as the change of the ith component of the deformation vector $\mathbf{du}(\mathbf{r}+\mathbf{dr})$ with respect to the derivative along the jth coordinate.

The term $\epsilon_{ii} = 1/2(\partial u_1/\partial x_1 + \partial u_2/\partial x_2 + \partial u_3/\partial x_3)$ is proportional to the volume change of the deformed cube, as discussed in Chapter 1. Therefore, ϵ_{ii} is denoted as the dilatational strain tensor and plays an important role in describing compressional wave propagation. On the other hand, the strain tensor $\epsilon_{ij} = 1/2(\partial u_i/\partial x_j + \partial u_j/\partial x_i)$ accounts for shear strains when $i \neq j$. See Figure 1.3 for the case when $i = 1$ and $j = 3$ so that $\epsilon_{13} = 1/2\partial u/\partial z$.

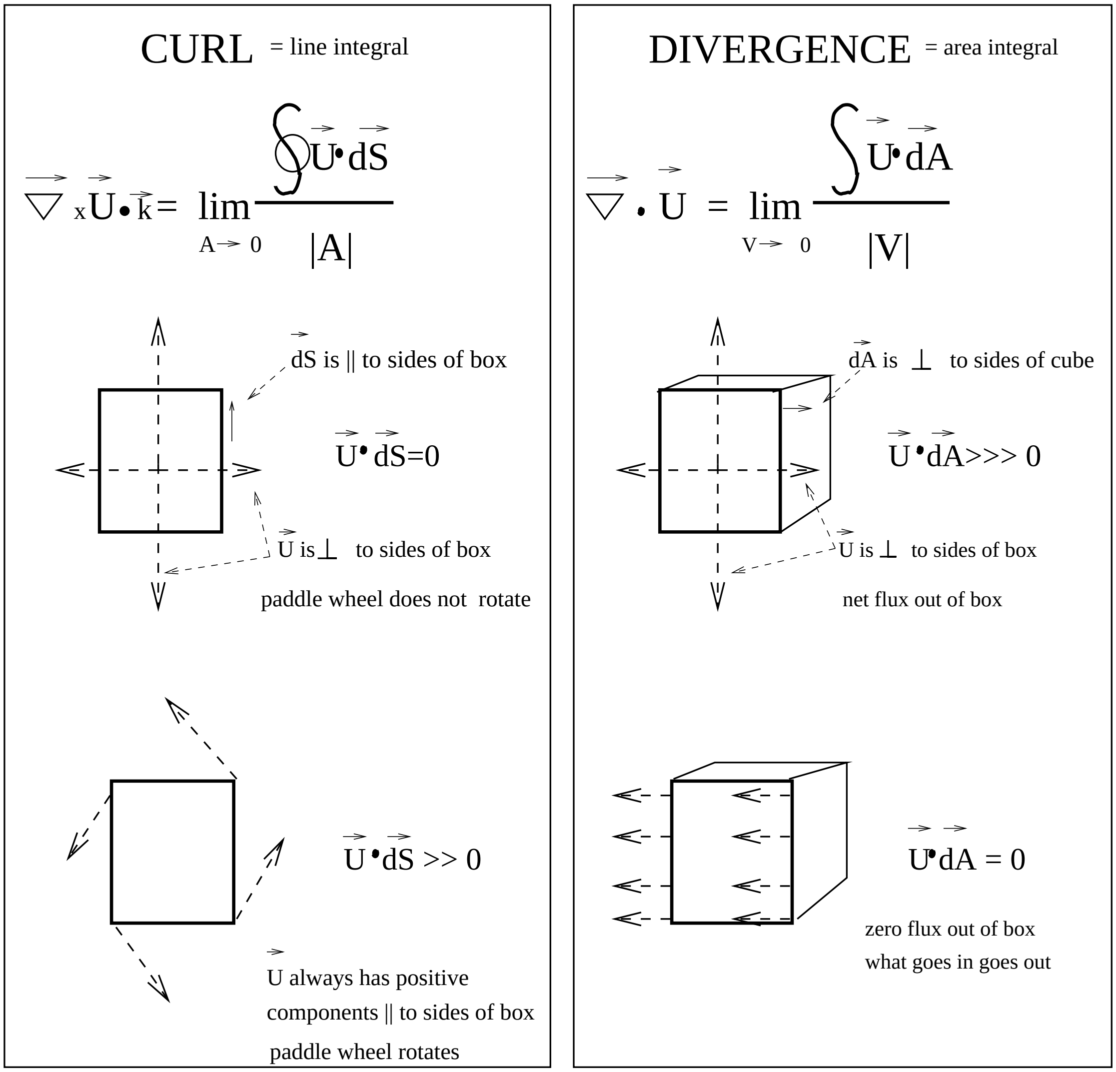

Figure 1.7: Definitions of curl $\nabla \mathbf{u} \times \hat{\mathbf{k}}$ as the limit of a line integral and the divergence $\nabla \cdot \mathbf{u}$ as an area integral. Here, $\hat{\mathbf{k}}$ is the unit vector pointing out of the page and the line integral circles counterclockwise around the box. The area integral is along the surface of the cube on the right. If the box in the left panel is undergoing pure rotation then the projection of the vector $\mathbf{u}$ on the sides of the box, i.e., $\mathbf{u} \cdot \mathbf{ds}$, will always be positive, leading to a large value of curl. If the vector $\mathbf{u}$ represents the vector of water velocity flow then large positive curl means fast counterclockwise rotation of a paddle wheel placed in the middle of the box. In contrast, if the velocity field $\mathbf{u}$ has zero projection onto the surface then the curl is zero and the paddle wheel does not turn, as shown in the middle diagram in the left panel. Divergence is only non-zero if there is a net water flow in or out of the cube, i.e., the net projection of velocity vector onto the normals is non-zero as shown in the right panel.

1.2 Generalized Hooke's law

Laboratory experiments can establish the linear relationship between the stress on an elastic rock and its resulting deformation. These experiments might confine a block of rock and press forward in the z direction, measuring the longitudinal deformation in the z (i.e.,$\partial w/\partial z$) and have constraints so that the lateral directions are not deformed. Another experiment might allow for deformation of the rock in the x-direction responding to a downward normal stress on the horizontal face. Since there are 9 different strains and 9 different types of stresses, then there will $9x9 = 81$ proportionality constants to determine. Therefore, the generalized Hooke's law is given by

$$\tau_{ij} \quad = \quad c_{ijkl}\epsilon_{ij}, \tag{1.6}$$

where c_{ijkl} constitute 81 parameters and are called elastic constants. Fortunately, symmetries (Aki and Richards, 1980) in the stress (i.e., $\tau_{ij} = \tau_{ji}$) and strain tensors (i.e., $\epsilon_{ij} = \epsilon_{ji}$) and conservation considerations reduce the number of unknowns from 81 to 21 independent constants. In the acoustic case these constants reduce to one independent constant known as the bulk modulus.

For an elastic isotropic material, there are only two independent elastic constants (Aki and Richards, 1980):

$$\tau_{ij} \quad = \quad \lambda\delta_{ij}\epsilon_{kk} + 2\mu\epsilon_{ij}, \tag{1.7}$$

where τ_{ij} is the stress tensor that denotes the force/area imposed by the outside medium in the *ith* direction along the face with normal j. Also, μ is the shear modulus and λ is Lame's constant. Appendix 1 provides a listing of elastic stiffness coefficients and their relationship to one another.

1.3 Elastic Wave Equation

We now discuss the case where a transient source is excited in an elastic medium to generate elastic waves. Similar to the acoustic case, the elastic form of Newton's law can be found by summing the body and deformation forces within a small cube and equating the result to the inertial forces. That is, Newton's law is given by

$$\rho\ddot{u}_i \quad = \quad \partial\tau_{i1}/\partial x_1 + \partial\tau_{i2}/\partial x_2 + \partial\tau_{i3}/\partial x_3 + f_i = \tau_{ij,j} + f_i, \tag{1.8}$$

where Einstein notation says that repeated indices indicate summation over all three components. Here, f_i is the ith component of the body force vector.

Inserting equation 1.7 into equation 1.8 gives the elastic wave equation in terms of strains for a homogeneous medium:

$$\rho\ddot{u}_i \quad = \quad \lambda\frac{\partial e_{kk}}{\partial x_j}\delta_{ij} + 2\mu\frac{\partial\epsilon_{ij}}{\partial x_j}. \tag{1.9}$$

But $\epsilon_{kk} = \partial u_k/\partial x_k = \nabla\cdot\mathbf{u}$ and $\epsilon_{ij} = 1/2(\partial u_i/\partial x_j + \partial u_j/\partial x_i)$ so the above equation becomes

$$\rho\ddot{u}_i \quad = \quad \lambda\frac{\partial\nabla\cdot\mathbf{u}}{\partial x_i} + \mu\frac{\partial}{\partial x_j}(\frac{\partial u_i}{\partial x_j} + \frac{\partial u_j}{\partial x_i}),$$

$$\begin{aligned} &= \lambda\frac{\partial\nabla\cdot\mathbf{u}}{\partial x_i} + \mu[\nabla\cdot\nabla(u_i) + \frac{\partial\nabla\cdot\mathbf{u}}{\partial x_i}], \\ &= (\lambda+\mu)\frac{\partial\nabla\cdot\mathbf{u}}{\partial x_i} + \mu\nabla\cdot\nabla(u_i), \qquad (1.10) \end{aligned}$$

or in vector notation we have the vectorial wave equation

$$\rho\ddot{\mathbf{u}} = (\lambda+\mu)\nabla(\nabla\cdot\mathbf{u}) + \mu\nabla\cdot\nabla\mathbf{u}. \qquad (1.11)$$

The above partial differential equations is tedious to use when a boundary value problem needs to be solved, such as finding the reflection coefficients in a layered medium. It is much easier to solve these types of problems when the governing equation of motion is a simple scalar equation, as demonstrated in Chapter 1 with the acoustic wave equation in terms of the pressure field. Fortunately, for a homogeneous medium, the elastic wave equation 1.11 can be transformed into two simpler equations by equating the vector field **u** into a sum of potentials:

$$\mathbf{u} = \nabla\phi + \nabla\times\psi, \qquad (1.12)$$

where ϕ is a scalar potential and ψ is a vector potential. We have an extra degree of constraint we need because we are equating a 3-component vector **u** into an expression with 4 unknowns. The extra constraint that will be useful is that $\nabla\cdot\psi = \mathbf{0}$.

Plugging this expression for $\mathbf{u}\nabla\phi + \nabla\times\psi$ into equation 1.11 yields

$$\rho(\nabla\ddot{\phi} + \nabla\times\ddot{\psi}) = (\lambda+\mu)\nabla(\nabla\cdot[\nabla\phi + \nabla\times\psi]) + \mu\nabla\cdot\nabla[\nabla\phi + \nabla\times\psi]. \qquad (1.13)$$

We know that $\nabla\cdot\nabla\times\psi = 0$ so the above expression becomes

$$\rho(\nabla\ddot{\phi} + \nabla\times\ddot{\psi}) = (\lambda+\mu)\nabla[\nabla^{\mathbf{2}}\phi] + \mu\nabla^{\mathbf{2}}[\nabla\phi + \nabla\times\psi]. \qquad (1.14)$$

We can separate the ϕ terms from the ψ terms by multiplying both sides of the above equation by $\nabla\cdot$, recalling the constraint $\nabla\cdot\psi$, and noting the commutative property of ∇^2 when applied to a ∇ or $\nabla\times$ operation:

$$\rho\nabla^2\ddot{\phi} = (\lambda+\mu)\nabla^2[\nabla^2\phi] + \mu\nabla^2\nabla^2\phi. \qquad (1.15)$$

Rearranging gives

$$\nabla^2[\rho\ddot{\phi} - (\lambda+2\mu)\nabla^2\phi] = 0, \qquad (1.16)$$

which implies

$$\rho\ddot{\phi} - (\lambda+2\mu)\nabla^2\phi = 0. \qquad (1.17)$$

This last expression is the wave equation for the scalar potential. Similar to the acoustic wave equation in Chapter 1, it is satisfied by plane waves that propagate with velocity $c_p = \sqrt{(\lambda+2\mu)/\rho}$.

The wave equation for the vector potential can be derived in a similar manner except we multiply equation 1.14 by $\nabla\times$ (remembering the identity $\nabla\times\nabla\phi = 0$) to give

$$\rho\ddot{\psi} - \mu\nabla^2\psi = 0. \qquad (1.18)$$

and the shear velocity is given by $c_s = \sqrt{\mu/\rho}$.

In summary, we have the wave equations for the scalar and vector potentials

$$\ddot{\phi} = c_p^2 \nabla^{\mathbf{2}} \phi; \qquad \ddot{\psi} = c_s^2 \nabla^{\mathbf{2}} \psi, \tag{1.19}$$

where we use the identities $\nabla \cdot \nabla \times \psi = \mathbf{0}$, $\nabla \times \nabla \phi = 0$, and $\nabla^2 \psi = \nabla(\nabla \cdot \psi) - \nabla \times (\nabla \times \psi)$. These potential equations are much more simple compared to the elastic wave equation, and can be used to more easily solve for boundary value problems.

1.4 P, PSV, and SH Waves

We can examine a plane wave solution to the elastic wave equation and deduce that there can be three types of waves in an elastic medium: P, SV, and SH waves. The SV and SH waves are shear waves with particle motion perpendicular to the direction of wave propagation, and P waves have particle motion parallel to the direction of wave propagation.

The starting point in the derivation is to recall the Chapter 1 expression for a propagating plane wave $\mathbf{u} = e^{i(\mathbf{k}\cdot\mathbf{x}-\omega t)}\mathbf{s}$ in a homogeneous medium, except we now include the particle displacement vector $\mathbf{s}$. Here, $\mathbf{k}$ is the wavenumber vector that points in the direction of propagation. For a homogeneous medium and plane wave, the $\mathbf{s}$ particle motion vector is parallel to a fixed line and describes the motion of the medium's particles affected by the passing wave. Plugging this plane-wave expression into the vector wave equation 1.11 we get

$$\rho\omega^2 \mathbf{s} - (\lambda + \mu)(\mathbf{s} \cdot \mathbf{k})\mathbf{k} - \mu k^2 \mathbf{s} = 0. \tag{1.20}$$

Applying the dot product of the above equation with $\mathbf{s}$ gives

$$\rho\omega^2 |\mathbf{s}|^2 - (\lambda + \mu)(\mathbf{s} \cdot \mathbf{k})^2 - \mu k^2 |\mathbf{s}|^{\mathbf{2}} = 0, \tag{1.21}$$

which is a quadratic equation in $|\mathbf{s}|$ with two solutions. One of the solutions is found by setting the particle motion to be perpendicular to the propagation direction $\mathbf{s} \cdot \mathbf{k} = \mathbf{0}$, which reduces the above equation to the dispersion equation for S waves:

$$\omega/k \;\; = \;\; \sqrt{\mu/\rho} = c_s. \tag{1.22}$$

We can also choose the particle motion vector $\mathbf{s}$ to be parallel to the wave propagation vector $\mathbf{k}$ so that $\mathbf{s} \; || \; \mathbf{k}$. This gives us the dispersion equation for P waves:

$$\omega/k \;\; = \;\; \sqrt{(\lambda + 2\mu)/\rho} = c_p. \tag{1.23}$$

The above analysis says that S waves propagate perpendicular to the particle motion in a homogeneous medium while the particle motion is parallel to the propagation direction for P waves. Comparing equation 1.23 to equation 1.22 says that the $c_p > c_s$, and in practice the P-wave velocity is about twice or more faster than the S-wave velocity. For a layered medium, there can be two types of S waves, SV waves where the particle motion is parallel to to the vertical plane and SH waves where the particle motion is parallel to the horizontal plane. For a layered medium, the SH can get trapped between the free surface and a layer

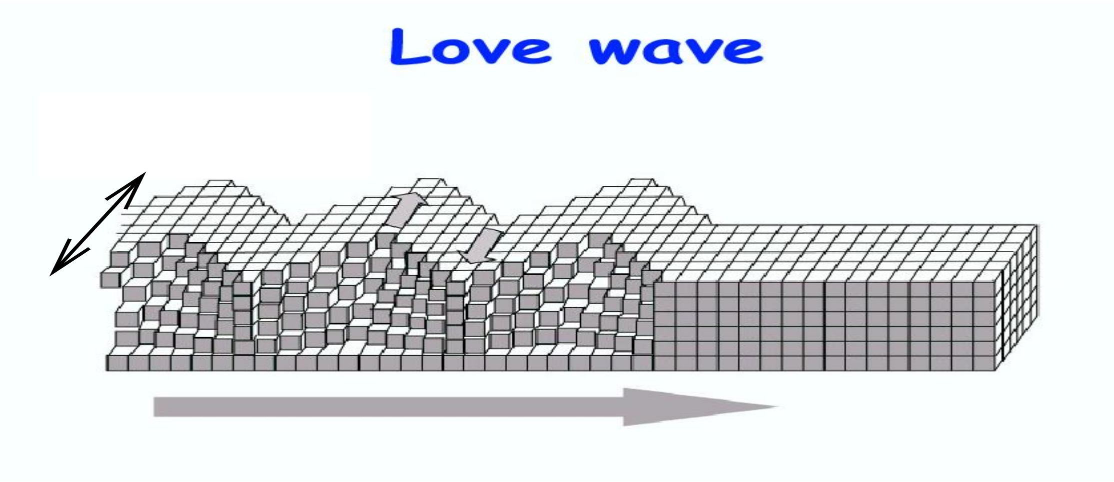

Figure 1.8: Love wave particle motion.

interface that seperates a low-velocity layer from its faster layer underneath it. The motion diagram for Love waves is shown in Figure 1.8.

If a plane wave is propagating parallel to the plane of this page in a layered medium with horizontal interfaces, then SH waves will honor the scalar wave equation

$$\ddot{\psi}_y \quad = \quad c_s^2\nabla^{\mathbf{2}}\psi_{\mathbf{y}}, \tag{1.24}$$

in each layer with shear velocity c_s. In contrast, the associated PSV plane waves will honor the equations

$$\ddot{\psi}_x = c_s^2\nabla^{\mathbf{2}}\psi_{\mathbf{x}}; \qquad \ddot{\psi}_z = c_s^2\nabla^{\mathbf{2}}\psi_{\mathbf{z}}, \tag{1.25}$$

where the $y-$coordinate axis is perpendicular to this page.

1.5 Reflection Coefficient at the Free Surface

The reflection coefficients will now be derived for a plane P wave incident from below on the free surface in Figure 1.9a. Here we assume the particle motion of the plane P wave to be restricted to be along the vertical plane. There are two reflected waves in Figure 1.9a, a PP and a SV wave. The SV wave is needed in order to satisfy the equations of constraint at the free surface, namely that $\tau_{zz} = 0, \tau_{zx} = 0$ at $z = 0$ along the free surface. Two equations of constraint mean that there must be two unknowns, the reflection coefficients PP and PS. Here, symmetry considerations say that only a PP wave and a SV wave are reflected from the surface and not a SH wave which has particle motion in and out of the page and no component along the vertical plane.

The starting point for deriving the unknown reflection coefficients PP and PS in Figure 1.9a is to write the *total* traction components as

$$\mathbf{T} \quad = \quad (\tau_{zx}, \tau_{zy}, \tau_{zz}), \tag{1.26}$$

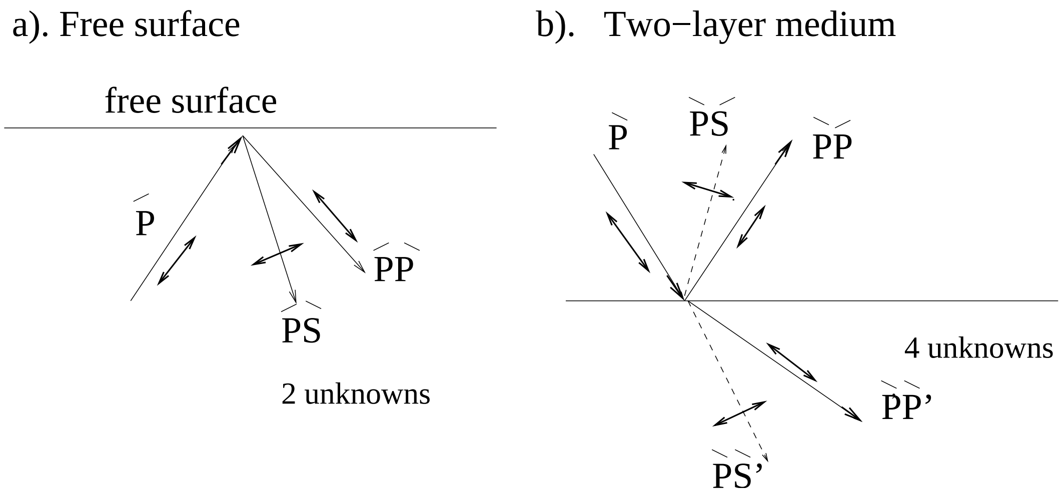

Figure 1.9: Plane wave impinging upon a horizontal interface at the a). free surface and b). along a 2-layer interface.The double-sided arrows indicate the direction of particle motion.

where $\tau_{zy} = 0$ because there is no PSV particle motion along the y axis, so there is no strain ϵ_{yz}; no strain means no shear stress $\tau_{zy} = 0$.

1. The next step is to write the stress components in terms of the P-wave displacement $\mathbf{u}$ in equation 1.7, and then rewrite the displacements in terms of potentials (i.e., $(u, 0, w) = (\partial\phi/\partial x, 0, \partial\phi/\partial z)$ in equation 1.12 to get the traction components in terms of the P-wave potential:
$$\mathbf{T}^P = (2\mu\partial^2\phi/\partial z\partial x, 0, \lambda\nabla^2\phi + 2\mu\partial^2\phi/\partial z^2). \tag{1.27}$$

2. Similarly the stress components (where $(u, 0, w) = (-\partial\psi/\partial z, 0, \partial\psi/\partial x)$) for the SV wave are given as
$$\mathbf{T}^{SV} = (\mu(\partial^2\psi/\partial x^2 - \partial^2\psi/\partial z^2), 0, 2\mu\partial^2\psi/\partial z\partial x). \tag{1.28}$$

3. The plane wave forms for the total potential wavefields is given as
$$\phi = \overbrace{e^{i(k_x x + k_z z)}}^{incident\ P-wave} + \overbrace{PPe^{i(k_x x - k_z z)}}^{reflected\ PP-wave},$$
$$\psi = \overbrace{PSe^{i(\kappa_x x - \kappa_z z)}}^{reflected\ PS-wave}, \tag{1.29}$$
where κ is the wavenumber vector for the PS wave. The unknowns we wish to solve for are the reflection coefficients PP and PS. To solve for two unknowns we need two linear equations of constraint.

4. The boundary conditions at the free surface
$$\mathbf{T}^P + \mathbf{T}^S = (0, 0, 0), \tag{1.30}$$

provide two non-trivial equations of constraint. Plugging equations 1.27-1.29 into equation 1.30 gives two linear equations with the two unknowns PP and PS. These unknowns can be solved for to give the free-surface reflection coefficients (Aki and Richards, 1980):

$$\begin{aligned} PP &= \frac{4\beta^4p^2cos(i)cos(j)/(\alpha\beta) - (1-2\beta^2p^2)^2}{4\beta^4p^2cos(i)cos(j)/(\alpha\beta) + (1-2\beta^2p^2)^2}, \\ PS &= \frac{-4\beta^2pcos(i)(1-2\beta^2p^2)/\alpha}{4\beta^4p^2cos(i)cos(j)/(\alpha\beta) + (1-2\beta^2p^2)^2}, \end{aligned} \tag{1.31}$$

where α, β, and ρ indicate P-wave velocity, S-wave velocity and density respectively. The $\mathbf{p}$ slowness vector is equal to $\mathbf{k}/\omega$; and the angles i and j correspond to the PP and PS reflection angles, respectively, measured with respect to the vertical axis.

1.6 Reflection Coefficients for a Two-Layer Medium

Figure 1.9b depicts a plane P wave impinging upon a horizontal elastic interface. Here, there are 4 different wave types to consider because reflected and transmitted converted shear waves can be generated at the interface, as well as a reflected and transmitted P wave. The shear waves have particle motion that is perpendicular to the propagation direction while the compressional components are parallel to the direction of propagation. Imposing continuity of vertical and horizontal particle velocity and normal $\tau_z z$ and shear stress τ_{zx} tractions provide four equations of constraint. Similar to the acoustic case, we can solve these four equations for the unknown amplitudes $PP, PS, PS', \ and \ PP'$. The PP reflection coefficient is given in Aki and Richards (1980):

$$PP \;=\; [(bcos(i_1)/\alpha_1 - ccos(i_2)/\alpha_2)F - (a + dcos(i_1)cos(j_2)/\alpha_1\beta_2)Hp^2]/D, \tag{1.32}$$

where $a, b, c, d,$and D are constants defined in Aki and Richards (1980). The subscripts 1 and 2 refer to the top and bottom layers respectively and j corresponds to the angle of the converted S waves.

1.7 Rayleigh Waves at the Free Surface

For a SV plane wave incident on the free surface in Figure 1.10a, it produces reflected body waves SP and SS. The vertical wavenumber components of these reflected waves are given as

$$k_z = \sqrt{\omega^2/\alpha^2 - k_x^2}; \qquad \kappa_z = \sqrt{\omega^2/\beta^2 - k_x^2}; \tag{1.33}$$

where $k_x = sin\theta/\beta$ and θ is the incidence angle of the SV wave measured with respect to the vertical. Since $\alpha > \beta$, there will be incidence angles where $k_x \geq \omega/\alpha$, which leads to vertical wavenumber components that are purely imaginary. This means that the SP plane wave represented by $\phi = e^{i(k_xx+k_zz)} = e^{(ik_xx-|k_z|z)}$ will have a decaying component in the z direction and a propagating component in the horizontal x direction[1]. This is similar to the case of refraction arrivals discussed in Chapter 1, except now the propagation is along the free surface. Working through this boundary value problem here in the same manner as the previous section shows this inhomogeneous wave to have unusual properties. It is known as a Rayleigh wave and has the following characteristics.

1. The Rayleigh wave has retrograde ellipitical motion as shown in Figure 1.10b. An actual recording is shown in Figure 1.11.
2. For a homogeneous medium it has a velocity about 0.9β.
3. Rayleigh waves spread along the planar free surface rather than a 3D medium, so the attenuation due to geometrical spreading is not strong compared to body waves. Consequently, the surface waves have much stronger amplitudes than body waves as shown in Figure 1.13.
4. Earthquakes deep in the earth are strong generators of surface waves because they are efficient in generating shear waves (faults tear or shear, not compress) along a fault plane. See Figure 1.12 for an illustration of 4 types of fauilts. Shallower earthquakes generate stronger shear waves.
5. The shear wave propagation velocity of Rayleigh waves is very sensitive to the shear velocity distribution, but not the P-wave velocity distribution. Consequently they are inverted by seismologists for S wave distributions.
6. Rayleigh wave amplitudes decay exponentially with depth, and become insignificant deeper than two wavelengths. Thus, low-period surface waves probe to deep depths of about 1 or 2 wavelengths while high-frequency Rayleigh waves are only sensitive to shallow velocity structures.

1.8 AVO Effects

The variation of reflection and transmission coefficients with incident angle and thus offset is commonly known as offset-dependent reflectivity. The Zoeppritz equations (1919) describe the reflection and transmission coefficients as a function of incident angle and elastic media properties (density, P-wave velocity, and S-wave velocity), of which the PP Zoeppritz equation is given in equation 1.32. They apply to a reflection of plane-waves between two half-spaces, and do not include wavelet interferences due to layering. Furthermore, amplitudes are a measure of the reflection coefficient only when effects that cause amplitude distortions have been removed. Thus, preprocessing to remove transmission loss, source and receiver effects, spherical divergence, multiples, and so on, is essential to the successful recovery of the reflection coefficients. The last 20 years has seen the practical use of AVO effects as a direct hydrocarbon indicator.

---

[1] If all the wavenumber components are real this type of wave is known as a body wave. If at least one of the wavenumber components is imaginary then this is known as an inhomogeneous or interface wave.

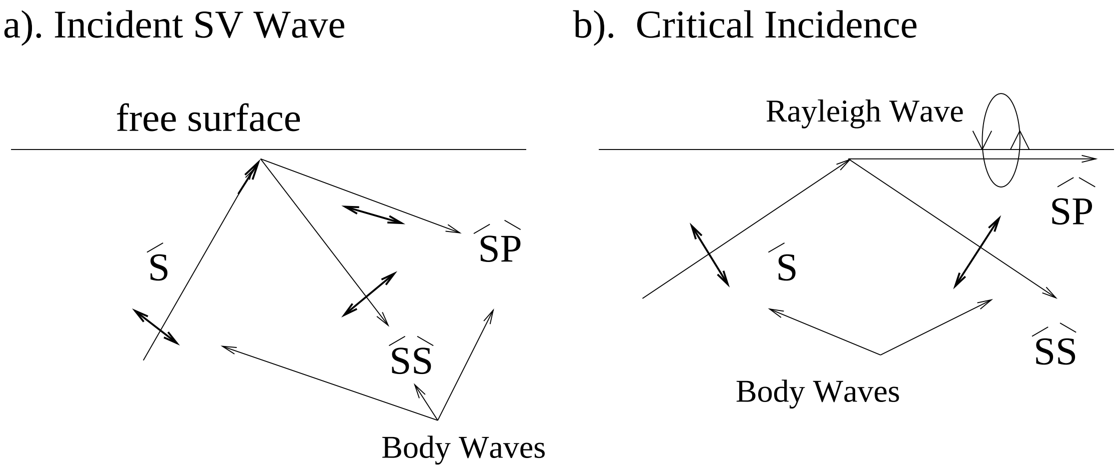

Figure 1.10: At critical SV incidence angles, the converted SP wave in b). propagates parallel to the free surface. This situation produces an inhomogeneous wave that decays in depth and only propagates along the lateral direction. For this example, the surface wave is a Rayleigh wave with retrograde ellipitcal particle motion.

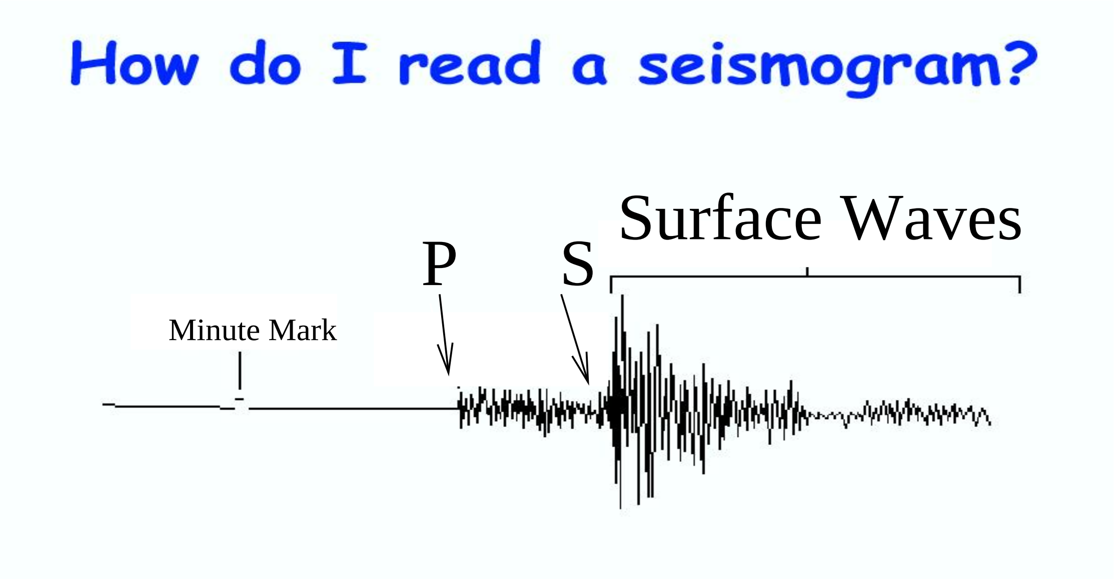

Figure 1.11: Actual seismogram showing the first arrival as the P wave and the secondary arrival of the S wave followed almost immediately by the Rayleigh wave and other surface-related modes. Recall, surface waves have less geometrical spreading than body waves.

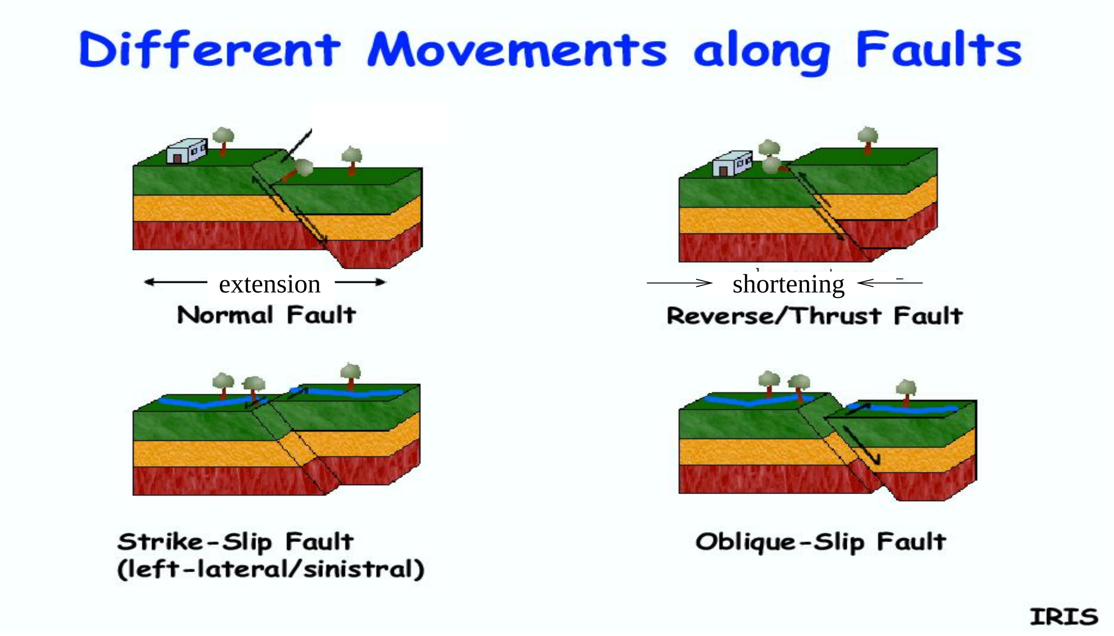

Figure 1.12: Four types of faults that are observed along the earth's surface.

An example of a a shot gather collected in Saudi Arabia is shown in Figure 1.13. Here, the surface waves (primarily Rayleigh waves) propagate much with a much slower apparent velocity than do the reflected PP arrivals. The reflection events fall along a hyperbola curve in $x-t$ space, and the first arrivals are refraction events. A reflecting event of interest is identified (e.g., the events along the hyperbola with time intercept at approximately 1 s in Figure 1.13) and the amplitude of this event is picked and displayed as a function of offset parameter x. For young sedimentary rocks such as Tertiary sands in the Gulf of Mexico, the amplitude vs offset (AVO) behavior can often distinguish brine-filled sands from gas sands (Ostrander, 1984). To simplify the analysis, an approximation based on small changes in elastic parameters is used to approximate equation 1.32.

1.8.1 Small Angle Approximation to Reflection Coefficients

A modified version of Ekert's AVO report is given below.

For a two layered medium separated by a horizontal interface the PP reflection coefficient for small jumps in the medium parameters are given by

`(C. Ekert, SEP Report http://sepwww.stanford.edu/public/docs/sep96/paper_html/node34.html)`

$$R(\theta) \quad = \quad \frac{1}{2\cos^2\theta} I_p - 4\gamma^2 \sin^2(\theta) I_s + (2\gamma^2 sin^2\theta - \tan^2\theta) D \tag{1.34}$$

where

$$I_p = (\Delta v_p/v_p + \Delta\rho/\rho); I_s = (\Delta v_s/v_s + \Delta\rho/\rho); D = \Delta\rho/\rho; \tag{1.35}$$

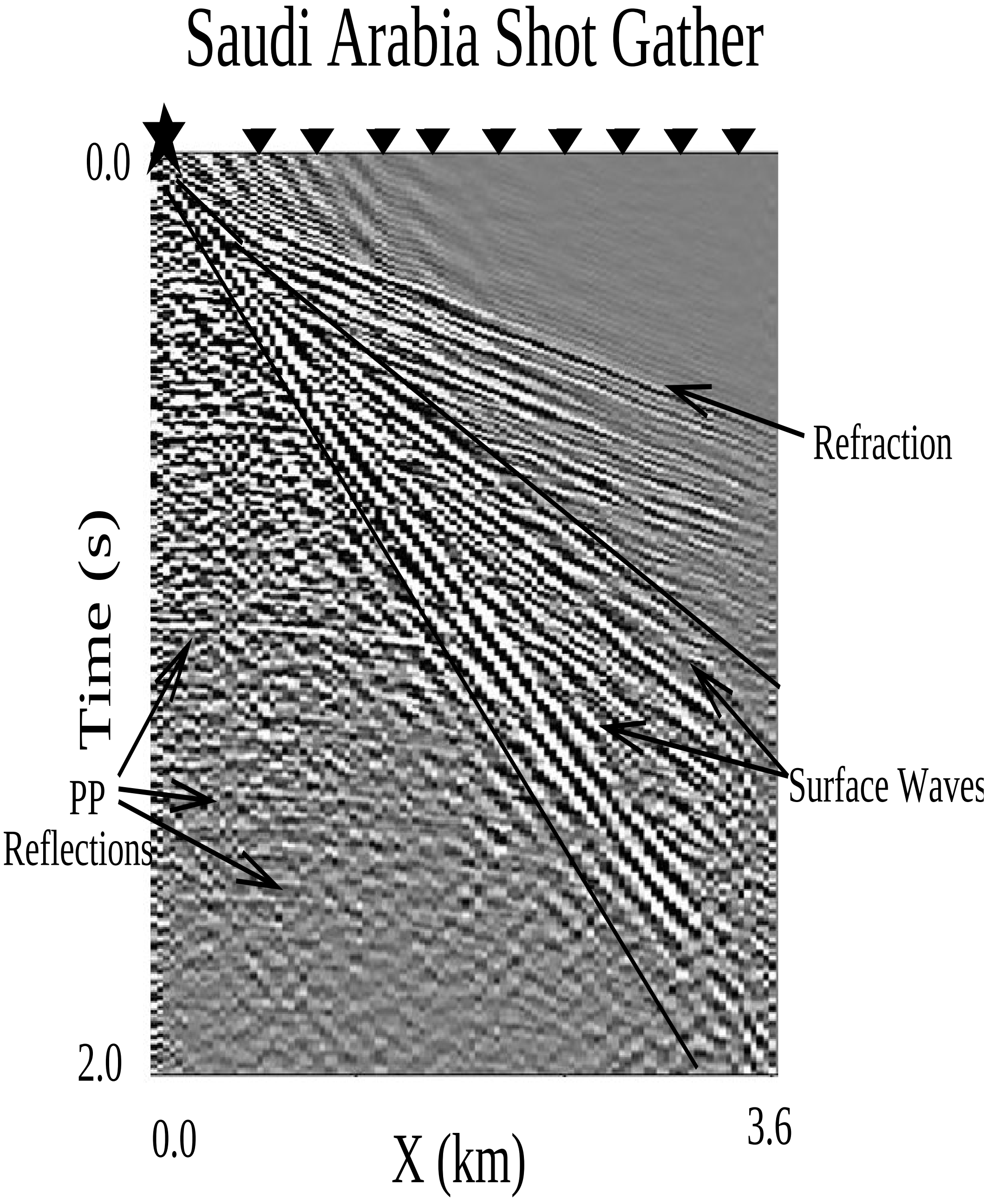

Figure 1.13: Shot gather from Saudi Arabia.

with

$$\Delta v_p = v_{p2} - v_{p1}; \Delta v_s = v_{s2} - v_{s1}; \Delta\rho = \rho_2 - \rho_1;$$
$$v_p = (v_{p2} + v_{p1})/2; v_s = (v_{s2} + v_{s1})/2; \rho_s = (\rho_{s2} + \rho_{s1})/2; \tag{1.36}$$

The first angle-dependent term in equation 1.34 significantly contributes for $0 < \theta < 30$ *degrees, while the second starts to significantly contribute for* $\theta > 30$ *degrees. The term* γ *is the background* v_s/v_p *estimate.*

The reflectivity curves corresponding to either a unit perturbation in P-impedance contrast ($\mathrm{I_p} = 1, \mathrm{I_s} = 0, \mathrm{D} = 0$*), S-impedance contrast or density contrast can be seen in Figure 1.14. For a unit perturbation in relative P-impedance contrast, the P-impedance inversion curve dominates at small angles of incidence and increases with increasing offset. For a unit perturbation in relative S-impedance contrast, the S-impedance inversion curve is zero at normal incidence and is increasingly negative with increasing offset. Over the conventional range of surface reflection data acquisition geometry illumination, which is typically* 0° *to* 35°*, the density inversion curve is not significant, as most of the density contrast contributes to the reflection AVO through the impedance contrasts alone. As the reflection amplitudes are mostly a combination of the P- and S-impedance contrast inversion curves, reflectors with P- and S-impedance contrasts of the same polarity and magnitude are expected to show approximately constant amplitude versus offset. On the other hand, reflectors with P- and S-impedance contrasts of opposite polarities, indicating a transition zone of changing rock pore fluid properties, should show increasing amplitudes versus offset. Reflectivity data can be inverted for changes in P- and S-impedance across an interface and therefore for possible pore fluid transitions.*

For $\theta < 30$ degrees, geophysicists will use the small angle approximation to equation 1.34:

$$R(\theta) \quad \approx \quad A + B\sin^2\theta, \tag{1.37}$$

and plot up crossplot curves (Foster et al., 1997) to assess geology. Shuey showed that linearization of the fluid factor (Shuey, 1985)

$$A = R_0; B = 1/2\Delta v_p/v_p tan^2\theta, \tag{1.38}$$

where $\tan^2\theta \approx \sin^2\theta$ for small angles.

For example, Figure 1.15 depicts the crossplot of A and B pairs taken from a well log. These A and B pairs can be obtained by estimating the density and P- and S-wave velocities from the sonic log at each depth point, plug in these values into equation 1.34 to estimate $R(\theta)$ for a particular depth level, and find A and B from equation 1.37. The resulting A-B plot shows a linear trend, and the idea is that any deviations from this trend represent a significant change of geology such as oil or gas bearing rocks. The departures can be estimated by finding A and B pairs from the $R(\theta)$ vs θ curves estimated from the seismic reflection amplitudes along a horizon of interest.

In detail, AVO analysis might bbe carried out using the following steps.

1. Take a common midpoint gather, identify a reflection of interest, and plot its amplitude vs offset A midpoint gather is a collection of traces where the source and receiver for any trace has the same midpoint. Often the data are redatumed down to the reflector of interest.

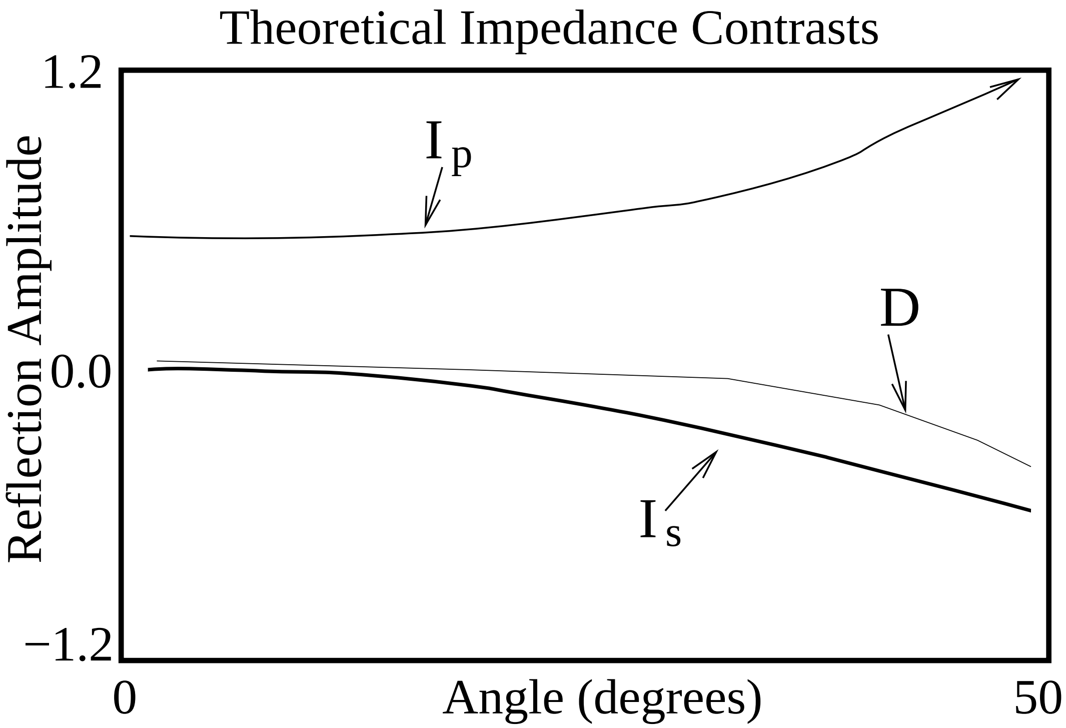

Figure 1.14: Theoretical P, S, and Density impedance inversion curves (from Ekert, SEP) .

2. Pick $R(\theta)$ from the data and plot on a graph. Find the slope and the intercept of the best fit lines as a function of angle using the above formula. That is, find A and B.

3. Plot A vs B for different midpoints as shown in the crossplot of Figure 1.15.

4. The most interesting midpoint is where the oil or gas fluids have a marked signature in the crossplot shown in Figure 1.16. Simms et al. (2000) writes the following.

   AVO crossplots are a simple and elegant way of representing AVO data. Offset variations in amplitude for reflecting interfaces are represented as single points on a crossplot of intercept and gradient. The advantage of this type of plot is that a great deal of information can be presented and trends can be observed in the data that would be impossible to see with a standard offset (or angle) versus amplitude plot. The crossplot is an ideal way of examining differences in AVO responses that may be related to lithologic or fluid-type variations. Commonly used techniques for revealing these differences include color-coding samples from the crossplot and using this as an overlay to a seismic display or creating weighted (or "equivalent angle") stacks (i.e., linear combinations of intercept (R0) and gradient (G).

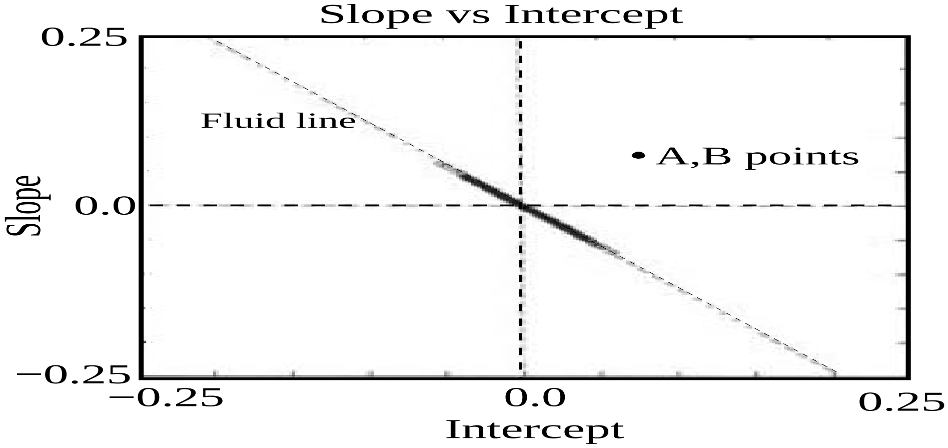

Figure 1.15: Crossplot of slope (B) and intercept (A) pairs using well log data from the North Sea. The dashed line corresponds to the fluid line for $\alpha/\beta = 1.9$. The A and B pairs tend to lie on a trend that is consistent with the fluid line. Note, the fluid line assumes a constant density, the actual density profile is used to compute A and B.

1.9 Practical Aspects of AVO.

Simm et al. (2000) writes that *The early literature approached AVO crossplots from the point of view of rock properties. A central concept that emerged from this work was the "fluid line," a hypothetical trend based on a consideration of brine-filled rock properties together with simplifications of the reflectivity equations (Figure 1). If the intercept is plotted on the x axis and the gradient on the y axis, then for consolidated sand/shale rocks the top and base reflections form a trend from the upper left to the lower right quadrant of the crossplot that passes through the origin. When it was realized that data points for equivalent hydrocarbon-filled rocks plot to the left of this line, it became clear that normalizing the data against the fluid line might provide an optimum AVO indicator.* A real data plot is given in Figure 1.17.

Details for implementing this AVO (i.e., Amplitude vs Offset) procedure are non-trivial because much data processing must be performed before the A and B pairs can be picked. Nevertheless, significant oil and gas deposits have been discovered by the AVO method.

The following is copied from Simms et al. (2000). *Consider a single point in the lower right quadrant on a crossplot (Figure 1.18). This point was generated from the AVO attributes (derived by least squares regression) associated with the maxima of a single zero-phase reflection on a synthetic gather with no noise. It represents a class I response from the top of a brine-filled consolidated sand at the boundary with an overlying shale, i.e., the amplitude is decreasing with offset. This representation might be called a "horizon crossplot" as it relates to a single reflecting interface.*

If data from several gathers with the same reflection are crossplotted, then the crossplot signature is of course the same?a single point on the plot. However, if random noise is added

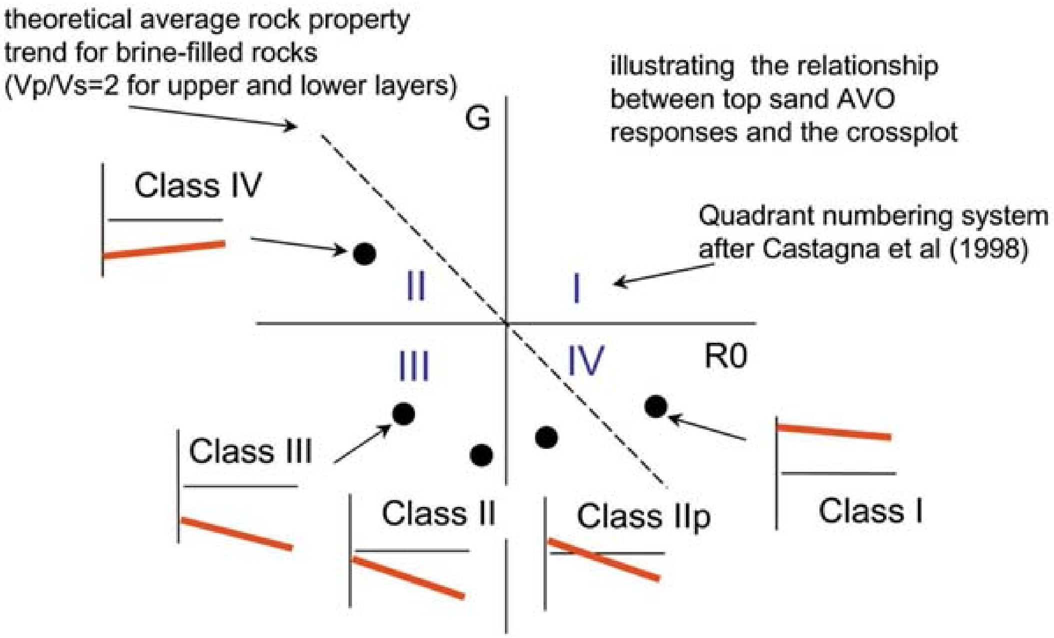

Figure 1.16: Schematic of crossplot of slope (B) and intercept (A) pairs. A fluid line for $\alpha/\beta = 2.0$ was assumed. Different classes of rock will plot in different quadrants of the plot (Simm et al., 2000).

uniformly across the gathers (such that the S/N decreases with offset), the crossplot response becomes an oval distribution of points around the real location (Figure 1.18b). This is due to the sensitivity of the gradient estimation to noise. Hendrickson has termed this the "noise ellipse." This noise trend is easily recognized on real data, for example by crossplotting a limited number of samples from the same horizon from a seismic section. The extension of the trend parallel to the gradient axis is an indication of the amount of noise in the data. On real data the noise trend usually has a slope of about ?5 or more. The effects of other types of noise (such as RNMO) will not be dealt with here.

Cambois indicated that the slope of the noise trend is dependent on two-way traveltime, velocity structure, and offset. On real data the general position of a data cluster (such as that shown in Figure 1.18b) is dependent on the relative scaling of R0 and G (and may be affected by residual moveout or uncorrected amplitude decay). However, the slope of the noise trend is independent of this scaling.

Although random noise appears to be the principal component of noise on AVO crossplots, other types of noise can have an influence on the observed trends (such as RNMO).

Porosity and shale content. *A change in lithology can be modeled by varying the porosity of the sand or the shale content. Increasing the porosity has two effects?to decrease the AVO gradient (i.e., the Poisson ratio contrast with the overlying shale has been reduced) and to decrease the intercept (owing to a decrease in the impedance contrast). The decrease in intercept gives rise to a low-angle porosity trend that intercepts the gradient axis.*

Changing the porosity of the sand in the model (but still maintaining the criteria of

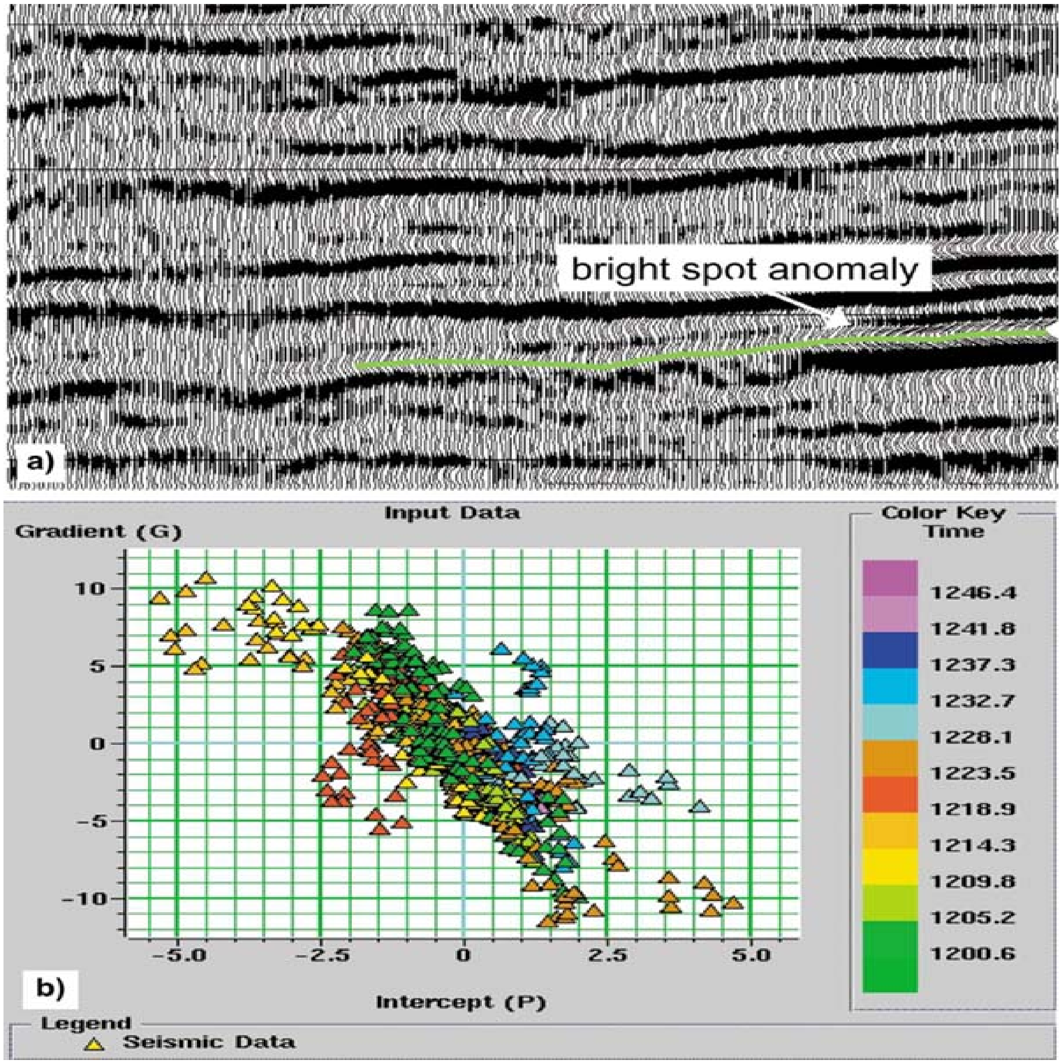

Figure 1.17: A real data example. (a) Stacked section illustrating a bright spot with a top sand pick in green. (b) Time-window crossplot generated from a 40-ms window around the top-sand pick. (Simm et al., 2000).

noninterfering reflections) results in a crossplot that shows a series of ellipses aligned at an angle to the gradient axis (Figure 1.18c). The trend imposed by the eye on this data cluster would be somewhere between the porosity trend and the noise trend.

A change in lithology due to increasing shale content of the sand also lowers the gradient and intercept, but the trend is steeper than the porosity trend. It may even be close to the noise trend. In the case where the shale component in the sand is different from the overlying shale (as might be found at a sequence boundary), then the "lithologic trend" would have a nonzero intercept value.

This discussion illustrates that a given area might not have one background trend but a possible variation, depending on the relative contributions of shale and porosity which, in turn, are determined by sedimentary facies. This is a moot point, however, given that in practice noise obscures the lithologic trend.

The gas effect. *Figure 1.18 shows the effect of fluid substituting the sands of varying porosity (again the reflections are separate and noninterfering). The effect of the hydrocarbon is not so much to define a trend as to create a separate data cluster occupying a position to the left of the brine-bearing data points. The greater the effect of the hydrocarbon on the VP/VS ratio of the sand, the further the data points will plot away from the brine-filled data points.*

In these models, the optimum discriminator can be determined statistically (Figure 1.18). This will depend on the amount of noise, the lithologic variation, and the magnitude of the gas effect. This trend may or may not pass through the zero point. In the real-world case, knowledge of the noise trend could be used to model the optimum discriminator (assuming all other effects on R0 and G could be accounted for). If the lithologic variation is not large, a range of trends may exist that would discriminate equally well.

So far, discussion has centered on the horizon crossplot. If samples from a time window are incorporated into the crossplot, the horizon sample points, together with reflections from the base of the sand (plotting in the upper left quadrant), are included in an ellipse of points centered on the origin (Figure 1.18f). The organization of data around the origin does not have a physical significance; it is simply the result of the fact that the mean of seismic data is zero. Noise related to sampling parts of the waveforms other than the maxima is infilling the area between the two data clusters.

Cambois has shown that the slope of what might be called the "time-window" trend (i.e., a line drawn through the data which passes through the origin) is dependent on the S/N of the data. The lower the S/N, the steeper the trend. This trend may be close to the optimum discriminator or it may not. The noisier the data, the closer this time-window trend will be to the noise trend.

In the case where S/N is very high, it could be argued that the line derived from a time-windowed crossplot is equivalent to an average rock property trend (call it the fluid line if you must) that can be inferred from a crossplot derived from well data. Given the general level of S/N of most seismic data, this occurrence is likely to be rare.

Crossplots in practice. *It is clear that the authors see little value in time-window crossplots, owing to the effects of noise. However, these crossplots have successfully recognized hydrocarbon-related AVO anomalies, usually related to gas where the change in crossplot*

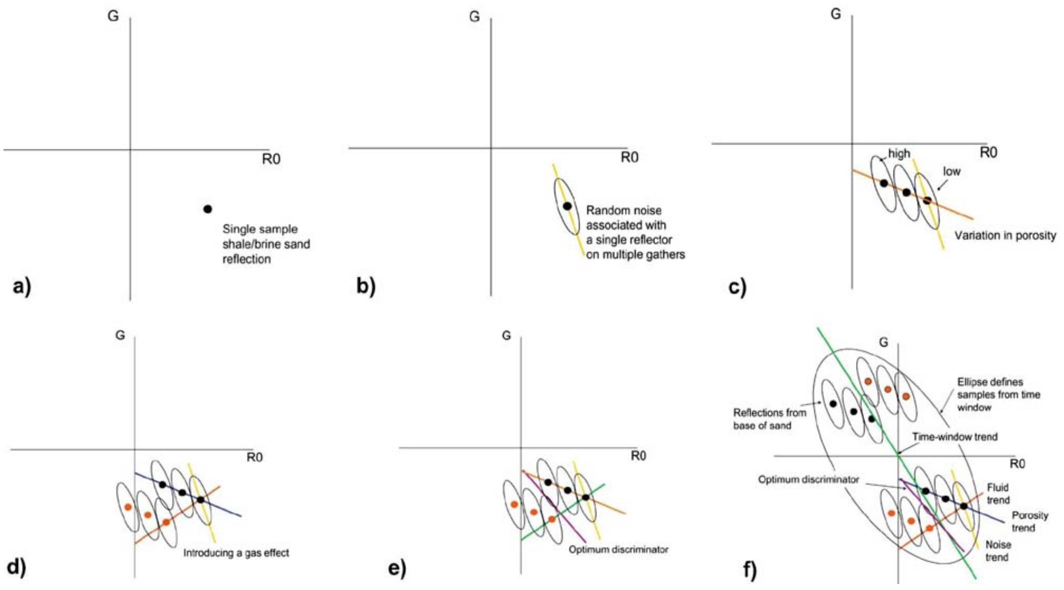

Figure 1.18: The anatomy of AVO crossplots. (a) A single class I reflection. (b) The noise associated with the measurement of gradient on numerous gathers. (c) The porosity effect. (d) The gas effect. (e) The optimum discriminator. (f) The time-window crossplot. (Simm et al., 2000).

position is dramatic. Oil-related anomalies are usually well hidden in the noise of the plot. Figure 1.17 shows an example of a time-window crossplot related to a bright spot and its correlative reflector. The samples from the bright spot are clearly anomalous in terms of their AVO behavior.

On the other hand, the horizon crossplot clearly targets the reservoir of interest and helps determine the noise trend while revealing the more subtle AVO responses. Figure **??** *shows the horizon crossplot for the portion of reflector marked in Figure* **??**. *The responses are characterized by negative reflections and positive gradients (i.e., a class IV response). The nonbright part of the reflector has a high angle slope shown on the near/far crossplot to be almost totally due to noise. The bright spot has a lower-angled slope on the crossplot (owing to higher S/N), and it is possible to see the noise trend as a second-order effect.*

Horizon crossplots can be generated from maps created from AVO attributes or partial stack 3-D interpretations. These crossplots need to be made in a number of locations to make sure that an adequate sample has been analyzed. In practice it may not be easy to identify an optimum discriminator from the crossplots, but the noise trend is usually straightforward to determine.

AVO anomaly maps can be created from linear combinations of R0 and G. These combinations are usually of the form $R_0 + Gx$, *where* $x = -G/R_0$ *and is determined from the slope of the trend on the crossplot. Considering that the reflection amplitude is described by* $Rc = R_0 + G\sin 2\theta$, *x represents an "effective" angle. Any slope on an AVO crossplot is an "effective angle stack." However, which trend should be used to create the AVO anomaly map?*

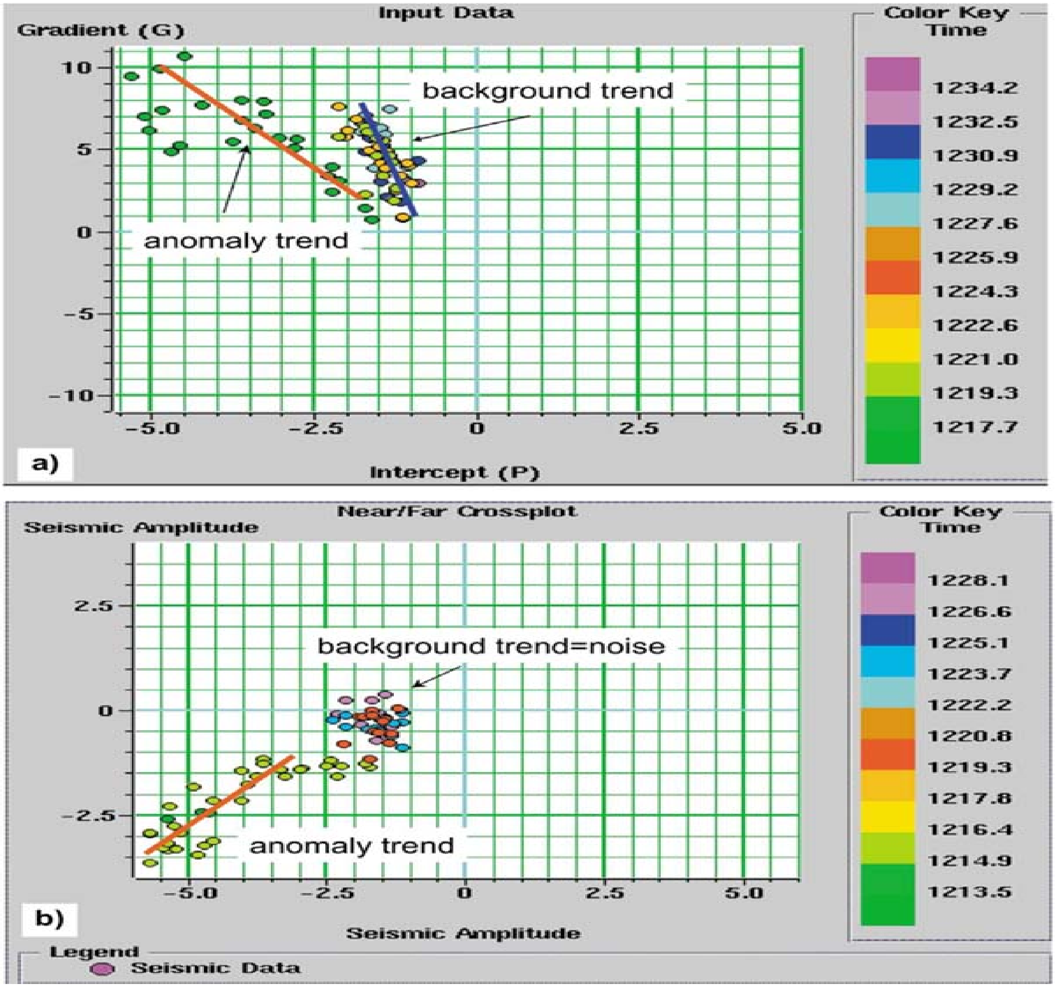

Figure 1.19: Horizon crossplots. (a) R0/G crossplot for the pick shown in real data Figure and illustrating the different trends associated with the bright spot and the "background" reflectivity. (b) Near/Far crossplot illustrating that the background trend on the R0/G crossplot is related to noise and not to lithology. (Simm et al., 2000).

The answer (as in many issues in seismic interpretation) is that it is impossible to be definitive. Although crossplots are useful to determine which equivalent stack is likely to be most discriminatory in terms of fluids, they are only a one-dimensional view of a limited amount of seismic data. The real interpretation issue is whether the anomalous responses represent porosity or hydrocarbon effects, and the only way to determine which interpretation to make is to analyze the relationship of the anomaly to mapped structure. In some cases, the equivalent angle stacks representing the noise trend, the time-window trend, and the optimum discriminator may give similar results, owing to the fact that the hydrocarbon effect is a displacement at a high angle to all these trends.

Probably the best approach to the use of crossplots in interpretation is to be published by Hendrickson (in press). He illustrates the use of a range of equivalent angle stacks in an interpretation, examining the amplitude conformance to structure on each stack as well as recognizing their significance in terms of the AVO crossplot. Interpretation is a question of "covering all the angles" so to speak. **Further Reading.** *"AVO attributes and noise: pitfalls of crossplotting" by Cambois (SEG 1998 Expanded Abstracts). "Framework for AVO gradient and intercept interpretation" by Castagna et al. (GEOPHYSICS, 1998). "Principles of AVO crossplotting" Castagna and Swan (TLE, 1997). "Another perspective on AVO crossplotting" by Foster et al. (TLE, 1997). "Stacked" by Hendrickson, (Geophysical Prospecting, 1999). "Yet another perspective on AVO crossplotting" by Sams (TLE, 1998).*

1.10 Summary

The stress-strain relations are introduced for an elastic medium, and the resulting equations of motion are derived. There are two types of solutions to this equation, P waves and S waves. Solving a boundary value problem for a layered medium reveals the analytic formula for PP and converted PS reflection waves. These formula show the existence of two types of S waves, SV and SH waves. Particle motions of S waves is perpendicular to the direction of wave propagation, and the S-wave velocity is typically slower by a factor of two or more compared to P waves. The analytic expressions for the PP reflection coefficient reveals that the AVO curves can be used to distinguish gas-filled sands from sediment-brine-filled sands. AVO analysis applied to real data is typically implemented by picking $R(\theta)$ values from horizons of interest in CMPs, estimating and plotting the associated A-B curves, and searching for deviations of points from the fluid line. Deviations can sometimes be associated with gas plays, or other types of lithologies. The fluid line is found by predicting the $R(\theta)$ curves from the density and velocity values in a well log devoid of gas shows. In practice AVO analysis appears to work best for young sand-shale sediments, and not work so well for older consolidated rocks such as limestones or older stiff sands. This is because the stiffness of the rock is primarily controlled by the hard rock matrix (such as limestone) and not by the fluid filling its pores. In this case, filling pores with gas or brine should not greatly change the impedance properties.

1.11 Problems

1. Identify the direct arrival, air wave, surface waves, refraction arrivals, and reflection arrivals in the CSG shown in Figure 1.13. Estimate the apparent velocity in the x-direction Vx and the associated period for each event. From these calculations determine the wavelengths. Show work.

2. Which arrivals have the same apparent velocity as the actual propagation velocity of that event? Why?

3. The 1-D SH wave equation is the same form as the 1-D acoustic wave equation, except c becomes the shear wave velocity, P becomes the y-component of displacement v, c=sqrt(mu/rho) where mu is the shear modulus, and the SH wave equation is

$$1/c^2 \partial^2 v/\partial t^2 - \partial^2 v/\partial z^2 = 0 \tag{1.39}$$

   SH (or shear horizontal) refers to the fact that the shear wave particle motion is perpendicular to the direction of particle motion, and is along the horizontal direction (in and out of plane of paper). The SH continuity conditions at the interface at z=0 are a). Continuity of y-displacement $v^+ = v^-$., b). Continuity of shear traction: $\mu \partial v/\partial z^+ = \mu \partial v/\partial z^-$, where μ is the shear modulus.

   Derive the y-displacement reflection and transmission coefficients for a plane SH wave normally incident on a planar interface in an elastic medium.

1.12 Appendix 1: Elastic Parameters

Some elastic parameters are are described below by Professor Steven Dutch in his course notes at http://www.uwgb.edu/dutchs/structge/strsparm.htm.

Elastic material deforms under stress but returns to its original size and shape when the stress is released. There is no permanent deformation. Some elastic strain, like in a rubber band, can be large, but in rocks it is usually small enough to be considered infinitesimal. Many elastic materials obey Hooke's Law behavior: the deformation is proportional to the stress. This is why spring balances work: twice the weight results in twice the deformation.

For materials, Hooke's Law is written as: Stress = E Strain. Alternatively, the relationship is sometimes written E = Stress/Strain. This is the reverse of the way the law is written in most physics texts. In physics, we can often apply the stress in a controlled way and we are interested in predicting the behavior of the spring, for example, how it oscillates. In materials science and geology, we often know the strain and want to know what stress produced it. The two versions are equivalent; the only difference is which side the constant is written on. The constant E is called Young's Modulus. Because strain is dimensionless, Young's Modulus has the units of pressure or stress, i.e. pascals.

1.12.1 Physical Meaning of Young's Modulus

If strain = 1, stress = E, then Young's Modulus can be considered the stress it would take (theoretically only!) to result in 100 percent stretching or compression. In reality, most rocks fracture or flow when deformation exceeds a few percent, that is, at stresses a few percent of Young's Modulus.

The seismic P- and S-wave velocities in rocks are proportional to the square root of E. For most crystalline rocks, E ranges from 50-150 Gpa, averaging about 100. If we take 100 Gpa as an average, and consider one bar (100,000 pa) of stress, we have: 105 = 1011 Strain, or Strain = 10-6. Thus, rocks typically deform elastically by 10-6 per bar of stress. This is a useful quantity to remember. Elastic strain in rocks is tiny - even ten kilobars typically results in only one percent deformation - if the rock doesn't fail first.

1.12.2 Poisson's Ratio

When a material is flattened, it tends to bulge out at right angles to the compression direction. If it's stretched, it tends to constrict. Poisson's Ratio is defined at the ratio of the transverse strain (at right angles to the stress) compared to the longitudinal strain (in the direction of the stress).

Note that the ratio is that of strains, not dimensions. We would not expect a thin rod to bulge or constrict as much as a thick cylinder. For most rocks, Poisson's Ratio, usually represented by the Greek letter nu (ν averages about 1/4 to 1/3). Materials with ratios greater than 1/2 actually increase in volume when compressed. Such materials are called dilatant. Many unconsolidated materials are dilatant. Rocks can become dilatant just before failure because microcracks increase the volume of the rock. There are a few weird synthetic foams with negative Poisson's Ratios. These materials are light froths whose bubble walls collapse inward under compression.

1.12.3 Shear Modulus

Poisson's Ratio describes transverse strain, so it obviously has a connection with shear. The Shear Modulus, usually abbreviated G, plays the same role in describing shear as Young's Modulus does in describing longitudinal strain. It is defined by G = shear stress/shear strain. G can be calculated in terms of E and v: $G = E/2(1 + \nu)$. Since v ranges from 1/4 to 1/3 for most rocks, K is about 0.4 E.

1.12.4 Bulk Modulus

The bulk modulus, K, is the ratio of hydrostatic stress to the resulting volume change, or K = pressure/volume change.

It's easy to show the relationship between K, E, and Poisson's ratio (ν Consider the effects of pressure P acting on a unit cube equally along the x- y- and z-axes. The

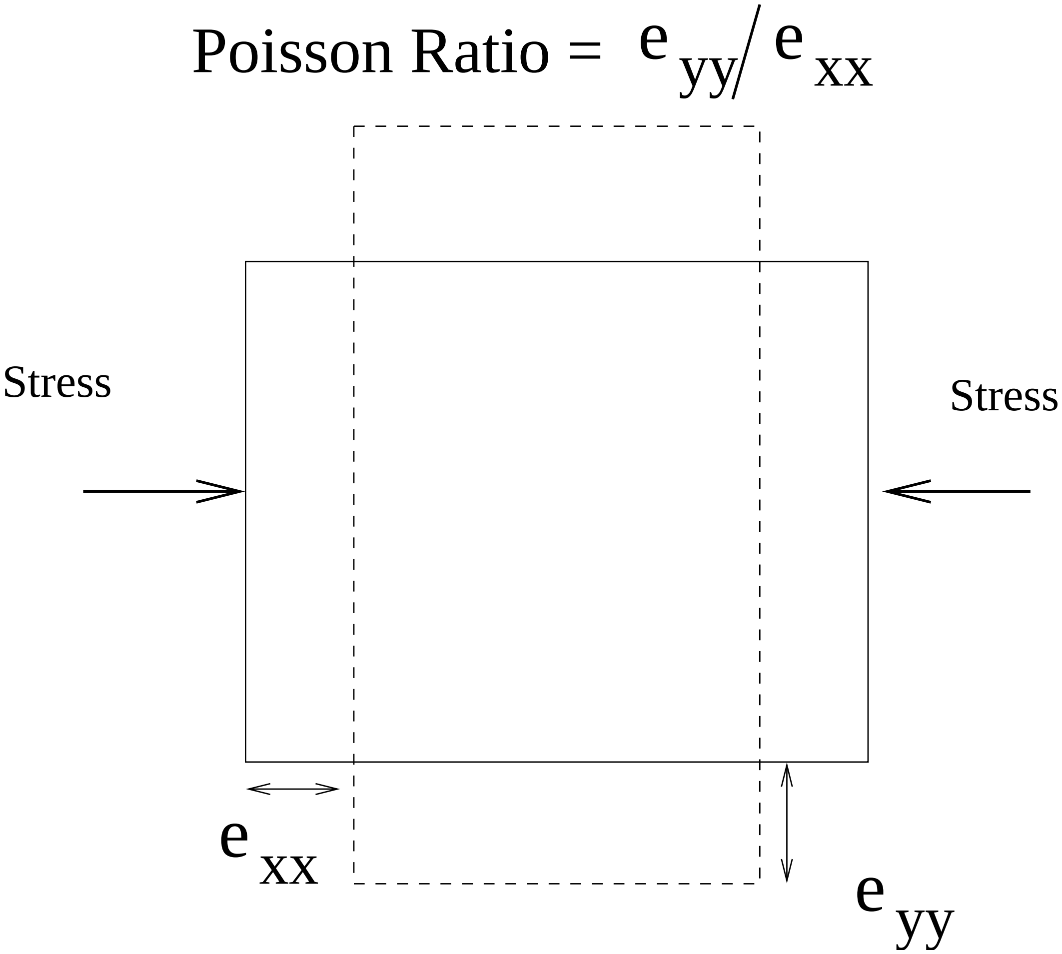

Figure 1.20: Compressing a box in one direction elongates it in the perpendicular direction.

Known	E=	ν =	G =	K =
E, n	E	ν	(E/2)/(1+ ν)	(E/3)/(1− 2 ν)
E, G	E	(E/2G)−1	G	(E/3)/(3−E/G)
E, K	E	(1−E/3K)/2	E/(3−E/3K)	K
G, n	2G (1+ν)	ν	G	2/3G(1+ν)/(1−2ν)
G, K	$12G^2/(3K+4G)$	(2G−3K)/(3K+4G)	G	K
K,ν	3K/ (1− 2ν)	ν	3/2K(1−2 ν)/(1 +ν)	K

Figure 1.21: Table of elastic constants. Only two of the constants are independent in an isotropic medium.

pressure along the x-axis will cause the cube to contract longitudinally by an amount P/E. However, it will also bulge to the side by an amount vP/E, in both the y- and z-directions. The net volume change just due to the component in the x-direction is (1 - 2ν P/E. The minus sign reflects the fact that the bulging counteracts the volume decrease due to compression. Similarly, compression along the y- and z- axes produces similar volume changes. The total volume change is thus 3(1 - 2ν P/E. Since K = P/volume change, thus K = E/(3(1 - 2ν Since v ranges from 1/4 to 1/3 for most rocks, K ranges from 2/3E to E.

Physically, K can be considered the stress it would take to result in 100 per cent volume change, except that's physically impossible and elastic strain rarely exceeds a few percent anyway.

If $\nu = 1/2$, then K becomes infinite - the material is absolutely incompressible. Obviously real solids cannot be utterly incompressible and therefore cannot have $\nu = 1/2$.

1.12.5 Relations Between Elastic Parameters

There are really only two independent quantities, so if we know any two quantities E, ν, G and K, we can calculate any others. The relations are shown in Figure 1.21. Find the two known parameters and read across to find the other two.

1.12.6 Viscous Deformation

Viscous materials deform steadily under stress. Purely viscous materials like liquids deform under even the smallest stress. Rocks may behave like viscous materials under high temperature and pressure.

Viscosity is defined by N = (shear stress)/(shear strain rate). Shear stress has the units of force and strain rate has the units 1/time. Thus the parameter N has the units force times time or kg/(m-sec). In SI terms the units are pascal-seconds. Older literature uses the unit poise; one pascal-second equals ten poises.

Bibliography

[1] Abma, R., 2006, Numerical precision and triangle filter antialiasing in Kirchhoff migrations: The Leading Edge, **25**, 20-23.

[2] Abramowitz, M. and I.A. Stegun, 1965, *Handbook of mathematical functions*, Dover, New York.

[3] Aki, K., A. Christoffersson, and E.S. Husebye, 1977, Determination of the three-dimensional seismic structure of the lithosphere, *J. of Geophysical Research*, **82, no. 2**, 277-296.

[4] Aki, K., and P. Richards, 1980, *Quantitative seismology*, Freeman and Company.

[5] Bakulin, A., A. Mateeva, R. Calvert, P. Jorgensen, and Jorge Lopez, 2007, Virtual shear source makes shear waves with air guns, *Geophysics*, **72**, A7-A11.

[6] Behura, J., 2007, Virtual real source, *77th Ann. Internat. Mtg., SEG Expanded Abstracts*, 2693-2697. of multiple reflections, *Geophysics*, **71**, SI209-SI220.

[7] Berryhill, J. R., 1979, Wave-equation datuming, *Geophysics*, **44**, 1329-1344.

[8] Berryhill, J., 1984, Wave-equation datuming before stack, *Geophysics*, **49**, 2064-2066.

[9] Bevc, D., 1995, *Imaging under rugged topography and complex velocity structure*, Ph.D. Thesis, Stanford University.

[10] Beylkin, G., 1985. Imaging of discontinuities in the inverse scattering problem by inversion of a causal generalized Radon transform: J. Math. Phys., 26, 99–108.

[11] Biondi, B., 2001, Kirchhoff imaging beyond aliasing: Geophysics, **66**, 654-664.

[12] Bishop, T., K. Bube, R. Cutler, R. Langan, P. Love, J. Resnick, R. Shuey, D. Spindler, and H. Wyld, 1985, Tomographic determination of velocity and depth in laterally varying media, *Geophysics* **50**, 903-923.

[13] Bjarnason, I. T. and J. Pechmann, 1989, Contemporary tectonics of the Wasatch front region, Utah, from earthquake focal mechanisms, *Seism. Soc. Am. Bull.*, **79**, 731-755.

[14] Bleistein, N., 1984. *Mathematical methods for wave phenomena*, Academic Press Inc., New York.

[15] Bleistein, N., J. Cohen, and J. Stockwell, 2001, *Mathematics of multidimensional seismic imaging, migration, and inversion*, Springer Verlag, Berlin.

[16] Bostock, M. G., and S. Rondenay, 1999, Migration of scattered teleseismic body waves, *Geophys. J. Int.*, **137,** 732–746.

[17] Brebbia, C.A., 1978, *The boundary element method for engineers*, J. Wiley and Co., New York.

[18] Bube, K., and Langan, R., 1994, A Hybrid l^1/l^2 minimization with applications to tomography: Geophysics, 62, 1183-1195.

[19] Calvert, R.W., A. Bakulin, A. and T.C. Jones, 2004, Virtual sources, a new way to remove overburden problems, 66th Mtg., European Association of Geoscientists and Engineers, Extended Abstracts, P234.

[20] Chen, J., and Schuster, G.T., 1999, Resolution limits for migration images: Geophysics, 1046-1053.

[21] Claerbout, J., 1968, Synthesis of a layered medium from its acoustic transmission response, *Geophysics*, **33**, 264–269.

[22] Claerbout, J., 1985, *Fundamentals of geophysical data processing: with applications to petroleum prospecting*, Blackwell Science. Inc., San Francisco, Calif.

[23] Claerbout, J., 1992, *Earth soundings analysis: Processing versus inversion*, Blackwell Scientific Publications, Cambridge, MA.

[24] de Hoop, A. T., 1995, *Handbook of radiation and scattering of waves*, Academic Press, New York.

[25] Derode, A., E. Larose, M. Tanter, J. de Rosny, A. Tourin, M. Campillo, and M. Fink, 2003, Recovering the Green's function from field-field correlations in an open scattering medium, *J. Acoust. Soc. Am.*, **113**, 2973-2976.

[26] Dong, S., R. He, and G.T. Schuster, 2006a, Interferometric prediction and least-squares subtraction of surface waves, *76th Ann. Internat. Mtg., SEG Expanded Abstracts*, 2783-2786.

[27] Dong, S., J. Sheng, and G.T. Schuster, 2006b, Theory and practice of refraction interferometry, *76th Ann. Internat. Mtg., SEG Expanded Abstracts*, 3021-3025.

[28] Dueker, K. G., and A. F. Sheehan, 1998, Mantle discontinuity structure beneath the Colorado Rocky Mountains and High Plains, *J. Geophys. Res.*, **103,**, 7153-7169.

[29] Eaton, D., 2006, Backscattering from spherical elastic inclusions and accuracy of the Kirchhoff approximation for curved interfaces, *Geophys. J. Int.*, **166**, 1249-1258.

[30] Elmore C. W. and Heald A. M., 1969, Physics of Waves: McGraw-Hill Book Company, New York, US.

[31] Fletcher, R., l987, Practical Methods of Optimization: J. Wiley and Sons, NY, NY.

[32] Fink, M., 1993, Time reversal mirrors, J. Phys. Rev.: Appl. Phys.,**26**, 1330-1350.

[33] Fink, M., 1997, Time reversal acoustics, Phys. Today, **50**, 34-40.

[34] Fink, M., 2006, Time-reversal acoustics in complex environments, *Geophysics*, **71**, SI151-SI164.

[35] Foster, D., Keys, R., and Reilly, J., 1997, Another perspective on AVO crossplotting: The Leading Edge, September issue.

[36] Gesbert, S., 2002, From acquisition footprints to true amplitude: Geophysics, **67**, 830-839.

[37] Gill, P., Murray, W., and Wright, M., 1981, Practical Optimization: Academic Press, NY, NY.

[38] Goertzel,, G., and N. Tralli, 1960, *Some mathematical methods of physics*, McGraw-Hill Book Co., New York.

[39] Groetsch, C., 1993, Inverse Problems in Mathematical Science: Vieweg Publ., Wiesbaden, Germany.

[40] Hilterman, F., 1970, Three-dimensional seismic modeling: *Geophysics*, **40**, 745-762.

[41] Kelly, K., S. Ward, S. Treitel, and R. Alford, 1976, Synthetic seismograms: A finite-difference approach, *Geophysics*, **41**, 2-27.

[42] Kinsler, L. and A. Frey, 1961, Fundamentals of Acoustics, . ley and Sons, NY, NY.

[43] Keys, R., 1985, Absorbing boundary conditions for acoustic media: Geophysics, **50**, 892-902.

[44] Kuperman, W.A, and F. Ingenito, 1980, Spatial correlation of surface generated noise in a stratified ocean, *J. Acoust. Soc. Am.*, **67**, 1986-1996.

[45] Langan, R., I. Lerche, and R. Cutler, 1985, Tracing of rays through heterogeneous media: An accurate and efficient procedure, *Geophysics*, **50**, 1456-1465.

[46] Langston, C. A., 1977, The effect of planar dipping structure on source and receiver responses for constant ray parameter, *Seism. Soc. of Am. Bull.*, **67,** 1029-1050.

[47] Langston, C. A., 1979, Structure under Mount Rainer, Washington, inferred from teleseismic body waves, *J. of Geophysical Research*, **84**, 4749-4762.

[48] Langston, C. A., A. Nyblade, and T. Owens, 2001, The vertical component P-wave receiver function, *Seism. Soc. of Am. Bull.*, **91**, 1805-1819.

[49] Levander, A. R, 1988, Fourth-order, finite-difference P-SV seismograms, *Geophysics*, **53**, 1425-1436.

[50] Lobkis, O., and R. Weaver, 2001, On the emergence of the Green's function in the correlations of a diffuse field, *J. Acoust. Soc. Am.*, **110**, 3011-3017

[51] Loeb, D. T., 1986, The P-wave velocity structure of the crust-mantle boundary beneath Utah, M. S. Thesis, Univ. of Utah, Salt Lake City, Utah.

[52] Loeb, D. T., and J. Pechmann, 1986, The P-wave velocity structure of the crust-mantle boundary beneath Utah from network travel time measurement, *Earthquake Notes*, **57**, 10.

[53] Lumley, D., Claerbout, J., and Bevc, D., 1994, Anti-aliased Kirchhoff 3-D migration: 64th Ann. Internat. Mtg., Soc. Expl. Geophys. Expanded Abstracts, 1282-1285.

[54] Mercier, J., M. Bostock, and A. Baig, 2006, Improved Green's functions for passive-source structural studies, *Geophysics*, **71**, SI95-SI102.

[55] Mitchell, A., and D. Griffitchs, 1980, The Finite Difference Method: Wiley, New York.

[56] Morse, P., and H. Feshbach, 1953, *Methods of theoretical physics (Part I)*, McGraw-Hill book Co., New York.

[57] Nemeth, T., Qin, F., and Normark, E, 1997, Dynamic smoothing in crosswell traveltime tomography: Geophysics, 62, 168-176.

[58] Nolet, G., 1987, *Seismic tomography: with applications in global seismology and exploration*, Springer Publ. Co..

[59] Nowack, R.L., S. Dasgupta, G.T. Schuster, and J. Sheng, 2003, Correlation migration of scattered teleseismic body waves with application to the 1993 Cascadia experiment, *Eos. Trans. AGU*, **84(46)**, S32A-0835.

[60] Nowack, R.L., S. Dasgupta, G.T. Schuster, and J.M.Sheng, 2006, Correlation migration using Gaussian beams of scattered teleseismic body waves, *Bull. Seism. Soc. Am.*, **96**, 1-10.

[61] Oppenheim, A. and Wilsky, A., 1983, *Signals and systems*, Prentice-Hall Publ. Co., New Jersey.

[62] Ostrander, W.,1984, Plane-wave reflection coefficients for gas sands at nonnormal angles of incidence: Geophysics, **49**, 1637-1648.

[63] Qin F., Y. Luo, K. Olsen, W. Cai, and G.T. Schuster, 1992, Finite difference solution of the eikonal equation along expanding wavefronts, *Geophysics*, **57**, 478-487.

[64] Rickett, J., and J. Claerbout, 1999, Acoustic daylight imaging via spectral factorization: Helioseismology and reservoir monitoring, *The Leading Edge*, **18**, 957-960.

[65] Schmerr, N. and E. Garnero, 2007, Upper mantle discontinuity from thermal and chemical heterogeneity, *Science*, **318**, 623-626.

[66] Schneider, W., 1978, Integral formulation for migration in two and three dimensions, *Geophysics*, **43**, 49-76.

[67] Schuster, G.T., 1996, Resolution limits for crosswell migration and traveltime tomography: Geophysical J. Int., 427-440.

[68] Schuster, G., and J. Rickett, 2000, Daylight imaging in V(x,y,z) media, Utah Tomography and Modeling-Migration Project Midyear Report and SEP Report at Stanford University.

[69] Schuster, G. T., 2001, Seismic interferometric/daylight imaging: Tutorial, *63rd Ann. Conference, EAGE Extended Abstracts.*

[70] Schuster, G. T., 2002, Reverse time migration = generalized diffraction stack migration, *72nd Ann. Internat. Mtg., SEG Expanded Abstracts*, 1280-1283.

[71] Schuster, G. T., Z. Jiang, and J. Yu, 2003, Imaging the most bounce out of multiples, *65th Annual Conference, EAGE Expanded Abstracts: session on Multiple Elimination.*

[72] Schuster, G. T., J. Sheng, J. Yu, and J. Rickett, 2004, Interferometric/daylight seismic imaging, *Geoph. J. Internat.*, **157**, 838-852.

[73] Shuey, R.T., 1985, Application of the Zoeppritz equations: Geophysics, 609-614.

[74] Sheng, J., G.T. Schuster, and R. Nowack, 2002, Imaging of crustal layers by teleseismic ghosts, *American Geophysical Union, Fall Mtg.*, S32C-0658.

[75] Sheng, J., and Schuster, G.T., 2003, Finite-frequency resolution limits of wave path traveltime tomography for smoothly varying models: Geophys. J. Int., **152**, 669-676.

[76] Shragge, J., B. Artman, and C. Wilson, 2006, Teleseismic shot-profile migration, *Geophysics*, **71**, SI221-SI229.

[77] Simm, R., White, R., and Uden, R., 2000, The anatomy of AVO crossplots, The Leading Edge, Vol. 19, No. 2, pp. 150-155.

[78] Snieder, R., 1987, Surface wave holography, in ”Seismic Tomography by Guust Nolet”, 323-337.

[79] Snieder, R., A. Gret, H. Douma, and J. Scales, 2002, Coda wave interferometry for estimating nonlinear behavior in seismic velocity, Science, **295**, 2253–2255.

[80] Snieder, R., 2004, Extracting the Green’s function from the correlation of coda waves: A derivation based on stationary phase, *Phy. Rev. E*, **69**, 046610.

[81] Snieder, R. and E. Safak, 2006, Extracting the building response using seismic interferometry: Theory and application to the Millikan library in Pasadena, California, *Seism. Soc. of Am. Bull.*, **96**, 586-598.

[82] Snieder, R. , 2006, Extracting the Green’s function of attenuating heterogeneous acoustic media from uncorrelated sources, *J. Acoust. Soc. Am.*, **121**, 2637-2643.

[83] Stolt, R., and A. Benson, 1986, *Seismic migration: theory and practice, in Handbook of Geophysical Exploration* , Volume 5, Geophysical Press, London, UK.

[84] Tenghamn, R., Vaage, S., and Borresen, C., 2007, A dual-sensor, towed marine streamer: Its viable implementation and initial results: SEG Expanded Abstracts **26**, 989-992.

[85] Verschuur, D. H., A.J. Berkhout, and C.P.A. Wapenaar, 1992, Adaptive surface related multiple elimination, *Geophysics*, **57**, 1166-1177.

[86] Vidale, J.E., 1990, Finite-difference calculation of traveltimes in three dimensions: Geophysics, **58**, 521-526.

[87] Wapenaar, K., 2004, Retrieving the elastodynamic Green's function of an arbitrary inhomogeneous medium by cross correlations, *Phys. Rev. Lett.*, **93**, 254301–1-254301-4.

[88] Wapenaar, K., J. Fokkema, and R. Snieder, 2005, Retrieving the Green's function in an open system by cross-correlation: a comparison of approaches, *J. Acoust. Soc. Am.*, **118(5)**, 2783-2786.

[89] Wapenaar, K, and J. Fokkema, 2006, Green's function representations for seismic interferometry, *Geophysics*, **71**, SI33-SI46.

[90] Wapenaar, K., 2006, Seismic interferometry for passive and exploration data: Reconstruction of internal multiples, *76th Ann. Internat. Mtg., SEG Expanded Abstracts*, 2981-2985.

[91] Wapenaar, K., D. Draganov, and J. Robertsson, 2006, Supplement seismic interferometry: Introduction, *Geophysics*, **71**, SI1-SI14.

[92] Xiao, X., 2008, *Local reverse-time migration with VSP Green's functions,* Ph.D Dissertation, University of Utah.

[93] Xue, Y. and G.T. Schuster, 2007, Surface-wave elimination by interferometry with nonlinear local filter, *77th Ann. Internat. Mtg., SEG Expanded Abstracts*, 2620-2624.

[94] Yan, Y., and Brown, R., 2001, The suppression of water-column multiples by wavefield separation and cross-correlation: SEG Expanded Abstracts **20**, 1309-1303.

[95] Yilmaz, O., 2001, *Seismic data analysis (2nd edition)*, SEG Publishing, Tulsa, Oklahoma.

[96] Yu, J. and G.T. Schuster, 2006, Crosscorrelogram migration of inverse vertical seismic profile data, *Geophysics*, **71**, S1-S11.

[97] Zhang, J. and Toksoz, N., 1998, Nonlinear refraction traveltime tomography: **63**, 1726-1737.

[98] Zoeppritz, K., 1919, Erdbebenwellen VIII B, On the reflection and penetration of seismic waves through unstable layers: Goettinger Nachr., pages 66-84.

Index